

©2015

SEBASTIÁN L. VEGA

ALL RIGHTS RESERVED

SINGLE CELL ORGANIZATIONAL IMAGING OF CYTOSKELETAL AND NUCLEAR PROTEINS:
CORRELATIONAL STUDIES AND CLASSIFICATION OF STEM CELL STATES

by

SEBASTIÁN L. VEGA

A Dissertation submitted to the

Graduate School-New Brunswick

Rutgers, The State University of New Jersey

in partial fulfillment of the requirements

for the degree of

Doctor of Philosophy

Graduate Program in Chemical and Biochemical Engineering

written under the direction of

Dr. Prabhas V. Moghe

and approved by

New Brunswick, New Jersey

January 2015

ABSTRACT OF THE DISSERTATION

SINGLE CELL ORGANIZATIONAL IMAGING OF CYTOSKELETAL AND NUCLEAR PROTEINS:
CORRELATIONAL STUDIES AND CLASSIFICATION OF STEM CELL STATES

By SEBASTIÁN L. VEGA

Dissertation Director:

Dr. Prabhas V. Moghe

Two major challenges plague the robust design of stem cell-derived tissues for regenerative therapies: (1) the phenotypic and functional heterogeneity inherent in stem cell cultures, and (2) the dynamic, long-term nature of stem cell responses to microenvironmental cues. Several tools have emerged to precisely characterize how stem cells respond to various stimuli and scaffold properties; however, these tools are limiting because they are population-based and rely on the detection of markers expressed in fully differentiated cells. Thus, methods to characterize individual stem cells from a population is key for establishing cell-biomaterial relationships necessary to design scalable constructs for tissue engineering applications.

This thesis dissertation focuses on the utility of single cell profiling techniques to identify the heterogeneity within cell cultures and characterize responses to controllable changes in diverse microenvironments. This method relies on the quantification of metrics derived from images of cytoskeletal and nuclear proteins that

are sensitive to microenvironmental cues that influence cell state. This is achieved by pursuing two thesis-specific aims: (1) to utilize single cell biological imaging and machine learning techniques to identify cell subtypes in heterogeneous cultures, and (2) to use early morphological descriptors of intranuclear mechanotransductive proteins to predict long-term stem cell responses to biomaterials.

In this study we report that single cell imaging-based profiling of cytoskeletal actin and nuclear mitotic apparatus (NuMA), a cell cycle regulating protein, can identify different cell phenotypes in heterogeneous stem cell cultures, progenitor cells derived from different tissue sections *ex vivo*, and stem cell responses to a diverse set of surface chemistries. We also show that the early (3 day) organization of interchromatin domains varies in human mesenchymal stem cells exposed to a variety of growth factor combinations and complex topographical microenvironments that induce long-term (> 7 day) divergent phenotypic outcomes.

In summary, the results presented in this thesis dissertation show that single cell imaging-based profiling can be utilized to identify cell subtypes and predict microenvironment-induced differentiation fates at earlier times and with more resolution than current screening assays. This work can help lay the foundation for a new generation of single cell-based biomaterial screening tools and cellular phenotyping techniques.

ACKNOWLEDGMENTS

These past six years I have grown as a scientist, as a thinker, and as a mentor. The interdisciplinary nature of my research has exposed me to a diverse set of experimental and computational tools, and has trained me to become an efficient scientific reader and writer. As a Ph.D. candidate I had the chance to constantly interact with extremely talented people, publish in peer-reviewed journals, present in national conferences, and participate in an international internship with a collaborating laboratory. There are no words that describe how rewarding the Ph.D. experience has been for me, and I am extremely thankful and grateful for the people that have made it all possible.

I would first and foremost like to thank Dr. Prabhas Moghe, my primary thesis advisor. Over the years he has provided me with a balance between guidance when needed, and the intellectual independence to pursue research in several different directions. As a result, I took ownership of my own projects which taught me the frustrations of poorly-designed experiments, and the successes of carefully planned, hypothesis-driven research. Dr. Moghe's mentoring approach has helped me become a strong, independent thinker, and has set a foundation on which I can continue to advance my scientific career. For that, Dr. Moghe, I thank you.

I would like to thank Dr. Joachim Kohn, my thesis co-advisor. Opportunities to collaborate with several members from his laboratory instilled a growing interest in biomaterials and their expanding applicability in regenerative medicine, which I plan to pursue in my next academic appointment. Dr. Kohn has also invited me on several

occasions to present my research at his group meetings, which gave me the opportunity to improve my presentation skills, and get feedback from an extremely intelligent group of people. I am also thankful for the one-on-one meetings we had; I received very good advice and insights that I will never forget.

Next, I would like to thank Dr. Yannis Androulakis and Dr. Lourdes Serrano for supporting my research plans and for being part of my thesis committee. I also thank Dr. Evelyn Erenrich for giving me the chance to participate in outreach activities. Together we have hosted several workshops aimed at helping students develop skills to succeed in academia, which has exposed me to grant writing, networking, and event planning.

I thank Dr. Jan de Boer for inviting me to do an academic internship in his laboratory at Twente University in the Netherlands. During my time there, I learned new biomaterial fabrication, imaging, and computational analysis techniques. I would also like to thank Priya, Nick, Frits, Natalie, Ivan, and Miriam for all of their help in the lab, and for the memorable experiences we had outside of the lab. Dr. de Boer, thank you for making me feel like a member of your research team.

I would like to thank Dr. Matthew Treiser for taking me under his wing when I first joined Dr. Moghe's laboratory, and Dr. Er Liu for being both a good mentor and friend. Simon Gordonov and Tony Kulesa, you were both very talented and dedicated undergraduates, and I cannot thank you enough for your contributions to my research.

Parth Patel, you are the first undergraduate student that I formally trained, and I thank you for teaching me how to be a good mentor. I also thank you for the countless hours you spent by my side culturing cells, immunostaining, imaging, and running

Matlab scripts. When going over my experimental designs with you, if you thought that something could be done more efficiently, you always voiced your opinion. Even though it was not appreciated at times, in hindsight I am thankful for your input. You were a great colleague, and I am looking forward to the day that I can call you a medical doctor.

Out of all the undergraduates I have worked with, I have known Varun Arvind the longest. I met Varun during my first summer at Rutgers, when he was a high school freshman shadowing the Moghe lab. Varun continued to come every summer, and then joined the Rutgers Biomedical Engineering undergraduate program. Over the many years we have worked together I have taught him everything I know. He has helped me with all aspects of my graduate life, from everyday lab work, to designing experiments and reviewing research documents. Varun, thank you so much for everything you have done for me. I am really proud of you, and I am certain that your successes as a scientist will continue to grow in the future.

My experience at Rutgers would not have been complete without the friends I made in the graduate program along the way. I especially would like to thank Dominik, George, Sven, Adam, Craig, Leonardo, Emmanuel, Joe, Jocie, Margot, Jing, Maria, Aaron, Shirley, Devang, Latrisha, and Jay. Their friendships and the good times we spent, both in and out of the laboratory I will never forget and always cherish.

Last but not least, I would like to thank my family, Pittsburgh friends, Carnegie Mellon friends, and Samsung buddies. You have all supported me and helped me get through the Ph.D. program, whether you realize it or not. And for all of those who I have not mentioned but have helped me over these years, I thank you.

DEDICATION

I would like to dedicate my thesis dissertation to my family. Your unconditional love and support has given me the strength to be the best I can be to earn my Ph.D. This journey has been a long one, with many obstacles and challenges along the way, and you were always by my side, both in times of celebration, and in times of need.

My mother, Susana Fuentes, you are the best mom any son could ever ask for. You have never fallen short of reminding me to be responsible, to work hard, and to rest and relax. You also never thought twice if I ever needed anything, whether it was someone to talk to if something was troubling me, or a little bit of money to get groceries between paychecks. I want to reciprocate the love you constantly give me by making you as proud as can be.

My father, Rodolfo Vega, the most knowledgeable man I know. When I was a boy, you taught me how things worked, and from a young adult onwards you have continued to motivate my curiosity to learn by posing interesting philosophical questions that have made me think for hours on end. You have shaped me into the intellectual that I am today, and my ability and will to write this dissertation is a direct consequence of that.

My brother, Gonzalo Vega, you have been my best friend since the day you were born. You have shown a strong interest in my research, and have been extremely supportive throughout the years. Calli Vega, you are a great sister-in-law. Your encouragement and support resonates strongly with me. I would also like to dedicate my thesis dissertation to Keehn Leonardo Vega, my baby nephew. I cannot wait to teach

him about how the world works, so that he can develop the same passion and love for science that his uncle has.

My sister, Karina Vega, you took care of my brother and I when mom and dad were at work, and you always remind me of how proud you are of your baby brother. Mis abuelitas, Regina and Alicia, I also dedicate my thesis dissertation to you. You have spoiled me with love, sweets, and amazing Chilean food - the least I can do is give you your first Ph.D. grandson.

I am grateful to have you all in my life, and I love you and thank you for that.

TABLE OF CONTENTS

ABSTRACT OF THE DISSERTATION	ii
ACKNOWLEDGMENTS.....	iv
DEDICATION	vii
TABLE OF CONTENTS.....	ix
LIST OF TABLES.....	xiii
LIST OF FIGURES.....	xiv
CHAPTER 1. INTRODUCTION	1
1.1 TISSUE ENGINEERING.....	2
1.2 ORTHOPEDIC TISSUE ENGINEERING	6
1.2.1 Cells	7
1.2.2 Biodegradable Materials.....	12
1.3 LIMITATIONS OF CURRENT CELL-MATERIAL SCREENING TOOLS.....	16
1.4 HYPOTHESIS AND AIMS OF THE DISSERTATION	18
CHAPTER 2. SINGLE CELL IMAGING-BASED PROFILING	22
2.1 INTRODUCTION OF FLUORESCENCE IMAGING OF CELL-BIOMATERIAL INTERACTIONS.....	23
2.2 SINGLE CELL IMAGING-BASED PROFILING: PAST AND PRESENT	25
2.2.1 Imaging of Cell Cytoskeletal Remodeling and Apoptosis on Biomaterials	27
2.2.2 Fluorescence Imaging of 3-D Polymer Scaffolds and Cellular Organization	30
2.2.3 Fluorescent Reporter Imaging for Analysis of Cell-Material Interactions	32
2.2.4 High Content and High-Throughput Imaging of Cell-Biomaterial Interactions	35
2.3 CURRENT LIMITATIONS OF PROFILING CELL-MATERIAL INTERACTIONS.....	39
2.4 OUTSIDE-IN SIGNALING	40
2.4.1 Actin	42
2.4.2 Chromatin	45
2.4.3 NuMA	46
2.4.4 Interchromatin Domains.....	49
CHAPTER 3. ACTIN- AND NUMA-BASED IMAGING FOR SINGLE CELL PHENOTYPING	52
3.1 ABSTRACT.....	53
3.2 INTRODUCTION.....	54
3.3 MATERIALS AND METHODS	57
3.3.1 Fabrication of SAM Gradients	57

3.3.2 Preparation of Polymer Films Copolymerized with PEG	57
3.3.3 Cell Culture.....	58
3.3.4 Stem Cell Staining and Immunocytochemistry	59
3.3.5 High Content Imaging of Stem Cells	60
3.3.6 Numerical Descriptor Acquisition and Analysis	60
3.3.7 Statistical Analysis.....	61
3.4 RESULTS	65
3.4.1 Overview of Imaging-Based Profiling.....	65
3.4.2 hESC Nuclear Features are Reflective of Phenotypic States.....	68
3.4.3 Nuclear Features of iPSCs Are Unique to Sox2 Expression.....	71
3.4.4 Polymer Film PEG Content Induces Changes in hMSC Cytoskeleton.....	73
3.4.5 NuMA Descriptors Discern hMSC Differentiation on SAM Gradients	77
3.5 DISCUSSION.....	81
CHAPTER 4. NUMA ORGANIZATION AS A DETERMINANT OF STEM CELL PHENOTYPIC STATES...	87
4.1 ABSTRACT.....	88
4.2 INTRODUCTION.....	89
4.3 MATERIALS AND METHODS	91
4.3.1 Cell Culture.....	91
4.3.2 Preparation of OPC Samples for Early (4 Hour) NuMA-Based Image Analysis	93
4.3.3 Long-Term (10 Day) Clonal Analysis of OPCs	93
4.3.4 NuMA Expression in HEK-293 Cells.....	94
4.3.5 Etoposide and Taxol Treatments of HEK-293 Cells.....	94
4.3.6 Immunocytochemistry (ICC)	95
4.3.7 High Content Imaging and Profiling.....	95
4.3.8 Preparation of Polymeric Substrates for hMSC Transformation Study	102
4.3.9 Characterization of hMSC Oncogenic Transformation via FISH.....	102
4.4 RESULTS	105
4.4.1 NuMA-Based Metrics Predict Oncogenicity of Surface Chemistries for NiSO ₄ -Treated hMSCs	105
4.4.2 NuMA-Based Metrics Distinguish OPCs from Different Brain Regions of Neonatal Rats	108

4.4.3 NuMA Descriptors Parse Between Live HEK-293 Cells with and without DNA-Damage Treatment	111
4.5 DISCUSSION.....	114
CHAPTER 5. INTERCHROMATIN DOMAINS USED TO PREDICT STEM CELL DIFFERENTIATION	121
5.1 ABSTRACT.....	122
5.2 INTRODUCTION.....	124
5.3 MATERIALS AND METHODS	130
5.3.1 Cell Culture.....	130
5.3.2 Fabrication of Surface Textures	131
5.3.3 Fabrication and Characterization of Microfibrous Scaffolds	131
5.3.4 Fabrication of Micropillars	132
5.3.5 Fluorescence- and Immuno-staining for Confocal Imaging.....	133
5.3.6 Analysis of Nuclear Protein Organization	133
5.3.7 Assessment of Cell Differentiation.....	135
5.3.8 Inhibition of RhoGTPase, FAK, and β -Catenin.....	136
5.3.9 Statistics	137
5.4 RESULTS	138
5.4.1 Nuclear Proteins as a High Content Screen to Parse Stem Cell Differentiation	138
5.4.2 High Content Analysis of SC-35 Descriptors Discern <i>Dex</i> -Induced Bone Predisposition within 3 Days.....	146
5.4.3 SC-35 Descriptors Discern Surface Topography-Induced Osteogenic Fates within 3 Days.....	149
5.4.4 3 Day SC-35 Descriptors Distinguish Bone Predisposition Outcomes in Response to Fibrous Scaffold Features.....	152
5.4.5 Analysis of SC-35 Descriptors can Track hMSC Differentiation on Micropillars within 3 Days.....	156
5.4.6 Pharmacological Inhibition of Signaling Molecules Governing Osteogenesis Results in Quantifiable Alterations in SC-35 Organization	160
5.4.7 Tracking Microenvironment-Mediated Osteogenic Differentiation Using Haralick Texture Features of SC-35 Domains.....	164
5.5 DISCUSSION.....	169
5.6 CONCLUSIONS.....	175
CHAPTER 6. SUMMARY AND FUTURE DIRECTIONS	176

6.1 RESEARCH SUMMARY	177
6.2 FUTURE DIRECTIONS	180
6.2.1 Actin Morphology and Signaling Kinetics: A Systems Biology Approach	180
6.2.2 High Content and High-Throughput Profiling of Live Cell Cultures	187
6.3 CLOSING THOUGHTS	193
CHAPTER 7. APPENDIX	194
7.1 TOOLS AND TECHNIQUES FOR CELLULAR IMAGING	195
7.1.1 Epifluorescence and Deconvolution Microscopy	195
7.1.2 Confocal Microscopy	197
7.1.3 Multiphoton Microscopy	202
7.1.4 FRET and TIRFM	206
7.1.5 Flow Cytometry	209
7.2 FLUORESCENCE-BASED PROBES FOR CELLULAR PROFILING	210
7.2.1 Fluorophore-Tagged Antibodies	210
7.2.2 Quantum Dot-Based Probes	211
7.2.3 GFP and Variants	212
CHAPTER 8. REFERENCES	214

LIST OF TABLES

Table 3.1: Table of Descriptors Used in Chapter 3 Study	63
Table 3.2: SVM Classification Results for hMSCs on PEG-Containing Films	76
Table 3.3: SVM Classification Results for Several Locations on SAM Gradient	80
Table 3.4: Top Descriptors for Parsing Between Pluripotent and Differentiating Cells	84
Table 3.5: Top Descriptors for Parsing hMSCs on Films of Varying % PEG	85
Table 4.1: List of Nuclear and NuMA Protein Descriptors	100
Table 4.2: Biomaterial Library Used to Rank Effects of NiSO ₄ -Induced Oncogenic Transformation	104
Table 4.3: Most Influential Descriptors in Parsing TSRs from hMSCs	118
Table 4.4: Most Influential Descriptors in Parsing OPCs from Different Sources	119
Table 4.5: Most Influential Descriptors in Parsing HEK-293 Cells with and without DNA- Damage Treatment	120
Table 5.1: Summary of Electrospinning Parameters for Fibrous Scaffolds	132
Table 5.2: List of the 13 Haralick Texture Features Used in Chapter 5	135
Table 5.3: Summary of Most Significant Haralick Features Across Growth Factor Conditions	167
Table 5.4: Summary of Most Significant Haralick Features Across Different Topographies	168
Table 7.1: Comparison of Wide-Field, Confocal, and Multiphoton Microscopy	205
Table 7.2: List of Common Fluorescence Proteins	213

LIST OF FIGURES

Figure 1.1: Cartoon of Different Stem Cell Types and Sources	8
Figure 1.2: Simplified Cartoon of Osteogenic Differentiation Pathway	12
Figure 1.3: Chemical Structure of Poly(DTE-co-XX%DT-co-YY%PEG carbonate)	14
Figure 2.1: Imaging of Actin and Functional Reporters During Apoptosis.....	29
Figure 2.2: Comparison of MPM and CLSM Images of GFP-Fibroblasts in 3-D Scaffolds	31
Figure 2.3: GFP-Tagged Subcellular Reporters on a Subset of Biomaterials	34
Figure 2.4: Cell Attachment Characterization on Roughness Gradient Chip	37
Figure 2.5: High Content Imaging of GFP-f Saos-2 Cells on Roughness Gradient.....	38
Figure 2.6: Simplified Overview of ECM-Induced Outside-In Signaling	41
Figure 2.7: Actin Morphology is Dependent of Key Signaling Molecules and Yields Divergent Differentiation Outcomes	44
Figure 2.8: Role of NuMA During Asymmetric Cell Division	47
Figure 2.9: SC-35 Domains and Their Localization to Euchromatic Regions.....	51
Figure 3.1: Imaging-Based Profiling Methodology for Two Subgroups	64
Figure 3.2: Single Cell Imaging, Feature Extraction, and Computational Modeling	67
Figure 3.3: NuMA Descriptors Dependent on Oct4 Expression in hESC Cultures	70
Figure 3.4: NuMA Descriptors Dependent on Sox2 Expression in iPSC Cultures.....	72
Figure 3.5: hMSC Actin Descriptors Dependent on % PEG in Polymer Films	75
Figure 3.6: NuMA Organization of hMSCs Cultured on Hydrophobicity Gradient	79
Figure 4.1: Image Processing and Feature Extraction from the Cell Nucleus.....	98
Figure 4.2: In Silico Data Processing of NuMA Morphometric Descriptors	101
Figure 4.3: Chemical Structures of Biomaterials Used in Transformation Study	103
Figure 4.4: NuMA Protein Imaging Used to Profile Synthetic Materials for Long-Term Oncogenic Effects on Stem Cells.....	107
Figure 4.5: NuMA Descriptors Distinguish OPCs from Different Brain Regions	110
Figure 4.6: NuMA-Based Metrics can Parse Between Live HEK-293 Cells with and without DNA- Damage Treatment	113
Figure 5.1: Workflow Highlighting Utility of Nuclear Imaging-Based Profiling.....	128
Figure 5.2: SC-35 Organization as a Screen to Parse Stem Cell Differentiation	139
Figure 5.3: Osteogenic and Adipogenic Differentiation of hMSCs	140
Figure 5.4: Fluorescence Intensity of hMSCs in BA, AD, or OS for 3 Days	140
Figure 5.5: SC-35 Gene Expression of hMSCs Cultured in AD or OS for 3 Days.....	142
Figure 5.6: EZH2 Organization Results of hMSCs Cultured in BA, AD, and OS for 3 Days	143
Figure 5.7: RUNX2 Organization Results of hMSCs Cultured in BA, AD, and OS for 3 Days	143
Figure 5.8: Lamin Organization Results of hMSCs Cultured in BA, AD, and OS for 3 Days	144
Figure 5.9: H3K4me3 Organization Results of hMSCs Cultured in BA, AD, and OS for 3 Days	144
Figure 5.10: List of SC-35 PCs and Descriptors of hMSCs Cultured in BA, AD, or OS Medium	145
Figure 5.11: SC-35 Domain Descriptors Distinguish Dex-Induced ALP Expression within 3 Days	147
Figure 5.12: List of PCs and Descriptors of hMSCs Cultured in Varying Dex Concentrations.....	148

Figure 5.13: SC-35 Descriptors Discern Differences in Surface Topography-Induced ALP Expression within 3 Days	150
Figure 5.14: List of PCs and Descriptors of hMSCs Cultured on Different Surface Patterns	151
Figure 5.15: SC-35 Descriptors Discern Fibrous Scaffold Topography-Induced ALP Expression within 3 Days.....	153
Figure 5.16: List of PCs and Descriptors of hMSCs Cultured on Small versus Large Random Fibers	154
Figure 5.16: List of PCs and Descriptors of hMSCs Cultured on Small versus Large Aligned Fibers	155
Figure 5.18: SC-35 Descriptors can Identify ALP Expression on Micropillars within 3 Days.....	158
Figure 5.19: List of PCs and Descriptors of hMSCs Cultured on Micropillars	159
Figure 5.20: Pharmacological Inhibitors Do Not Affect Cell Viability	161
Figure 5.21: Classification of hMSCs Treated with Different Inhibitors Using SC-35 Descriptors.....	162
Figure 5.22: List of PCs and Descriptors of hMSCs Cultured with Pharmacological Inhibitors....	163
Figure 5.23: Tracking Microenvironment-Modulated Osteogenic Differentiation Using SC-35 ..	165
Figure 5.24: Microarray Analysis of RhoA, FAK, and β -Catenin Expression in hMSCs Cultured in BA, AD, and OS Media.....	174
Figure 6.1: Evolution of Actin Polymerization of an hMSC for 3 Days.....	182
Figure 6.2: Actin Dynamics Show Progressively Divergent Descriptor Sets	183
Figure 6.3: RhoA Expression Undergoes Temporal Media-Dependent Changes	185
Figure 6.4: Preliminary Pharmacological Inhibitor Study	186
Figure 6.5: Schematic of LCM Workflow.....	189
Figure 6.6: Zeiss PALM used to selectively ablate MSCs.....	190
Figure 6.7: Schematic of FACS Workflow.....	192
Figure 7.1: Schematic of an Epifluorescence Microscope System.....	196
Figure 7.2: Schematic of a Laser Scanning Confocal Microscope System	198
Figure 7.3: Schematic of a Spinning Disk Confocal Microscope System.....	201
Figure 7.4: Schematic of a Multiphoton Microscope System	203

CHAPTER 1. INTRODUCTION

1.1 TISSUE ENGINEERING

Tissue engineering is an emerging field that seeks to repair or restore tissues tailored to patients with the aim of mimicking the body's native tissue as closely as possible. In its simplest form, tissue engineering seeks to develop scaffolds that provide chemical, mechanical, and structural cues for cells to integrate for the creation of neo-tissues and -organs *in vitro* or *in vivo* [1]. The bulk chemistry of these scaffolds typically consists of either synthetic polymers (e.g., poly(lactic acid) (PLA), poly(lactic-glycolic acid) (PLGA), or polycaprolactone (PCL)) or naturally-derived polymers (e.g., hyaluronic acid (HA), chitosan, collagen, or fibrin) [2]. To engineer a wide range of stiffness, shapes, porosities, and architectures, many fabrication techniques have been developed [3, 4]. However, in order to utilize these scaffolds to their full potential, there is a need for robust and quantitative methods of assessing cellular responses to a diverse set of scaffold properties.

Tissue engineering emerged from concurrent advances in cell biology and the field of transplantation. The synergy between the two date back to as early as 1933, when Bisceglie and coworkers implanted a polymer membrane with mouse tumor cells into the abdominal cavity of a pig, noting that the mouse cells were not killed by the pig's immune system [5]. In 1975, Chick et al. successfully showed that they were able to control insulin release of encapsulated pancreatic islet cells by varying glucose levels [6]. Since then, technological advances have led to the development of functional tracheas [7], bladders [8], and urethras [9], which have been grown *in vitro* prior to patient implantation.

The ultimate goal of tissue engineering strategies is to develop scaffolds that elicit desired cellular outcomes (e.g., proliferation, differentiation, and/or phenotype retention). To accomplish, cell-scaffold constructs can either be assembled *in vivo*, or *in vitro*. *In vivo* tissue engineering strategies take advantage of the ability of the recipient's native cells to integrate and make an acellular implant functional. The implant is fabricated from either natural or synthetic polymers that are permanent, or degrade over time [10]. The scaffold provides the chemical cues and mechanical support necessary to promote and maintain cellular attachment, growth, differentiation, and maintenance of cellular phenotype [11, 12]. To-date, *in vivo* tissue engineering has been utilized in applications including hernia repair [13], sutures [14], and orthopedic devices [15, 16]. Due to the lack of a vascular network, most of the work performed involving *in vivo* tissue engineering focuses on the replacement and repair of connective tissues, including bone, cartilage, and skin [17]. Without vasculature, there are significant oxygen diffusion limitations which restrict the use of *in vivo* tissue engineering for more complex tissues and organs [18].

An alternative to the use of acellular scaffolds prior to implantation is the application of *in vitro* tissue engineering strategies [19]. These strategies focus on the manipulation of isolated cells *in vitro* prior to implantation *in vivo* [20]. The cell-scaffold constructs are either maintained in static cultures, or within a bioreactor until the cells proliferate and differentiate into a biomaterial construct that features biological and mechanical functions of the tissue or organ that it is intended to replace or repair. This approach has the potential to address the limitations of *in vivo* tissue engineering, since

it theoretically allows for the creation of a whole living organ *ex vivo* due to the possibility of introducing vasculature and cues that promote angiogenesis [21]. For example, using micropatterning techniques, vascular networks can be created and integrated into a scaffold system to allow for adequate nutrient and oxygen transfer within the cell-material hybrid [22, 23]. More recently, using three-dimensional printing of sacrificial carbohydrate cylinders onto hydrogels, Chen et al. were able to perfuse endothelial cells which assembled into vasculature networks of various geometries and patterns [23].

Despite advances of *in vivo* and *in vitro* tissue engineering, these strategies are far from reaching their full potential. To engineer more complex and reproducible constructs, there needs to be an enhanced scale-up of vascularized tissues with carefully balanced bioactivity landscapes, which will require a stronger fundamental understanding of cell biology and material properties. Additionally, the interactions between cells and scaffolds must be well understood and optimized to develop robust and functionally active tissue constructs [24]. A recent publication released by Jansen et al. conducted a strategic assessment of limiting factors that need to be overcome to allow for tissue engineering strategies to possess wide clinical success by the year 2021. Using a modified Hoshin process, the answers from a worldwide body of 24 leaders in the field of tissue engineering were ranked into 14 critical activity categories. The top four included: (1) angiogenic control; (2) stem cell science; (3) molecular biology and systems biology; and (4) cell sourcing and cell/tissue characterization [25].

While current biomaterial screening assays are informative, they generally provide a single readout to assess a population-based response to a test condition. Due to the heterogeneous nature of stem cells, a major emerging cell source for regenerative therapies, screening methods will require more sophisticated measurements based on data-rich readouts that account for multivariate and spatially divergent cellular responses within one test condition. This thesis dissertation is focused on the goal of advancing improved methodologies rooted in molecular and cellular biological readouts to characterize single stem cell responses to biomaterials for their use in tissue engineering strategies.

1.2 ORTHOPEDIC TISSUE ENGINEERING

Within the field of tissue engineering in general and in orthopedic cell transplants in particular, there is a significant need for alternative therapies. Bone and cartilage-related diseases affect millions of people worldwide. Arthritis is the most common cause of disability in the United States, resulting in annual costs exceeding \$128 billion dollars [26]. The Centers for Disease Control and Prevention estimated that between 2007 and 2009, 50 million Americans were diagnosed with arthritis [27]. Osteoarthritis, a degenerative disease that results in the decay of cartilage in joints, is the most common form of arthritis. In 2008, 51.2 million Americans were living with osteoarthritis [28]. Another prevalent degenerative disease is osteoporosis which affects over 50% of Americans over the age of 50 [29]. Currently, there are no methods that can restore cartilage or bone loss resulting from osteoarthritis or osteoporosis, respectively. Treatment options for bone-related cancers are extremely limited as well. For example, osteosarcoma is generally treated with adjuvant chemotherapy followed by the removal of the primary tumor, resulting in missing bone at the site of surgery [30].

Strategies for treating bone defects involve either the transplantation of natural bone tissue or synthetic implants. Natural bone tissue is acquired from autografts or xenografts. Autografts are beneficial because they run low risk of immunological rejection. However, this procedure requires two sites of invasive surgery, and permanent tissue loss from the donor site [31]. Xenografts circumvent this; however, the demand exceeds the supply of donors and there is the potential of disease

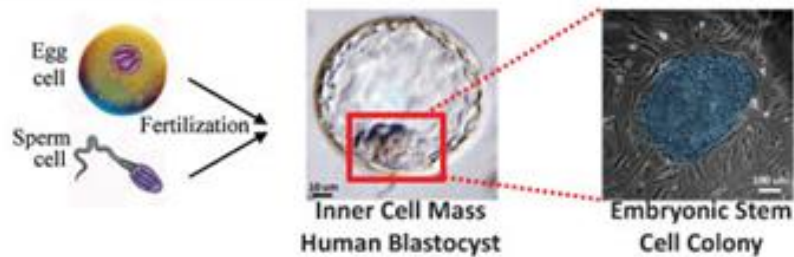
transmission and immunologic rejection [32]. To address the limitations of autografts and xenografts, metal and ceramic-based implants can be used to fill defects after the removal of damaged bone tissue. However, this first-generation of materials have their limitations, including a poor material-tissue interface and an inclination towards fatigue and corrosion. Since current strategies are limiting, there is a need for a new generation of biomaterials capable of restoring damaged and missing bone tissue without any adverse side effects. To this end, there has been a growing interest in the generation of more advanced biomaterials that induce tissue remodeling, which will be discussed in **Section 1.2.1** and **Section 1.2.2**.

1.2.1 Cells

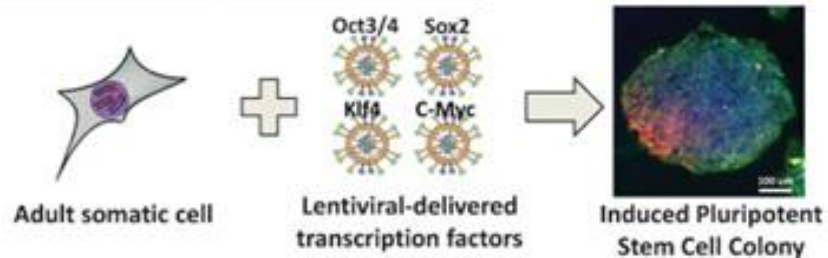
Two commonly used cell types in tissue engineering are somatic cells and stem/progenitor cells. Somatic cells have been utilized to develop several tissue substitutes *in vitro* including skin [33], cartilage [34, 35], and bone [35]. Although somatic cells can be exploited to generate specialized tissues, such as the FDA approved therapies Carticel [36] and Apligraf [37], they are not good candidates for regenerative therapies since terminally differentiated cells are unable to undergo extensive self-renewal. Additionally, somatic cells pose two other drawbacks: (1) they are difficult to adequately expand for use in engineered tissues [38] and (2) are highly specific, restricting their use to tissues from which they originated from. As such, stem cells are now being increasingly considered as an alternative cell source, due to their ability of self-renewal, and their potential to differentiate into multiple lineages [39, 40].

Stem cells can be categorized into three types, each with its own set of benefits and limitations: (1) embryonic stem cells (ESCs), (2) induced pluripotent stem cells (iPSCs), and (3) adult stem cells (ASCs). A cartoon demonstrating these stem cell types and strategies used to isolate them can be found in **Figure 1.1** below.

Embryonic Stem Cells



Induced Pluripotent Stem Cells



Adult Stem Cells

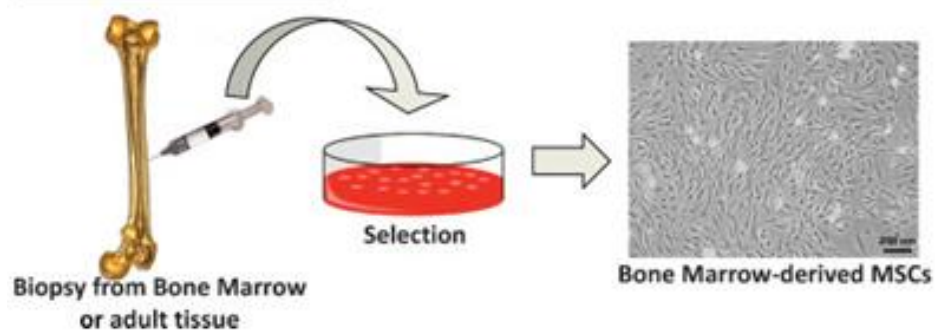


Figure 1.1: Cartoon of Different Stem Cell Types and Sources

An overview of the sources and techniques used to generate ESCs, iPSCs, and ASCs.

Figure is reproduced from [41].

ESCs are derived from the inner cell mass of a blastocyst, and were first isolated in 1998 by Thomson and coworkers [42]. This cell line is advantageous because they are pluripotent and under the right culture conditions can proliferate indefinitely while maintaining their stemness. However, ESCs are not autologous, and thus may require the use of immunosuppressive drugs post-implantation. Additionally, the acquisition of ESCs requires the destruction of an embryo, which raises ethical concerns.

An alternative stem cell line that has comparable differentiating and self-renewal capacity to ESCs are iPSCs, which were first harvested in the Yamanaka laboratory in 2006 [43, 44]. This was achieved by exposing fibroblasts to a cocktail of four transcription factors, resulting in the reprogramming of a small percentage of the somatic cells into cells that behave like ESCs. In theory, iPSC populations derived from a skin biopsy could be expanded and differentiated into any cell type. However, iPSC technology remains fairly immature and much more research is needed before clinical applications can come to fruition.

Due to the limitations of ESCs and iPSCs in tissue engineering applications, more translational advances have been achieved with ASCs. ASCs are a multipotent and capable of providing patients with specialized tissues derived from an autologous cell source. In bone marrow, ASC populations contain two prevalent cell types: hematopoietic stem cells (HSCs) and mesenchymal stem cells (MSCs). HSCs can differentiate into blood cell types, including erythrocytes, leucocytes, and lymphocytes [45, 46]. In contrast, MSCs have been shown to differentiate into various connective tissues including adipocytes, osteoblasts, and chondrocytes [47].

Human MSCs are traditionally differentiated into osteoblasts *in vitro* by introducing dexamethasone, sodium ascorbate, and β -glycerophosphate to serum-containing medium [47]. When plated at a low density and cultured with growth medium supplemented with osteogenic growth factors, hMSCs will differentiate into osteoblasts after several weeks in culture [47, 48]. hMSC-derived osteoblasts are characterized by the generation of a calcified extracellular matrix as well as the expression of osteoblast-associated messenger RNAs including osteocalcin and osteopontin [49]. In lieu of soluble growth factors, several laboratories have discovered alternative ways to induce osteogenic differentiation. For example, by inhibiting histone deacetylases (HDAC), Jung et al. induced osteogenic differentiation in a dose-dependent manner *in vitro* [50]. HDAC inhibition exposes DNA regions that would normally be suppressed, suggesting that epigenetic mechanisms play a large role in the onset of osteogenesis. Additionally, genetic modifications to hMSCs that cause them to express recombinant bone morphometric protein 2 (BMP-2) or adenovirus runt-related transcription factor 2 (RUNX2) have also been shown to increase osteogenic differentiation [51, 52].

Inducing osteogenesis via the use of synthetic growth factors or by constitutently expressing and/or silencing certain genes is not practical for clinical use due to the adverse effects these methods may create *in vivo*, particularly in off-target sites. As such, biomaterial-induced osteogenic differentiation presents a more attractive, site-directed alternative approach. Current biomaterial screening approaches rely on the measure of markers, which take several weeks for cells to produce enough of to obtain

a reliable readout. Therefore, improved methods to rapidly and accurately characterize stem cell interactions with biomaterials at earlier time-points need to be developed. One possibility may involve the quantification and assessment of interactions that occur shortly after cell attachment and prior to the expression of phenotype-specific markers.

During the early stages of osteogenesis, runt-related transcription factor 2 (RUNX2) is activated. RUNX2 is a transcription factor whose expression has been linked with the downstream expression of two pre-osteoblast markers: type I collagen and alkaline phosphatase [53-55]. Concurrently, global changes in gene expression and organizational changes of cytoskeletal and nuclear proteins occur within the first 3 days of osteogenic induction [56, 57]. As osteogenesis continues, undifferentiated MSCs become pre-osteoblasts, as defined by high levels of type I collagen and alkaline phosphatase. The abundance of these proteins leads to the expression of two more transcription factors, distal-less 5 and osterix [58, 59]. The continuous expression of distal-less 5 and osterix are largely responsible for the transition from a pre-osteoblast to a mature osteoblast. A simplified cartoon showing the osteogenic pathway can be found in **Figure 1.2** below.

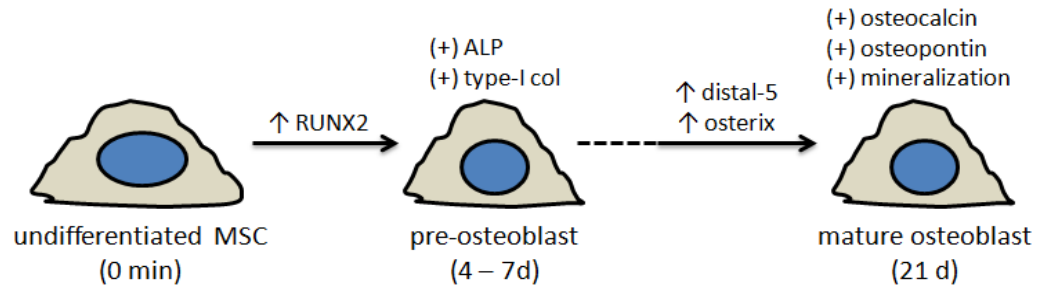


Figure 1.2: Simplified Cartoon of Osteogenic Differentiation Pathway

An overview of some of the transcription factors (denoted by \uparrow) required for the transition from undifferentiated MSC to mature osteoblast along with measurable markers (denoted by (+)).

1.2.2 Biodegradable Materials

For both *in vivo* and *in vitro* tissue engineering strategies, the use of degradable biomaterials instead of permanent materials has been of high interest. This is largely because an implant engineered with degradable chemistries does not have to be removed surgically, thus the safety issues that come with permanently implanted devices are not a concern. Degradable biomaterials can either be derived from natural polymers (e.g., collagen, fibrinogen, chitosan, starch, and hyaluronic acid (HA) [60-63]), or synthesized in the laboratory. Both natural and synthetic degradable biomaterials can feature chemical and structural versatility as well as high reproducibility. Material properties including density, hydrophobicity, crystallinity, surface roughness, topography, and degradation rate can all be controlled and tailored for specific tissue engineering applications [64-66].

Poly(lactic acid) (PLA) and poly(lactic-glycolic acid) (PLGA) are the most widely studied synthetic degradable polymers. PLA and PLGA have demonstrated biocompatibility with relatively non-toxic and non-immunogenic degradation products and possess a degradation rate comparable to the healing process of bone wounds [67]. However, during the degradation process, there is a significant loss of mechanical strength and accumulation of acidic components [68]. To address these concerns, chemical changes (e.g., mixing PLA or PLGA with hydroxylapatite or β -tricalcium phosphate [69]) and physically increasing the effective surface area by introducing an assortment of surface topographies [70] has been investigated. Although these modifications have improved polymer properties, the material design and optimization protocols rely on a trial-and-error approach, which is laborious and time-consuming. Therefore, to more effectively advance the discovery of desirable biomaterial properties (e.g., chemical, physical, and mechanical), there is a need for more rational approaches to design and optimize scaffolding materials that promote bone regeneration.

In addition to PLA and PLGA, the effects of biomaterial properties on cell behavior have been investigated with a family of tyrosine-derived polymers developed by Kohn and coworkers at Rutgers University. Poly(desaminotyrosyl-tyrosine ethyl ester carbonate) (PDTEC) is a highly versatile and degradable polymer system [71]. Copolymers of DTE can be copolymerized with desaminotyrosyl-tyrosine (DT), which adds a negative charge due to a free carboxylic acid [72], and/or copolymerized with poly(ethylene glycol) (PEG), which increases hydrophilicity, water uptake, and decreases protein adsorption [73, 74]. Varying the ratio of these three components results in an

array of polymer properties, allowing for a wide range of biomedical applications [75, 76]. For example, by increasing the ratio of DTE to DT, the degradation rate of the polycarbonate will increase. Additionally, by increasing the percentage of PEG, the polymer will swell in aqueous environments and cell adhesion will decrease due to a reduction in protein adsorption. The chemical structure of these tyrosine-derived terpolymers from DTE, DT, and PEG are shown in **Figure 1.3**.

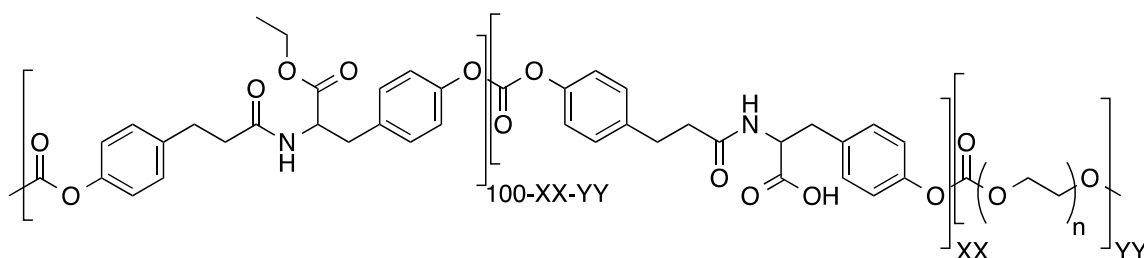


Figure 1.3: Chemical Structure of Poly(DTE-*co*-XX%DT-*co*-YY%PEG carbonate)

Molar composition of polycarbonate with (100-XX-YY)% DTE, XX% DT, and YY% PEG.

Schematic adapted from [77].

In addition to chemistry, substrate compliance and topography are two very important biomaterial parameters. For example, stem cells cultured on stiff biomaterials have a higher tendency of differentiating towards phenotypes native to hard tissues (e.g., bone) *in vivo* [78, 79]. On non-compliant substrates, several studies have cited that changes in topography direct stem cell lineage commitment [80-82]. These changes also affect the early organization and presence of integrins, focal adhesions, actin, and nuclear shape. Leong et al. showed that cells placed in gratings that promoted

alignment showed a decrease in expression of several integrin subunits, in addition to an increase in actin alignment and focal adhesion polarity [83]. Additionally, topography-based regulation of actin also influences nuclear shape and gene regulation [84, 85]. These findings suggest that changes in topography not only affect stem cell lineage commitment, but changes in morphology as well.

1.3 LIMITATIONS OF CURRENT CELL-MATERIAL SCREENING TOOLS

Tissue engineering strategies have the potential to integrate with personalized medicine by providing customizable constructs that utilize autologous cells to meet patient needs. In order for this vision to become reality, a thorough understanding of the interplay between cells and scaffold systems needs to be established so that techniques to produce controllable cellular proliferation, differentiation, and maintenance of phenotype can be developed. Therefore, in addition to developing methods of producing state-of-the-art scaffolding materials, the next generation of tissue engineering strategies must also rely on the elucidation of stem cell responses to extracellular stimuli, including but not limited to scaffold properties and culture environments.

Scaffolds featuring a diverse range of chemical and physical properties, as well as different architectures and topographies yield differences in protein adsorption and cell adhesion, resulting in various changes in cellular processes including proliferation, differentiation, and extracellular matrix production [70, 86]. Tunable parameters such as architecture, hydrophobicity and protein adhesion potential strongly influence cell function, differentiation commitment, and phenotypic stability [73, 87, 88]. To date, most of the studies conducted to elucidate these mechanisms focus on either the detection of lineage-specific markers or gene expression levels of whole stem cell populations for a limited number of material conditions. This poses two problems: (1) only a small subset from a theoretically infinite number of conditions is being tested,

and (2) readouts are data-limited and may not be representative of heterogeneous stem cell cultures.

As such, scientists have worked on developing methods to expand the number of test conditions from several candidate conditions to a much larger, combinatorial design of biomaterial libraries [89-91]. Other high-throughput screening methods include: extracellular matrix microarrays [92], fluorescence-based polymer screening [93], and lab-on-a-chip substrates [94]. Combinatorial libraries and high-throughput screening platforms allow for the exploration of thousands of conditions that could be controlled both incrementally and simultaneously to expedite the discovery of desired structure-function relationships. Due to the larger number of conditions screened, there is a substantial increase in the probability of finding suitable cell-material interactions that would have otherwise gone unnoticed with smaller test sets.

Traditional approaches to screen condition-dependent cell outcomes generally rely on detecting unitary fluorescence readouts representative of the whole condition. Singer et al. argue that gene expression of cell populations is strikingly different than the average gene expression of many single cells representative of a cell population [95]. Thus, alongside higher-throughput screening tools, there is a growing need to develop methods that go beyond traditional characterization approaches and can quantitatively profile multiple cellular responses at the scale of single cell resolution. Therefore, a desirable high content screening system should allow for single cell analyses and for the collection of quantitative readouts to account for population heterogeneity as well as single cell responses.

1.4 HYPOTHESIS AND AIMS OF THE DISSERTATION

Two major challenges plague the robust design of stem cell-derived tissues for regenerative therapies: (1) the phenotypic and functional heterogeneity inherent in stem cell cultures, and (2) the dynamic, long-term nature of stem cell responses to microenvironmental cues. Several tools have emerged to precisely characterize how stem cells respond to various stimuli and scaffold properties; however, they are limiting because they are population-based and rely on the detection of markers expressed in fully differentiated cells. Thus, methods to characterize individual stem cells from a population is key for establishing cell-biomaterial relationships necessary to design scalable constructs for tissue engineering applications.

Cells first respond to their environment by forming focal adhesion complexes that anchor to the surrounding matrix. These binding events induce early outside-in signaling events that connect the nuclear space to adhesion proteins via the cytoskeleton, resulting in structural changes to overall cell shape and various mechanoresponsive cytoskeletal and nuclear elements. Thus, we hypothesize that quantitative metrics descriptive of cytoskeletal and nuclear proteins involved in outside-in signaling can be utilized to define cell state mediated by microenvironmental cues.

As such, the goal of this thesis is to develop single cell biological imaging and machine learning techniques to identify the heterogeneity of stem cell cultures and characterize responses to controllable changes in diverse microenvironments. This was achieved by pursuing two thesis-specific aims: (1) to utilize single cell biological imaging and machine learning techniques to identify cell subtypes in heterogeneous stem cell

populations, and (2) to use early morphological descriptors of intracellular mechanotransductive proteins to predict long-term stem cell responses to biomaterials. Each of these aims requires a thorough understanding and utility of imaging modalities and cell biology. **Chapter 2** is a review of imaging tools and techniques used to visualize cellular proteins, previous progress made in single cell imaging-based profiling, and the hypothesized outside-in signaling relevance of proteins used for the thesis work.

Chapter 2 lays the foundation and rationale for the studies in **Chapter 3**, where we show that single cell imaging-based profiling of cytoskeletal actin and nuclear mitotic apparatus (NuMA) protein can identify single cell phenotypes in different stem cell populations. We found that actin organization could identify minute distinctions in the phenotypes of human mesenchymal stem cells (hMSCs) cultured on polymeric films with varying degrees of poly(ethylene glycol) to modulate osteogenic differentiation. Additionally, hMSCs cultured on a platform featuring a hydrophobicity substrate gradient were screened and descriptors obtained to correlate substrate variations with adipogenic lineage commitment. Further, we demonstrated that NuMA organizational features were able to distinguish self-renewing subpopulations of human embryonic and induced pluripotent stem cells from heterogeneous populations, which showcases our ability to identify heterogeneity, a current challenge that limits the use of stem cells in the clinic.

In **Chapter 4** we apply the quantitative methodologies presented in **Chapter 3** to identify cell phenotypes in confluent cultures that have potential impact in tissue engineering. Since it is not possible to segment single cells in confluent cultures using

actin, for the studies in **Chapter 4** we used the NuMA protein, a cell cycle regulating protein, as our morphometric reporter. As a screening tool, we predicted the oncogenicity of a biomaterial library by showing a high-degree of correlation between early NuMA metrics and long-term hMSC telomerase activity. Next, we showed our method's ability to classify cell subtypes *ex vivo* by identifying three neural precursor cell populations extracted from different murine brain regions that have identical antigen expression but divergent proliferation and differentiation profiles. Lastly, to show the applicability of recognizing and removing unwanted cells in heterogeneous live cell populations, we identified and ablated DNA-damaged cells in a co-culture labeled with fluorescently-tagged NuMA. The result was an increase of population viability after treatment with a drug that selectively kills DNA-damaged cells.

This thesis also examined the role of other nuclear proteins besides NuMA in parsing stem cell phenotypes within more complex microenvironments. In **Chapter 5** we found that the early (3 day) organization of SC-35 speckle domains, which host post-transcriptional machinery within the interchromatin regions of the nuclear space, vary in hMSCs exposed to a variety of growth factor combinations that induced divergent phenotypic outcomes. As a biomaterial screening tool, via SC-35 imaging we could also classify the extent of 14 day osteogenic differentiation commitment across a series of surface patterns, fibrous scaffolds, and micropillar topographies.

The results presented in these chapters show that single cell imaging-based profiling can be utilized to identify cell subtypes in heterogeneous stem cell cultures and predict microenvironment-induced differentiation fates at earlier times and with more

resolution than current screening assays. This work can help lay the foundation for a new generation of single cell-based biomaterial screening tools and cellular phenotyping techniques.

CHAPTER 2. SINGLE CELL IMAGING-BASED PROFILING

Note: Sections of this chapter have been reproduced from the following publication:

Liu E, Vega S, Treiser MD, Sung H-J, and Moghe PV. (2011) Fluorescence Imaging of Cell-Biomaterial Interactions. In: P Ducheyne, KE Healy, DW Hutmacher, DW Grainger, CJ Kirkpatrick (eds.) Comprehensive Biomaterials, vol. 3, pp. 291-303 Elsevier.

2.1 INTRODUCTION OF FLUORESCENCE IMAGING OF CELL-BIOMATERIAL INTERACTIONS

Numerous studies document the potential role of biomaterials in tissue engineering and regenerative medicine [96-99]. Biomaterials modulate a wide range of cellular phenomena, including cell attachment, spreading, migration, survival, growth, differentiation, and immune responses [100-105]. The characterization of chemical and mechanical properties of biomaterials is a well-established field of study. However, the biological characterization of cellular responses to biomaterials is typified by a large number of divergent readouts that are challenged by the lack of standardized conditions and objective standards. Methods based on optical imaging, in general, and fluorescence microscopy, in particular, have witnessed rapid growth and gained widespread acceptance in real-time, high-resolution studies of cell cultures as well as high-throughput cell screening assays. Not surprisingly, these advances have inspired the application of a new generation of techniques to the field of cell-biomaterial interactions.

Advances in fluorescence microscopy have heralded the development of single cell and intracellular imaging methods. As epifluorescence microscopy became an entrenched tool in cell biology laboratories, multilabeled indirect immunofluorescence techniques enabled biologists to examine the associations of different antigens within the same subcellular compartments [106]. Thereafter, advances in fluorescence *in situ* hybridization (FISH) permitted the localization of individual genes on chromosomes and specific mRNAs [107-110]. The more recent introduction of high-resolution confocal and

multiphoton microscope systems has made it possible to capture three-dimensional images resolving the organization of structures within cells, with speeds in the order of milliseconds [111-114].

Fixed cellular images acquired from high-resolution immunofluorescence techniques have revealed the remarkable complexity of cellular architecture and provided important insights of major cellular structures, including different cytoskeletal proteins, the nucleus and its various compartments, and membranous organelles [115-117]. However, images of fixed and stained cells are static, providing only a brief snapshot of the organization and properties of these structures. This drawback has inspired scientists to develop fluorescence-based methods with high sensitivity for studying specific types of molecules and multi-component complexes in living cells.

Some of the first proteins that were tracked via fluorescence imaging were cytoskeletal proteins such as actin, paxillin, or vinculin directly conjugated with a fluorophore such as X-FITC or X-Texas Red. These fluorophore-conjugated proteins were microinjected into cells, resulting in the FITC or Texas Red incorporation into targeted endogenous structures [118-120]. More recently, fluorescent imaging technology heralded the development of genetically encoded fluorescent proteins that could be expressed in cells and organisms through the use of green fluorescent protein (GFP), a protein that revolutionized the use of fluororeporters in cell biology [121]. The use of GFP-tagged proteins has many advantages, but primary among these is the ability to capture more time-resolved images, which enables the tracking of the dynamic properties of tagged molecules for extended periods of time.

2.2 SINGLE CELL IMAGING-BASED PROFILING: PAST AND PRESENT

In an attempt to facilitate the progress of tissue engineering, there has been an increased focus on developing novel methods of obtaining information-rich readouts of stem cell responses to a diverse set of culture conditions [25]. As such, methods are being developed to rapidly screen a number of experimental conditions while increasing the amount of information gathered per test condition. By increasing the quantity and quality of data, these approaches may accelerate the discovery of desirable biomaterial-driven cell behaviors for tissue engineering applications.

Current biological characterization methods generally rely on qualitative readouts and lack quantitative and reliable results. To increase the amount of information attained per test condition, the pharmaceutical industry has implemented high-throughput cell-based screening approaches to assess the efficacy and activity of small molecules [122, 123]. These assays utilize a handful of quantitative morphometric features to screen biological compounds of potential interest in a high-throughput manner. Additionally, recent advances in confocal microscopy, as well as novel image processing techniques have made the analysis of cell-biomaterial interactions permissive.

In order to improve upon current characterization methods of cell-biomaterial interactions, our laboratory has developed a high content imaging-based platform capable of parsing numerical morphological descriptors from images of individual stem cells cultured on various microenvironments [56, 57, 124-128]. By combining fluorescence imaging, quantitative image analysis, and computational data mining, this

approach can provide insights about the organization of various cellular proteins at a single cell level. Our laboratory has made several advances in the field of imaging-based cellular profiling, and key findings are highlighted in four case studies that utilize labeling methods and advanced fluorescence imaging modalities to capture cellular interactions with polymeric biomaterials. All case studies used members of a tyrosine-derived polycarbonate library with generic composition poly(desaminotyrosyl-tyrosine ethyl ester carbonate) (**Figure 1.3**).

In the first study (**Section 2.2.1**), epifluorescence microscopy was used to track cells tagged with GFP-actin, and confocal microscopy was used to characterize the nuclear translocation of GFP-GAPDH when cells were cultured in a library of polycarbonate-derived substrates [129]. In the second study (**Section 2.2.2**), we review the application of multiphoton microscopy to visualize cells in three-dimensional synthetic biomaterial scaffolds [125]. The third case study (**Section 2.2.3**) illustrates the concept of using high content imaging to identify cell adhesion, spreading, membrane modifications, and cytoskeletal organization on biomaterials [127]. In the final study (**Section 2.2.4**), an advanced method combining high-throughput and high content imaging platforms is highlighted in terms of its ability to screen cellular responses to gradient properties of biomaterials. This case study represents one of the future directions in biomaterial design and optimization [126].

2.2.1 Imaging of Cell Cytoskeletal Remodeling and Apoptosis on Biomaterials

This case study highlights the role of reactive oxygen species (ROS) in cell apoptosis on biomaterials. Polymers derived from the amino acid L-tyrosine were used as synthetic matrix substrates [129]. Tyrosine-derived polycarbonates were synthesized by copolymerizing hydrophobic L-tyrosine derivatives with uncharged hydrophilic PEG, and negatively-charged DT. These substrates were characterized in terms of their intrinsic ability to generate ROS, as well as their ability to regulate intracellular ROS production, actin remodeling, and apoptosis in Saos-2 cells (**Figure 2.1A**).

PEG-containing substrates induced both exogenous and intracellular ROS production, whereas DT-containing anionic polymeric substrates reduced the production of both types, indicating a coupling of exogenous ROS generation and intracellular ROS production. The effects of ROS activity on the cytoskeletal actin reorganization was probed using a GFP-fluororeporter for actin (**Figure 2.1B**). In order to visualize dynamic changes in actin, live time-lapse imaging of GFP-actin Saos-2 cells was performed on a heated chamber perfused with carbon dioxide. Images were taken every 3 minutes for 1 hour with a Zeiss fluorescence microscope fitted with a 60X objective lens. Six single cells from three independent experiments were imaged in each condition. Image contrast and brightness were adjusted to equalize fluorescence intensity. Contrast-adjusted images were then filtered utilizing a series of flattened filters. Fluorescence pixels were then converted to 8-bit dots with a constant thresholding process to allow the individual actin proteins to be segmented. The 8-bit dot images provided a higher resolution of actin organization. To measure actin area

fraction, 12 single cells were live-imaged at 3 days post-seeding. From the 8-bit dot image, a summated dot area, which represents the total actin area, was obtained through particle analysis. A ratio of the actin area to the whole cell area was presented as an actin area fraction.

This study showed that the dynamic processes of actin remodeling were regulated by biomaterials induced with ROS and played causative roles in cellular apoptosis. Briefly, PEG-mediated ROS induction caused nuclear translocation of glyceraldehyde-3-phosphate dehydrogenase and an increase in caspase-3 activity, confirming a link with apoptosis. PEG-rich pro-oxidant substrates caused cytoskeletal actin remodeling through β -actin cleavage by caspase-3 into fractins. The fractins colocalized to the mitochondria and reduced the mitochondrial membrane potential. The remnant cytosolic β -actin was polymerized and condensed, events consistent with apoptotic cell shrinkage (**Figure 2.1C - 2.1E**). The cytoskeletal remodeling was integral to the further augmentation of intracellular ROS production. Conversely, the antioxidant DT-containing charged substrates suppressed the entire cascade of apoptotic progression. It was demonstrated that ROS activity serves as an important role in outside-in signaling for cells grown on substrates. The ROS activity couples exogenous stress, driven by substrate composition to changes in intracellular signaling. This signaling causes cell apoptosis, which is mediated by actin remodeling.

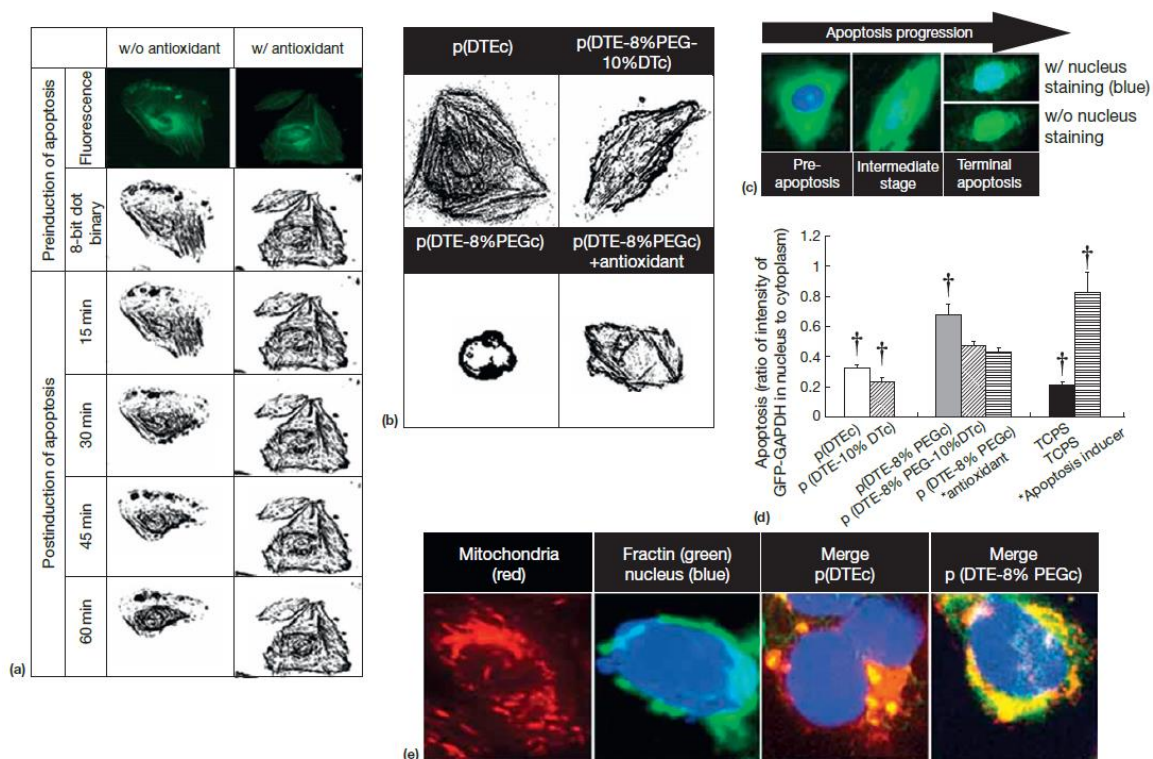


Figure 2.1: Imaging of Actin and Functional Reporters During Apoptosis

(A) Time lapse of GFP-actin Saos-2 cells during apoptosis with apoptosis promoter treatment. Morphologic changes over time were observed with and without the presence of an antioxidant. **(B)** Visualization of actin organization (GFP-actin Saos-2 cells) on various biomaterial substrates with and without the presence of an antioxidant. **(C)** Demonstration of nuclear translocation of GFP-GAPDH (green) to the nucleus (blue) during apoptosis. **(D)** Ratio of GFP-GAPDH signal within the nucleus to the cytoplasm was utilized to assess oxidative stress resulting from substrate chemistry. **(E)** Visualization of fractin formation via staining with a polyclonal antifractin antibody. Fractins (green) localized to the mitochondria (red). Colocalization (yellow) was more evident in PEG-containing samples. ‡ indicates statistical differences.

2.2.2 Fluorescence Imaging of 3-D Polymer Scaffolds and Cellular Organization

Because confocal imaging of three-dimensional substrates is limited by light scattering, MPM was used as an alternative approach to image and quantitatively characterize the microstructure and cell-substrate interactions within microporous scaffold substrates fabricated from synthetic biodegradable polymers. Poly(desaminotyrosyl-tyrosine ethyl ester carbonate) (PDTEC) and poly(desaminotyrosyl-tyrosine octyl carbonate) (PDTOC) were blended, and a fluorescent dye was mixed with the blend to visualize the scaffold architecture. The porosity of PDTEC/PDTOC blend scaffolds was varied to achieve a distribution of microporous and macroporous regions within the porous scaffolds. GFP-engineered fibroblasts were seeded onto the scaffolds, which allowed the imaging of both cell morphological patterns and the porous scaffolds (**Figure 2.2A**). The porosity, pore size and distribution, strut size, pore interconnectivity, and orientation of both macroscale and microscale pores in the three-dimensional scaffolds were effectively quantified and validated using complementary imaging techniques. MPM was used to obtain images of the scaffold thickness, which was $>100\ \mu\text{m}$, with a high signal-to-noise ratio that resulted in reduced bulk photobleaching and eliminated the need for deconvolution (**Figure 2.2B**). In this study, the morphology and cytoskeletal organization in cells located inside the scaffold was tracked with high resolution and within the limits of penetration of the excitation beam. Thus, this study showed that MPM offers a promising integrated platform for imaging cell-material interactions within polymeric biomaterial scaffolds.

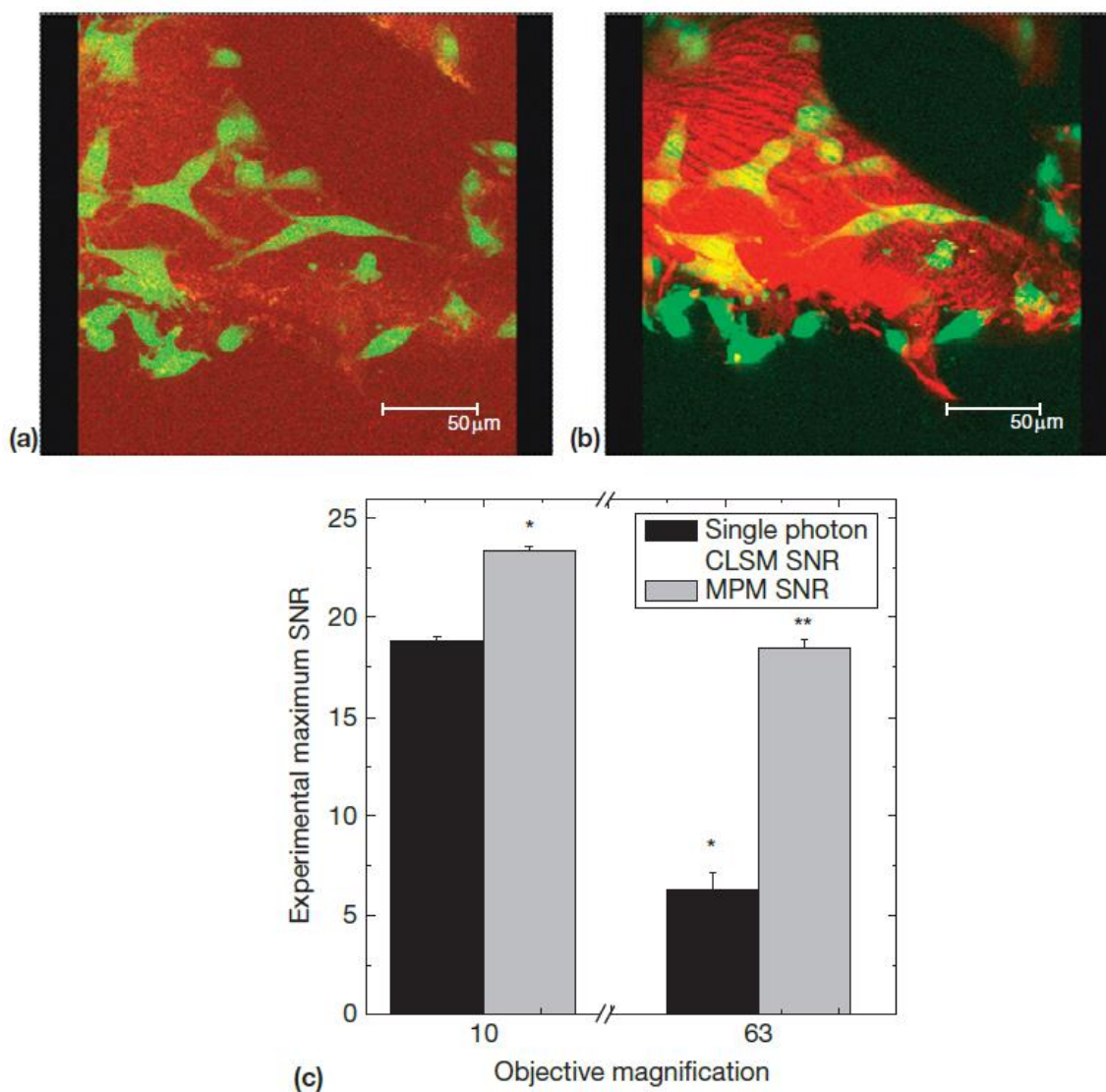


Figure 2.2: Comparison of MPM and CLSM Images of GFP-Fibroblasts in 3-D

Scaffolds

(A-B) CLSM and MPM images of GFP-fibroblast cells on 50/50 PDTEC/PDTCO scaffold blend. **(C)** Comparison of experimental maximum signal-to-noise (SNR) ratio of CLSM and MPM images of Texas Red doped PDTEC/PDTCO scaffold blends with macro and micro pores. * and ** represent a statistically significant difference, $p < 0.05$, compared with 10X and 63X single-photon CLSM images, respectively.

2.2.3 Fluorescent Reporter Imaging for Analysis of Cell-Material Interactions

Traditionally, mainstream high-throughput cell assays are primarily fluorescence intensity-based detection systems such as plate readers and flow cytometers. Such cellular assays only focus on bulk changes in intensity of fluorescent probes of whole cell or cell lysates. Such cell assays can provide quick readouts but provide much less information than can be captured by analyzing cells at the microscopic level. Methods such as flow cytometry can render pseudo high content readouts by detecting multiple fluorescent probes associated with individual cells.

A recent study utilized a high content imaging approach to correlate cytoskeletal responses of cells to systematically varied chemical changes in biomaterial substrate chemistry [127]. Cell-biomaterial interactions were captured utilizing high-resolution images obtained with confocal microscopy. Mammalian cell lines (CHO and Saos-2) were transfected with GFP fusion proteins to highlight functional and morphological responses of the cells. The fusion proteins used in this study were GFP-actin, GFP-actinin, and GFP-paxillin. Actin, actinin, and paxillin represent cytoskeletal proteins involved in both the structural determination of cell shape as well as integrated members of a number of biochemical pathways that mediate the outside-in signaling of cells. High-resolution images of the GFP-transfected cells in the context of a subset of a library of polycarbonates were captured using confocal microscopy. Single cell morphometric features (cell descriptors) were then extracted from the images through the use of commercially available software Image Pro Plus 5.1 (Media Cybernetics). The general feature extraction steps included background subtraction, segmentation of

whole cells and individual cytoskeletal proteins (actin), and parametric measurements. The extracted cell descriptors contain three categories of subcellular features including: (1) cellular morphologic parameters such as area, perimeter, mean radius, mean diameter, roundness, protrusions, and protrusion length; (2) reporter localization and texture parameters such as heterogeneity of actin stress fibers, clumpiness, average fiber length/width, focal adhesions per cell, strength of focal adhesion region, and total area of paxillin-rich structures per cell; (3) reporter expression parameters such as integrated optical density per cell, and mean fluorescence (**Figure 2.3A**).

As an example, the morphological changes of reporter cells in response to changes of substrate properties are summarized in the heat map shown in **Figure 2.3B**. A strong statistical difference in descriptor value (Student's t-test, p value $\rightarrow 0$) is represented by blue, a moderate difference by turquoise, a minor difference by orange, and no statistical difference (p value $\rightarrow 1$) by red. This study shows how descriptors of GFP-tagged proteins in living cells can be used to discern combinatorial variations in substrate composition, resulting in significantly richer data sets than analyses conducted in fixed samples that provide only one snapshot in time [127].

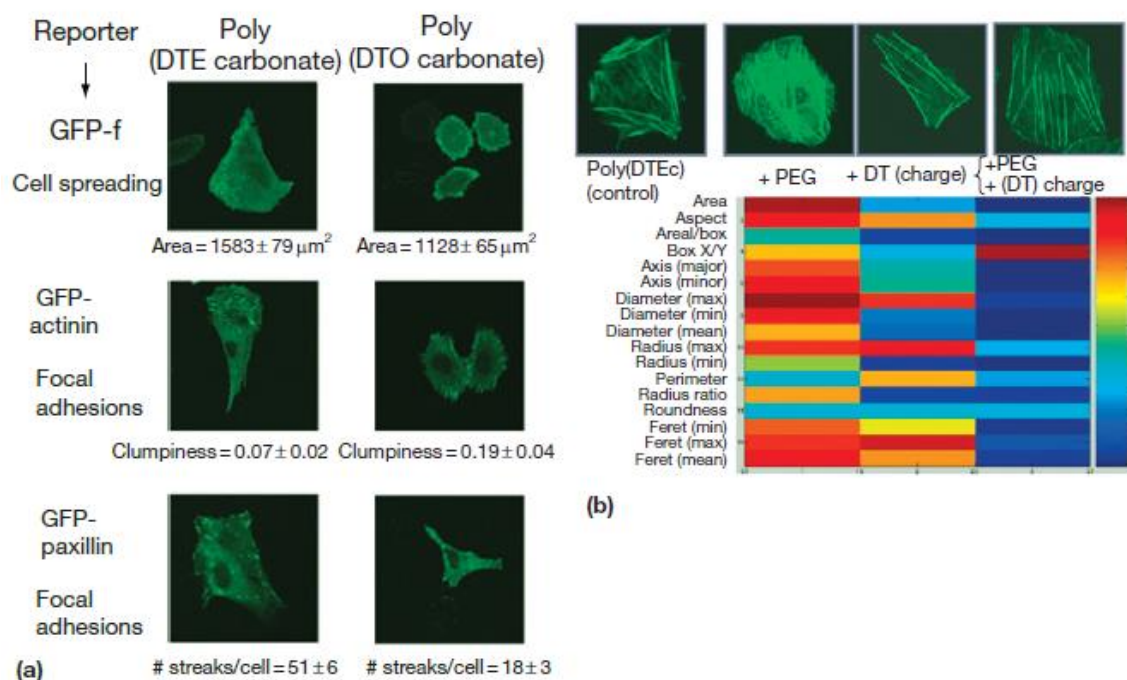


Figure 2.3: GFP-Tagged Subcellular Reporters on a Subset of Biomaterials

(A) Confocal micrographs of GFP-engineered Saos-2 cells on two polymeric substrates with different backbone compositions leading to differing hydrophobicities. **(B)** Cell responses to a combinatorial variation in substrate properties can be discerned using high content imaging of GFP reporters and a heat map representation of variations in morphometric descriptors.

A more recent study shows how high content imaging can be used to discern early morphological changes in stem cells cultured on synthetic biomaterials [57]. Actin-based morphology, texture, and intensity descriptors were obtained by single cell imaging of human mesenchymal stem cells (hMSCs). The descriptors were reduced in dimensionality using multidimensionality scaling (MDS), which combines the large number of descriptors into three groupings. The use of such groupings allowed the

classification of heterogeneous subpopulations of stem cells within the first 24 hours of stem cell culture on biomaterials. The use of high content imaging allowed this classification early on, much before biochemical and molecular assays established the lineage classification of stem cells toward osteogenic (bone) versus adipogenic (fat) lineages.

2.2.4 High Content and High-Throughput Imaging of Cell-Biomaterial Interactions

Advances in polymeric biomaterial synthesis have allowed for the transition from synthesizing a small number of materials to the design and execution of large libraries of bipolymer blends derived from systematic combinations of biomaterials [130, 131]. In a recent report, a combination of high content imaging and high-throughput screening was proposed in the context of cell-biomaterial interactions. The substrate processing platform was based on different combinations of polymer blends exhibiting a continuous range of chemical and topographical properties on a single 42 mm round cover glass. As an example, the tyrosine-derived polycarbonates, PDTEC (E: ethyl) and PDTOC (O: octyl) homopolymers and their blends (70/30, 50/50, 30/70 ratio of PDTEC/PDTC by mass), were flow coated on round glass cover slips. The fabricated PDTEC/PDTC blends exhibited well-characterized surface gradients in hydrophobicity and surface roughness. Human Saos-2 cells transfected with GFP-tagged farnesylation (GFP-f) gene were examined for their responsiveness to the surface texture gradients of PDTEC/PDTC blends. The morphology and organization of Saos-2 cells were examined

in real-time using a temperature-controlled chamber on the motorized stage of a confocal laser scanning microscope (CLSM).

The adhesion of Saos-2 cells was rapidly screened via tile scanning and was found to be maximized at intermediate regions, characterized by intermediate levels of roughness and the steepest roughness gradient (**Figure 2.4**). Through high content imaging, we identified different morphometric parameters of the organization and intensity of GFP-f that correlate with the most adhesive substrate compositions (chemistry) or with the degree of surface roughness (**Figure 2.5**). The correlation between defined polymer blend parameters and cellular function was obtained. In conclusion, this study showed that by quantifying descriptors of GFP-f Saos-2 cells, the cellular adhesive responses to texture and compositional variations of polymer blends could be dissected via CLSM.

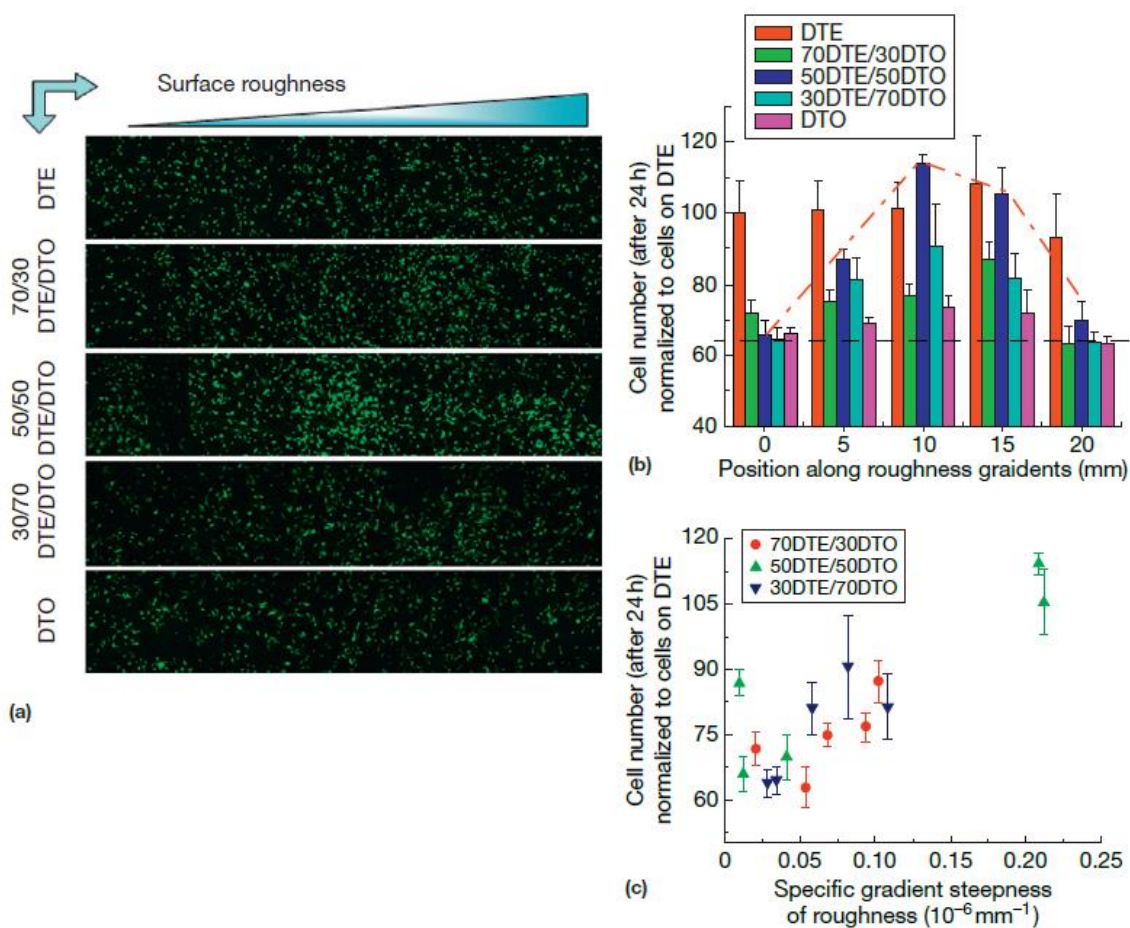


Figure 2.4: Cell Attachment Characterization on Roughness Gradient Chip

(A) GFP-f Saos-2 cells on a roughness gradient chip. **(B-C)** Quantification of cell attachment on the roughness gradient chip. Saos-2 GFP-f cell attachment was plotted against the roughness **(B)** or the local steepness of the gradient **(C)**.

(A) High-resolution single cell imaging of GFP-f Saos-2 cells on a roughness gradient chip. **(B)** Heat map representation of a pool of cell descriptors along roughness gradients. **(C)** Correlation study of cell descriptors with substrate surface roughness. **(D)** Correlation study of cell descriptors with cell function (adhesion).

2.3 CURRENT LIMITATIONS OF PROFILING CELL-MATERIAL INTERACTIONS

To-date, imaging-based profiling of cell-biomaterial interactions has only been applied to cells cultured on a limited set of conditions, largely restricted to simple, two-dimensional surfaces. Although considerable progress has been made already, ongoing challenges remain in capturing the dynamics of multiple cellular functional readouts and signals in physiological and complex biological milieu. A major challenge lies ahead regarding imaging of cellular phenomena within three-dimensional microscale scaffolds. To apply this imaging-based screening to more clinically-relevant settings, profiling techniques need to be adapted so that cell states can be identified in stem cell cultures featuring biomaterials with diverse physicochemical and mechanical properties.

Dynamic cell-biomaterial interactions result in changes to the organization of focal adhesion, cytoskeletal, and many nuclear proteins, which regulate gene expression. Although it is well established that cell shape and actin are good indicators of cellular phenotype, in confluent populations it is challenging to identify single cells using cytoskeletal proteins alone. Additionally, cell shape and actin stress fibers are overly sensitive to complex scaffold properties (e.g., substrate compliance, topography). As such, there is a need to explore other intracellular fluorescent reporters, particularly in the nuclear space that can be identified for single cells within confluent stem cell cultures and are sensitive to differentiation-inducing biomaterial properties. In **Section 2.4** we will review several candidate reporter molecules that are involved in the outside-in signaling cascade that may serve as good markers of cell state induced by interactions with complex microenvironments.

2.4 OUTSIDE-IN SIGNALING

There exists a continuous link between the pericellular matrix and the nucleus via cell adhesion complexes and the cytoskeleton [132-136]. Cell adhesion to the underlying substrate is initiated via cell membrane receptors establishing contact with specific matrix molecules in the surrounding environment. For example, in native tissue, the extracellular matrix (ECM) is composed of an intricate combination of collagen, elastin, and glycoproteins (e.g., fibronectin and lamin). Immediately following cell adhesion, outside-in signaling events trigger changes in the three-dimensional organization and ultrastructure of several signaling proteins. There are two facets to outside-in signaling: (1) biochemical signal transduction, whose processes include phosphorylation cascades and protein translocation to the cell nucleus, and (2) mechanotransduction, which refers to processes that convert mechanical stimuli into signaling events mediated via cytoskeletal remodeling [137, 138]. Thus, the ECM, cytoskeleton, and nucleus are all connected and modulated via mechanical forces and other microenvironmental cues. Consequentially, microenvironment-induced outside-in signaling result in early (< 3 days) morphological changes that precede long-term (> 10 days) cellular functions (**Figure 2.6**).

Given the key role of the nucleus in cellular reprogramming, scientists have gained interest in the study of the cell nucleus. Many of the structures within the cell nucleus (e.g., nucleoli, chromatin, cell cycle regulating proteins, and interchromatin domains) have been identified as regulators of stem cell phenotypes [139-144]. For example, the concentration and location of heterochromatin and the presence of

transcriptionally active regions in close proximity to interchromatin domains (i.e., SC-35 domains), have been shown to differ between undifferentiated and lineage committed cells [145-147]. In the next sections we will review the biology and potential role in outside-in signaling of several molecules that may serve as indicators of microenvironment-induced cell state: actin (**Section 2.4.1**), chromatin (**Section 2.4.2**), interchromatin domains (**Section 2.4.3**), and nuclear mitotic apparatus (NuMA) protein (**Section 2.4.4**).

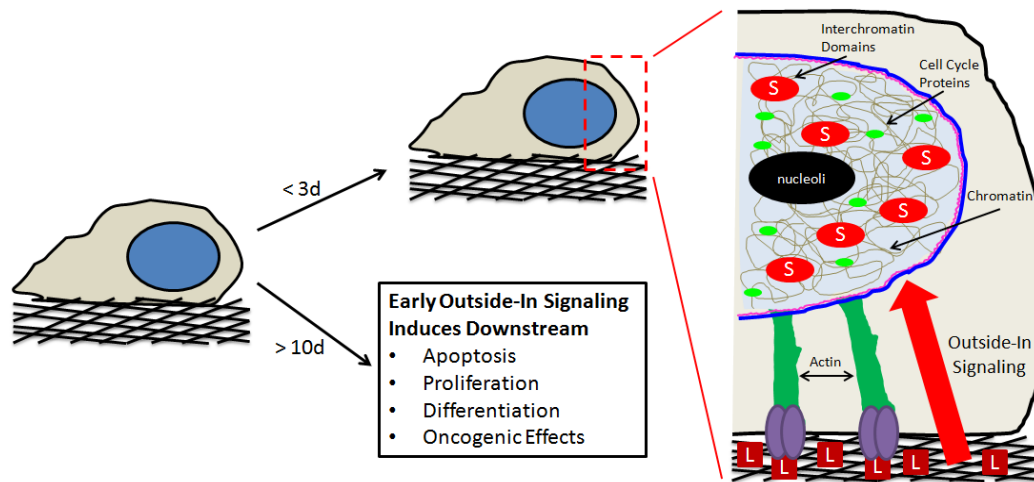


Figure 2.6: Simplified Overview of ECM-Induced Outside-In Signaling

Cell contact with the ECM initiates an immediate outside-in signaling cascade that traverses from the ECM to integrins (purple ovals) followed by actin (green), and onto lamins and the nuclear space (pink and blue semi-ovals, respectively). This results in early (< 3 days) changes to the presence and organization of many cellular structures, including actin, chromatin (light brown), cell cycle proteins (e.g., NuMA, green), interchromatin domains (e.g., SC-35, red), and nucleoli (black). Outside-in signaling also induces downstream (> 10 days) cellular behaviors (e.g., apoptosis, proliferation, differentiation, and oncogenicity).

2.4.1 Actin

Actin is one of the main components of the eukaryotic cytoskeleton. The cytoskeleton provides a path for the transmission of ECM mechanical signals from integrins onto the nucleus, which is the control center of the cell [148]. Actin is primarily involved in integrin mechanical coupling and signal propagation to the nucleus [149-151]. Actin polymerization is regulated by many signaling molecules, including RhoA and Rac1, two central members of the Ras GTPase superfamily [152, 153]. More specifically, studies have shown that high levels of GTP-bound RhoA and Rac1 result in the assembly of stress fibers and lamellipodia, respectively [154]. Taken together, actin is both connected to the microenvironment and is regulated by molecules involved in outside-in signaling (**Figure 2.7A**).

It has become increasingly evident that cell shape and the formation of cytoskeletal stress fibers are regulators of several stem cell states, including cell cycle progression and apoptosis. The dependence of cell state on cell shape may be due to the link between focal adhesions and changes in cytoskeletal arrangements [155]. Integrin clustering is regulated by actin, whereas actin is regulated by integrin-activated Rho GTPases [156]. Actin-mediated shape-based activation of RhoA, followed by its downstream effector Rho-associated kinase (ROCK) induces changes in cytoskeletal actin [133]. Additionally, several studies have shown that changes to actin regulate cell cycle progression and apoptotic events [157, 158]. By confining cells to certain shapes via micropatterning of adhesive molecules, it was found that cell shape is a prevailing factor in the regulation of cell cycle progression [159, 160].

The role of cell shape, actin, RhoA, and ROCK in controlling stem cell state is not limited to cell cycle progression and apoptosis. Cell shape has also been shown to preferentially regulate stem cell differentiation into particular phenotypes. McBeath and coworkers proposed a detailed mechanism underlying this shape-mediated differentiation phenomena [133]. It was shown that spread cells and the upregulation of RhoA and its downstream effector ROCK steered undifferentiated hMSCs towards an osteogenic (OS) phenotype rather than adipogenic (AD) in mixed AD / OS medium. In contrast, hMSCs cultured in conditions that restrict cell shape and confine cells to round morphologies are more predisposed towards becoming adipocytes (**Figure 2.7B**). Cell shape and RhoA were needed to trigger osteogenesis; however, only ROCK, regardless of cell shape, was able to induce the same response [139]. Thus, actin is related and responsive to RhoA and ROCK, which serve as signaling moderators that control differentiation programming.

The role of actin in several cellular processes and signaling events demonstrates that it is sensitive to microenvironmental cues. Actin-mediated cell shape induces changes in the activity of RhoA and ROCK, amongst other signaling molecules necessary for lineage commitment [133, 152]. At the interface between actin and the nuclear envelope lie nesprins and emrins, which permit mechanotransductive signaling between the nuclear space and the cytoskeleton [161, 162]. Additional interactions between actin and the intermediate filament lamin proteins result in tension forces within the nuclear space [137, 163]. Additionally, actin connects the nucleus to the pericellular

matrix. As such, actin dynamics could affect chromatin as well as several nuclear proteins that we will review in **Sections 2.4.2 - 2.4.4**.

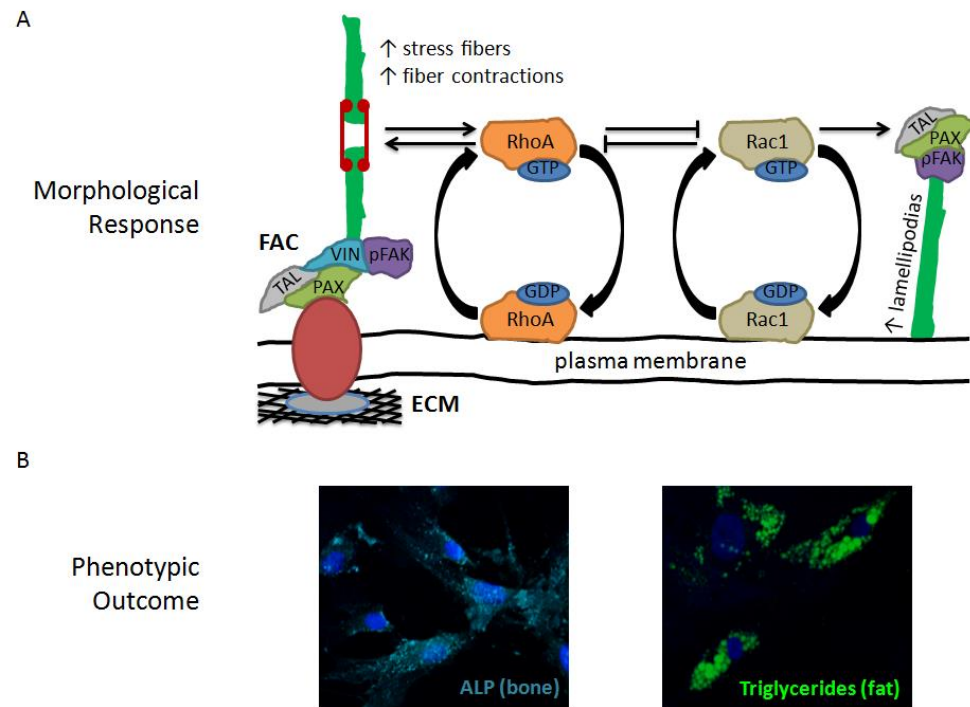


Figure 2.7: Actin Morphology is Dependent of Key Signaling Molecules and Yields Divergent Differentiation Outcomes

(A) Integrin-ECM protein binding results in focal adhesion complexes (FACs), which form stress fibers (actin, green; myosin, red). Active (GTP-bound) RhoA increases stress fiber contractions and stress fiber formation, which further influences the levels of GTP-bound RhoA. RhoA and Rac1 are antagonists, and GTP-bound Rac1 induces the formation of lamellipodias. **(B)** Early differences in actin induce divergent phenotypic outcomes. Stem cells cultured on ECMs that promote spread morphologies with stress fiber formation differentiate towards osteoblasts, as seen by a high degree of ALP signal (blue). In contrast, stem cells with low stress fiber formation differentiate towards adipocytes, as evidenced by positive staining for intracellular triglycerides (green).

2.4.2 Chromatin

In order for eukaryotic cells to create protein macromolecules, snippets of DNA containing genetic information that codes for proteins must first be exposed to transcriptional machinery. This process is largely governed by chemical modifications to chromatin complexes, which organize the DNA in the cell's nucleus. These modifications either promote a closed chromatin structure (termed heterochromatin), preventing transcription, or an open chromatin structure (termed euchromatin), which promotes gene transcription [164, 165]. Thus, a lot of information about the cell's state can be garnered by studying the presence, organization, and conformation (heterochromatin versus euchromatin) of chromatin domains.

Changes to chromatin structures that result in DNA exposure or suppression are accomplished via two mechanisms: (1) methylation of DNA or (2) posttranslational modifications (PTMs) to histones. DNA methylation results in structural changes to chromatin, leading to the silencing or activation of gene transcription [166, 167]. Low methylation generally results in euchromatin (open chromatin structure), whereas regions of high methylation promote heterochromatin (closed chromatin state) [168]. Direct chemical modifications to histone complexes can also induce gene activation or silencing. There are many types of posttranslational modifications (PTMs), and their mechanism is based on chemical changes to amino acid residues in chromatin complexes [169]. PTMs regulate many cellular functions, including the self-renewal, pluripotency, and differentiation of stem cells [170-172]. Taken together, it is apparent that a lot of information can be gained about the state of the cell by characterizing

chromatin structures, as well as the mechanisms that promote regions of euchromatin and heterochromatin.

2.4.3 NuMA

The nuclear mitotic apparatus (NuMA) protein is a high molecular weight (238 kDa) molecule featuring head (N-terminus) and tail (C-terminus) domains separated by a long amino acid coiled-coil domain [173]. The C-terminus contains a nuclear localization signal (NLS) and an amino acid sequence capable of several functions, including the binding and bundling of microtubules [174, 175]. Additionally, both globular ends have motifs thought to bind DNA [176]. NuMA is essential for the assembly of spindle poles during mitosis [177], and is ubiquitously expressed in interphase nuclei. Due to its unique characteristics, several studies have been conducted to shed light on additional roles NuMA may be involved in, particularly its role in asymmetric cell division and in the structural integrity of a nuclear scaffolding matrix [178].

During mitosis, the extent of asymmetry at the metaphase plate is a determinant of self-renewal versus lineage commitment for dividing cells [178]. **Figure 2.8** shows a simplified overview of a parent cell undergoing asymmetric cell division. Centrosomes (dark green circles) align at the polarity axis (dashed horizontal red line). Chromosomes (dark brown) align at the metaphase plate and are bound to kinetochores (pink circles), which are attached to kinetochore microtubules (MTs) (dark green lines). NuMA proteins (blue squiggly lines) tether kinetochore MTs to non-kinetochore MTs (light green lines). The tethering of the mitotic spindle to one pole of the cell (square box)

results in an asymmetric positioning of the metaphase plate (dashed vertical black line). Cell polarity is determined by external cues and an adherens junction/Cdc42 complex (dark red) [179, 180]. Cortical NuMA (blue squiggly lines) proteins are then recruited to the polar region and form a NuMA/LGN/G α ternary complex that binds to dynein (pink), which attaches to astral MTs (gray) from the closest spindle pole, and provides a pulling force that results in an asymmetric positioning of the metaphase plate [174, 181].

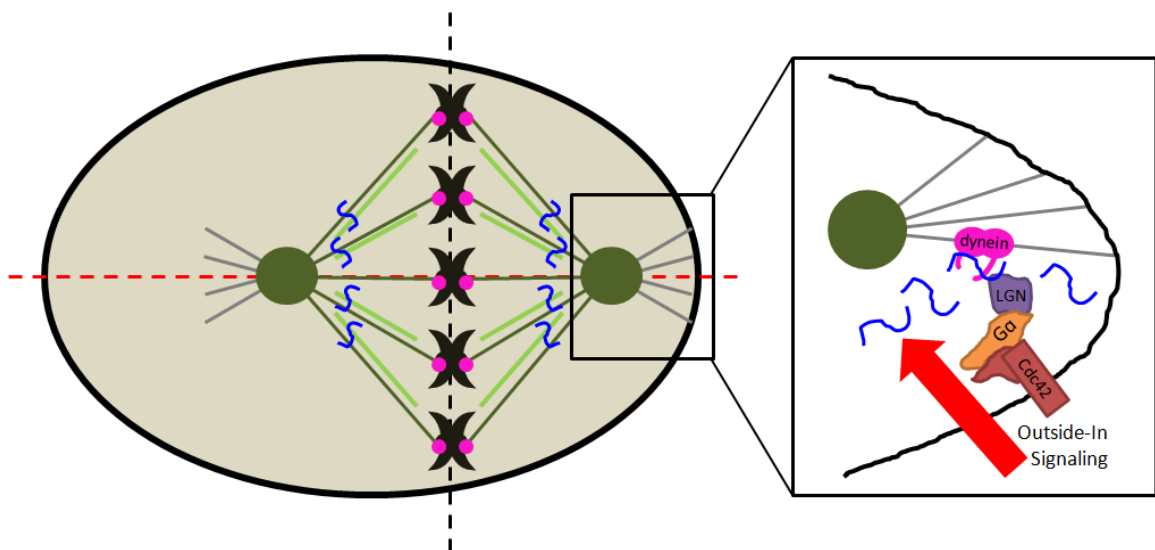


Figure 2.8: Role of NuMA During Asymmetric Cell Division

NuMA (blue squiggly line) binds kinetochore (dark green lines) and non-kinetochore (light green lines) microtubules, which is essential for spindle assembly. **(Inset)** External cues (red arrow) recruit adherens/Cdc42 complexes (red) and cortical NuMA (blue squiggly lines) to a polar end of the cell. Next, NuMA proteins bind to G α and LGN to form a ternary complex that links the adherens/Cdc42 complexes to dynein (pink), which binds to astral MTs (gray lines) and pulls the centrosome (dark green circle) towards one end, resulting in an asymmetric positioning of the metaphase plate.

In addition to its role in mitotic spindle assembly and asymmetric cell division, NuMA may also play an important role in the formation and maintenance of a nuclear scaffolding matrix. The nucleus is a complex landscape that contains highly condensed and organized DNA in the form of chromatin, as well as a vast array of enzymes and complexes involved in gene expression and DNA replication / repair [178]. Additionally, the nuclear space has discrete interchromatin domains (e.g., PML bodies and SC-35 domains) and nucleoli [182, 183]. As such, it has been suggested that a nuclear scaffolding matrix exists that compartmentalizes these structures within the nucleus [184-186]. Nuclear lamins have been identified as part of the nuclear scaffolding matrix and are responsive to outside-in signaling from cytoskeletal actin. However, lamins reside at the nuclear periphery and therefore are unable to provide the high degree of compartmentalization that is observed with nuclear organelles. Due to its physical properties and abundance in interphase nuclei, several studies have suggested that NuMA may serve as a key member of the nuclear scaffolding matrix. There are over 1 million copies of NuMA per eukaryotic nucleus [187], and NuMA's large coiled-coil domains are capable of assembling into filaments [188]. Additionally, a recent study identified a relationship between nuclear shape and NuMA levels, further enforcing its potential role in the formation and maintenance of a nuclear scaffolding matrix [189].

Due to the implications of NuMA protein in proliferation, differentiation, and maintenance of a nuclear scaffolding matrix, its morphology may serve as a reliable identifier of cellular phenotype. A recent study reported quantifiable differences in NuMA between DNA-damaged and non DNA-damaged breast epithelial cells [190]. Liu

et al. also showed that the early morphology of NuMA protein can identify different differentiation-inducing growth factor culture conditions for single hMSCs [56]. Thus, NuMA may serve as a good reporter of single cell phenotypes.

2.4.4 Interchromatin Domains

In eukaryotic cells, interchromatin domains contain pre-mRNA splicing machinery, comprised of small nuclear ribonucleoprotein particles (snRNPs), spliceosome subunits, and other non-snRNP protein splicing factors, which form aggregates termed SC-35 domains [191]. To control the pre-mRNA splicing machinery, SC-35 domains also contain several kinases and phosphatases that either phosphorylate or dephosphorylate factors required for pre-mRNA splicing [192]. Immunofluorescence imaging reveals that SC-35 domains appear as 20 to 30 clusters (1 to several microns in diameter) that vary in size and shape. Higher resolution studies based on electron microscopy show that each SC-35 domain is comprised of a network of granules (20 to 25 nanometers in diameter) that are connected by thin fibrils [193].

In addition to hosting and controlling pre-mRNA splicing machinery required for protein synthesis, SC-35 domains have been observed close to highly active transcription sites, despite having little, if any DNA. A recent study has shown that the periphery of SC-35 domains contain significantly more euchromatin (open chromatin) than heterochromatin (closed chromatin) regions [194]. Within euchromatic regions it has also been found that groups of related genes are associated with the same speckle [194]. Thus, SC-35 domains form euchromatic domains that recruit and organize related

genes along their periphery to initiate gene splicing (**Figure 2.9**). Consequently, SC-35 domains have been found to be in close proximity to genes that are highly expressed at the onset of stem cell differentiation of several phenotypes including adipocytes [145], osteocytes [146], and myocytes [147].

To investigate how the morphology of SC-35 domains is affected by transcriptional activity, inhibitors and enhancers of transcription have been introduced to cells (**Figure 2.9**). When transcription is halted via the use of inhibitors, the number of SC-35 domains decreases and their shape increases in size and roundness [195, 196]. Since the splicing machinery is not necessary in heterochromatin regions, it makes sense that low levels of euchromatin result in a decrease in number and increase in size of SC-35 domains. In contrast, when transcription is enhanced via viral infection, the size of SC-35 speckles is reduced, their number increases, and they relocate to euchromatic regions [197, 198]. Taken together, the organization of SC-35 domains may serve as an indirect measure of early microenvironment-induced gene transcription activity that is required for the progression and maintenance of stem cell differentiation.

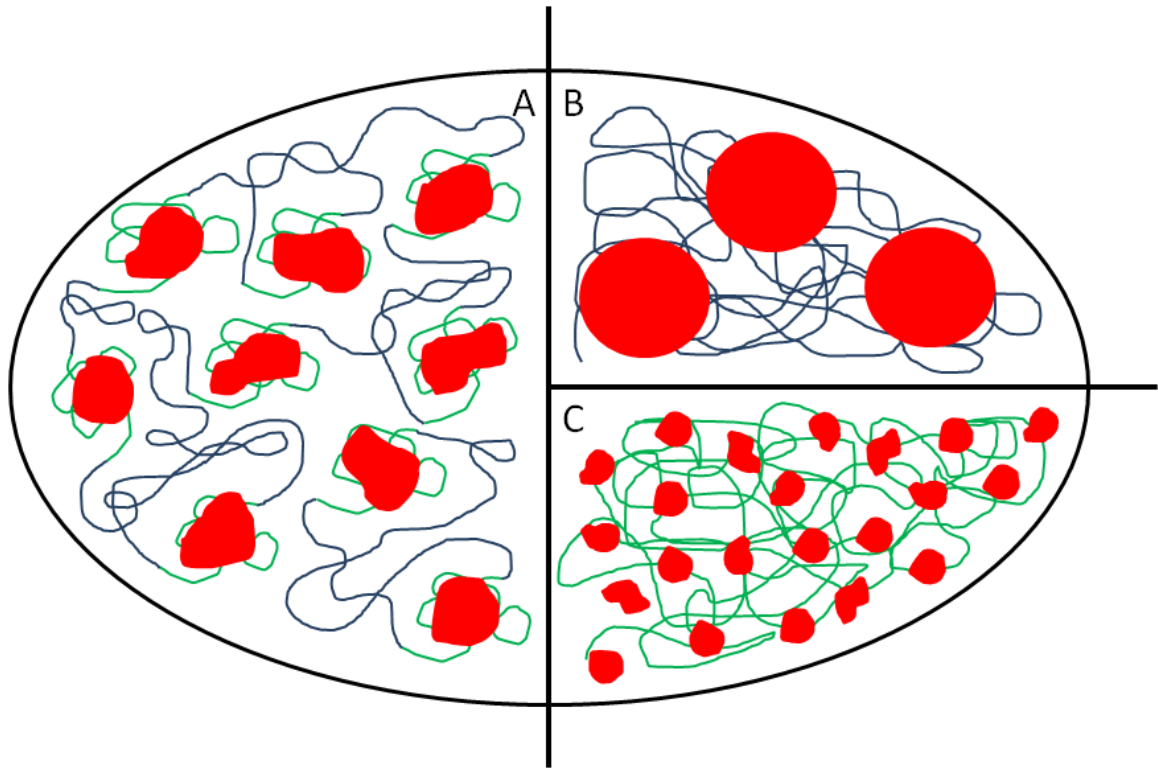


Figure 2.9: SC-35 Domains and Their Localization to Euchromatic Regions

(A) Regions of high transcription (euchromatic neighborhoods, green squiggly lines) aggregate around SC-35 domains (red) in normal interphase nuclei, whereas heterochromatin (dark blue squiggly lines) does not localize near SC-35 domains. **(B)** When transcription is halted, chromatin is predominantly in the heterochromatin state and SC-35 domains decrease in number and increase in size (large red circles). **(C)** When transcription is enhanced, chromatin is predominantly in the euchromatin state and SC-35 domains increase in number and decrease in size (red).

CHAPTER 3. ACTIN- AND NUMA-BASED IMAGING FOR SINGLE CELL PHENOTYPING

Note: Sections of this chapter have been reproduced from the following publication:

SL Vega, E Liu, PJ Patel, AB Kulesa, AL Carlson, Y Ma, ML Becker, PV Moghe. (2012)
High-Content Imaging-Based Screening of Microenvironment-Induced Changes to Stem
Cells. Journal of Biomolecular Screening 17:1151-1162.

3.1 ABSTRACT

Effective screening methodologies for cells are challenged by the divergent and heterogeneous nature of phenotypes inherent to stem cell cultures, particularly on engineered biomaterial surfaces. In this study, we showcase a high content, confocal imaging-based methodology to parse single cell phenotypes by quantifying organizational signatures of specific subcellular reporter proteins, and applied this profiling approach to three human stem cell types: human embryonic stem cells (hESC's), induced pluripotent stem cells (iPSCs), and human mesenchymal stem cells (hMSCs). We demonstrate that this method could distinguish self-renewing subpopulations of hESCs and iPSCs from heterogeneous populations. This technique can also provide insights into how incremental changes in biomaterial properties, both physiochemical and mechanical, influence stem cell fates by parsing the organization of stem cell proteins. For example, hMSCs cultured on polymeric films with varying degrees of poly(ethylene glycol) to modulate osteogenic differentiation were parsed using high content organization of the cytoskeletal F-actin. In addition, hMSCs cultured on a self-assembled monolayer platform featuring compositional gradients were screened and descriptors obtained to correlate substrate variations with adipogenic lineage commitment. Taken together, high content imaging of structurally sensitive proteins can be used as a tool to identify stem cell phenotypes at the single cell level across a diverse range of culture conditions and microenvironments.

3.2 INTRODUCTION

Obtaining purified stem cell-derived tissues for biomedical applications presents significant challenges due to the heterogeneity inherent to stem cell cultures as well as the dynamic nature of their responses to their microenvironments. Several tools have emerged to precisely characterize how stem cells react to various stimuli (e.g., growth factors or externally applied forces) and substrate properties [199, 200]. Typical screening methods focus on either the detection of lineage-specific markers or gene expression levels of whole stem cell populations [201-204], which are difficult to scale down quantitatively to single cell levels. In addition, due to the end-point nature of these assays, stem cells have to be cultured for several weeks before these methods can be applied to assess cellular responses.

To further accelerate the pace of stem cell studies in engineered microenvironments, high-throughput screening approaches have been developed that allow simultaneous analysis of multiple culture conditions within a single test platform. Multiple treatment conditions can now be presented on a single plate, allowing a large array of combinatorial variations to be concurrently screened [205]. Representative high-throughput screening platforms include high-throughput extracellular matrix microarrays [92], fluorescence-based polymer screening [93], and lab-on-chip substrates [94]. Although these methodologies permit a higher number of conditions to be tested in parallel, their ability to parse cellular responses to different stimuli is still limited by the end-point nature of biological assays and low stability of imprinted arrays. Thus, a

major need exists for the development of profiling tools to screen early cell phenotypic responses and predict long-term cell behaviors.

With the advent of genomics, gene microarray studies can provide differences in gene expression of thousands of transcripts across many conditions [204, 206]. Although this increases the amount of information that can be obtained from stem cell cultures, the resulting data do not account for the innate heterogeneous nature of stem cell populations [95]. Gene expression of cell populations has been shown to be strikingly diverse when compared with the average gene expression of many single cells representative of a cell population [95]. Methods to distinguish individual cells from a population would be extremely advantageous for selecting cells that have potential utility in tissue engineering applications.

Our laboratory has proposed a high content imaging-based profiling methodology that can characterize how cells respond to different microenvironments on a single cell level [56, 57, 127, 207]. As a first proof of concept, to characterize cell-adhesive responses to alterations in substrate topography, Saos-2 cells engineered with a green fluorescent protein (GFP) reporter for farnesylation (GFP-f) were cultured on substrates of different roughness and subsequently used to relate cell morphology to surface properties in a high-throughput manner [207]. More recently, a quantitative analysis of the early (24 hour) actin morphology of human mesenchymal stem cells (hMSCs) was used to predict downstream osteogenic differentiation [57]. In this study, we extended these approaches and applied our high content image analysis to evaluate single cell responses of various human stem cell types (adult mesenchymal, induced

pluripotent, and embryonic) to extracellular stimuli and various microenvironments. Using high-resolution confocal images of biologically relevant nuclear and cytoskeletal protein markers, we identified morphometric features that are distinct to culture conditions and stem cell subtypes for a given culture group. Specifically, we examined the ability of the technique to distinguish between high-dimensional features of the nuclear organization in spontaneously differentiation human embryonic stem cells (hESCs) at the periphery versus the putatively undifferentiated hESCs at the core of proliferating colonies. Similarly, induced pluripotent stem cell (iPSC) subpopulations with varying degrees of plasticity were identified.

This method also provided insights into how biomaterial properties, both physiochemical and mechanical, influence the high-dimensional organization of intracellular stem cell proteins. For example, differences in the actin cytoskeletal organization of hMSCs cultured on films with varying degrees of poly(ethylene glycol) (PEG) were elucidated. In addition, to screen different engineered materials, hMSCs were cultured on a self-assembled monolayer (SAM) platform that features a gradient of multiple substrate conditions within a single chip. hMSCs cultured in milieu that favored adipogenic differentiation featured nuclear mitotic apparatus protein (NuMA) signatures that were markedly different from those cultured in conditions that favored pluripotency, highlighting the possibility of using high-dimensional organizational biology as a probe for phenotypic stem cell screening.

3.3 MATERIALS AND METHODS

3.3.1 Fabrication of SAM Gradients

Glass microscope slides were rinsed with ethanol, blown dry with nitrogen, and exposed to UV radiation for 15 minutes to create a clean hydroxide surface layer. Slides were then rinsed with toluene and immersed in a 2.5% solution of n-octyldimethylchlorosilane in toluene. SAMs made from n-octyldimethylchlorosilane were deposited onto clean oxide surfaces, and the SAM-coated slides were placed on a motorized stage beneath the slit aperture of a UV lamp. A range of UV exposure times was obtained by decelerating the motion of the stage. The rise in UV exposure time led to increasing amounts of ozone-derived oxidation of the n-octyldimethylchlorosilane SAM, generating a gradient in surface energy across the slide.

3.3.2 Preparation of Polymer Films Copolymerized with PEG

Poly(desaminotyrosyl-tyrosine ethyl ester carbonate)-co-x%PEG polymers were dissolved into a 1.5% (v/v) methanol in methylene chloride solvent solution, resulting in a 1% (wt/v) polymer solution. Polymer solutions were then spin-coated onto 12 mm diameter glass coverslips. Spin coating was conducted at 3000 RPM for 30 seconds. Five films of increasing PEG content were prepared: 0%, 2%, 3%, 4%, and 8%. Prepared films were stored in a dessicator, and prior to culturing stem cells, films were sterilized with UV light for 900 seconds.

3.3.3 Cell Culture

National Institutes of Health (NIH)-approved hESCs (H9 line) and iPSCs were commercially obtained from WiCell Research Institute (Madison, WI). Undifferentiated hESCs and iPSCs were routinely maintained under feeder-free conditions on Matrigel-coated dishes in mTeSR-1 medium (Stem Cell Technologies, Vancouver, BC, Canada), as previously described [208]. For immunostaining and high content imaging studies, clusters of hESCs or iPSCs were passaged with dispase and plated in mTeSR-1 medium onto LabTek (Nunc, Naperville, IL) multiwell chambers. To induce early neural differentiation of hESCs or spontaneous differentiation of iPSCs, we switched medium 24 hours post-plating to N2SFM (Dulbecco's modified Eagle's medium [DMEM] / F12 with L-glutamine, 1% N2 Supplement, 1% nonessential amino acids, 2 µg/mL heparin, 0.5% penicillin/streptomycin) or to EB20 (DMEM/F12 with L-glutamine, 20% fetal bovine serum [FBS], 0.5% penicillin/streptomycin), respectively. Both cultures were maintained for 2 to 3 days prior to fixing and staining.

hMSCs were obtained from Texas A&M University (College Station, TX). Cells were expanded in T-75 flasks in a humidity-controlled environment under 5% CO₂ and 37°C and fed every 3 to 4 days with growth medium (basal culture condition, BA) supplemented with commercial SingleQuot's (catalog number PT-3001; Lonza, Basel, Switzerland). Cells were received at passage 1 and used for up to four passages. Cells were passaged upon reaching 80% confluence. Osteogenic (OS) and adipogenic (AD) induction media were reconstituted as per the manufacturer (Lonza). Mixed AD / OS medium was prepared by combining Lonza hMSC AD medium and Lonza hMSC OS

medium in a 1:1 ratio. Adipogenic medium in both the AD and mix conditions were cycled with a 3 day induction followed by 1 day maintenance.

3.3.4 Stem Cell Staining and Immunocytochemistry

Stem cells were first fixed with 4% paraformaldehyde (Electron Microscopy Sciences, Hatfield, PA) for 15 minutes. Then, a 30 minute blocking and permeabilization step was performed with a 0.1% Triton X-100 (Sigma, St. Louis, MO) / 5% normal goat serum (MP Biomedicals, Solon, OH) solution in phosphate-buffered saline (PBS; Lonza). After two washes with blocking buffer (5% NGS in PBS), primary NuMA (ab36999; Abcam, Cambridge, UK) antibodies in blocking buffer at a 1:500 ratio were added overnight at 4°C. Three 15 minute washes in blocking buffer were then performed. Secondary antibodies (Alexa Fluor; Invitrogen, Carlsbad, CA) with different fluorophores and corresponding isotype controls in blocking buffer at a 1:250 ratio were added for 2 hours at room temperature. Three 15 minute washes in blocking buffer were then performed. To label the actin cytoskeleton, cells were fixed and stained with Alexa Fluor 488 phalloidin (Invitrogen) per the manufacturer's instructions. All samples were counterstained with 1 µg/mL DAPI (Sigma) in PBS. Similar staining procedures were followed for Oct4 (MAB4401; Millipore, Billerica, MA), Sox2 (MAB4343; Millipore), and CD90 (15-0909-42; eBioscience, San Diego, CA).

3.3.5 High Content Imaging of Stem Cells

All samples were imaged under a 63X immersion objective (NA = 1.3) with a Leica TCS SP2 system (Leica Microsystems, Inc., Wetzlar, Germany). Average projections of 15 μm thick image sets of hESC and iPSC cultures were acquired from images at 2 μm intervals. To image hMSCs in the SAM gradients, tile scans of the cells were taken using the NuMA protein and DAPI channels. Since surface hydrophobicity varied from left to right, hMSCs attached at different focal planes on the tile. Thus, the entire slide was divided into multiple sections spaced 5 mm apart. The full spread of the gradient was approximately 35 mm in length, so the imaging was discretized over approximately seven tiles. To image hMSCs in PEG-containing films, the films were first mounted onto microscope slides with Fluorogel (Electron Microscopy Sciences) prior to imaging.

3.3.6 Numerical Descriptor Acquisition and Analysis

Image Pro Plus Version 7.0 (Media Cybernetics, Bethesda, MD) was used for image analysis. To isolate regions of interest (ROIs) for single cell descriptor acquisition, nuclear and cytoskeletal masks were first made using the DAPI and actin cytoskeleton channels, respectively. These masks were then superimposed to either nuclear or cytoskeletal channels to isolate signal from NuMA and actin protein channels, respectively. 43 numerical descriptors were then extracted for each cell's NuMA or actin protein signal. A list of the 43 descriptors calculated along with their definitions is provided in **Table 3.1**. These descriptors represent quantifiable measurements of cytoskeletal and nuclear protein morphology and organization by including shape,

intensity, and texture-based features. For single cell-based functional marker expression analyses, Oct4, Sox2, and CD90 mean signal intensity values were calculated for each cell using cytoskeletal masks as ROIs.

Descriptors from two different groups identified by the user (e.g., Oct4-expressing versus non-Oct4-expressing cells in a heterogeneous population) were exported to Matlab (MathWorks, Natick, MA) for analysis (**Figure 3.1**). First, principal component analysis (PCA) was used to linearly reduce 43 descriptors down to three principal components. This resulted in a plot in which each point represents a stem cell in a three-dimensional space where each axis consists of the combined features of either NuMA or actin protein in each analyzed cell. The location of each point is unique to the descriptor values for that particular cell. To assess how different the descriptor values are across two subpopulations, a support vector machine (SVM) was used to calculate sensitivity, specificity, and accuracy using 10-fold cross-validation (**Figure 3.1**). Unless otherwise noted, error reported on SVM classification represents the standard deviation for $n = 50$ pseudoexperiments (number of iterations using original data set).

3.3.7 Statistical Analysis

Statistical analysis was performed on morphometric parameters using SPSS Version 16.0 (SPSS Inc., an IBM Company, Chicago, IL) and included analysis of variance (ANOVA) with Tukey's honestly significant difference (HSD) post hoc method and other multivariate tools. The differences were considered significant for $p < 0.05$ unless otherwise noted. Error bars indicate the standard deviation around the mean.

*Features**Definitions*

Angle	Reports the angle between the vertical axis and the major axis of the equivalent ellipse. Within the context of this study, it would capture randomly oriented versus aligned cell populations.
Area	Reports the total actin/nucleus area of each cell.
Polygonal Area	Reports the area of the polygon that defines the object's outline.
Area/Box	Reports ratio between the area of each object and the area of the imaginary bounding box.
Aspect	Reports the ratio between the major and minor axes of the ellipse with the same area, first, and second order moments of the cell.
Axis (major)	Reports the length of the major axis of the ellipse with the same area, first and second order moments of the cell/nucleus.
Axis (minor)	Reports the length of the minor axis of the ellipse with the same area, first and second order moments of the cell/nucleus.
Box Height	Reports the height of the smallest bounding box that completely encompasses the cell/nucleus.
Box Width	Reports the height of the smallest bounding box that completely encompasses the cell/nucleus.
Box Ratio	Reports the ratio between the Box Width and the Box Height.
Dendrites	Reports the number of 1-pixel thick open branches. Represents the number of actin processes stemming from the cell.
Dendritic Length	Reports the total length of all dendrites.
Maximum Diameter	Reports the length of the longest line joining two outline points and passing through the centroid of the cell/nucleus.
Mean Diameter	Reports the average length of the diameters.
Minimum Diameter	Reports the length of the shortest line joining two outline points and passing through the centroid of the cell/nucleus.
End Points	Reports the number of 1-pixel thick processes stemming from the cell.
Maximum Feret Length	Reports the longest caliper length.
Mean Feret Length	Reports the average caliper length.
Minimum Feret Length	Reports the shortest caliper length.
Fractal Dimension	Reports the fractal dimension of the outline of the cell/nucleus.
Cell Area/Total Area	Reports the ratio between the areas of the cell/nucleus to that of the entire field of view.
Perimeter	Reports the length of the outline of each cell/nucleus using a polygonal outline.
Perimeter 2	Faster but less accurate measure of the perimeter.
Perimeter 3	Reports a corrected chain code length of the perimeter.
Convex Perimeter	Reports the perimeter of the convex outline of each cell/nucleus.
Elliptical Perimeter	Reports the perimeter of the ellipse surrounding the outline of each cell/nucleus.
Perimeter Ratio	Reports the ratio of the convex perimeter to the perimeter outline of each cell/nucleus.
Maximum	Reports the maximum distance between each cell's centroid pixel position and its perimeter.
Minimum Radius	Reports the minimum distance between each cell's centroid pixel position and its perimeter.
Radius Ratio	Reports the ratio between the Max Radius and Min Radius for each cell/nucleus.
Roundness	Reports the roundness of each cell/nucleus determined by the following formula: $(\text{perimeter}^2) / (4 \cdot \pi \cdot \text{area})$. Circular cells have a roundness of 1.
Size (Length)	Reports the feret diameter along the major axis of the cell/nucleus.
Size (Width)	Reports the feret diameter along the minor axis of the cell/nucleus.

Mean Density	Reports the mean intensity of all pixels within a cell/nucleus. Correlates to the average amount of fluorescence present within a given area.
Standard Deviation of Density	Reports the standard deviation of the intensity of pixels within a cell/nucleus. In the case of actin, this represents the degree to which the phalloidin stained cytoskeleton is localized into distinct filaments of equal staining intensity. In the case of nuclear proteins, this represents the degree to which the proteins are localized into distinct clusters of equal staining intensity in the nucleus.
Sum of the Density	Reports the sum of the total intensity values of all pixels within a cell/nucleus. Corresponds to the total amount of fluorescence within the cell/nucleus.
Integrated Optical Density	Reports the average intensity of each object normalized by the area of the cell/nucleus.

Holes	Reports the number of independent contiguous areas with no staining within a cell/nucleus.
Hole Area	Reports the area of holes within a cell/nucleus.
Hole Ratio	Reports the ratio of the object area excluding holes to the total area of the object as determined by $\text{Area} / (\text{Area} + \text{Hole Area})$.
Margination	Reports the distribution of intensity between the center of the cell and the edge of the cell. Describes the relative spatial distribution of actin filaments within the cell or nuclear proteins within the nucleus.
Heterogeneity	Reports the fraction of pixels that vary more than 10% from the average intensity of the cell. Describes the degree to which actin filaments or nuclear proteins are organized into homogeneously stained structures.
Clumpiness	The fraction of heterogeneous pixels remaining in a cell after a binary erosion process. Reflects the object texture and the degree to which actin filaments are organized into filamentous structures or the degree to which nuclear proteins are organized into clusters.

Table 3.1: Table of Descriptors Used in Chapter 3 Study

This table lists a pool of morphological descriptors quantified for each cell. The definition of the features and their possible biological relevance are listed. Shape-based features based on the ROIs are labeled in blue, intensity-based features are highlighted in green, and textural / spatial organizational features are highlighted in red.

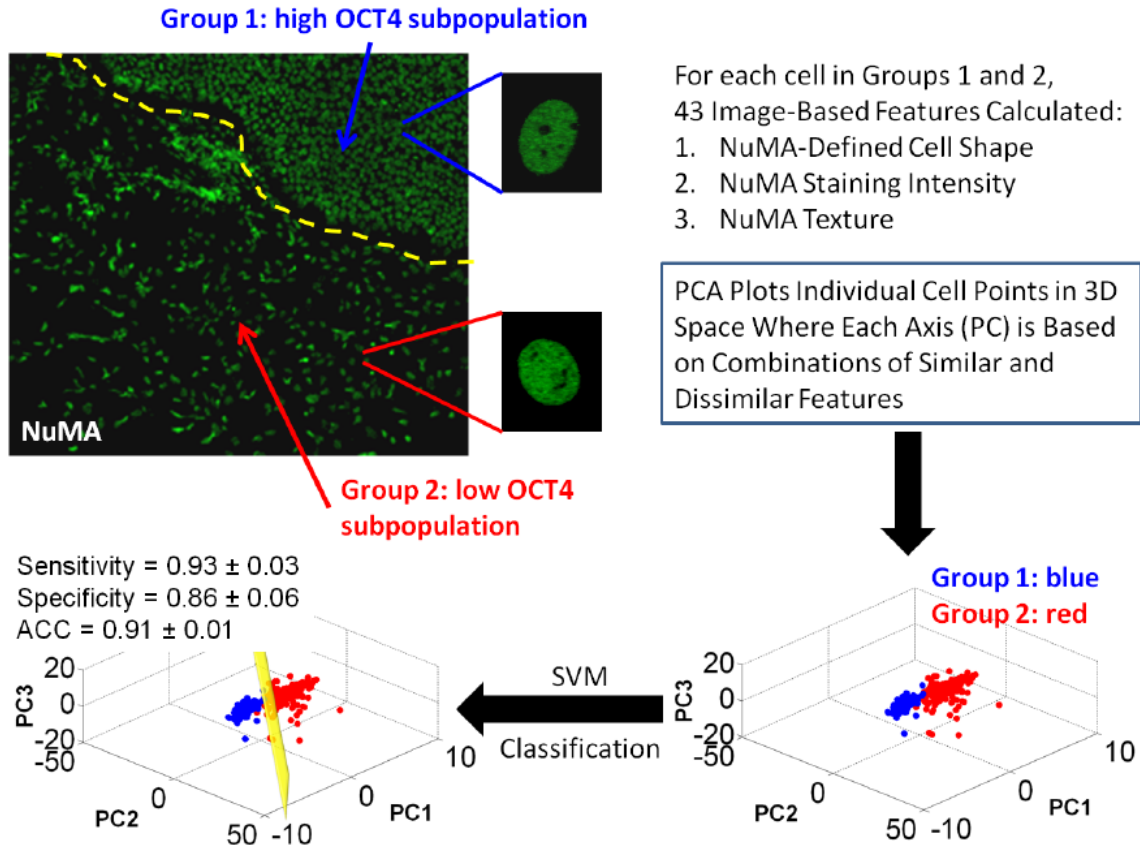


Figure 3.1: Imaging-Based Profiling Methodology for Two Subgroups

A heterogeneous population of stem cells, divided into two subgroups (e.g., high OCT4 and low OCT4 expression), was immunolabeled with nuclear mitotic apparatus (NuMA) protein antibodies and imaged at high-resolution. All 43 morphometric features were calculated for each cell based on NuMA shape, intensity of staining, and spatial distribution. PCA allows the 43 features of individual cells to be grouped and remapped in three-dimensions, such that red and blue dots represent cells from Group 1 and Group 2, respectively. Closely related cells are grouped together while distinct cells are not. Support vector machine (SVM) classification of the PCA remapping is then used to calculate sensitivity, specificity, and accuracy (ACC).

3.4 RESULTS

3.4.1 Overview of Imaging-Based Profiling

To acquire morphological information indicative of cell state, several stem cell types cultured in various conditions were imaged via confocal microscopy. Fixed cellular samples were immunolabeled with antibodies specific to cytoskeletal and nuclear proteins, as highlighted in **Figure 3.2A**, to extract numerical descriptors from reporter proteins. First, each image was split into channels corresponding to nuclear and cytoskeletal proteins of interest (**Figure 3.2B**). Next, single cell segmentation was accomplished by defining regions of interest (ROIs) for the nuclear and intracellular space. To create the nuclear ROIs, DAPI-stained images were subject to a series of image processing steps that included Gauss filtering, contrast enhancement, and fluorescence-based thresholding followed by binarization (**Figure 3.2C**). Similarly, the actin channel was used to create intracellular ROIs. To isolate the reporter protein's signal at single cell level, both nuclear and intracellular masks were superimposed onto nuclear and cytoskeletal channels, respectively.

Next, 43 numerical shape, intensity, and texture-based descriptors were isolated for each cell (**Table 3.1** and **Figure 3.2D**). Numerical descriptors of cells in two distinct groups were then obtained and merged into a “feature set” (**Figure 3.2E**). PCA was then employed to reduce the 43 descriptors from stem cells cultured in at least two different conditions down to three dimensions, which are derived from a linear combination of the original 43 descriptors (**Figure 3.2F**). These dimensions, termed principal components (PCs), are orthogonal from one another and account for most of the

variance in the binary data set. Furthermore, to evaluate the subcellular feature differences between two selected cell subpopulations, a support vector machine (SVM) classifier was used, which utilizes k-fold cross-validation to define test sets and training sets for each condition. SVM output sensitivity, specificity, and accuracy for each analysis. In addition, a hyperplane that best separates the two populations in the PCA domain was generated for visualization purposes. All of the analyses presented were conducted using a 10-fold k-fold cross-validation and repeated 50 times ($n = 50$) to acquire reported error in the form of standard deviation.

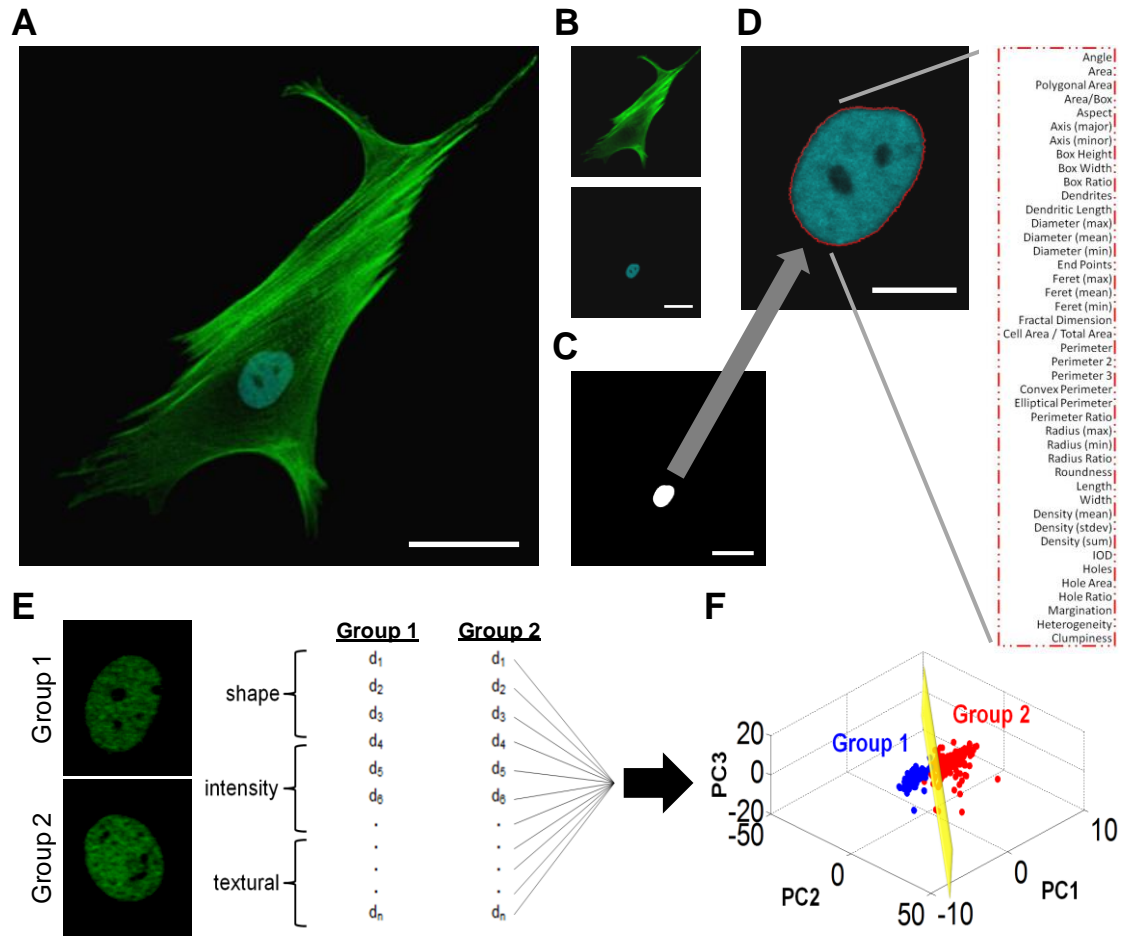


Figure 3.2: Single Cell Imaging, Feature Extraction, and Computational Modeling

(A) Stem cell labeled with actin (green) and NuMA protein (teal). **(B)** NuMA and actin channels separated prior to feature extraction. **(C)** To define the nuclear space, DAPI mask was generated. **(D)** NuMA protein (teal) channel isolated and 43 descriptors (listed in the red dotted rectangle) were computed. **(E)** To perform binary classification, descriptor sets from two different conditions were acquired. **(F)** PCA used to generate combinations of descriptors defining subcellular state of the two conditions. Stem cell population parsing efficiency was characterized by calculating sensitivity, specificity, and accuracy using SVM classification. Scale bars: **(A-C)** = 25 μm , **(D)** = 7.5 μm .

3.4.2 hESC Nuclear Features are Reflective of Phenotypic States

To realize the potential profiling capabilities of our imaging-based approach, we first identified differences in NuMA protein-based nuclear features of two subpopulations of hESC cultures: pluripotent and lineage-committed hESCs, as denoted by both pluripotency marker Oct4 expression and cellular morphology. hESCs in colonies were immunolabeled by antibodies specific for NuMA and Oct4 and were counterstained with DAPI (**Figure 3.3A**). After labeling these colonies, we noticed that Oct4 (an hESC pluripotency marker) expression was strongest within the hESC colonies (indicative of embryoid bodies), whereas Oct4 expression noticeably weakened away from the center of the hESC colonies, as evident from **Figure 3.3A**. By visual inspection, cells expressing low levels of Oct 4 (termed Oct4^{low}) are mainly located outside the cell clusters (bulk region of colonies), whereas cells expressing high levels of Oct4 (termed Oct4^{high}) reside inside the bulk regions of colonies (**Figure 3.3A**, third panel).

The observed Oct4 expression pattern, as denoted by quantitative mean fluorescence intensity (MFI) after image-based analysis, demonstrated a bimodal distribution pattern when plotted (**Figure 3.3B**). A k-means clustering algorithm determined the boundaries of the two subpopulations, resulting in an MFI threshold value of 45 (validated by manual gating performed on isotype controls, showing a baseline MFI = 42 to cover 95% of all negative controls). Tracking the locations of the cells over the lifetime of the culture, it was further confirmed that cells with high Oct4 and low Oct4 regions were located within the colony and outside the colony,

respectively. This served as a functional indicator and supervisor of two distinctive subpopulations to perform nuclear descriptor analysis and classification.

For each cell in the high Oct4 and low Oct4 subpopulations, 43 quantitative descriptors of the NuMA protein were acquired. Dimension reduction (PCA) followed by a support vector machine (SVM) classifier was used to classify cell subpopulations that were outside the colony (low Oct4 regions) versus inside the colony (high Oct4 regions). The PCA plot showed that subpopulations expressing high Oct4 (blue circles) and low Oct4 (red circles) were in small clusters, suggesting that the measured NuMA morphology of hESCs in the subpopulations is highly homogeneous (**Figure 3.3C**). SVM classification of the two populations resulted in a sensitivity of 0.93 ± 0.03 , a specificity of 0.86 ± 0.06 , and an overall accuracy of 0.91 ± 0.01 . Our results show that PCA together with SVM classification is capable of identifying and parsing differentiating versus pluripotent hESCs in culture.

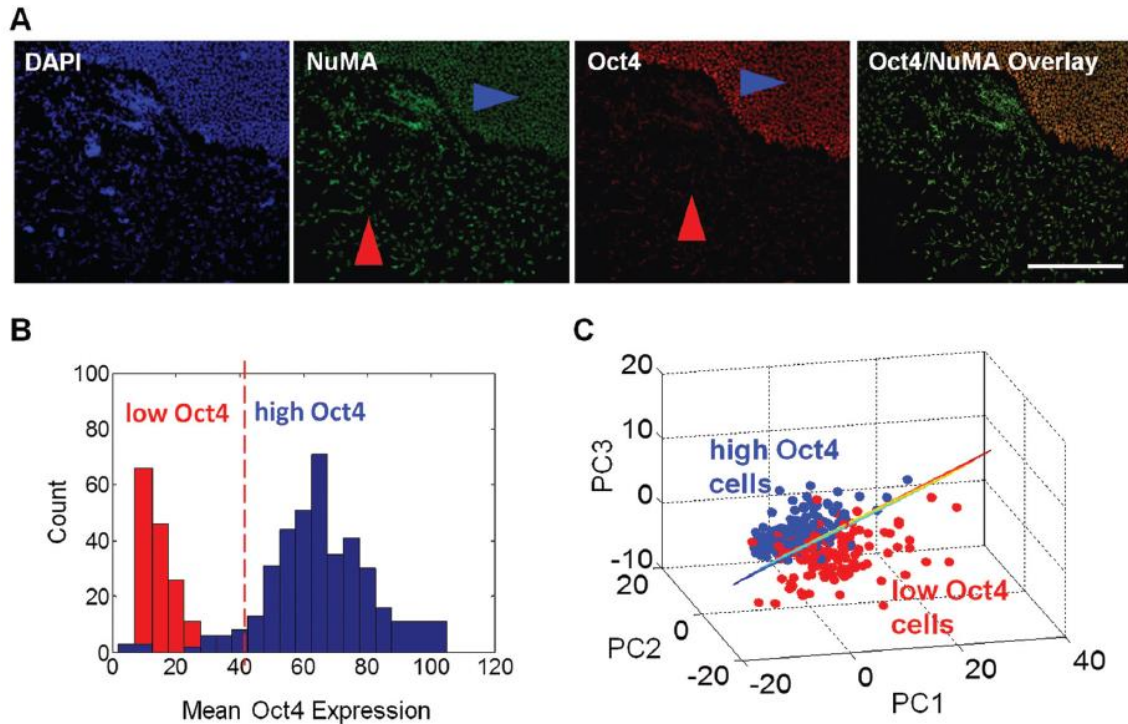


Figure 3.3: NuMA Descriptors Dependent on Oct4 Expression in hESC Cultures

(A) hESCs were immunolabeled with antibodies specific for NuMA (green) and Oct4 (red) and counterstained with DAPI (blue). Blue and red arrows highlight the NuMA and Oct4 signal of hESCs that would be classified as high Oct4 and low Oct4 expression, respectively. **(B)** K-means clustering of Oct4 fluorescence was used to determine low Oct4 and high Oct4 subpopulations. **(C)** PCA plot of numerical NuMA descriptors of low Oct4 versus high Oct4 cells shows that cells in each population are distinct based on three-dimensional plots of high-dimensional descriptors. SVM statistics yielded sensitivity, specificity, and accuracy of 0.93 ± 0.03 , 0.86 ± 0.06 , and 0.91 ± 0.01 , respectively. PC, principal component. Scale bars: 100 μm .

3.4.3 Nuclear Features of iPSCs Are Unique to Sox2 Expression

Next, we expanded the utility of our imaging-based profiling methodology to iPSC phenotypes. Differences in nuclear features of iPSCs, based on different degrees of pluripotency, were classified. To determine pluripotency, Sox2, a transcription factor essential for stem cell self-renewal, was used. iPSCs were immunolabeled for antibodies specific for NuMA and Sox2 and were counterstained with DAPI (**Figure 3.4A**). Sox2 expression (represented by MFI values) of iPSCs was quantified via imaging-based analysis of the red channel, and the MFI cutoff threshold value determined from the isotype controls (baseline MFI = 42 to cover 95% of all negative controls) was used to identify subpopulations of cells containing high (Sox2^{high}) and low (Sox2^{low}) levels of Sox2 (**Figure 3.4B**) in heterogeneous iPSC colonies.

For each cell in the Sox2 expression group (Sox2^{high}, n = 75; Sox2^{low}, n = 153), 43 nuclear descriptors of the NuMA protein were attained. PCA was then used to reduce the dimensionality of nuclear features for cell subpopulations that were Sox2^{high} versus Sox2^{low}. PCA plot shows that the Sox2^{high} (blue circles) and Sox2^{low} (red circles) subpopulations primarily centralized in respective single clusters, inferring that nuclear features calculated from the iPSCs were highly homogeneous within the same Sox2 expression group (**Figure 3.4C**). In contrast, NuMA-based nuclear features between Sox2^{high} and Sox2^{low} subpopulations were found to be distinct, as indicated by the hyperplane in **Figure 3.4C**. SVM classification of the two subpopulations resulted in a sensitivity of 0.91 ± 0.05 , a specificity of 0.82 ± 0.11 , and an overall accuracy of 0.87 ± 0.03 . Similar to our hESC imaging-based analysis, PCA in combination with SVM

classification was effective at identifying and parsing pluripotent ($\text{Sox2}^{\text{high}}$) iPSCs from those with low Sox2 expression, indicative of a low-pluripotency phenotype.

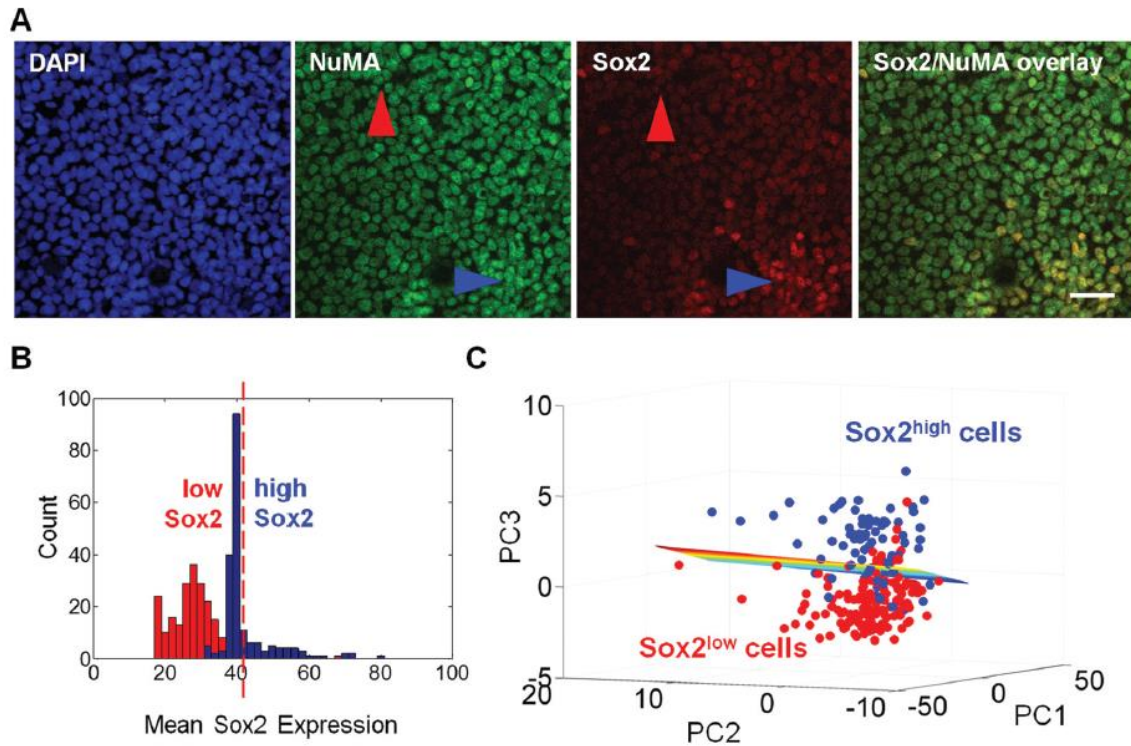


Figure 3.4: NuMA Descriptors Dependent on Sox2 Expression in iPSC Cultures

(A) iPSCs labeled with NuMA (green), Sox2 (red), and DAPI (blue). Red and blue arrows highlight the NuMA and Sox2 signal of iPSCs that would be classified as having low Sox2 (Sox2^{low}) and high Sox2 ($\text{Sox2}^{\text{high}}$) expression, respectively. iPSCs to the left of the red dotted line in **(B)** were binned as Sox2^{low} and the remainder as $\text{Sox2}^{\text{high}}$. **(C)** PCA plot of numerical NuMA descriptors of cells expressing high Sox2 versus low Sox2 expressing iPSCs show that cells in each population are morphologically different. SVM statistics yielded sensitivity, specificity, and accuracy of 0.91 ± 0.05 , 0.82 ± 0.11 , and 0.87 ± 0.03 , respectively. PC, principal component. Scale bars: 25 μm .

3.4.4 Polymer Film PEG Content Induces Changes in hMSC Cytoskeleton

Next, hMSCs were used as a test case to adapt our high content imaging-based method to cultures on synthetic biomaterials with systematically varied hydrophobicity and protein adsorption behaviors. To achieve differences in hydrophobicity, polyethylene glycol-co-poly(desaminotyrosyl-tyrosine ethyl ester carbonate) copolymers with varying degrees of PEG were fabricated into films. Copolymers with higher PEG content resulted in decreased hydrophobicity. Several literature accounts suggest that PEG has a vital role in various stem cell functions. For example, Briggs et al. showed that hMSCs cultured in poly(desaminotyrosyl-tyrosine ethyl ester carbonate) films with low PEG content exhibited increased osteogenic marker expression [209]. Higher levels of PEG content have also been attributed to highly selective protein adsorption and cell motility [73]. Although the influence of PEG content on cell function has been widely studied, high content differences in the organization of cytoskeletal proteins such as F-actin have not been examined.

Cells were cultured on tyrosine-derived films with varying weight percentages of PEG (termed 2%, 3%, 4%, and 8% versus 0% controls). Representative images of the F-actin cytoskeleton for each condition show that there are differences in organization as PEG content increases (**Figure 3.5A**), including a decrease in actin stress fibers (green) and cell size. To quantify these differences, actin mean intensity (actin signal per unit area) and area (size) were acquired and analyzed as traditional low-content features (**Figure 3.5B**). As expected, the overall area exhibited a decreasing trend with increasing PEG content due to increasing hydrophilicity and nonfouling polymer film properties;

however, a one-way ANOVA yielded no statistical significance ($p > 0.05$) between the various PEG-containing conditions (2% PEG and above). In addition, when comparing just the signal intensity across all conditions, no statistical significance was found (0% PEG and above). Therefore, using conventional low-content image features such as cell area and cell intensity, we were unable to readily distinguish across PEG-containing conditions. To identify morphological changes, higher content analyses capable of identifying more sensitive changes in morphology are necessary.

Using our imaging-based profiling approach, a PCA plot comparing copolymers with 2% versus 8% PEG resulted in almost complete separation (0.97 ± 0.01 sensitivity, 0.87 ± 0.02 specificity, and an accuracy of 0.92 ± 0.01) (**Figure 3.5C**). Since differences in actin morphology can be easily visualized, this supports the validity of our proposed classifier. To assess the sensitivity of this classifier, PCA was employed to compare two conditions that cannot otherwise be discerned using a low-content approach (**Figure 3.5C- 3.5D**). Sensitivity, specificity, and accuracy of copolymers with 4% versus 8% PEG yielded values of 0.83 ± 0.02 , 0.74 ± 0.02 , and 0.78 ± 0.01 , respectively. Next, classification of condition A (x-axis) versus condition B (points on plot) of all substrate combinations was employed, and the resulting accuracy was plotted (**Figure 3.5E**). Using a 10-fold cross-validation, SVM was able to correctly classify differences between most conditions with $> 80\%$ accuracy and differences between all conditions with $> 60\%$ accuracy. Sensitivity, specificity, and accuracy with error reported as standard deviation of $n = 50$ pseudoexperiments for all substrate combinations can be found in **Table 3.2**.

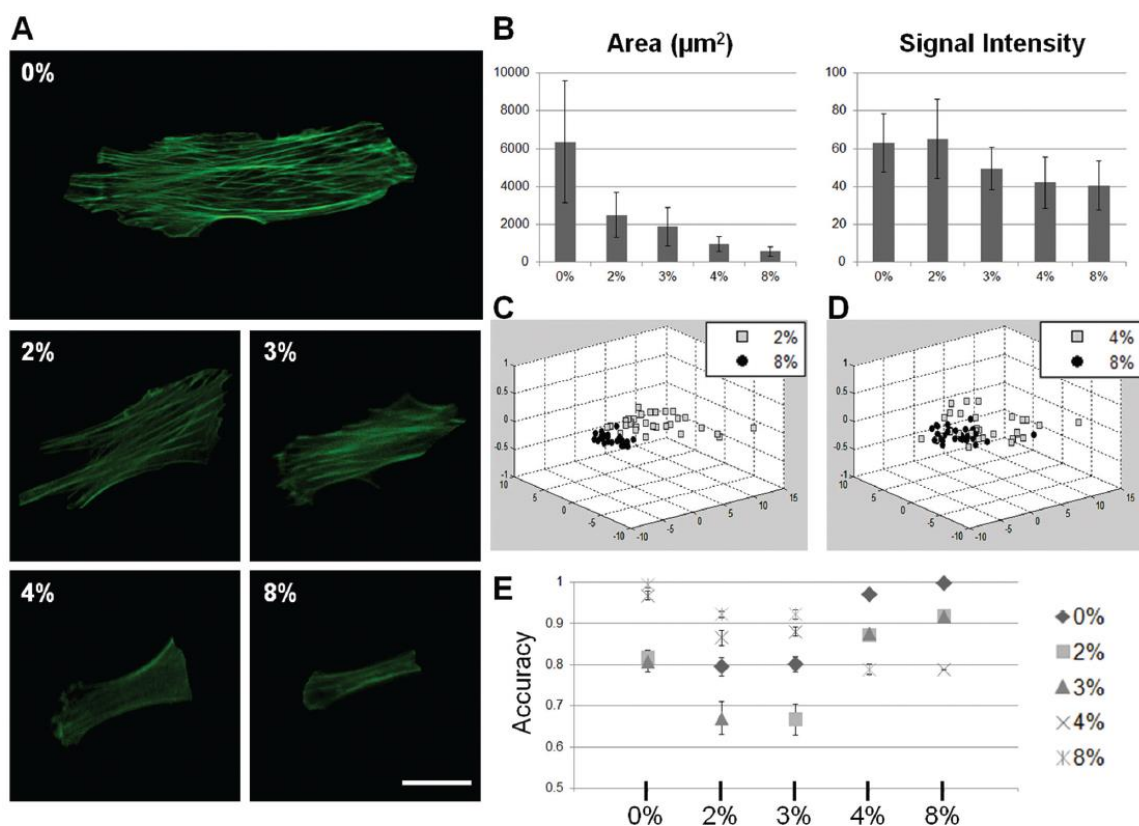


Figure 3.5: hMSC Actin Descriptors Dependent on % PEG in Polymer Films

(A) Representative images of the actin cytoskeleton of hMSCs cultured on films copolymerized with different degrees of PEG. **(B)** Plots of area and signal intensity of the actin yield little information about morphological differences across the different PEG-containing biomaterial conditions (error bars represent standard deviation for $n = 30$ cells per condition). **(C)** PCA plot of actin descriptors of hMSCs cultured in 2% versus 8% PEG copolymer films yields almost complete parsing between the conditions. **(D)** PCA plot of two conditions yielding morphologically similar cells, 4% versus 8% PEG copolymer films, yields an improved classification of cell populations based on high content analysis. **(E)** Summary of PCA accuracy of condition A (x-axis) versus condition B (points in plot) is shown. Scale bar: 25 μm .

N = 50 pseudoexperiments		0% PEG		2% PEG		3% PEG		4% PEG		8% PEG	
		AVG	STDEV	AVG	STDEV	AVG	STDEV	AVG	STDEV	AVG	STDEV
0% PEG	Sens			0.84	0.03	0.83	0.02	0.99	0.01	1.00	0.01
	Spec			0.76	0.03	0.77	0.02	0.95	0.02	1.00	0.00
	ACC			0.80	0.02	0.80	0.02	0.97	0.01	1.00	0.01
2% PEG	Sens	0.77	0.02			0.29	0.08	0.91	0.02	0.97	0.00
	Spec	0.87	0.02			0.28	0.06	0.84	0.01	0.87	0.01
	ACC	0.82	0.02			0.29	0.04	0.87	0.01	0.92	0.01
3% PEG	Sens	0.77	0.05	0.29	0.05			0.92	0.01	0.97	0.00
	Spec	0.85	0.03	0.25	0.09			0.83	0.02	0.87	0.00
	ACC	0.81	0.03	0.27	0.03			0.88	0.01	0.92	0.00
4% PEG	Sens	0.94	0.02	0.83	0.03	0.84	0.01			0.83	0.02
	Spec	0.99	0.01	0.90	0.02	0.92	0.02			0.75	0.02
	ACC	0.97	0.01	0.87	0.02	0.88	0.01			0.79	0.00
8% PEG	Sens	1.00	0.00	0.88	0.02	0.88	0.02	0.72	0.02		
	Spec	0.99	0.02	0.97	0.00	0.97	0.00	0.85	0.02		
	ACC	1.00	0.01	0.92	0.01	0.92	0.01	0.79	0.01		

Table 3.2: SVM Classification Results for hMSCs on PEG-Containing Films

Sensitivity, specificity, and accuracy for Group 1 (rows) versus Group 2 (columns) can be seen, with error reported as standard deviation for n = 50 pseudoexperiments.

3.4.5 NuMA Descriptors Discern hMSC Differentiation on SAM Gradients

In our last case study, we applied our high content profiling approach to a self-assembled monolayer (SAM) gradient substrate platform, which allowed us to investigate how hMSCs respond to incremental changes of substrate properties. In this study, a -COOH / -OH gradient via a "click" biofunctionalization described previously [210-212], with a varying molar ratio of -COOH to -OH groups on a functionalized glass slide was used (**Figure 3.6A**). Multipotency of hMSCs cultured on the SAM gradients for 7 days under adipogenic induction was measured via expression of CD90, a protein that decreases in expression when stem cells differentiate to osteoblasts, chondrocytes, or adipocytes [213, 214]. CD90 expression across all regions of SAM gradients was low, ranging from 5% to 16% across the SAM gradient when compared with naïve stem cell controls (**Figure 3.6B**). As the gradient became more hydrophilic (more -COOH groups, less -OH groups), CD90 expression increased along the gradient, suggesting increased loss of pluripotency due to the progression of adipogenic differentiation, mediated by an increase in substrate hydrophilicity.

In parallel, NuMA protein descriptors were acquired for hMSCs cultured in adipogenic induction medium on the SAM gradient at 3 days. It is important to note that at 3 days, traditional functional markers fail to denote the onset of lineage commitment [56]. Confocal images of hMSCs immunolabeled with the NuMA protein were acquired in seven locations on the SAM gradient with 5 mm increments. PCA-based nuclear feature dimensionality reduction was then used to reduce the dimensionality of nuclear features for cell populations compared with that of naïve hMSCs. **Figure 3.6C** shows a

comparison made between the -COOH region 5 mm from the hydrophilic end and hMSCs cultured on the SAM chip with basal medium. Further SVM classification was performed on cells at each individual location compared with naïve hMSC controls (cultured on the SAM chip in basal medium for 3 days). Classification results showed that cells cultured on the hydrophilic end (with the lowest level of CD90 expression) feature different NuMA protein morphologies versus the naïve hMSC controls, with classification sensitivity, specificity, and accuracy of 0.99 ± 0.01 , 0.96 ± 0.02 , and 0.98 ± 0.01 , respectively. Comparisons between all SAM gradient locations and naïve hMSC controls are shown in **Figure 3.6D**, where an incremental decrease of nuclear difference (classification accuracy) was observed on gradient locations ranging from within -COOH (hydrophilic)-rich regions to -OH (hydrophobic)-rich regions, with the lowest difference value (65%) observed at the hydrophobic end. Sensitivity, specificity, and accuracy with error reported as standard deviation of $n = 50$ pseudoexperiments for all substrate combinations can be found in **Table 3.3**.

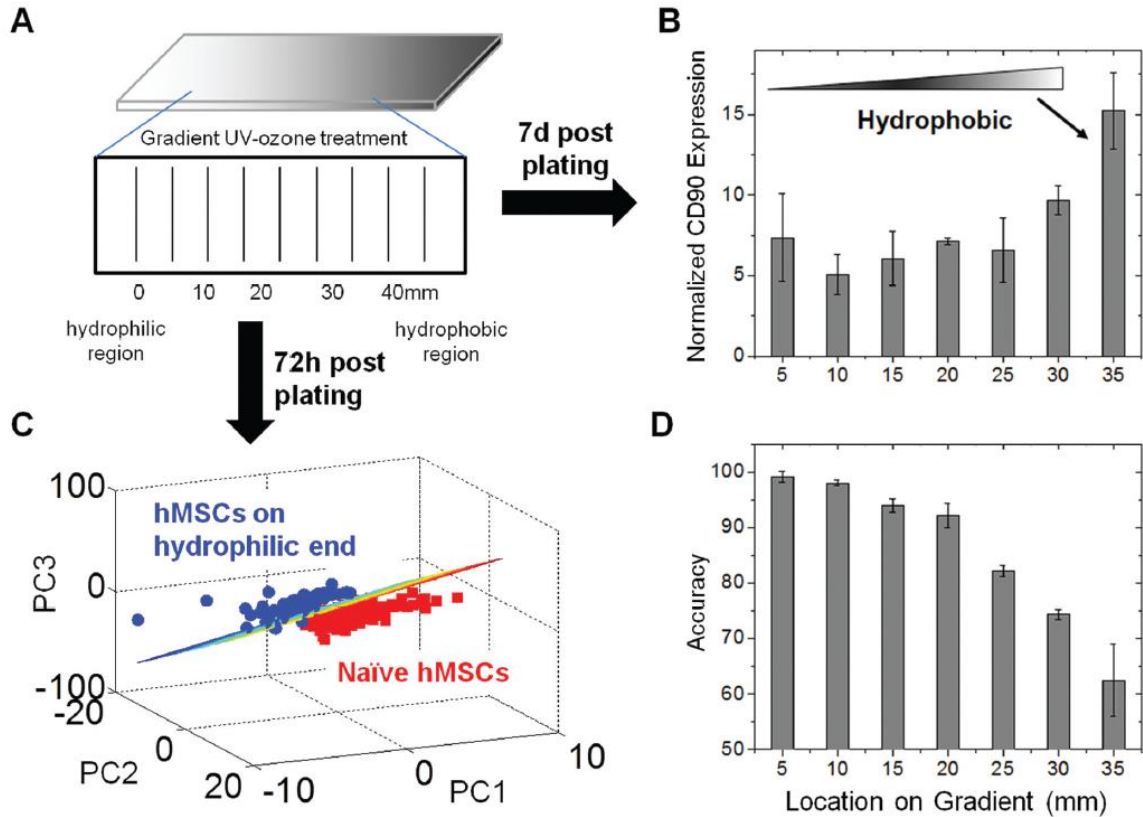


Figure 3.6: NuMA Organization of hMSCs Cultured on Hydrophobicity Gradient

(A) Hydrophobicity gradient prepared by increasing levels of ozone-derived oxidation resulted in a SAM glass slide featuring a hydrophilic (-COOH rich) region that incrementally changes to a highly hydrophobic (-OH rich) end. **(B)** hMSCs express variable CD90 levels along the SAM gradient after 7 days of AD induction. **(C)** Cells cultured on the hydrophilic end (expressing lowest levels of CD90) had different nuclear features from the control group, which expressed high CD90 levels and was cultured in basal growth medium (with SVM classification results being 0.99 ± 0.01 , 0.96 ± 0.02 , and 0.98 ± 0.01 for sensitivity, specificity, and accuracy, respectively). **(D)** SVM classification accuracy demonstrated differences in nuclear features of hMSCs cultured on the SAM gradient when compared with naïve hMSC controls.

Location on Gradient (mm)	Sensitivity	Specificity	Accuracy
5 (COOH rich region)	0.99 ± 0.01	0.93 ± 0.09	0.99 ± 0.01
10	0.99 ± 0.01	0.96 ± 0.02	0.98 ± 0.01
15	0.94 ± 0.05	0.94 ± 0.03	0.94 ± 0.01
20	0.94 ± 0.04	0.90 ± 0.07	0.92 ± 0.02
25	0.88 ± 0.04	0.69 ± 0.10	0.82 ± 0.01
30	0.81 ± 0.04	0.69 ± 0.08	0.74 ± 0.01
35 (OH rich region)	0.71 ± 0.05	0.53 ± 0.12	0.62 ± 0.06

Table 3.3: SVM Classification Results for Several Locations on SAM Gradient

SVM classification results for adipogenically-induced hMSCs cultured on SAM gradient at different locations versus hMSCs cultured in basal medium. Sensitivity, specificity, and accuracy for a given location versus a two-dimensional basal control can be seen, with error reported as standard deviation of $n = 50$ pseudoexperiments.

3.5 DISCUSSION

Typical high-throughput screening approaches are insufficient for examining heterogeneous cell cultures as they only provide data on the cell population as a whole. This shortcoming is particularly acute for stem cells, including embryonic, induced pluripotent, and mesenchymal adult stem cells, which can commonly adopt divergent phenotypes as a function of culture time and environmental conditions. We have proposed a high content imaging-based platform that is capable of parsing numerical morphological descriptors from images of individual stem cells cultured in varied microenvironments. By combining integrated fluorescence imaging, quantitative image analysis, and computational data mining, this approach can provide insights about the organization of various cellular proteins at a single cell level. In this Chapter, we demonstrate the potential of high content imaging-based profiling to reveal subpopulations across a wide spectrum of stem cell types in different stages of development and their responses to a diverse range of material configurations.

Our high content analyses of descriptors derived from intracellular reporter proteins support the notion that NuMA and actin are sensitive biological markers for classifying how cells interact with their environmental milieu. Stem cell signaling events are triggered by early cell attachment, for example, when focal adhesions reinforce receptor-mediated cell adhesions to adsorbed extracellular matrix (ECM) proteins on the substrate [156]. Integrin-mediated mechanotransduction results in changes within cytoskeletal structures, which in turn influence the organization of nucleoskeletal scaffolding and nuclear proteins, triggering a cascade of signaling pathways that lead to

microenvironment-driven cell behaviors, including the switch between cell differentiation and self-renewal [215]. Thus, cytoskeletal and nuclear protein morphologies were likely influenced by outside-in signaling pathways stemming from chemical, physical, and biological changes in the microenvironment. In addition, the organization of the NuMA and actin may provide information about cell state. For example, the distribution of NuMA is cell cycle-dependent, as it is essential in mitotic spindle positioning and asymmetric cell division during mitosis [178]. Actin stress fiber thickness, density, and actin-mediated cell shape are all influenced by cell adhesion to the underlying substrate [73, 209] and have also been linked with lineage commitment [133].

Stem cell culture systems are limited by scalable techniques to discern pluripotent hESC and iPSC subpopulations from those that are already lineage committed. Pluripotent cells, demarcated by marker expression, exhibit highly distinguishable NuMA protein features (high sensitivity and specificity) from differentiating stem cells. This suggests that the NuMA protein organization can be used as an indicator of the hESC and iPSC phenotype, either pluripotent or lineage committed, although the latter has not been explicitly addressed in this study. Previously, we have reported that NuMA protein organizational features display distinctive patterns when hMSCs undergo osteogenic versus adipogenic differentiation [56]. Follow-up studies need to be conducted to assess whether lineage commitment of iPSCs and hESCs (e.g., specific cell types from the endoderm, mesoderm, or ectoderm) can be similarly captured through profiling of the NuMA protein. The identification of

early nuclear morphological signatures predictive of long-term lineage commitment in iPSCs and hESCs could significantly enhance the throughput of biomaterial screening methods since it typically takes these stem cell lines weeks or even months to differentiate into mature phenotypes.

In regenerative medicine, stem cells are induced to desirable lineages via the use of extracellular stimuli based on soluble factors and engineered substrates with controlled surface chemistry and physical properties. We sought to assess whether outside-in signaling emanating from synthetically engineered biomaterials translates to morphological differences seen in our reporter proteins. As previously shown, hMSCs cultured on tyrosine-derived biodegradable scaffolds containing varying degrees of PEG exhibited differences in actin stress fiber formation under conditions that induce changes in adhesion and differentiation [73, 209]. This suggests that stem cells can function as biological probes to discern subtle variations in biomaterial properties that dictate stem cell functions.

Our high content descriptor-based methods were able to sensitively discern differences in morphology resulting from changes in PEG molar fraction of the tyrosine-derived polycarbonate polymers. Notably, the classification efficiency was lower when comparing cell descriptors across conditions with smaller differences in PEG content. This could be due to the fact that most of the descriptors used in this study are shape-based (**Table 3.4** and **Table 3.5**). For each axis (termed PC, principal components) the descriptors were identified as influential if the weighting factor was more than half of the highest weighting factor in the linear transformation equation. The number next to

each PC in **Table 3.4** and **Table 3.5** represents the percentage of variance that the axis accounts for, and the descriptor values represent the weight factors in the linear transformation equation; the larger the value, the more influential the descriptor is. Higher PEG content results in a decrease in cell size and actin stress fibers. For example, texture-based descriptors resolving minute differences in the intracellular actin architecture could likely improve the degree of classification. Studies using texture-based descriptor sets are shown in **Chapter 5**.

Oct4 high vs. Oct4 low

PC1 = 20.29		PC2 = 5.91		PC3 = 4.49	
Feature	Value	Feature	Value	Feature	Value
Feret (mean)	0.220	Radius (min)	0.284	Density (std.dev.)	0.317
Perimeter (convex)	0.220	Area/Box	0.279	Density (mean)	0.310
Perimeter (ellipse)	0.218	Diameter (min)	0.258	Heterogeneity	0.304
Perimeter2	0.216	Axis (minor)	0.203	Perimeter (ratio)	0.239
Perimeter3	0.216	Perimeter (ratio)	0.192	Clumpiness	0.217
Perimeter	0.216	Per Area (Obj./Total)	0.180	Area/Box	0.192
Area	0.214	Feret (min)	0.155	Radius (min)	0.183
Area (polygon)	0.214	Size (width)	0.154	IOD	0.178
Diameter (mean)	0.213			Density (sum)	0.178
Feret (max)	0.211				

Sox2 high vs. Sox2 low

PC1 = 23.23		PC2 = 9.52		PC3 = 4.14	
Feature	Value	Feature	Value	Feature	Value
Feret (mean)	0.204	Perimeter (ratio)	0.267	Density (mean)	0.414
Perimeter (ellipse)	0.203	Area/Box	0.240	Density (std.dev.)	0.328
Diameter (mean)	0.201	Hole Ratio	0.228	Heterogeneity	0.303
Area	0.201	Radius (min)	0.187	Clumpiness	0.117
Per Area (Obj./Total)	0.201	Heterogeneity	0.170		
Area (polygon)	0.200	Density (std.dev.)	0.166		
Perimeter (convex)	0.197	Diameter (min)	0.153		
Diameter (max)	0.192				
Feret (max)	0.192				

Table 3.4: Top Descriptors for Parsing Between Pluripotent and Differentiating Cells

Blue, green, and red correspond to shape, intensity, and textural/organizational descriptors, respectively.

2% PEG vs. 8% PEG

PC1 = 56.67		PC2 = 14.38		PC3 = 8.33	
Feature	Value	Feature	Value	Feature	Value
Perimeter (convex)	0.195	Roundness	0.309	Aspect	0.387
Feret (mean)	0.193	Dendrites	0.275	Radius Ratio	0.386
Perimeter	0.190	End points	0.275	Radius (min)	0.261
Perimeter (ellipse)	0.187	Dendritic length	0.270	Area/Box	0.253
Diameter (mean)	0.187	Perimeter (ratio)	0.258	Diameter (min)	0.235
Area (polygon)	0.187	Fractal Dimension	0.258	Heterogeneity	0.233
Feret (max)	0.187	Hole Ratio	0.210	Den./Inten. (std.dev.)	0.205
Radius (max)	0.187	Clumpiness	0.207	Clumpiness	0.202
Size (length)	0.186	Holes	0.182	Den./Inten. (mean)	0.188
Perimeter3	0.186	Perimeter2	0.165	Axis (minor)	0.180

4% PEG vs. 8% PEG

PC1 = 42.49		PC2 = 22.43		PC3 = 12.54	
Feature	Value	Feature	Value	Feature	Value
Perimeter (convex)	0.225	Dendrites	0.249	Aspect	0.344
Feret (mean)	0.224	End points	0.249	Radius (min)	0.331
Perimeter (ellipse)	0.217	Dendritic length	0.247	Diameter (min)	0.330
Radius (max)	0.213	Holes	0.247	Radius Ratio	0.305
Feret (max)	0.213	Perimeter (ratio)	0.241	Axis (minor)	0.260
Size (length)	0.212	Perimeter2	0.235	Area/Box	0.202
Perimeter	0.211	Den./Inten. (mean)	0.235	Diameter (mean)	0.194
Diameter (max)	0.206	Roundness	0.230	Heterogeneity	0.182
Area	0.204	Fractal Dimension	0.219	Size (width)	0.179
Per Area (Obj./Total)	0.204	Den./Inten. (max)	0.215	Den./Inten. (std.dev.)	0.179

Table 3.5: Top Descriptors for Parsing hMSCs on Films of Varying % PEG

Blue, green, and red correspond to shape, intensity, and textural/organizational descriptors, respectively.

Self-assembled monolayers (SAMs) of alkanethiols have been modified to present well-defined and controllable surfaces featuring a wide range of chemical properties [216]. Specific modifications in surface chemistry alone can differentially modulate hMSC differentiation in a lineage-dependent manner [217]. Due to higher ECM protein adsorption at the -COOH rich region (hydrophilic end) of SAM substrates, more cells adhered when compared with the -OH rich regions (hydrophobic end), which in turn altered the rate of adipogenic differentiation on SAM gradient substrates. The

fact that these variations were identified as early as 3 days via NuMA profiling highlights the potential application of this platform towards the early detection of differentiation-inducing materials for biomaterial discovery in regenerative medicine.

In summary, we have demonstrated that heterogeneous phenotypes of stem cell populations can be captured using high-dimensional organizational mapping of intracellular protein reporters. Although the geometries for culture systems explored here are restricted to two dimensions, the high content imaging approach could be readily extended in the future to cell cultures in varied configurations, ranging from three-dimensional scaffolds to hydrogels. Although the data presented here were primarily derived from cells fixed and labeled with fluorophores, in theory, this approach can be easily applied to reporter cell lines in real-time in lieu of static, fixed cells. The high content imaging methods can also be potentially coupled with newer technologies for biomolecular screening, such as emerging, single cell gene readout assays to enable multimodal cell state analyses, as well as cell sourcing platforms for isolating cell subpopulations based on higher dimensional biological features [218].

CHAPTER 4. NUMA ORGANIZATION AS A DETERMINANT OF STEM CELL PHENOTYPIC STATES

Note: Sections of this chapter are in preparation for submission as the following publication:

E Liu, SL Vega, N Bennett, AB Kulesa, J Bushman, H-J Sung, ML Becker, P-A Vidi, S Lelièvre, J Kohn, PV Moghe. NuMA-Based Imaging Platform for Single Cell Phenotyping. *To be submitted to PLOS ONE, 2014.*

4.1 ABSTRACT

Current methods to identify cell phenotypes rely on population-based assays that are only expressed in fully differentiated cells and fail to capture the heterogeneity in cell cultures *in vitro*, and tissues *in vivo*. Here we present a single cell imaging-based methodology to derive quantitative metrics of the nuclear mitotic apparatus (NuMA) protein, a key nuclear structural protein with functions in mitosis, chromatin control, and DNA repair, to identify subpopulations that are indistinguishable using conventional techniques. To demonstrate the versatility of our approach, we apply it to identify cellular phenotypes in three distinct applications. First, as a screening tool, we utilize 3 day NuMA metrics to rank 10 day oncogenic responses of a biomaterial library. Second, to showcase our method's ability to classify cell subtypes *ex vivo*, we identify three neural precursor cell populations with identical antigen expression but divergent proliferation and differentiation profiles. Lastly, to demonstrate the application of single cell imaging-based profiling to increase the population homogeneity in live cell colonies, we utilized NuMA descriptors of human embryonic kidney cell (HEK-293) expressing fluorescent NuMA to distinguish between HEK-293 cells with and without DNA-damage treatment in a mixed population. Ablation of DNA-damaged cells resulted in a measurable increase in population viability after treatment with Taxol, a major drug used in cancer therapy that selectively kills DNA-damaged cells. In summary, our imaging-based approach is a powerful parsing tool for both predicting and discriminating cellular phenotypes *in vitro* and *ex vivo*, and to purify populations in live-cell systems.

4.2 INTRODUCTION

Recent breakthroughs in stem cell biology have the potential to advance tissue repair and regeneration after injury or disease [219]. Stem cell signaling programs are complex and vary tremendously across different tissues and niche-dependent developmental processes. As such, the ability to accurately assess the plasticity of stem cells to their environments is extremely challenging [220-222]. Identifying cell phenotypes and predicting single cell responses to biomaterials may provide new insights into differentiation mechanisms as well as lay the groundwork for new tools to purify and test cell cultures. However, current tools to characterize stem cell states are suboptimal because they are population-based and data limiting, and therefore unable to pinpoint cell phenotypes with single cell resolution.

Our group recently reported that minute quantifiable differences in the cytoskeleton capture early variations of human mesenchymal stem cell (hMSC) lineage commitment prior to detectable phenotypic marker expression [56, 57]. However, the use of actin as a reporter sensitive to the cellular milieu has only been challenged for fixed cells under non-confluent, two-dimensional environments. As the terminal gateway of outside-in signaling and mechanobiology, the nucleus could also hold important organizational cues descriptive of stem cell phenotype. Particularly, nuclear mitotic apparatus (NuMA) protein, a structure necessary for cell cycle progression in the nucleoplasm, may serve as a suitable biological marker for classifying cellular phenotypes due to its role in controlling cell fate and chromatin organization [178, 223]. Thus, the central premise of our methodology is that early signaling events underlying

stem cell differentiation are accompanied by slight changes in nuclear organization that can be revealed through high dimensional organizational metrics. When combined with *in silico* data processing techniques, these metrics can help parse stem cell phenotypes in a wide range of contexts relevant to the clinic, including *ex vivo* analyses and novel imaging-based live cell purification strategies.

In this study we identified nuclear morphologic features of the NuMA protein predictive of biomaterial-induced changes in phenotype, and we also identified cell subtypes in heterogeneous groupings. Using our high content imaging methodology, we identified early subcellular signatures that precede changes in phenotypic marker expression and cellular function. The predictive utility of this platform demonstrates that early morphological signatures of NuMA in hMSCs can be identified within the first 3 days of oncogenic transformation on various biomaterials. Similarly, we identified oligodendrocyte precursor cells derived from various developing brain tissue contexts *ex vivo* that express similar antigen expression and are thus traditionally indistinguishable. Lastly, we found differences in NuMA-based metrics between DNA-damaged and normal human embryonic kidney cells (HEK-293) and removed DNA-damaged cells in HEK-293 colonies via confocal laser ablation. In summary, these three diverse studies highlight the versatility of our imaging-based methodology to screen biomaterials, tissue sections, and purify live heterogeneous cell cultures in real-time.

4.3 MATERIALS AND METHODS

4.3.1 Cell Culture

Human mesenchymal stem cells (hMSCs) were obtained from commercial sources (Lonza; Walkersville, MD). Cells were cultured by following the protocol and reagents provided by Lonza (Walkersville, MD). Cells were received at passage 1 and used between passages 13-19. The *in vitro* oncogenic transformation process was performed via periodic nickel (II) sulfate (Sigma) treatment [224]. Briefly, 24 hours post-plating cells were treated with a 36-72 μ M nickel sulfate solution in mesenchymal stem cell growth medium (Lonza) for 48 hours. The medium was then replaced with basal medium for 48 hours, followed by nickel (II) sulfate treatment for 3 days, and ending with 3 days in basal medium. Genetically transformed hMSCs (termed TSRs in this Chapter) were acquired from Dr. Richard Gorlick. To transform hMSCs to TSRs, hMSCs underwent sequential transduction via the introduction of hTERT, inactivation of p53DD tumor suppressor gene and activation of K-Ras and C-Myc [225]. The osteogenic and adipogenic induction and phenotype characterization of hMSCs were performed following previously described protocols [57].

Oligodendrocyte precursor cells (OPCs) were isolated and cultured as previously described by Power et al. from P6-P7 rat neonates [226]. Briefly, after removing the cerebellum and olfactory bulb, the corpus collosum (CC) was carefully separated from the hippocampus, striatum, and cerebral cortices. To obtain cerebral cortex (CX) OPCs, the dorsal cortical tissue anterior to the underlying hippocampus was taken after carefully removing meninges and separating the hippocampus, corpus collosum, and

other ventral and anterior brain tissues. Lastly, to obtain OPCs from optic nerve (ON) sections encompassing the region ~1 mm from the eye and ~2 mm prior to the convergence of the optic chiasm, the meninges was carefully removed, and sliced with a scalpel prior to enzymatic and mechanical tissue separation.

For *in vitro* cell culture after extraction, OPCs were maintained in base medium, which consists of DMEM (Invitrogen, 11995) supplemented with Sato-components (0.0286% v/v BSA pathocyte, 0.2 μ M progesterone, 100 μ M putrecine, 0.2 μ M sodium selenite), 50 μ g/mL human apo-transferrin, and 1 μ g/mL bovine pancreas insulin. Flasks, glass cover slips, and multi-chamber plates used in OPC experiments were coated with poly-L-lysine. All components were obtained from Sigma Aldrich unless otherwise specified. Following dissection and purification, OPCs were cultured in base medium supplemented with 10 ng/mL rhPDGF-AA (Peprotech) at 37°C in a humidified incubator with 10% CO₂. To assess the percentage of OPCs, immunocytochemistry confirmed > 99% of cells were positive for A2B5 (Millipore, MAB312, 1:500 dilution) and negative for GalC (Millipore, Ab142, 1:500 dilution).

Human endothelial kidney cells (HEK-293) cells (Life Technologies) were cultured by the following protocol provided by Life Technologies and with commercially available reagents. Cells were plated onto cell culture plates coated with 0.1% gelatin solution (Millipore) in DMEM supplemented with 10% fetal bovine serum and 0.1 mM MEM non-essential amino acids (Life Technologies). HEK-293 cells were passaged at 80% confluence and plated at a density of 50,000 cells/cm².

4.3.2 Preparation of OPC Samples for Early (4 Hour) NuMA-Based Image Analysis

Following dissection and processing, OPCs were seeded onto LabTek chamber slides (Thermo Scientific, 177402) at densities of 10,000 to 20,000 cells per chamber with base medium supplemented with 10 ng/mL PDGF-AA. Cells were allowed to adhere for 4 hours, and samples were fixed and stained with antibodies specific for A2B5 and NuMA (Abcam, Cambridge, MA), and counterstained with Hoescht. Samples were then imaged and subject to image analysis.

4.3.3 Long-Term (10 Day) Clonal Analysis of OPCs

The day following isolation and purification, OPCs were plated at a low density in T25 flasks (100-250 cells per flask) in base medium supplemented with 10 ng/mL PDGF-AA for 24 hours to allow for adherence and visual verification of acceptable cell density. Next, flasks were either maintained with base medium supplemented with 10 ng/mL PDGF-AA for proliferation, or cultured with base medium supplemented with 1 ng/mL PDGF-AA and 0.49 nM thyroid hormone (T3/T4) for differentiation. Medium was changed on days three and five, and then fixed on day seven with 2% paraformaldehyde for 10 minutes. Cells were then stained for A2B5, GalC, and Hoescht. The composition of individual clones was ascertained by counting the number of cells (Hoescht positive), the number of OPCs (A2B5 positive and GalC negative), and the number of oligodendrocytes (A2B5 negative and GalC positive) in individual clones.

4.3.4 NuMA Expression in HEK-293 Cells

Human embryonic kidney (HEK-293) cells were cultured using previously established protocols [227]. Upon reaching 80% confluence, HEK-293 cells were seeded onto wells of 8-well glass-bottom LabTek chamber slides at a density of 50,000 cells/cm² and allowed to adhere for 24 hours. Next, an mCherry-NuMA plasmid (provided to us by Dr. Lelievre's laboratory) was introduced to the cells via polyethylenimine (PEI) transfection [228]. Briefly, HEK-293 medium was supplemented with 0.175 µg/cm² of plasmid in PEI at a ratio of 1 µg plasmid per 50 µL PEI for 24 hours and then replaced with fresh medium. The optimized protocol yielded > 70% mCherry-NuMA positive HEK-293 cells.

4.3.5 Etoposide and Taxol Treatments of HEK-293 Cells

To generate DNA-damaged and non DNA-damaged HEK-293 cell co-cultures, HEK-293 cells were plated onto wells of a 12-well TCPS culture plate at a density of 50,000 cells/cm² and allowed to adhere for 24 hours. Next, half of the wells were treated with HEK-293 medium supplemented with 1 µM etoposide, a pharmacological agent used in cancer chemotherapy, that induces DNA strand breaks in rapidly dividing cells [229]. 48 hours post-treatment, DNA and non DNA-damaged HEK-293 cells were split and seeded in a 50:50 ratio for co-culture, resulting in a total seeding density of 50,000 cells/cm². Dependent on experimental conditions, some HEK-293 cultures underwent treatment with Taxol (a drug used in cancer chemotherapy that selectively kills DNA-damaged cells [230]). Briefly, HEK-293 cultures were treated with HEK-293

medium supplemented with 0.25 μ M Taxol for 48 hours. The concentration was optimized such that it kills the majority of etoposide-treated cells without affecting nontreated HEK-293 cells. To supervise cell tracking, cells that were not exposed to etoposide were labeled with CellLight actin-GFP (Life Technologies), per manufacturer's instructions.

4.3.6 Immunocytochemistry (ICC)

Samples were first fixed with 4% paraformaldehyde (Electron Microscopy Sciences, Hatfield, PA) for 10 minutes. Next, a 1 hour blocking and permeabilization step was performed with a 0.1% Triton X-100 (Sigma, St. Louis, MO) / 5% normal goat serum (MP Biomedical, Solon, OH) solution in phosphate-buffered saline (PBS) (Lonza). Primary antibodies, directed either to proliferation marker Topoisomerase α -II or the nuclear mitotic apparatus (NuMA) protein were added at a 1:500 ratio overnight at 4°C, followed by secondary antibodies (Alexa Fluor; Invitrogen, Carlsbad, CA) at a 1:250 ratio for 2 hours at room temperature. To identify cell nuclei, samples were counterstained with 1 μ g/mL 4',6-diamidino-2-phenylindole (DAPI) (Sigma) in PBS.

4.3.7 High Content Imaging and Profiling

Samples were imaged under a 63X immersion objective (NA = 1.3) with a Leica TCS SP2 system (Leica Microsystems, Inc., Wetzlar, Germany). High-resolution images were then subject to nuclear feature extraction and dimensionality reduction, as previously reported (**Figure 4.1**) [56]. Once NuMA signal was individually segmented,

NuMA descriptors were calculated for each cell (**Table 4.1**). Next, Principal Component Analysis (PCA) was used to visualize the data by mathematically reducing the descriptor set into three new dimensions, termed Principal Components (PCs).

We quantified nuclear shape and NuMA morphology using a large pool of descriptors. Descriptors that were defined included: cell nuclear shape, intensity (relating to the expression level of the NuMA protein), and textural/organizational (describing the spatial distribution and location of the NuMA protein within the nucleus) (**Table 4.1**). To better visualize the high dimensional dataset, we used Principal Component Analysis (PCA) which groups a number of possibly correlated descriptors into a smaller set of uncorrelated "integrated descriptors", termed Principal Components (PCs). Using this methodology, the higher dimensional descriptor dataset was reduced to three new dimensions, each representing a linear combination of a group of raw descriptors. To identify differences across conditions, the PCs then underwent a classification scheme which utilized a support vector machine (SVM) with a randomized two-fold cross validation on individual datasets. Two parameters, sensitivity and specificity were calculated using SVM and used to evaluate the performance of the classification. Sensitivity represents the proportion of actual positives that are correctly identified as such, while specificity measure the proportion of negatives that are correctly identified. High classification / prediction is demarcated by high values of sensitivity and specificity, while low values of sensitivity and specificity indicate poor classification / discrimination between two datasets.

For validation purposes, two data sets with known divergent outcomes were compared (**Figure 4.2A**). To assess how different the descriptor values were across the two cell groups, a support vector machine (SVM) classifier was used to calculate sensitivity and specificity. For example, a sensitivity and specificity output of 100% represents perfect separation between two subpopulations. For prediction purposes, a test set was used to compare with positive and negative data sets in the SVM classifier. Two sets of sensitivity and specificity values were generated, reported the difference between test set and negative control, or test set and positive control. The sensitivity and specificity sets were then used to generate a receiver operating curve (ROC), such that the area under the ROC (A_z) is an estimate of how different the test set (black circle) is from the negative (green circle) and positive (red circle) controls (**Figure 4.2B**). By combining the A_z values from the two ROC's (test set versus negative control, and test set versus positive control), a Parsing Index was derived (**Figure 4.2C**). The Parsing Index estimates the location of the test set (black diamond) with respect to the negative (green diamond) and positive (red diamond) controls.

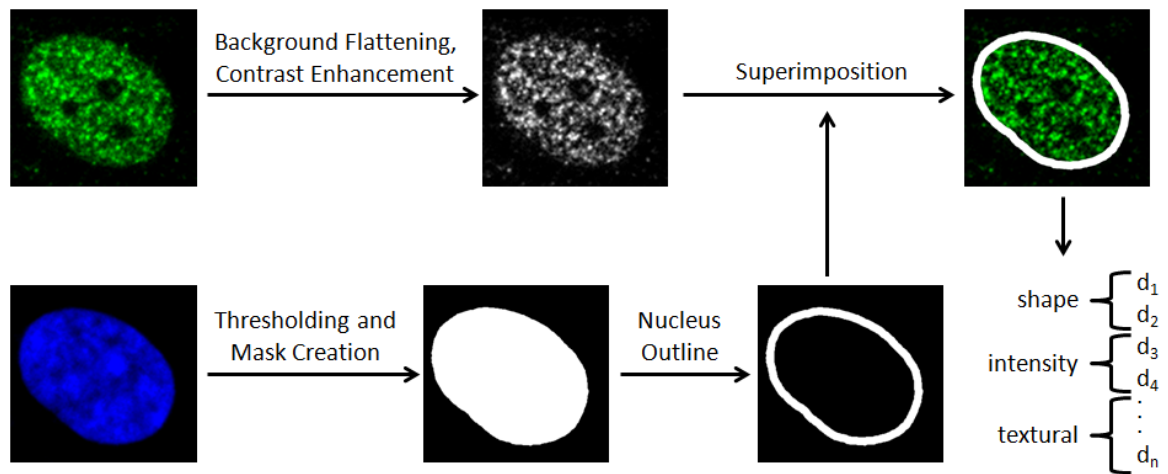


Figure 4.1: Image Processing and Feature Extraction from the Cell Nucleus

Images of cell nuclei labeled with DAPI (blue) were filtered to generate masks in the shape of the nucleus. Prior to superimposing masks onto images of fluorescently-labeled NuMA (green), these images were background flattened, filtered using a low-pass filter, and contrast-enhanced. The segmented NuMA signal was then used to generate over 40 shape-, intensity-, and texture-based descriptors for each individual nucleus.

<i>Nuclear Features</i>	<i>Description</i>
Angle	Reports the angle between the vertical axis and the major axis of the equivalent ellipse. Within the context of this study, it would capture randomly oriented versus aligned cell nuclei, which might be indicative of cell orientation itself.
Area	Reports the total actin/nucleus area of each cell nucleus.
Polygonal Area	Reports the area of the polygon that defines the object's outline. Another metric measurement for area of cell nucleus.
Area/Box	Reports ratio between the area of each object and the area of the imaginary bounding box.
Aspect	Reports the ratio between the major and minor axes of the ellipse with the same area; first and second order moments. The simplest way to define the cell nuclear shape factor.
Axis (major)	Reports the length of the major axis of the ellipse with the same area, first and second order moments of the nucleus.
Axis (minor)	Reports the length of the minor axis of the ellipse with the same area, first and second order moments of the nucleus.
Box Height	Reports the height of the smallest bounding box that completely encompasses the nucleus.
Box Width	Reports the width of the smallest bounding box that completely encompasses the nucleus.
Box Ratio	Reports the ratio between the Box Width and the Box Height.
Maximum Diameter	Reports the length of the longest line joining two outline points and passing through the centroid of the nucleus.
Mean Diameter	Reports the average length of the diameters.
Minimum Diameter	Reports the length of the shortest line joining two outline points and passing through the centroid of the nucleus.
Maximum Feret Length	Reports the longest caliper length.
Mean Feret Length	Reports the average caliper length.
Minimum Feret Length	Reports the shortest caliper length.
Fractal Dimension	Reports the fractal dimension of the cell nucleus's outline.
Cell Area/Total Area	Reports the ratio between the areas of the nucleus to that of the entire field of view.
Perimeter	Reports the length of the outline of each nucleus using a polygonal outline.
Perimeter 2	Faster but less accurate measure of the perimeter.
Perimeter 3	Reports a corrected chain code length of the perimeter.
Convex Perimeter	Reports the perimeter of the convex outline of each nucleus.
Elliptical Perimeter	Reports the perimeter of the ellipse surrounding the outline of each nucleus.
Perimeter Ratio	Reports the ratio of the convex perimeter to the perimeter outline of each nucleus.
Maximum Radius	Reports the maximum distance between each cell nucleus's centroid pixel position and its perimeter.
Minimum Radius	Reports the minimum distance between each cell nucleus's centroid pixel position and its perimeter.
Radius Ratio	Reports the ratio between the Max Radius and Min Radius for each nucleus.
Roundness	Reports the roundness of each nucleus, as determined by the following formula: $\text{Perimeter}^2 / (4 * \pi * \text{Area})$. Circular cells have a roundness of 1.
Size (Length)	Reports the feret diameter (caliper length) along the major axis of the nucleus.
Size (Width)	Reports the feret diameter (caliper length) along the minor axis of the nucleus.

Minimum Density	Reports minimum intensity inside the nucleus.
Maximum Density	Reports maximum intensity inside the nucleus.
Segmentation Range	Reports the intensity range that each nucleus was segmented into.
Mean Density	Reports the mean intensity of all pixels within a nucleus. Correlates to the average amount of fluorescence present within a given nucleus.
Sum of the Density	Reports the sum of the total intensity values of all pixels within a nucleus. Corresponds to the total amount of fluorescence within the nucleus.
Integrated Optical Density	Reports the average intensity of each nucleus normalized by its area.
Standard Deviation of Density	Reports the standard deviation of the intensity of pixels within a nucleus. This represents the degree to which NuMA protein is localized into nucleus of equal staining.
Holes	Reports the number of independent contiguous areas with no staining within a nucleus.
Hole Area	Reports the area of holes within a nucleus.
Hole Ratio	Reports the ratio of the object area excluding holes to the total area of the object as determined by $\text{Area} / (\text{Area} + \text{Hole Area})$.
Margination	Reports the distribution of intensity between the center and the edge of the nucleus. Describes the relative spatial distribution of NuMA protein within the cell nucleus.
Heterogeneity	Reports the fraction of pixels that vary more than 10% from the average intensity of the nucleus. Describes the degree to which NuMA protein is organized into homogeneously stained structures.
Clumpiness	The fraction of heterogeneous pixels remaining in nucleus after a binary erosion process. Reflects the object texture and the degree to which NuMA protein is organized into clusters.

Table 4.1: List of Nuclear and NuMA Protein Descriptors

This table lists the pool of nuclear and NuMA protein descriptors quantified for each cell nucleus. The definition of the feature and its possible biological relevance is listed. Nuclear shape features are highlighted in blue, NuMA intensity-based features in green, and NuMA texture/spatial organizational features in red.

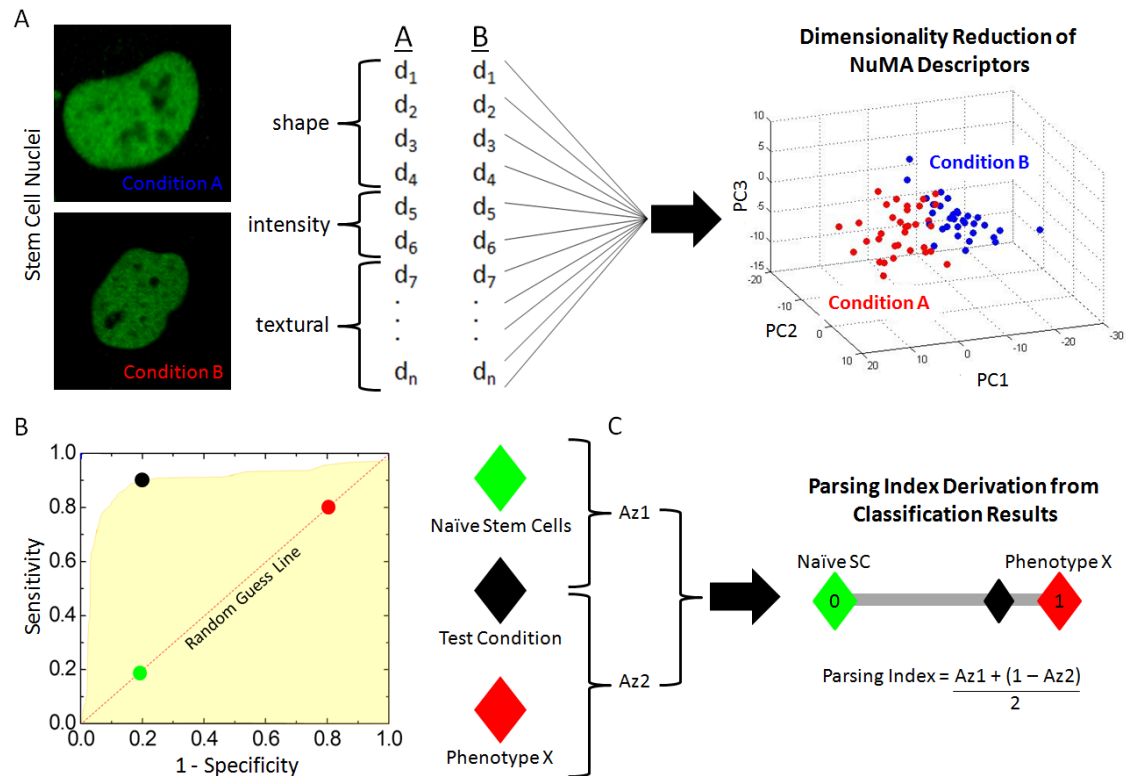


Figure 4.2: *In Silico* Data Processing of NuMA Morphometric Descriptors

(A) Dimensionality reduction (PCA) is applied to generate combinations of descriptors that define the subcellular state of different conditions. Utilizing support vector machine (SVM) classification, sensitivity and specificity were calculated and used to evaluate classification efficiency. **(B)** By shifting a hyperplane that best separates conditions A and B using PCA, a receiver operator curve (ROC) was generated. The ROC curve represents an estimate of how different the test set (black) is from the negative (green) and positive (red) controls. **(C)** Combining the area under the ROC curves (Az) between test set versus negative and test set versus positive controls, a Parsing Index is derived to assess the relative location of the test set in relation to the trained classifier conditions. The Parsing Index values for the test set is between 0 and 1, where 0 and 1 are the negative (green diamond) and positive (red diamond) controls, respectively.

4.3.8 Preparation of Polymeric Substrates for hMSC Transformation Study

Tyrosine-derived polycarbonates [231], polymethacrylates [232], and poly(L-lactic acid) (Resomer L-206) (Boehringer Ingelheim; Ridgefield, CT) were spin-coated on a 15 mm cover glass following previously described protocols [129]. The chemical structures of these polymers can be found on **Figure 4.3**, and the list of polymers used in this study in **Table S2**. hMSCs were seeded on polymer-coated substrates at density of 20,000 cells/cm² and underwent nickel sulfate treatment, as described earlier in this section for either 3 or 11 days. At 3 days, cells were immunolabeled with NuMA and imaged to calculate the Parsing Index, and at 11 days, cells were subject to a telomerase activity functional assay to calculate the Transformation Index, as described in the previous section.

4.3.9 Characterization of hMSC Oncogenic Transformation via FISH

Fluorescence in situ hybridization (FISH) was used to detect and localize the presence of telomerase to assess degree of transformation in hMSC populations. A cadmium selenium (CdSe) conjugated qdot probe (5'-NH₂(CH₂)₁₂-T*C*T*C*AGTTAGGG*T*T*A*G) was designed to be complimentary to human telomerase unit (hTR), an mRNA transcript and a portion of the holo-enzyme (emission peak = 594 nm). Using a FISH protocol from the manufacturer (Roche Applied Science Inc.), telomerase expression was acquired as mean fluorescence intensity (MFI) per cell through image analysis. Next, the extent of oncogenic transformation was interpreted as a normalized experimental "Transformation Index", which was determined by

calculating the fold change of telomerase expression of hMSCs under carcinogen treatment to that of genetically transformed hMSCs (TSRs). The Transformation Index ranges from 0 (no transformation) to 1 (fully transformed).

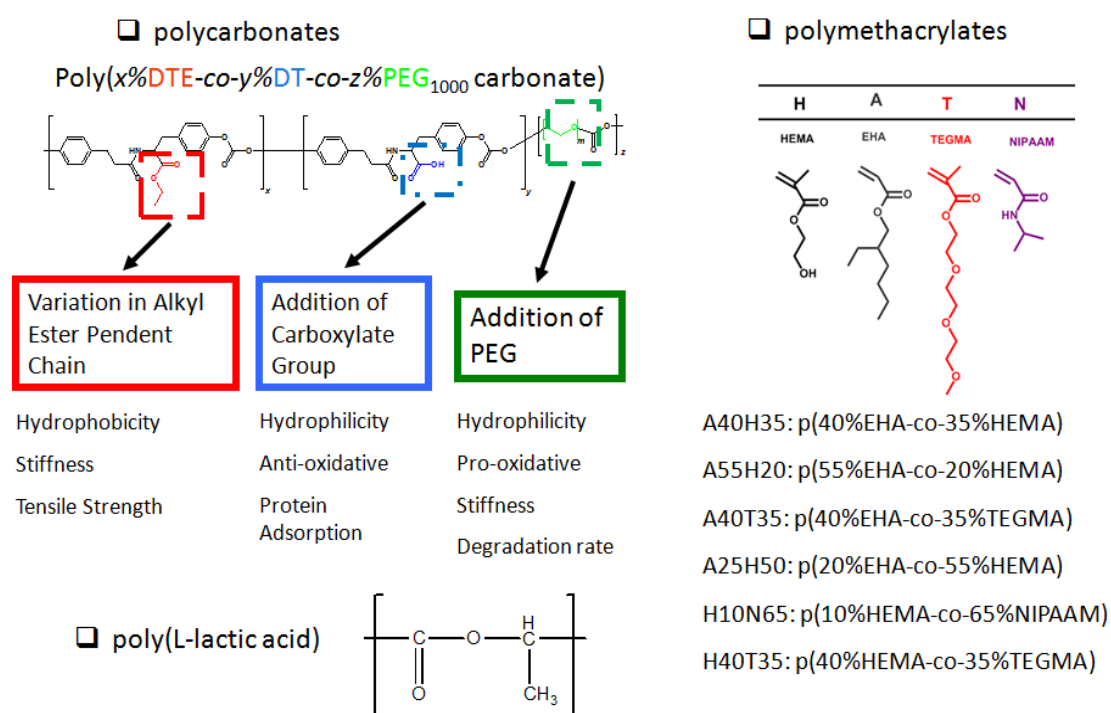


Figure 4.3: Chemical Structures of Biomaterials Used in Transformation Study

Tyrosine-derived polycarbonates (upper left) can be fine-tuned with variations in the alkyl ester pendent chain, via addition of a carboxylate group, and/or an addition of PEG, resulting in different physical and chemical properties that induce different stem cell responses. A polymethacrylate library (upper right) was also utilized. Different combinations of HEMA, EHA, TEGMA, and NIPAAAM result in differences in stiffness. Poly(L-lactic acid) (bottom left) was also included in this study.

Substrate index	Substrate name
1	poly(10%HEMA-co-65%NIPAAm)
2	poly(82%DTE-co-8%PEG-co-10%DT carbonate)
3	poly(DTE carbonate)
4	poly(40%HEMA-co-35%TEGMA)
5	poly(90%DTE-co-10%DT carbonate)
6	poly(55%EHA-co-20%HEMA)
7	poly(L-lactic acid)
8	poly(40%EHA-co-35%HEMA)
9	poly(20%EHA-co-55%HEMA)
10	coverglass
11	poly(40%EHA-co-35%TEGMA)
12	poly(92%DTE-co-8%PEG carbonate)

Table 4.2: Biomaterial Library Used to Rank Effects of NiSO₄-Induced Oncogenic Transformation

4.4 RESULTS

4.4.1 NuMA-Based Metrics Predict Oncogenicity of Surface Chemistries for NiSO₄-Treated hMSCs

We first applied our high content methodology to identify divergent malignant transformation outcomes. This is of particular interest because high levels of regenerative activity of stem cells, similar to those elicited by mutagenic factors under pathological environments, can result in stem cell transformation [221, 233-235]. We designed our first study with biomaterials in mind, particularly in our ability to identify the inhibitor effects of a library of surface chemistries on malignant transformation of stem cells cultured in the presence of nickel sulfate, a carcinogenic agent shown to induce a mutagenic phenotype [224].

Before applying our high content methodology to predict the inhibitory oncogenic effects of a biomaterials library, we tested the effectiveness of our approach at identifying hMSCs treated with nickel sulfate for 3 days. The mean fluorescence telomerase expression of human mesenchymal stem cells (hMSCs) either with or without nickel sulfate treatment was indistinguishable at day 3 of culture (**Figure 4.4A**). This was further confirmed by the Parsing Index, which was only 0.01 when using mean fluorescence intensity alone. In contrast, by applying our high content nuclear profiling methodology we were able to separate the carcinogen-treated hMSC population (black cluster) from the nontreated hMSC population (green cluster). The carcinogen-treated hMSC population localized between the non-treated and TSR populations (red cluster),

and had a 3 day Parsing Index of 0.48, which is significantly higher than the Parsing Index using mean fluorescence intensity alone (**Figure 4.4B**).

Next, high content NuMA protein descriptors were utilized to rank-order the early susceptibility of hMSCs to transformation when cultured on a set of surface chemistries. Twelve distinct substrate biomaterials from a combinatorial polymer library were chosen based on their ability to inhibit or accelerate nickel sulfate-induced hMSC transformation processes (**Figure 4.4C**). Comparison of the hMSC telomerase expression following an 11 day nickel sulfate treatment demonstrated differential degree of transformation, with the 11 day Transformation Index values ranging from 0 to 0.5. Using high content nuclear feature extraction and SVM-based classification, an early (3 day) Parsing Index value was calculated for cell populations on each individual biomaterial substrate and plotted against the experimentally observed 11 day Transformation Index, resulting in a Pearson correlation coefficient of 0.76 (**Figure 4.4D**). These results demonstrate that the NuMA protein descriptors can rank-order the extent of oncogenic responses of hMSCs cultured on a library of polycarbonate and polymethacrylate-derived biomaterials.

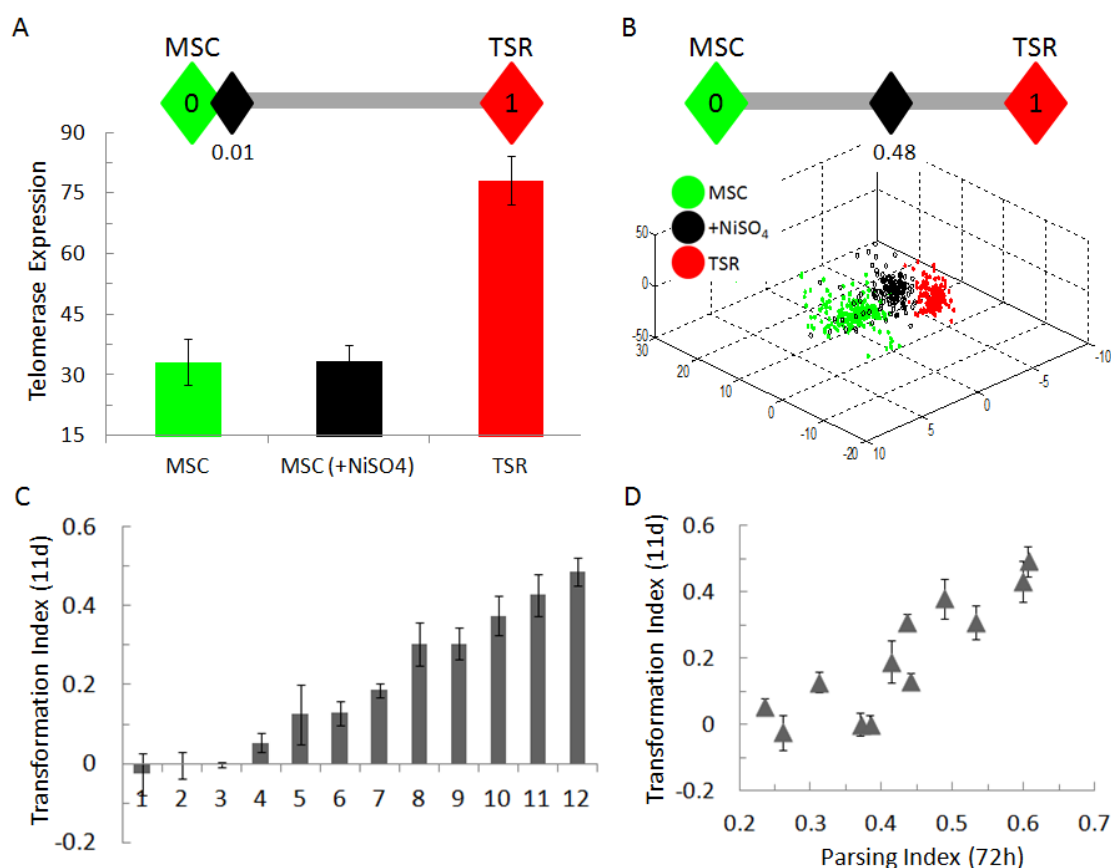


Figure 4.4: NuMA Protein Imaging Used to Profile Synthetic Materials for Long-Term Oncogenic Effects on Stem Cells

(A) Using telomerase expression, it is not possible to identify hMSCs primed to abnormal transformation at 3 days (bar graph), as seen by a Parsing Index value of 0.01 for cells exposed to carcinogenic induction. **(B)** High-content analysis of NuMA reporter is able to classify carcinogen-treated hMSCs with a Parsing Index value of 0.48. Additionally, PCA plot of 3 day NuMA protein descriptors form three distinct clusters, corresponding to hMSCs exposed to BA (green), nickel sulfate treatment (black), or TSRs in growth medium (red). **(C)** 11 day experimental Transformation Index shows that biomaterial properties influence degree of transformation, defined by extent of telomerase activity. **(D)** 11 day Transformation Indices (y-axis) are plotted against 3 day predicted Parsing

Indices (x-axis) for hMSCs cultured in polymers in **(C)**. This plot shows a high degree of correlation between the 11 day Transformation (experimental) and 3 day Parsing (predicted) Indices, as seen by a Pearson correlation coefficient of 0.76.

4.4.2 NuMA-Based Metrics Distinguish OPCs from Different Brain Regions of Neonatal Rats

For our next study we investigated our ability to distinguish cell subtypes obtained *ex vivo* that are indistinguishable using conventional assays but have divergent growth profiles *in vitro*. To do so, we designed an experiment to distinguish antigenically identical progenitor cells from different central nervous system (CNS) locations. Oligodendrocyte type-II astrocyte cells, also called oligodendrocyte precursor cells (OPCs), are progenitor cells in the developing and adult CNS that differentiate into myelin, the major component of white matter [236]. OPCs isolated from different regions of the CNS have intrinsic differences that govern their timing of myelination *in vivo*, which is retained *in vitro* and assessed through laborious experiments pertaining to clonal differentiation and proliferation profiles [226, 237].

To test the ability of high content imaging and analysis of nuclear features to distinguish these behaviorally distinct yet antigenically identical cells (OPCs are characterized by a high expression of A2B5, NG2, and PDGFR α antigens), precursors from the cerebral cortex (CX) and optic nerve (ON) were isolated from neonatal rats and analyzed. ON and CX-derived precursors are indistinguishable through surface marker staining of A2B5 (**Figure 4.5A**), yet could be separated based on the analysis of NuMA

descriptors between the two sources of isolation, as evidenced by a high classification performance ($86.8\% \pm 2.9\%$ sensitivity and $80.7\% \pm 3.7\%$ specificity, **Figure 4.5C**).

Since OPCs derived from ON and CX have myelination profiles at the extremes of the CNS scale, we next applied our methodology to precursors from spatially adjacent CNS regions with more proximate *in vivo* myelination profiles that have not been previously distinguished. OPCs from the corpus collosum (CC) are spatially adjacent to OPCs from the CX in contrast to OPCs derived from the ON. As expected, OPCs from the CC and CX were antigenically identical based on A2B5 expression (**Figure 4.5A**), whereas clonal analysis after 7 days demonstrated that CC precursors were comparatively less proliferative and more prone to differentiate than CX precursors (**Figure 4.5B**). NuMA-based high content imaging of CC and CX precursors was able to resolve two completely separable clusters when visualized in three-dimensional feature space (**Figure 4.5C**). OPCs from CC were distinguishable from CX precursors with very little overlap. SVM-based classification was performed and results indicated almost complete separation between the two clusters, with $94.7\% \pm 2.5\%$ sensitivity and $91.7\% \pm 6.9\%$ specificity. These findings support the ability of our imaging-based method to distinguish antigenically identical yet phenotypically divergent murine OPCs extracted from different brain regions.

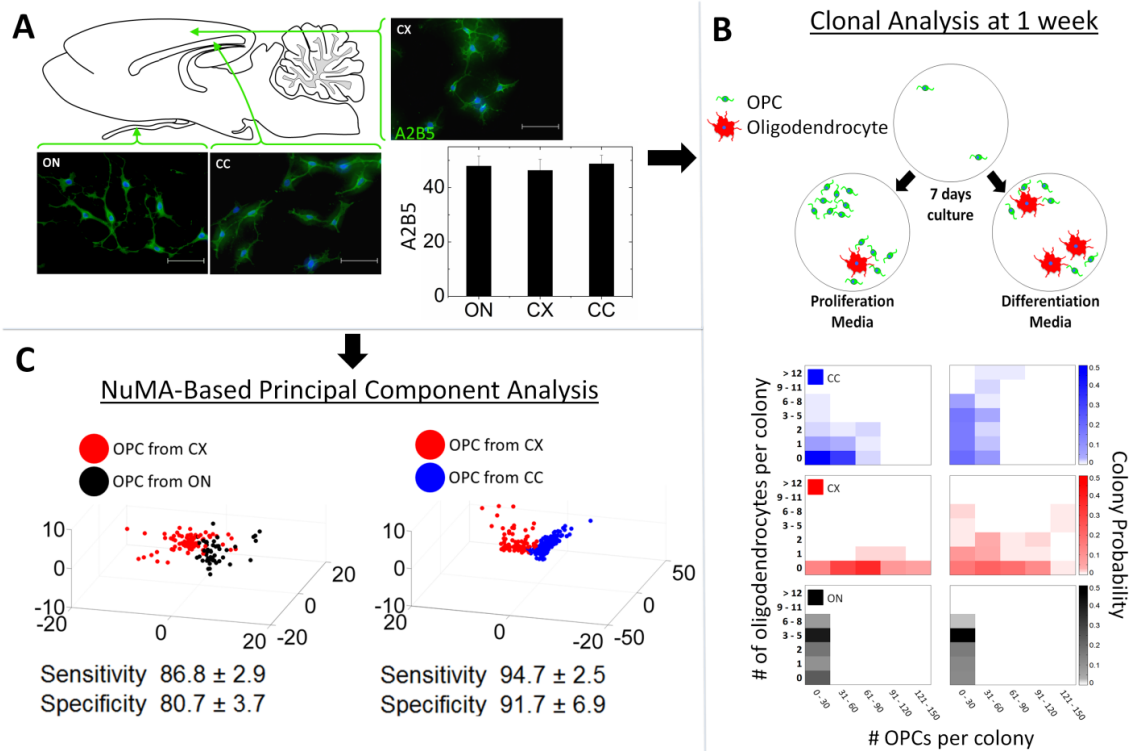


Figure 4.5: NuMA Descriptors Distinguish OPCs from Different Brain Regions

(A) Simplified diagram of sagittal section of neonatal rat brain and images of OPCs stained for A2B5 following isolation from the optic nerve (ON), cerebral cortex (CX), and corpus collosum (CC). Precursors from all three brain regions stain positive for A2B5 with indistinguishable differences in mean fluorescence intensity. **(B)** Clonal analysis of OPCs isolated from ON (black), CX (red), and CC (blue) of neonatal rats. OPCs were plated at clonal density and cultured in either proliferation or differentiation medium for 7 days. Each densitogram plot represents 100 clones, where the x-, y1-, and y2- axes indicate the number of OPCs, oligodendrocytes, and fractional number of clones with a particular composition (indicated via brightness of corresponding color), respectively.

4.4.3 NuMA Descriptors Parse Between Live HEK-293 Cells with and without DNA-Damage Treatment

The first two studies showcased our ability to identify divergent material-induced oncogenic responses, as well as cell phenotypes that are indistinguishable using conventional fluorescence-based assays. Even though these studies highlight the utility of NuMA-based profiling for material screening and cell phenotyping, these findings were only realized on fixed, static cells. This is not adequate for regenerative therapies since cells cannot be used after the immunostaining step required for phenotyping. As such, we designed a third study to test if our profiling platform can be applied to live cells.

Here, we generated two populations of human embryonic kidney (HEK-293) cells: DNA-damaged, via exposure to etoposide for 48 hours, and controls treated with vehicle (**Figure 4.6**). After treatment both cell populations were labeled with mCherry-NuMA. Vehicle-treated HEK-293 cells were also labeled with GFP-actin (**Figure 4.6A**). Using PCA, we were able to identify distinct clusters specific to the treatment conditions. SVM classification supported this observation with a sensitivity and specificity of $89\% \pm 2\%$ and $87\% \pm 2\%$, respectively (**Figure 4.6B**). Next, we co-cultured etoposide and vehicle-treated cells in a 50:50 ratio, and colonies were subject to one of three treatment conditions: (1) ablation of vehicle-treated cells (termed Etopo (-) Kill), (2) ablation of etoposide-treated cells (termed Etopo (+) Kill), or (3) no ablation of HEK-293 co-cultures (termed Control) (**Figure 4.6C**).

To determine the extent to which ablation treatments increased population homogeneity, HEK-293 cell colonies were exposed to Taxol, a pharmacological agent which selectively kills DNA-damaged cells [238]. We found that Taxol treatment for 48 hours does not affect population viability for vehicle-treated cells, but significantly decreases viability for etoposide-treated cells (**Figure 4.6D**). Taxol treatment for 48 hours resulted in 55% viability for Control colonies, and a substantial decrease and increase in viability for Etopo (-) Kill (41% viability) and Etopo (+) Kill (63% viability) treatments, respectively (**Figure 4.6E**). This experiment shows that imaging-based profiling has the potential to identify subpopulations in heterogeneous cell cultures and remove user-defined cell subtypes via confocal laser ablation. By doing so, we show that the colonies are either more (i.e., after Etopo (-) Kill treatment) or less responsive (i.e., after Etopo (+) Kill treatment) to pharmacological treatments.

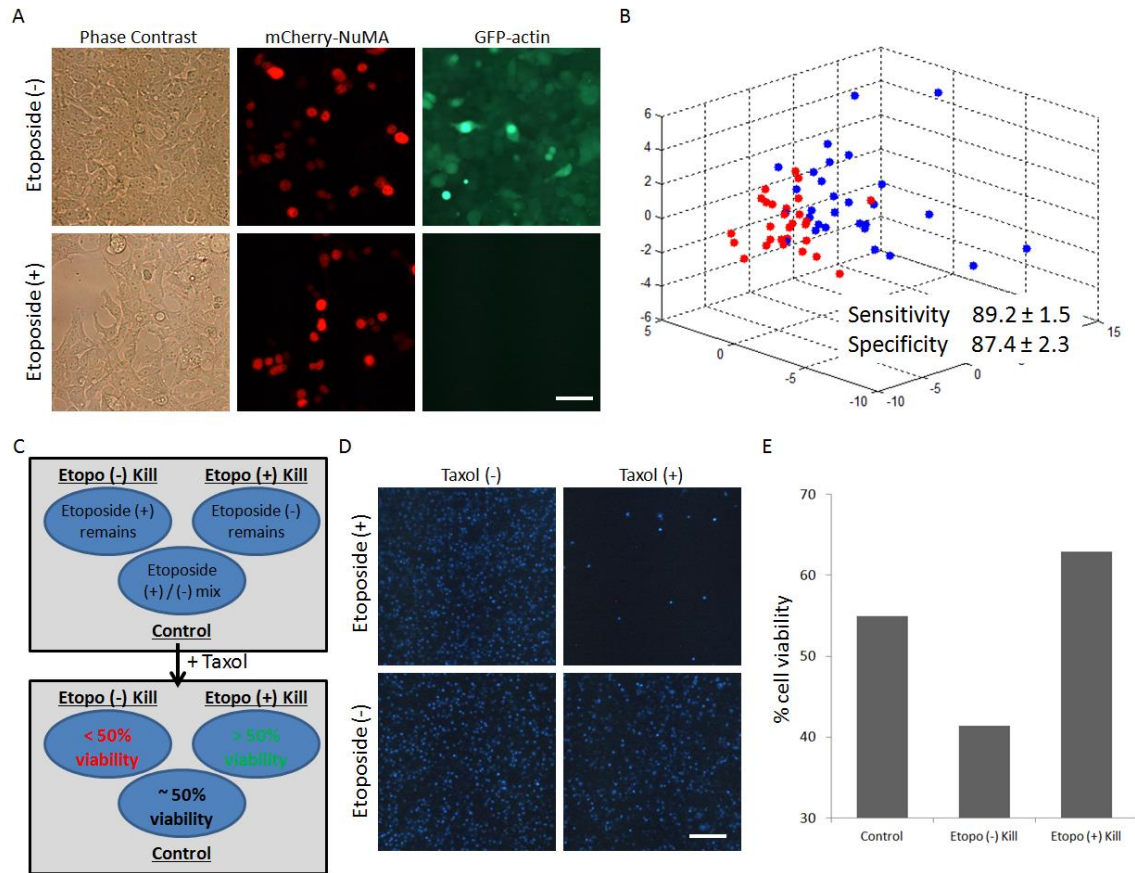


Figure 4.6: NuMA-Based Metrics can Parse Between Live HEK-293 Cells with and without DNA-Damage Treatment

(A) HEK-293s with DNA-damage treatment [etoposide (+)] and vehicle treatment [(etoposide (-))] were labeled with mCherry-NuMA. Etoposide (-) HEK-293s were also labeled with GFP-actin. **(B)** NuMA-based PCA plot shows two distinct clusters demarcating etoposide (-) (red) and etoposide (+) (blue) conditions. **(C)** Schematic showing the experimental design workflow. **(D)** DNA-damage treatment does not affect cell viability (top and bottom left images). 48 hour Taxol treatment selectively kills etoposide (+) cells (top right image) but does not affect viability in etoposide (-) cells (bottom right image). **(E)** Percentage of remaining cells in co-cultures after ablation and 48 hour Taxol treatment. Scale bars: **(A)** 25 μm , **(D)** 100 μm .

4.5 DISCUSSION

Our high content imaging-based nuclear profiling methodology is based on the higher dimensional variations in organizational nuclear protein markers of single cells instead of expression-based phenotypic readouts of whole cell populations. Given the resolution of high dimensional feature information, the resulting nuclear features parse cell behaviors in multiple domains earlier and more reliably than using conventional methods. As one of the four most abundant proteins in the cell nucleus in eukaryotic cells, NuMA is closely associated with cell cycle-related events, such as stem cell differentiation [141, 162, 239], apoptosis [240], and cancerous progression [241]. As such, in this study we utilized nuclear descriptors derived from the NuMA protein, and our findings support the premise that the shape and organization of nuclear proteins have cell- and tissue-specific signatures.

In our first study we investigated the role of biomaterials in influencing cell transformation processes. Some polymeric biomaterials, such as p(92%DTE-co-8%PEG carbonate), synergistically enhanced nickel sulfate treatment whereas other biomaterials, such as p(DTE-co-8%PEG-10%DT carbonate) reduced the effects of nickel sulfate in telomerase activity (**Figure 4.4A, Table 4.2**). The biomaterial-induced biological mechanisms responsible for divergent effects of nickel sulfate treatment are beyond the scope of this study. However, we suspect that the biomaterials are influencing the modulation of exogenous and intracellular production of reactive oxygen species (ROS). Several studies have reported a link between ROS and cancer [242-244]. In an earlier study we showed that PEG-containing substrates induced both exogenous

and intracellular ROS production, whereas negatively charged DT-containing polymers had an opposite effect [245]. The role of DT in reducing the effects of nickel sulfate-induced telomerase activity could be due to the electrostatic attraction of nickel ions to the polymer surface, thereby limiting the binding efficiency of nickel ions to cells in culture. Therefore, the reduced amount of nickel ions on DT-containing polymer substrates could result in a decrease of nickel sulfate-induced DNA-damage, subsequently resulting in a decrease in transformation.

To increase the applicability of our imaging-based method, for our next study we investigated the possibility of identifying cell subtypes acquired from tissues. Oligodendrocyte precursor cells (OPCs) derived from different murine brain regions exhibit different long-term self-renewal and oligodendrocyte differentiation patterns, which mirror myelination dynamics during development *in vivo* [226]. Although OPCs feature divergent behaviors, OPCs isolated from the optic nerve, cerebral cortex, and corpus collosum are antigenically indistinguishable. To our knowledge, prior to this study there was no effective way of identifying the origin of OPCs at early stages without performing long-term differentiation studies.

One fundamental limitation preventing the extensive use of stem cells in the clinic is the inability to differentiate cells into homogeneous populations of desired phenotypes [246, 247]. With the use of differentiation-inducing growth factors, populations of hMSCs only achieve upwards of 75% osteoblast and 40% adipogenic differentiation [47]. Additionally, the clinical use of cells derived from the central nervous system (e.g., neural stem cells) has been limited due to the inability of

separating NSCs from other cell types when derived from native tissues [248]. Thus, we sought to investigate whether we could identify cell subtypes in a heterogeneous group, remove the cells, and determine whether the end result is an increase in population homogeneity. We chose HEK-293 cells as our cell line of choice due to their ability to easily transfect DNA plasmids. To generate two cell subtypes, one subset of HEK-293 cells was subject to DNA-damage via etoposide, and the other was treated with a vehicle control. Although we identified morphological differences in the descriptors between both cell subtypes with high accuracy, we did not use a real-time classifier to remove unwanted cells in the treatments. A follow-up study should focus on utilizing training set descriptors to implement imaging-based classification in real-time.

To identify shape and organizational differences, we first quantified nuclear shape and NuMA morphology descriptors (**Table 4.1**). Then, we used high-dimensional reduction methods (i.e., Principal Component Analysis, PCA) to reduce large descriptor sets into smaller subsets of three principal components. In PCA, each principal component (PC1, PC2, PC3) represents a linear combination of nuclear descriptors. As such, it is possible to determine individual descriptors that have the largest contributions in each PC. The criterion to determine the most influential descriptors was based on the weighting factors of each descriptor in the linear transformation in PCA analysis. For each PC, the descriptors were identified as influential if the weighting factor was more than half of the highest weighting factor in that transformation equation. As a result, by reviewing the weighting factors of each linear combination, a subset of nuclear descriptors were identified as influential descriptors.

Following this protocol, a PCA-based dimension reduction was applied to NuMA-based nuclear descriptors of hMSCs and the transformed phenotypes (**Table 4.3**). The first PC (PC1) accounted for about 40% of the variability of the original nuclear descriptor dataset, and was composed of nuclear shape-based descriptors. The second and (PC2) and third (PC3) PCs accounted for about 14% and 11% of the variability in the original data, respectively, and had descriptors from all three categories (nuclear shape-, NuMA expression-, and NuMA spatial distribution-based descriptors). Next, PCA-based dimension reduction was performed on nuclear descriptors of OPCs derived from CC, CX, and ON (**Table 4.4**). PC1 accounted for about 50% of the variability of the original nuclear descriptor dataset, and was predominantly composed of nuclear shape descriptors. PC2 and PC3 accounted for about 15% and 7% of the variability in the original dataset and had descriptors that represented all three categories and nuclear shape descriptors exclusively, respectively. PC1 for parsing HEK-293 cells either treated or not-treated with etoposide accounted for about 54% of the variability, followed by PC2 and PC3 which accounted for about 18% and 4% of the variability of the original dataset, respectively (**Table 4.5**). The most influential descriptors in the first two PCs were entirely comprised of nuclear shape-based descriptors, and the third PC was a mix of intensity- and texture-based NuMA descriptors.

These findings show that for all of the case studies, nuclear shape descriptors were the most distinct, followed by NuMA intensity and nuclear distribution. For the oncogenic transformation study, divergent nuclear shape descriptors match qualitative differences observed in the nuclei of naïve hMSCs versus TSRs. In contrast, the

morphological differences between OPCs derived from different brain regions and HEK-293 cell subtypes were much more subtle. An interesting follow-up study would be to determine whether or not we can parse cells in these studies using NuMA intensity- and texture-based descriptors alone. By using less descriptors, we could identify morphological descriptor sets that identify cell subtypes more rapidly and robustly.

PC1 (eigenvalue = 19.55)		PC2 (eigenvalue = 6.62)		PC3 (eigenvalue = 5.05)	
Top Descriptors	Weight	Top Descriptors	Weight	Top Descriptors	Weight
Feret (mean)	0.222	Density (st dev)	0.300	Perimeter	0.245
Perimeter	0.222	Density (max)	0.296	Density (mean)	0.235
Diameter (mean)	0.220	Heterogeneity	0.289	Density (min)	0.213
Area (polygon)	0.218	IOD	0.265	IOD	0.212
Area	0.217	Density (sum)	0.262	Hole Ratio	0.209
Diameter (max)	0.215	Perimeter	0.245	Radius (min)	0.192
Feret (max)	0.215	Perimeter (ratio)	0.203	Area / Box	0.187
Size (length)	0.213	Aspect	0.152	Box X/Y	0.148
Radius (max)	0.212	Density (mean)	0.151	Segmentation Range	0.136
Perimeter3	0.211			Diameter (min)	0.135
Perimeter2	0.209			Heterogeneity	0.112
Feret (min)	0.191			Density (st dev)	0.112
Size (width)	0.190			Density (min)	0.110
Box Height	0.188				
Diameter (min)	0.181				
Box Width	0.175				
Radius (min)	0.167				
IOD	0.150				
Density (sum)	0.149				

Table 4.3: Most Influential Descriptors in Parsing TSRs from hMSCs

Descriptor categories were color-coded as blue, green, and red representing nuclear shape-, NuMA expression-, and NuMA spatial distribution-based descriptors, respectively.

PC1 (eigenvalue = 24.91)		PC2 (eigenvalue = 7.85)		PC3 (eigenvalue = 3.53)	
Top Descriptors	Weight	Top Descriptors	Weight	Top Descriptors	Weight
Feret (mean)	0.202	Density (mean)	0.322	Roundness	0.303
Perimeter	0.202	Density (max)	0.314	Radius Ratio	0.255
Perimeter (ellipse)	0.201	Heterogeneity	0.314	Fractal Dimension	0.253
Perimeter	0.199	Density (stdev)	0.312	Aspect	0.181
Perimeter2	0.199	Density (sum)	0.259		
Perimeter3	0.199	IOD	0.259		
Area	0.198	Density (min)	0.255		
Area (polygon)	0.197	Clumpiness	0.193		
Diameter (max)	0.197	Radius (min)	0.182		
Feret (max)	0.197	Margination	0.176		
Size (length)	0.196	Diameter (min)	0.151		
Radius (max)	0.196	Area/Box	0.143		
Diameter (mean)	0.196				
Axis (major)	0.194				
Box Width	0.194				
Box Height	0.194				
Feret (min)	0.191				
Size (width)	0.190				

Table 4.4: Most Influential Descriptors in Parsing OPCs from Different Sources

Descriptor categories were color-coded as blue, green, and red representing nuclear shape-, NuMA expression-, and NuMA spatial distribution-based descriptors, respectively.

The proposed method showcases a highly adaptable and versatile technique to assess cell phenotypes. While the current study focused on hMSCs, rat brain OPCs, and identification of cell subtypes in live HEK-293 cultures using NuMA-based descriptors, the application of the technique with additional cell types and fluorescent reporters merely requires effective staining of other nuclear proteins, fluorescent imaging equipment, and imaging-based feature extraction / data mining software. For example, the technique presented here can easily be adapted to probe several proteins to assess diverse behaviors, possibly in parallel. A limitation of the first two studies presented in

this report is the dependency of fixed cell cultures for NuMA staining. Thus, for our third study we implemented the analysis of live cells expressing fluorescently-tagged NuMA in order to extend our approach to identify and remove cells in heterogeneous cultures. Taken together, single cell phenotyping has been applied to three diverse, clinically-relevant contexts and has the potential for the study of many other cell types, processes, and protein organization.

PC1 (eigenvalue = 21.46)		PC2 (eigenvalue = 7.13)		PC3 (eigenvalue = 4.33)	
Top Descriptors	Weight	Top Descriptors	Weight	Top Descriptors	Weight
Perimeter	0.214	Radius Ratio	0.346	Density (stdev)	0.420
Perimeter Length	0.214	Roundness	0.342	Density (max)	0.402
Perimeter2	0.214	Aspect	0.336	Density (mean)	0.382
Perimeter3	0.214	Area/Box	0.289	Heterogeneity	0.322
Perimeter (convex)	0.214	Radius (min)	0.264	Clumpiness	0.313
Feret (mean)	0.214	Diameter (min)	0.239	Density (sum)	0.254
Perimeter (ellipse)	0.214	Axis (minor)	0.212	IOD	0.254
Per Area (Obj./Total)	0.211	Box X/Y	0.212	Density (min)	0.193
Area	0.211	Feret (min)	0.202		
Area (polygon)	0.211	Size (width)	0.200		
Diameter (mean)	0.209	Perimeter (ratio)	0.189		
Feret (max)	0.197				
Diameter (max)	0.197				
Radius (max)	0.195				
Size (length)	0.194				
Axis (major)	0.193				

Table 4.5: Most Influential Descriptors in Parsing HEK-293 Cells with and without DNA-Damage Treatment

Descriptor categories were color-coded as blue, green, and red representing nuclear shape-, NuMA expression-, and NuMA spatial distribution-based descriptors, respectively.

CHAPTER 5. INTERCHROMATIN DOMAINS USED TO PREDICT STEM CELL DIFFERENTIATION

Note: Sections of this chapter are under review as the following publication:

SL Vega, A Dhaliwal, V Arvind, PJ Patel, NRM Beijer, J de Boer, NS Murthy, J Kohn, PV Moghe. Organizational Metrics of Interchromatin Speckle Factor Domains: Integrative Classifier for Stem Cell Adhesion & Lineage Signaling. *Submitted to Integrative Biology*, 2014.

5.1 ABSTRACT

Stem cell fates on biomaterials are influenced by the complex confluence of microenvironmental cues emanating from soluble growth factors, cell-to-cell contacts, and biomaterial properties. Cell-microenvironment interactions influence the cell fate by initiating a series of outside-in signaling events that traverse from the focal adhesions to the nucleus via the cytoskeleton and modulate the subnuclear protein organization and gene expression. Here, we report a novel imaging-based framework that highlights the spatial organization of subnuclear proteins, specifically the splicing factor SC-35 in the nucleoplasm, as an *integrative marker* to distinguish between minute differences of stem cell lineage pathways in response to stimulatory soluble factors, surface topologies, and microscale topographies. This framework involves the high-resolution image acquisition of SC-35 domains and imaging-based feature extraction to obtain quantitative nuclear metrics in tandem with machine learning approaches to generate a predictive classification model. The acquired SC-35 metrics led to a > 90% correct classification of emergent human mesenchymal stem cell (hMSC) phenotypes in populations of hMSCs exposed for merely 3 days to basal, adipogenic, or osteogenic soluble cues, as well as varying levels of dexamethasone-induced alkaline phosphatase (ALP) expression. Early osteogenic cellular responses across a series of surface patterns, fibrous scaffolds, and micropillar topographies were also detected and classified using this imaging-based methodology. Complex cell states resulting from inhibition of RhoGTPase, β -catenin, and FAK could be classified with > 90% sensitivity on the basis of differences in the SC-35 organizational metrics. This indicates that SC-35 organization is

sensitively impacted by adhesion-related signaling molecules that regulate osteogenic differentiation. Our results show that diverse microenvironmental cues affect different attributes of the SC-35 organizational metrics and lead to distinct emergent organizational patterns. Taken together, these studies demonstrate that the early organization of SC-35 domains could serve as a "fingerprint" of the intracellular mechanotransductive signaling that governs growth factor- and topography-responsive stem cell states.

5.2 INTRODUCTION

Human mesenchymal stem cells (hMSCs) are a multipotent autologous cell source with significant utility in regenerative therapies due to their *in vitro* expansion and ability to differentiate into numerous connective tissues [47, 249]. Traditional strategies to direct hMSC differentiation towards one of the three mesodermal lineages (osteocytes, chondrocytes, and adipocytes) rely on the continuous induction by specific combinations of soluble growth factors [47]. More recently, stem cell differentiation has been achieved by manipulating biomaterial properties, including substrate chemistry [250], topography [251, 252], and stiffness [78, 79]. Optimizing these microenvironmental cues is of particular interest in regenerative medicine where biomaterial substrates may serve as a vehicle for directed cell delivery or as a system for tissue formation *in vivo*. To aid in identifying optimal microenvironments that efficiently elicit strategic stem cell phenotypes, high-throughput screening approaches that allow for the assessment of up to several thousand conditions within one experiment have been developed [91, 253, 254]. However, these approaches rely on population-based phenotypic readouts. This is particularly problematic since: (1) these assays fail to capture the heterogeneity inherent to stem cell-derived cell populations, and (2) the markers being measured are not robustly expressed in stem cells unless they are fully differentiated, a process which can take several weeks to manifest. Thus, a major need exists for the development of profiling tools to screen early phenotypic responses and predict longer-term cell behaviors.

Adherent stem cells interact with their extracellular matrix through cell surface receptors, which propagate a cascade of signaling events to the cytoskeleton via focal adhesions, and ultimately to the nucleus. Previous studies have shown that the shape of the cell is a precursor to stem cell differentiation [133, 251, 255]. We propose the premise that the organization of subcellular proteins involved in outside-in signaling, particularly those mediating mechanotransductive signaling, are regulated by microenvironmental cues during differentiation, and that these minute differences can be captured by enhanced content imaging. As a major evidence of this premise, our laboratory advanced an imaging-based profiling methodology that allows for the dissection of morphologic signatures in the cytoskeleton unique to a particular culture condition [56, 57, 128, 256]. Using this approach, early (24 hour) actin morphologic signatures of hMSCs were identified and used to predict downstream osteogenic differentiation [57]. More recently, this technique was applied to distinguish between image-based features of nuclear mitotic apparatus (NuMA) protein organization of pluripotent versus spontaneously differentiating embryonic and induced pluripotent stem cells [128]. Although these studies have shown that stem cells adopt a higher-order organization of cytoskeletal and nuclear proteins (NuMA) that can be defined by shape, intensity, and texture descriptors, developing methods to discern stem cell states on more physiologic and complex biomaterial substrates and scaffolds remains a major challenge. In this study, we have proposed a new molecular reporter-based approach to profile cell states using more sensitive subnuclear signatures defined by a smaller set of descriptors.

Pajerowski et al. demonstrated that differentiating cells undergo progressive changes in gene expression, structural reorganization, and nuclear shape [139]. One of the goals of this study was to identify highly sensitive nuclear proteins as reporters to offer calibrated organizational features via high content imaging. To accomplish this, a number of candidate proteins within the nucleoskeletal scaffolding complexes were considered, namely RUNX2, lamin, trimethylated H3K4 histone (H3K4me3), EZH2, and SC-35. These subnuclear proteins have been implicated in microenvironment modulated cell processes such as mechanotransduction, gene regulation, and stem cell differentiation (**Figure 5.1**). EZH2 is a histone lysine methyltransferase that controls hMSC osteogenic differentiation via the trimethylation of H3K27 [257]. Lamins are essential filaments of the nuclear envelope, and their presence have been associated with preferential osteogenic differentiation in hMSCs [258, 259], while RUNX2 is a transcription factor that directly promotes osteogenic differentiation [260]. Upon methylation, H3K4me3 histone induces a transcriptionally active state for many genes involved in stem cell proliferation and differentiation [261]. SC-35 nuclear speckle domains host small ribonucleoprotein particles (snRNPs), spliceosomes, and transcription factors that function in co-transcriptional modifications of RNA [191].

In this study, we employed high content image acquisition of various nuclear proteins in tandem with machine learning modeling to evaluate single cell responses of hMSCs to microenvironmental cues. hMSCs were cultured in different engineered microenvironments comprised of different topographies (i.e., patterns, fibers, micropillars) and soluble growth factors (**Figure 5.1**). In the course of our screening of

the panel of markers, we report that SC-35 is a highly responsive organizational reporter. We then focused subsequent experiments on investigating and validating the utility of SC-35 domain organization to predict osteogenic stem cell differentiation in hMSCs cultured across a series of more complex substrates, including surface patterns, fibrous scaffolds, and micropillar topographies.

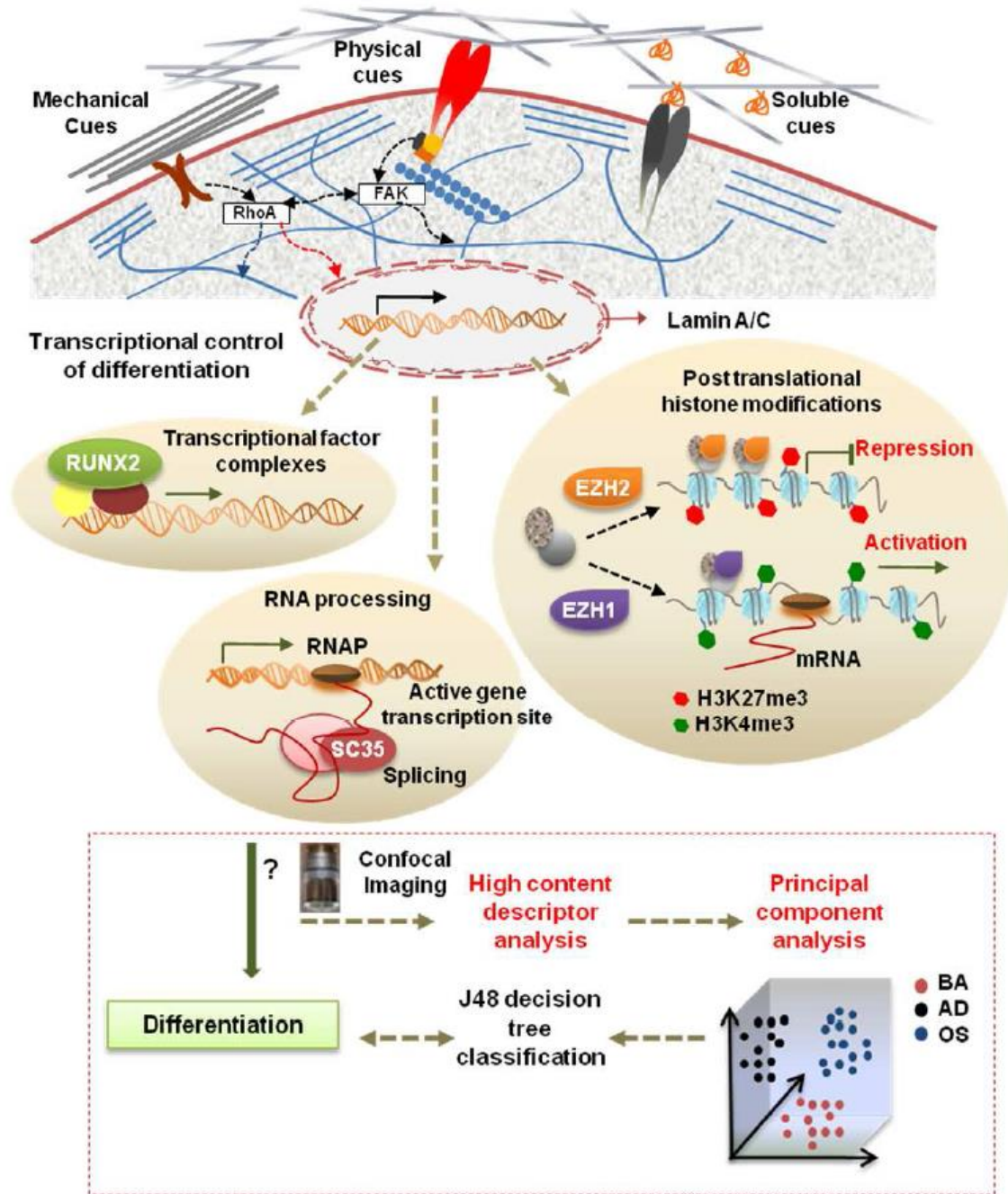


Figure 5.1: Workflow Highlighting Utility of Nuclear Imaging-Based Profiling

Cellular interactions with their microenvironment (e.g., mechanical cues, physical cues, soluble cues) modulate nuclear protein organization through signaling cascades as well as cytoskeletal-nuclear links, which regulate nuclear programs such as activation of

transcriptional factors (e.g., RUNX2), posttranslational histone modifications (e.g., EZH2 and trimethylated H3K4 / H3K27), and RNA processing (e.g., SC-35 dynamics) that direct gene expression and cell fate. In this study, hMSCs were cultured on different substrates in the presence of adipogenic (AD), osteogenic (OS), or basal medium (BA) for 3 days, and high-resolution images were acquired using confocal microscopy. High content analysis was then done to compute Haralick texture descriptors that define the spatial organization of several nuclear reporters. This set of descriptors was then dimensionally reduced using Principal Component Analysis (PCA). Subsequently, the principal components were taken as an input for a classifier that used machine learning approaches based on a J48 decision tree algorithm to classify cells exposed to different conditions. The predictive classification model was validated by correlations with 14 day endpoint assays. Using this framework, we can go through several iterations to analyze changes in nuclear reporter organization and thus screen and identify microenvironmental cues that elicit desired phenotypic responses.

5.3 MATERIALS AND METHODS

5.3.1 Cell Culture

Human mesenchymal stem cells (hMSCs) were obtained from Texas A&M University (College Station, TX). Cells were cultured in a humidity-controlled environment under 5% CO₂ and 37°C and fed every 3 to 4 days with basal growth medium (BA) supplemented with fetal bovine serum (FBS) (10% v/v) and penicillin-streptomycin (0.1% v/v). Cells were received at passage 1 and used for up to 5 passages. hMSCs were expanded in BA medium, and upon reaching 60% confluence trypsinized and plated according to experiment-dependent conditions.

Osteogenic differentiation (OS) was induced by culturing hMSCs in BA medium supplemented with L-ascorbic acid-2-phosphate, dexamethasone (*dex*), and β -glycerophosphate [47]. Adipogenic differentiation (AD) was induced with BA medium supplemented with *dex*, indomethacin, and 3-isobutyl-1-methyl-xanthine for induction, and adipogenic maintenance medium was composed of BA supplemented with insulin [47]. Adipogenic medium in AD conditions was cycled with 3 days induction followed by 1 day maintenance. hMSCs were plated at optimal differentiation-inducing densities of 10,000 cells/cm², 21,000 cells/cm², and 5,000 cells/cm² for BA, AD, and OS conditions, respectively. Unless otherwise stated, cells were allowed to adhere for 6 hours in basal growth medium, followed by a media change with appropriate induction medium.

5.3.2 Fabrication of Surface Textures

Surface patterns were fabricated using phase separation of two immiscible polymers via demixing using principles previously reported [262]. Varying ratios of poly(desaminotyrosyl-tyrosine ethyl ester carbonate) (PDTEC) and polystyrene (PS) were dissolved in tetrahydrofuran (THF) to create a 2% (w/v) polymer solution. Polymer solutions were spin-coated onto 12 mm glass coverslips at 4,000 RPM for 30 seconds, resulting in a thin film of phase-separated PDTEC and PS. Six different surface pattern topographies were created by varying the PDTEC:PS ratio (100:0, 80:20, 60:40, 40:60, 20:80, 0:100). Cyclohexane was used to remove PS, resulting in PDTEC polymeric surface patterns varying in degree of PDTEC polymer continuity. Coverslips were vacuum dried overnight to remove residual cyclohexane. Lastly, prior to culturing hMSCs, films were stored in a dessicator, sterilized with UV light for 900 seconds, and washed three times with phosphate buffered saline (PBS) (Lonza).

5.3.3 Fabrication and Characterization of Microfibrous Scaffolds

Fibrous scaffolds were fabricated using an electrospinning apparatus. Low viscosity solutions of PDTEC were prepared in a volatile solvent as tabulated in **Table 5.1** below. The needle of the syringe containing the solvent was maintained at a positive charge (+keV) and placed 6 cm from the collecting rotating mandrel that was maintained at a negative charge (-keV). The flow rate of the polymer solution was controlled by a syringe pump. The micrometer-sized fibers were deposited on the mandrel as the solvent evaporated from the solution streaming out of the syringe. The

alignment of these fibers was controlled by the speed of the mandrel; higher speeds resulting in higher orientation. The diameter of the fibers was controlled by the viscosity of the polymer solution by changing the polymer concentration (from 14% to 18% w/v). Higher viscosity resulted in larger diameter fibers in the scaffold [51]. Polymer solution compositions and the electrospinning conditions are summarized in **Table 5.1**.

Size	Polymer	Solvent	wt/v%	Flow Rate	+keV	-keV
S	DTE	HFIP	14	3 mL/hr	18	-6
L	DTE	MeCl ₂	18	3 mL/hr	24	-6

Table 5.1: Summary of Electrospinning Parameters for Fibrous Scaffolds

5.3.4 Fabrication of Micropillars

Topographies were designed and fabricated using previously published methods [91]. Briefly, micropillar patterns were generated by utilizing an algorithm that randomly selected parameters for: (1) size of pattern, (2) number and distribution of primitive shapes (i.e., triangles, circles, and rectangles), and (3) size and degree of alignment of primitives. The micropillar designs were then etched to a silicon wafer which was used to generate a silicon master. Hot embossing of polystyrene films (250 μm thick) was then performed by sandwiching between the silicon master and an Obducat UV Sheet Polyester (100 Micron 10638). Imprinting was carried out at 80°C at a pressure of 30 bars for 10 minutes. After cooling, assembly was demoulded and micropillars were detached using a wafer saw.

5.3.5 Fluorescence- and Immuno-staining for Confocal Imaging

hMSCs were fixed with 4% paraformaldehyde (Electron Microscopy Sciences) for 15 minutes. Next, samples were blocked and permeabilized using a 0.1% Triton X-100 (Sigma) / 5% normal goat serum (MP Biomedicals) solution in PBS. After two washes with blocking buffer (5% NGS in PBS), primary antibodies specific to proteins of interest were added at different concentrations overnight at 4°C. After three 15 minute washes in blocking buffer, secondary antibodies (Alexa Fluor; Invitrogen) with different fluorophores and corresponding isotype controls in blocking buffer at a 1:250 ratio were added for 2 hours at room temperature. To label the actin cytoskeleton, cells were fixed and stained with Alexa Fluor 488 phalloidin (Invitrogen) per the manufacturer's instructions. All samples were counterstained with 5 µg/ml Hoechst (Sigma) in PBS and stored at 4°C until imaging. To acquire high-resolution images, samples were imaged under a 63X objective with a Leica TCS SP2 system (Leica Microsystems).

5.3.6 Analysis of Nuclear Protein Organization

To analyze the organization of nuclear proteins, 26 texture-based Haralick features were acquired for each cell. First, images underwent intensity-based thresholding to create nuclear ROI masks for each nucleus in a given image, based on Hoechst DNA staining. Next, Haralick descriptors were obtained using a Matlab algorithm. A complete list of the calculated Haralick descriptors with their definitions is provided in **Table 5.2**. These descriptors are quantifiable measurements of texture features that represent the spatial organization of the nuclear proteins. The 26

descriptors were linearly reduced to a minimum number of eigenvectors that account for 95% variance of the data by performing principal component analysis (PCA) using Weka (Waikato Environment for Knowledge Analysis), an open-source machine learning software. PCA transformed data was exported and plotted in Matlab (MathWorks, Natick, MA) to obtain a PCA plot where each point represents a stem cell in three-dimensional space, and where each axis represents a computed principal component. Therefore, each point is represented by a unique set (x, y, z) of principal components (eigenvectors).

To illustrate differences between the various subpopulations, a predictive classification model was made using J48 decision tree analysis in the Weka software. J48 generated a C4.5 pruned decision tree, where tree pruning is used as a tool to correct for potential over fitting. The best performing classification tree was generated by using the experimental data as the training set. The quality of the tree is reported in terms of the percent of correctly classified instances, precision (positive predictive value), and recall (sensitivity).

Briefly, $\text{precision} = \text{TP} / (\text{TP} + \text{FP})$ and $\text{recall} = \text{TP} / (\text{TP} + \text{FN})$, where: true positives (TP) are the number of instances correctly classified as belonging to the positive class, false positives (FP) are the number of instances incorrectly classified to the positive class, and false negatives (FN) are the number of instances not classified to the class but belong to the class. Precision is also defined as the number of instances that truly have class X among all those which are classified as class X.

<i>Measure</i>	<i>Biological Relevance</i>
Entropy	Randomness of the intensity distribution; low values correspond to small differences in neighboring pixel intensity (e.g., even intensity of SC-35 domains across nuclear ROI).
Energy	A measure of image uniformity (opposite of entropy); low value when the window is not orderly (e.g., uneven distribution of SC-35 domains across nuclear ROI).
Sum Entropy	Measure of homogeneity of histogram of gray level similarities; low for uniform histograms.
Difference Entropy	Measure of homogeneity of histogram of gray level differences; high for uniform histograms.
Correlation	Image linearity; high value of Correlation if an image contains a considerable amount of linear structure (e.g., elongated SC-35 domains). Low value if intensity within ROI is perfectly uniform.
Information Measure 1	Information measure of the correlation (i.e., numerical uncertainty in correlation measure).
Information Measure 2	Information measure of the correlation (i.e., numerical uncertainty in correlation measure).
Sum Average AKA Granularity	Measure of grain size; high values indicate coarse texture having a grain size equal to or larger than the magnitude of the displacement vector (e.g., large versus small SC-35 domains).
Sum Variance	Standard deviation of Sum Average (e.g., uniform versus broad distribution in size of SC-35).
Difference Average	Measure of grain size; small values indicate coarse texture having a grain size equal to or larger than the magnitude of the displacement vector.
Difference Variance	The dispersion around the mean of combinations of reference and neighbor pixels in the summation histogram of the GLCM.
Inertia	Absolute value of the weighted averages away from the diagonal; Inertia exponentially increases in value according to homogeneity in protein intensity within ROI.
Inverse Difference Moment	Inverse of inertia. Inverse Difference Moment exponentially decreases in value according to homogeneity in protein intensity within ROI.

Table 5.2: List of the 13 Haralick Texture Features Used in Chapter 5

Descriptors were calculated using two different pixel groupings (termed C1, C2) resulting in 26 Haralick texture features in total. The features are divided into four groupings: entropy (red), correlation (blue), granularity (purple), and inertia (green), which represent a measure of speckle homogeneity, elongation, size, and distribution with respect to nuclear centroid, respectively. The potential biological relevance for each feature is also listed.

5.3.7 Assessment of Cell Differentiation

To quantify differentiation, hMSCs cultured in induction medium were either fixed or lysed at 14 days. Fixed cells were stained for alkaline phosphatase (ALP) (fast blue RR, Sigma) or intracellular triglycerides (AdipoRed, Lonza) per the manufacturer's

instructions. Samples were then counterstained with Hoescht to identify osteogenic- and adipogenic-positive cells. Lysed samples were either used to determine ALP concentrations using an ALP activity assay per manufacturer's instructions (QuantiChrom™), or the relative gene expression of ALP (Qiagen, ALP) or lipoprotein lipase (Qiagen, LPL), as previously reported [263].

5.3.8 Inhibition of RhoGTPase, FAK, and β -Catenin

Rho was specifically inhibited using cell permeable C3 transferase (Cytoskeleton, Denver, CO) and FAK was inhibited using FAK inhibitor 14 (SantaCruz Biotechnology, Dallas, TX). β -catenin was inhibited using cell permeable FH535 (SantaCruz Biotechnology, Dallas, TX) [264, 265]. hMSCs were cultured in an 8-well LabTek chamber slide at a cell density of 8,000 cells per well and allowed to attach overnight (~12 hours) in basal medium, before media in the wells was replaced with serum-free medium containing 0.5 μ g/ml C3 transferase for 4 hours, or 1 μ M FAK inhibitor 14 for 1 hour, or 15 μ M FH353 for 1 hour. After pre-treatment, media was changed with induction medium containing the inhibitor. Adipogenic medium in AD conditions was cycled with 3 day induction followed by 1 day maintenance. Basal and osteogenic media were cycled every 3 days. Cell proliferation was analyzed 3 days post induction (time of descriptor analysis) using Alamar Blue assay (Life Technologies) using manufacturer's instructions.

5.3.9 Statistics

Statistical analysis of morphometric parameters included analysis of variance (ANOVA) with Tukey's honestly significant difference (HSD) post hoc method and other multivariate statistical tools. The differences were considered significant for $p < 0.05$ unless otherwise noted. Error bars indicate the standard uncertainty around the mean.

5.4 RESULTS

5.4.1 Nuclear Proteins as a High Content Screen to Parse Stem Cell Differentiation

To screen for nuclear proteins whose early (3 day) organization is influenced by cell differentiation, hMSCs were cultured for 3 days and 14 days in either basal growth medium (BA), adipogenic (AD), or osteogenic (OS) differentiation medium prior to immunostaining for several nuclear reporters, namely RUNX2, lamin, H3K4me3, EZH2, and SC-35 domains (**Figure 5.2A**). The organization of the prescribed nuclear proteins was analyzed by performing a high content analysis on high-resolution images obtained at 3 days wherein 26 Haralick texture descriptors were computed to define the organization. Independently, we confirmed that hMSCs cultured in AD medium differentiated to adipocytes and stained positive for AdipoRed at 14 days, whereas AdipoRed was undetected in cells cultured in BA and OS culture conditions (**Figure 5.2B** and **Figure 5.3**). Additionally, hMSCs cultured in OS medium exhibited osteogenic differentiation and had significantly more ($p < 0.01$) fast blue staining as compared to cells cultured in BA and AD conditions for 14 days (**Figure 5.2B**).

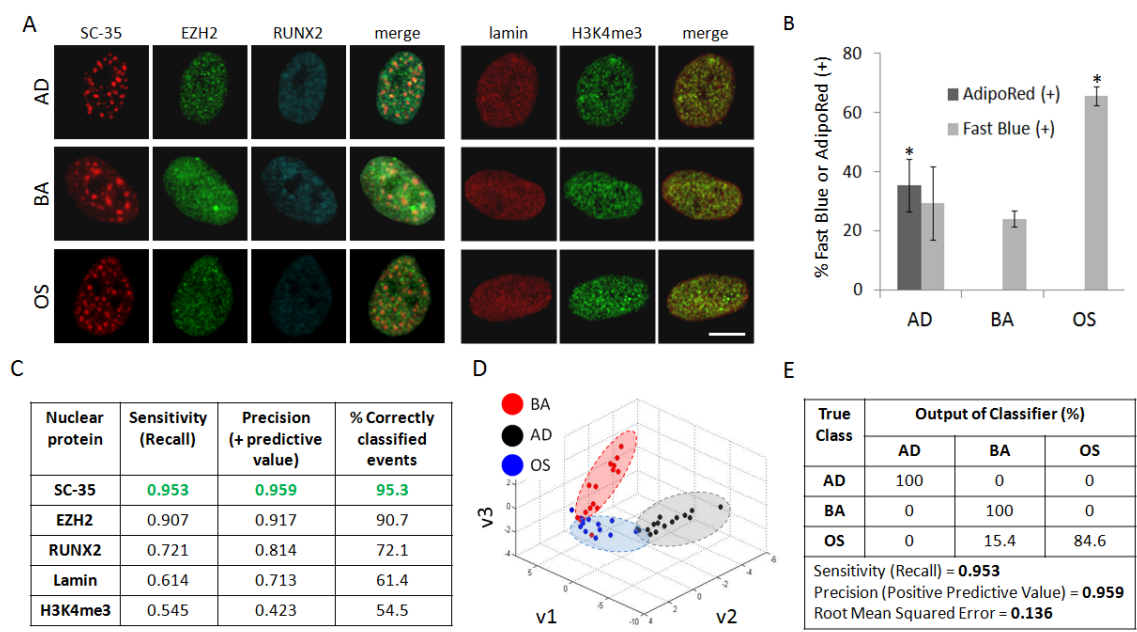


Figure 5.2: SC-35 Organization as a Screen to Parse Stem Cell Differentiation

hMSCs were cultured in AD, OS, or BA medium and **(A)** fixed and immunolabeled for a panel of either gene-modifying (H3K4me3, EZH2, RUNX2) or mechanoresponsive (lamin, SC-35) proteins 3 days post-plating. **(B)** hMSCs cultured in AD, OS, or BA medium for 14 days were stained for intracellular triglycerides (AdipoRed) and alkaline phosphatase (ALP) to identify % of adipocytes and osteoblasts, respectively. **(C)** 3 day analysis of nuclear proteins yields differences in sensitivity, precision, and % of correctly classified events. **(D)** PCA plot of SC-35 reporter shows that the three conditions cluster into three distinct groupings (blue = OS, black = AD, red = BA). **(E)** Decision tree analysis of PCA-derived principal components show that hMSCs parse well (> 95%). Scale bar: 5μm. * indicates statistical significance ($p < 0.01$).

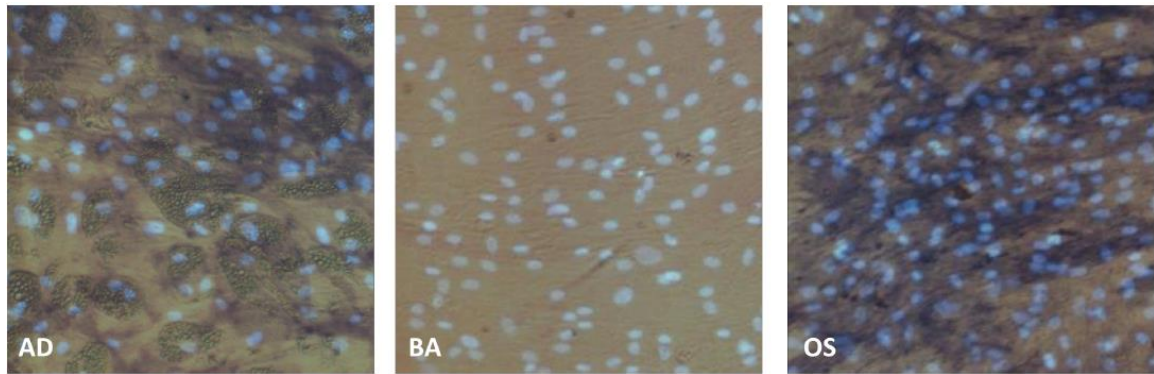


Figure 5.3: Osteogenic and Adipogenic Differentiation of hMSCs

hMSCs were cultured in AD, BA, or OS medium for 14 days. Osteogenic differentiation was analyzed using Fast Blue staining assay (blue) and adipogenic differentiation was analyzed using the AdipoRed assay (green). Images were taken using a fluorescent microscope at 10X magnification, and analysis was performed by counting number of nuclei expressing differentiation signal and dividing by total cell nuclei count.

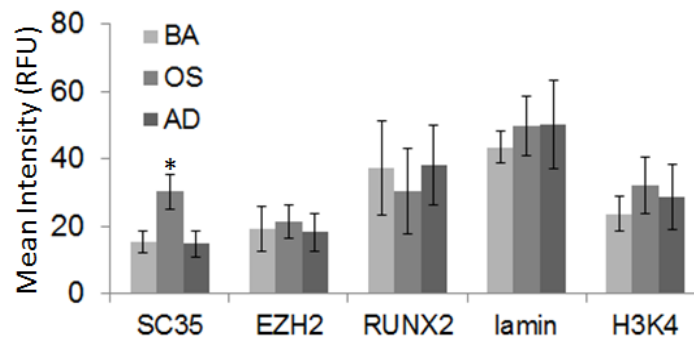


Figure 5.4: Fluorescence Intensity of hMSCs in BA, AD, or OS for 3 Days

* represents statistical significance ($p < 0.01$).

Based on our 3 day analysis of average fluorescence of nuclear proteins between cells exposed to BA, AD, and OS induction conditions, no significant differences were observed in intensity with the exception of SC-35 domains (**Figure 5.4**). The SC-35 fluorescence intensity of hMSCs cultured in the OS condition was significantly higher ($p < 0.01$) than in hMSCs cultured in AD and BA conditions (**Figure 5.4**). Furthermore, significant upregulation ($p < 0.05$) of SC-35 gene expression in osteogenic-inductive conditions was detected and a significant decrease ($p < 0.05$) in SC-35 expression during adipogenic induction for 24 hours by performing microarray analysis (**Figure 5.5**).

To identify differences in nuclear protein organization in response to growth factor induced differentiation, 26 numerical texture-based descriptor sets were computed after high content analysis for each nuclear protein within each condition. Principal component analysis (PCA) was then performed to dimensionally reduce the descriptors to vectors that account for > 95% variance in data, followed by decision tree classification of the principal components. By utilizing this approach, we observed that the organization of the panel of reporters studied was influenced during differentiation to differing degrees (**Figure 5.2C**). Interestingly, the organizational metrics of SC-35 were most sensitive to differentiation and led to maximum parsing between BA, AD, and OS treated cells (**Figure 5.2C, 5.2D**). The decision tree classification of principal components defining SC-35 organization resulted in > 95% correct classification between cells exposed to BA, AD, and OS culture media. The predictive model generated had a precision and sensitivity (recall) of 96% and 95%, respectively (**Figure 5.2D, 5.2E**).

The principal components computed in the analysis and the decision tree classifier results for the various nuclear proteins are shown in **Figures 5.6 - 5.10**. Based on these findings, we selected **SC-35** as a robust discriminant of stem cell lineages and further explored its organizational behavior as a function of osteogenic factors and microenvironmental cues. The decision tree classifier results and complete principal component vectors for the analysis using SC-35 organizational descriptors are shown in **Figure 5.10**.

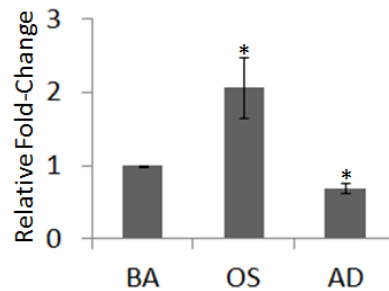


Figure 5.5: SC-35 Gene Expression of hMSCs Cultured in AD or OS for 3 Days

SC-35 gene expression relative fold change of hMSCs cultured in AD and OS for 3 days compared against 24 hours BA shows an increase and decrease in SC-35 gene expression in OS and AD conditions, respectively. * indicates statistical significance ($p < 0.01$).

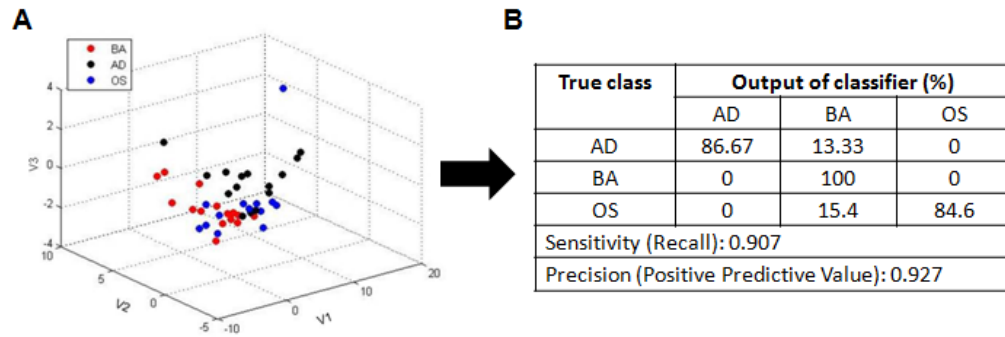


Figure 5.6: EZH2 Organization Results of hMSCs Cultured in BA, AD, and OS for 3 Days

(A) Principal Component Analysis (PCA) transformed data is plotted to depict cells in three-dimensional descriptor space. **(B)** Output of classifier using decision tree analysis shows an overall precision of 92.7%.

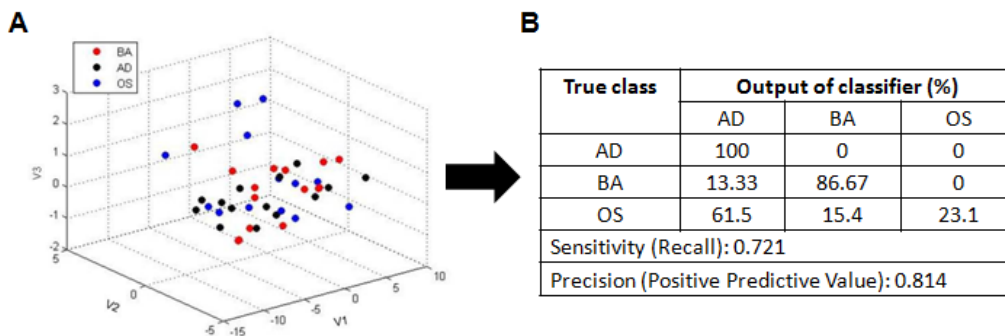


Figure 5.7: RUNX2 Organization Results of hMSCs Cultured in BA, AD, and OS for 3 Days

(A) Principal Component Analysis (PCA) transformed data is plotted to depict cells in three-dimensional descriptor space. **(B)** Output of classifier using decision tree analysis shows an overall precision of 81.4%.

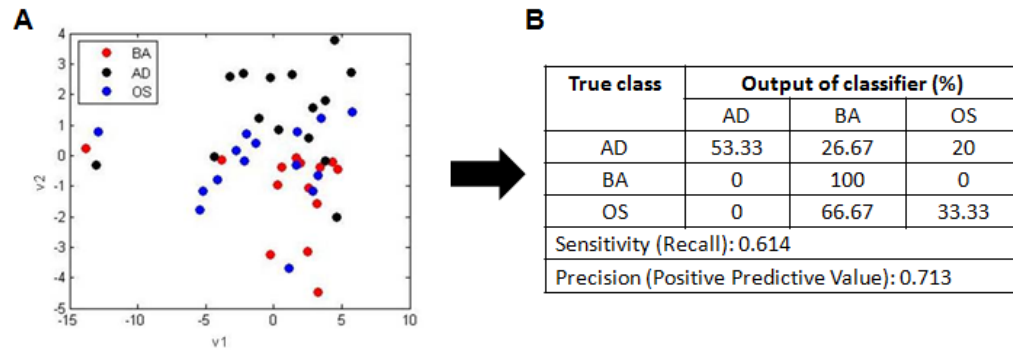


Figure 5.8: Lamin Organization Results of hMSCs Cultured in BA, AD, and OS for 3 Days

(A) Principal Component Analysis (PCA) transformed data is plotted to depict cells in three-dimensional descriptor space. **(B)** Output of classifier using decision tree analysis shows an overall precision of 71.3%.

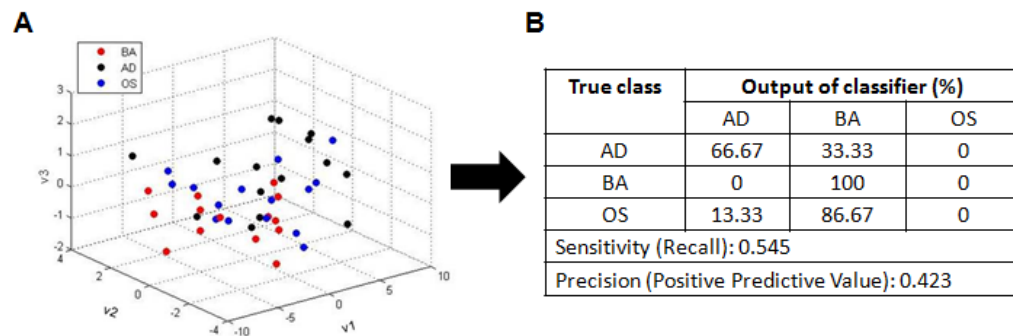


Figure 5.9: H3K4me3 Organization Results of hMSCs Cultured in BA, AD, and OS for 3 Days

(A) Principal Component Analysis (PCA) transformed data is plotted to depict cells in three-dimensional descriptor space. **(B)** Output of classifier using decision tree analysis shows an overall precision of 42.3%.

$$\begin{aligned}
V1 &= -0.234(C2 \text{ Information Measure1})+0.233(C2 \text{ Information Measure2})+0.233(C2 \text{ Difference Average})+0.232(C2 \text{ Difference Entropy})+0.23(C2 \text{ Sum Entropy})+0.23(C2 \text{ Entropy})+0.222(C1 \text{ Difference Average})+0.22(C2 \text{ Sum Average})+0.219(C1 \text{ Sum Average})+0.217(C2 \text{ Difference Variance})-0.215(C1 \text{ Inverse Difference Moment})+0.213(C1 \text{ Difference Entropy})+0.206(C1 \text{ Sum Entropy})+0.205(C2 \text{ Inertia})+0.205(C1 \text{ Inertia})+0.196(C1 \text{ Entropy})-0.184(C2 \text{ Inverse Difference Moment})-0.182(C1 \text{ Energy})+0.174(C1 \text{ Information Measure2})-0.172(C2 \text{ Correlation})+0.17(C2 \text{ Sum Variance})+0.159(C1 \text{ Difference Variance})-0.133(C1 \text{ Information Measure1})+0.128(C1 \text{ Sum Variance})-0.109(C1 \text{ Correlation})-0.031(C2 \text{ Energy}) \\
V2 &= 0.42(C2 \text{ Energy})-0.369(C1 \text{ Sum Variance})-0.34(C1 \text{ Difference Variance})-0.319(C2 \text{ Sum Variance})+0.277(C1 \text{ Entropy})+0.266(C1 \text{ Information Measure2})+0.229(C1 \text{ Sum Entropy})-0.225(C1 \text{ Information Measure1})-0.187(C2 \text{ Difference Variance})+0.174(C1 \text{ Difference Entropy})-0.17(C1 \text{ Energy})+0.156(C2 \text{ Inverse Difference Moment})-0.155(C1 \text{ Difference Average})-0.154(C2 \text{ Correlation})-0.135(C1 \text{ Inverse Difference Moment})-0.105(C2 \text{ Inertia})-0.104(C1 \text{ Inertia})-0.059(C2 \text{ Difference Average})+0.058(C2 \text{ Entropy})+0.052(C2 \text{ Sum Entropy})+0.041(C2 \text{ Difference Entropy})+0.038(C2 \text{ Information Measure1})+0.023(C1 \text{ Correlation})+0.007(C2 \text{ Sum Average})+0.007(C2 \text{ Information Measure2})+0.003(C1 \text{ Sum Average}) \\
V3 &= 0.476(C1 \text{ Information Measure1})-0.296(C1 \text{ Information Measure2})-0.291(C1 \text{ Sum Variance})+0.281(C1 \text{ Energy})-0.275(C2 \text{ Inverse Difference Moment})-0.232(C1 \text{ Difference Variance})+0.23(C1 \text{ Sum Average})+0.227(C2 \text{ Sum Average})-0.208(C2 \text{ Sum Variance})+0.1939(C1 \text{ Inertia})+0.191(C2 \text{ Inertia})+0.145(C2 \text{ Energy})-0.142(C1 \text{ Inverse Difference Moment})-0.134(C1 \text{ Difference Entropy})-0.13(C2 \text{ Correlation})-0.127(C1 \text{ Sum Entropy})+0.121(C2 \text{ Entropy})+0.117(C2 \text{ Sum Entropy})-0.115(C1 \text{ Entropy})-0.11(C1 \text{ Difference Average})+0.106(C2 \text{ Mean Difference Entropy})+0.081(C2 \text{ Information Measure2})-0.074(C2 \text{ Difference Variance})-0.03(C1 \text{ Correlation})-0.029(C2 \text{ Information Measure1})+0.029(C2 \text{ Difference Average}) \\
V4 &= -0.685(C1 \text{ Correlation})-0.459(C2 \text{ Correlation})-0.298(C2 \text{ Energy})-0.243(C2 \text{ Inertia})-0.242(C1 \text{ Inertia})-0.164(C1 \text{ Energy})-0.136(C2 \text{ Sum Average})-0.136(C1 \text{ Sum Average})-0.109(C1 \text{ Sum Variance})-0.093(C2 \text{ Inverse Difference Moment})+0.086(C1 \text{ Information Measure1})-0.073(C2 \text{ Sum Variance})-0.058(C1 \text{ Sum Entropy})-0.057(C1 \text{ Information Measure2})-0.052(C1 \text{ Inverse Difference Moment})-0.05(C1 \text{ Difference Entropy})+0.038(C2 \text{ Difference Average})+0.037(C2 \text{ Difference Variance})-0.033(C1 \text{ Entropy})-0.023(C1 \text{ Difference Variance})+0.021(C2 \text{ Difference Entropy})+0.016(C2 \text{ Entropy})-0.013(C1 \text{ Difference Average})+0.012(C2 \text{ Information Measure1})-0.005(C2 \text{ Sum Entropy})+0.004(C2 \text{ Information Measure2})
\end{aligned}$$

Figure 5.10: List of SC-35 PCs and Descriptors of hMSCs Cultured in BA, AD, or OS Medium

List of principal components (V1, V2, V3, V4) with corresponding descriptors and linear weights that account for > 95% of the variance between hMSCs exposed to BA, AD, or OS induction medium for 3 days by evaluating 26 Haralick texture features of the SC-35 nuclear reporter.

5.4.2 High Content Analysis of SC-35 Descriptors Discern *Dex*-Induced Bone Predisposition within 3 Days

Next, we investigated the effect of increasing concentrations of dexamethasone (*dex*), an osteogenic growth factor [48], on alkaline phosphatase (ALP) expression and SC-35 organization. Levels of 14 day osteogenic differentiation following increased concentrations of *dex* were measured by normalizing number of cells expressing ALP to total cell count (**Figure 5.11A**). As expected, at 14 days there was a positive correlation between increasing *dex* levels in the medium and percentage of ALP positive cells in the cell subpopulations. However, at 3 days, confocal images of immunolabeled SC-35 domains of cells exposed to varying concentrations of *dex* showed no observable differences in organization (**Figure 5.11B**). Quantification of individual morphometric features for cell nucleus (i.e., average intensity, nuclear roundness) yielded no observable trends at 3 days as well (**Figure 5.11C**), confirming that conventional imaging tools failed to parse these lineage variations.

Using our high content imaging-based algorithm, 26 nuclear texture features defining SC-35 organization within cells cultured in α -MEM, and low, medium, and high *dex*, were calculated and dimensionally reduced using PCA. A clear separation was observed between the four subpopulations of cells in the PCA plot (**Figure 5.11D**). The PCA plot showed that each of the subpopulations centralized in respective single clusters, indicating that SC-35 texture-based features were highly conserved within the same treatment condition. The predictive decision tree model was further able to correctly classify the cells with a precision of 94% and sensitivity of 93% (**Figure 5.11E**).

The decision tree classifier results and complete principal component vectors are shown in **Figure 5.12**.

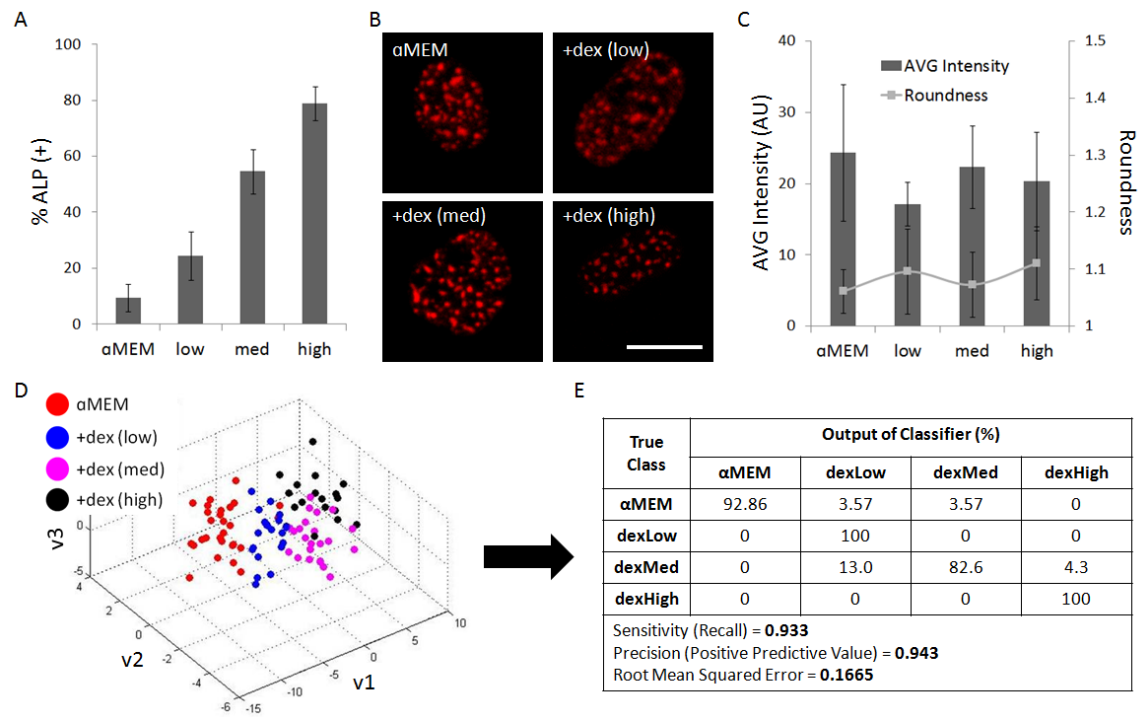


Figure 5.11: SC-35 Domain Descriptors Distinguish *Dex*-Induced ALP Expression within 3 Days

hMSCs were cultured in αMEM supplemented with increasing levels of *dex* (low = 0.1 μM, med = 0.5 μM, high = 1 μM), resulting in **(A)** an increasing percentage of ALP-positive cells after 14 days in culture. **(B)** Under the same culture conditions, representative SC-35 images, **(C)** average signal intensity of SC-35 (bars in plot), and nuclei roundness (dots in plot) are unable to discern differences between the different treatment groups at 3 days. However, 3 day analysis using 26 Haralick descriptors is capable of discerning differences between increasing *dex* conditions, confirmed by **(D)**

distinct cluster formation in PCA plot and **(E)** decision tree analysis, which shows that 93.3% of cells can be correctly classified using our approach. Scale bar: 10 μ m.

$$\begin{aligned}
 V1 &= -0.217(C2 \text{ Information Measure1}) + 0.217(C2 \text{ Information Measure2}) - 0.217(C1 \text{ Information Measure1}) + 0.216(C2 \text{ Difference Entropy}) + 0.216(C2 \text{ Difference Average}) + 0.215(C1 \text{ Difference Entropy}) + 0.213(C1 \text{ Information Measure2}) + 0.212(C1 \text{ Difference Average}) + 0.211(C2 \text{ Sum Entropy}) + 0.21(C2 \text{ Entropy}) + 0.209(C1 \text{ Sum Entropy}) + 0.208(C2 \text{ Difference Variance}) + 0.206(C1 \text{ Sum Average}) + 0.206(C2 \text{ Sum Variance}) + 0.205(C2 \text{ Sum Average}) + 0.204(C1 \text{ Difference Variance}) - 0.204(C1 \text{ Energy}) + 0.203(C1 \text{ Sum Variance}) + 0.202(C2 \text{ Inertia}) + 0.201(C1 \text{ Inertia}) + 0.192(C1 \text{ Entropy}) - 0.177(C2 \text{ Inverse Difference Moment}) - 0.167(C2 \text{ Energy}) - 0.122(C1 \text{ Inverse Difference Moment}) - 0.074(C1 \text{ Correlation}) - 0.066(C2 \text{ Correlation}) \\
 V2 &= 0.552(C1 \text{ Correlation}) + 0.482(C2 \text{ Correlation}) - 0.34(C1 \text{ Inverse Difference Moment}) + 0.322(C2 \text{ Energy}) + 0.187(C2 \text{ Inverse Difference Moment}) + 0.183(C1 \text{ Entropy}) + 0.178(C2 \text{ Sum Average}) + 0.171(C1 \text{ Sum Average}) - 0.137(C2 \text{ Difference Variance}) + 0.114(C2 \text{ Sum Entropy}) + 0.105(C1 \text{ Sum Entropy}) + 0.104(C2 \text{ Entropy}) + 0.096(C1 \text{ Inertia}) + 0.095(C2 \text{ Inertia}) - 0.089(C1 \text{ Difference Variance}) - 0.086(C2 \text{ Difference Average}) - 0.086(C1 \text{ Difference Average}) + 0.085(C1 \text{ Energy}) + 0.068(C1 \text{ Information Measure2}) - 0.053(C2 \text{ Sum Variance}) - 0.045(C1 \text{ Sum Variance}) + 0.032(C2 \text{ Difference Entropy}) + 0.029(C2 \text{ Information Measure2}) + 0.025(C1 \text{ Difference Entropy}) + 0.025(C2 \text{ Information Measure1}) + 0.006(C1 \text{ Information Measure1}) \\
 V3 &= 0.446(C1 \text{ Inverse Difference Moment}) + 0.43(C2 \text{ Correlation}) + 0.282(C1 \text{ Correlation}) - 0.269(C1 \text{ Entropy}) + 0.235(C1 \text{ Sum Variance}) - 0.218(C2 \text{ Energy}) - 0.205(C2 \text{ Inverse Difference Moment}) + 0.205(C2 \text{ Inertia}) + 0.205(C2 \text{ Sum Variance}) + 0.203(C1 \text{ Inertia}) + 0.193(C1 \text{ Difference Variance}) - 0.165(C1 \text{ Sum Entropy}) + 0.159(C1 \text{ Energy}) - 0.153(C2 \text{ Entropy}) + 0.124(C1 \text{ Difference Average}) - 0.124(C2 \text{ Sum Entropy}) - 0.11(C2 \text{ Difference Entropy}) - 0.11(C1 \text{ Information Measure2}) - 0.092(C1 \text{ Difference Entropy}) + 0.084(C2 \text{ Difference Variance}) + 0.06(C1 \text{ Sum Average}) - 0.058(C2 \text{ Information Measure2}) + 0.049(C2 \text{ Sum Average}) + 0.022(C2 \text{ Difference Average}) - 0.015(C1 \text{ Information Measure1}) - 0.008(C2 \text{ Information Measure1})
 \end{aligned}$$

Figure 5.12: List of PCs and Descriptors of hMSCs Cultured in Varying *Dex* Concentrations

List of principal components (V1, V2, V3) with corresponding descriptors and linear weights that account for > 95% of the variance between hMSCs exposed to BA, low, medium, and high concentrations of *dex* for 3 days by evaluating 26 Haralick texture features.

5.4.3 SC-35 Descriptors Discern Surface Topography-Induced Osteogenic Fates within 3 Days

hMSCs were cultured on films prepared using different ratios of poly(desaminotyrosyl-tyrosine ethyl ester carbonate) (PDTEC) to polystyrene (PS), thus achieving three distinct surface topographies: flat, continuous, and discontinuous (PDTEC islands and glass pits) (**Figure 5.13A**). Culturing hMSCs in osteogenic induction medium for 14 days on these topographies resulted in significant differences in the percentage of ALP positive cells (**Figure 5.13B**).

hMSCs cultured on continuous surfaces yielded the highest percentage of ALP positive cells ($72\% \pm 2\%$) whereas cells cultured on discontinuous surfaces had significantly less osteogenic cells ($52\% \pm 4\%$) when compared to the control flat surface ($63\% \pm 2\%$). These findings show that the substrate topography patterns sensitively modulate osteogenic differentiation.

To predict these downstream effects, we sought to investigate how SC-35 organization is affected by the engineered substrates after 3 days in culture. Representative SC-35 images for each condition show that there are no observable differences in SC-35 domains at 3 days for hMSCs cultured on the different surface topographies (**Figure 5.13A**). However, high content analysis of SC-35 organization illustrated that cell populations cultured on continuous, discontinuous, and flat surfaces were separated in the three-dimensional principal component space (**Figure 5.13C**). Decision tree analysis generated a predictive classification model that was able to differentiate between cells cultured on the three different topographies with 91%

precision and correctly classified instances (**Figure 5.12D**). The associated principal component vectors and the decision tree classifier generated are included in **Figure 5.14**.

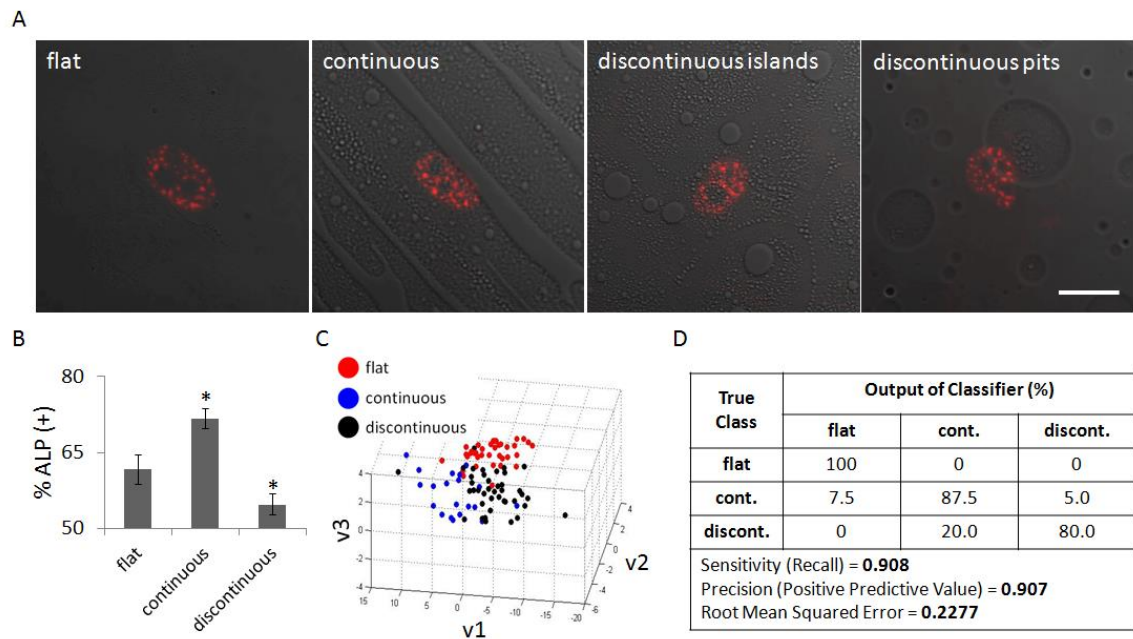


Figure 5.13: SC-35 Descriptors Discern Differences in Surface Topography-Induced ALP Expression within 3 Days

hMSCs were cultured on three distinct surface topographies: flat, continuous, or discontinuous for either 3 or 14 days. **(A)** 3 day representative images of SC-35 domains of hMSCs cultured in different surface topographies show no observable differences between the conditions. However, hMSCs cultured for 14 days under the same conditions **(B)** show significant differences in percentage of ALP positive cells. hMSCs cultured in the continuous surfaces are significantly more fast blue positive than the control condition (flat), and the discontinuous surfaces feature hMSCs that have

significantly less fast blue positive cells than the control condition. **(C)** PCA plot of 3 day SC-35 domain descriptors show that flat, continuous, and discontinuous surface patterns can be parsed with a good degree of separation. **(D)** This is independently verified using decision tree analysis. Scale bar: 10 μm . * indicates statistical significance ($p < 0.01$).

$$\begin{aligned}
 V1 &= -0.219(C2 \text{ Information Measure1}) - 0.218(C1 \text{ Information Measure1}) + 0.216(C2 \text{ Sum Entropy}) + 0.216(C2 \text{ Information Measure2}) + 0.216(C2 \text{ Difference Entropy}) + 0.216(C1 \text{ Difference Entropy}) + 0.214(C1 \text{ Sum Entropy}) + 0.214(C1 \text{ Information Measure2}) + 0.213(C2 \text{ Difference Average}) + 0.21(C2 \text{ Entropy}) + 0.209(C1 \text{ Difference Average}) + 0.206(C1 \text{ Sum Average}) + 0.205(C2 \text{ Sum Average}) + 0.2(C1 \text{ Entropy}) + 0.196(C2 \text{ Difference Variance}) + 0.195(C2 \text{ Inertia}) - 0.194(C2 \text{ Inverse Difference Moment}) + 0.194(C2 \text{ Sum Variance}) + 0.194(C1 \text{ Inertia}) + 0.193(C1 \text{ Sum Variance}) + 0.191(C1 \text{ Difference Variance}) - 0.181(C1 \text{ Energy}) - 0.171(C1 \text{ Inverse Difference Moment}) - 0.16(C2 \text{ Energy}) + 0.112(C2 \text{ Correlation}) + 0.078(C1 \text{ Correlation}) \\
 V2 &= -0.463(C1 \text{ Correlation}) - 0.428(C2 \text{ Correlation}) - 0.321(C2 \text{ Energy}) - 0.297(C1 \text{ Energy}) - 0.22(C2 \text{ Inertia}) - 0.219(C1 \text{ Inertia}) - 0.214(C1 \text{ Sum Variance}) - 0.189(C1 \text{ Difference Variance}) - 0.188(C2 \text{ Sum Variance}) + 0.17(C2 \text{ Entropy}) + 0.158(C1 \text{ Entropy}) - 0.127(C2 \text{ Inverse Difference Moment}) + 0.125(C2 \text{ Difference Entropy}) - 0.124(C2 \text{ Sum Average}) - 0.122(C1 \text{ Sum Average}) + 0.117(C1 \text{ Sum Entropy}) + 0.115(C2 \text{ Information Measure2}) + 0.114(C1 \text{ Difference Entropy}) + 0.102(C2 \text{ Sum Entropy}) - 0.099(C2 \text{ Difference Variance}) + 0.099(C1 \text{ Information Measure2}) - 0.076(C1 \text{ Difference Average}) - 0.053(C1 \text{ Inverse Difference Moment}) - 0.044(C1 \text{ Information Measure1}) - 0.025(C2 \text{ Information Measure1}) + 0.015(C2 \text{ Difference Average}) \\
 V3 &= -0.437(C1 \text{ Inverse Difference Moment}) - 0.348(C1 \text{ Correlation}) + 0.321(C2 \text{ Difference Variance}) + 0.298(C1 \text{ Difference Variance}) + 0.272(C2 \text{ Sum Variance}) + 0.259(C1 \text{ Sum Variance}) - 0.251(C2 \text{ Correlation}) + 0.231(C1 \text{ Difference Average}) - 0.214(C2 \text{ Energy}) - 0.2129(C1 \text{ Entropy}) + 0.211(C2 \text{ Difference Average}) + 0.145(C2 \text{ Inverse Difference Moment}) - 0.135(C1 \text{ Information Measure2}) - 0.115(C2 \text{ Sum Average}) - 0.114(C1 \text{ Sum Average}) - 0.1(C2 \text{ Entropy}) - 0.099(C1 \text{ Sum Entropy}) - 0.097(C2 \text{ Sum Entropy}) - 0.056(C2 \text{ Information Measure2}) + 0.048(C1 \text{ Energy}) + 0.046(C1 \text{ Information Measure1}) + 0.03(C2 \text{ Inertia}) + 0.025(C2 \text{ Difference Entropy}) + 0.022(C1 \text{ Inertia}) + 0.014(C1 \text{ Difference Entropy}) - 0.007(C2 \text{ Information Measure1})
 \end{aligned}$$

Figure 5.14: List of PCs and Descriptors of hMSCs Cultured on Different Surface Patterns

List of principal components (V1, V2, V3) with corresponding descriptors and linear weights that account for > 95% of the variance between hMSCs cultured on surface topographies of different degree of continuity (flat, continuous, discontinuous) for 3 days by evaluating 26 Haralick texture features.

5.4.4 3 Day SC-35 Descriptors Distinguish Bone Predisposition Outcomes in Response to Fibrous Scaffold Features

To further highlight the utility of our approach to predict osteogenic differentiation on diverse materials, hMSCs were cultured on fibrous scaffolds featuring fibers of two different sizes (small, large) and orientations (aligned, random) (**Figure 5.15A**). Electrospinning settings were optimized so that the fiber diameters were similar ($\sim 2\ \mu\text{m}$ for small, $\sim 5.5\ \mu\text{m}$ for large) for both randomly-oriented and aligned fibers (**Figure 5.15B**). hMSCs were cultured in BA medium for 14 days and osteogenic differentiation was assessed by measuring ALP activity normalized to cell count (**Figure 5.15C**). ALP activity was significantly lower ($p < 0.01$) for hMSCs cultured on the small fibers versus large fibers, irrespective of orientation, while the cells cultured on randomly-oriented, larger fibers had the highest ALP activity.

As illustrated in the PCA plots, our results show that using high content analysis of SC-35 domains at 3 days, cells cultured on small versus large randomly-oriented or large fibers could be parsed (**Figure 5.15D, 5.15F**). The predictive classification models made using J48 decision tree analysis to classify cells cultured on small versus large fibers had a precision (positive predictive value) and recall of 88% for random fibers, and $> 77\%$ for aligned fibers (**Figure 5.14E, 5.14G**). Complete principal component vectors and the decision tree classifier results are included in **Figure 5.16** and **Figure 5.17**.

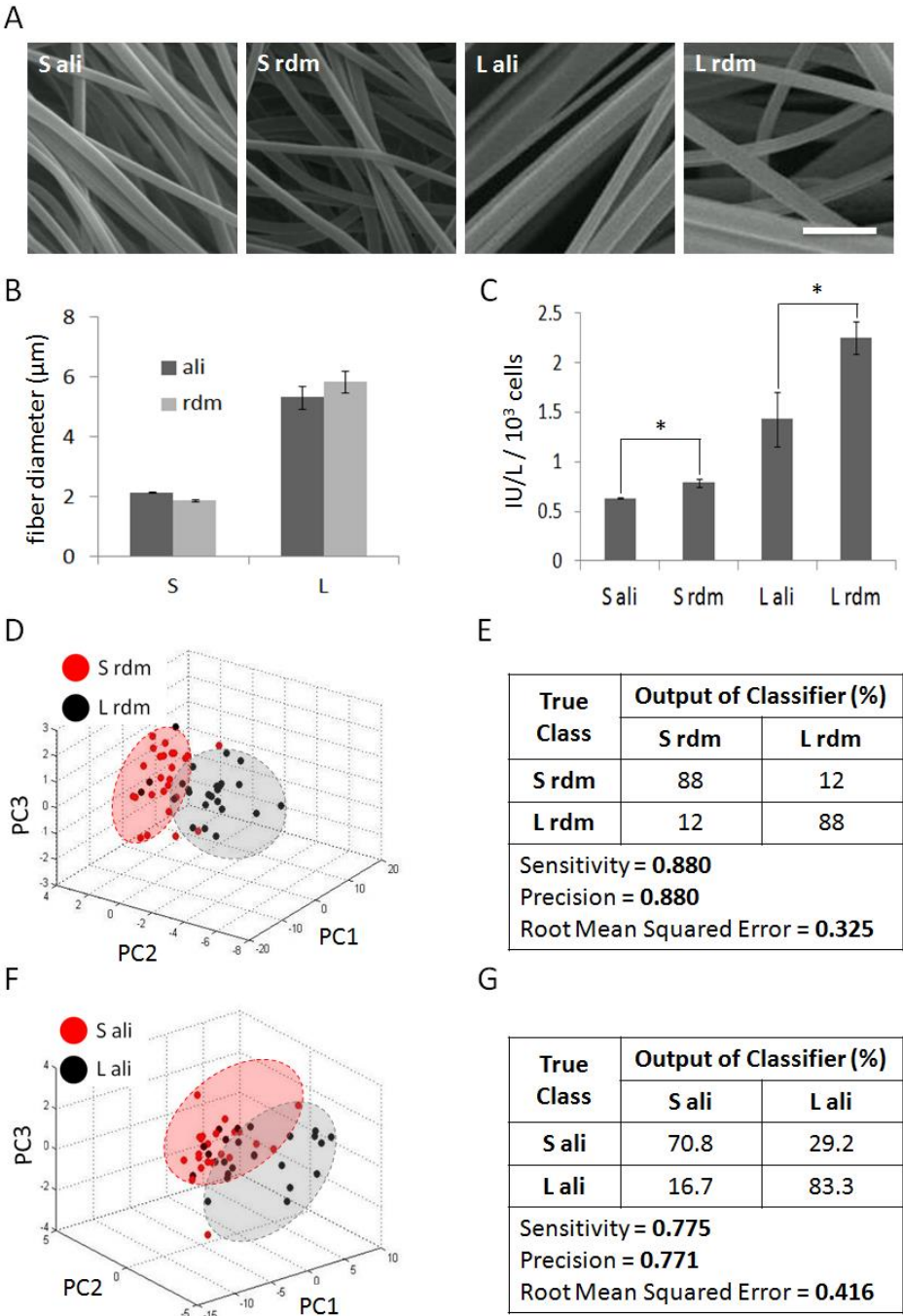


Figure 5.15: SC-35 Descriptors Discern Fibrous Scaffold Topography-Induced ALP Expression within 3 Days

hMSCs were cultured in BA medium on **(A)** fibrous scaffolds featuring fibers of two different sizes and orientations. SEM micrographs of electrospun scaffolds of two sizes

(small, large) and fiber orientations (aligned, random) were used to **(B)** quantify fiber diameters and show that fiber orientation does not significantly affect fiber diameter. Small fibers are distinctly smaller ($\sim 2 \mu\text{m}$) than the large fibers ($\sim 5.5 \mu\text{m}$). **(C)** hMSCs cultured on these fibrous scaffolds for 14 days show distinct ALP activity profiles. High content analysis of SC-35 descriptors at 3 days show that hMSCs cultured on **(D-E)** small versus large randomly-oriented fibers and **(F-G)** small versus large aligned fibers can be identified, as confirmed by **(D-F)** distinct clusters in PCA plots and **(E-G)** decision tree classification analysis results of PCA-derived principal components. Scale bar: 10 μm . * indicates statistical significance ($p < 0.01$).

$$\begin{aligned}
 V1 &= -0.221(\text{C2 Information Measure1})+0.219(\text{C2 Information Measure2})+0.217(\text{C2 Difference Average})+0.216(\text{C2 Sum Entropy})+0.216(\text{C2 Difference Entropy})+0.216(\text{C1 Difference Average})+0.214(\text{C2 Entropy})-0.212(\text{C1 Information Measure1})+0.21(\text{C2 Sum Average})+0.21(\text{C1 Sum Average})+0.209(\text{C1 Difference Entropy})+0.203(\text{C1 Information Measure2})+0.202(\text{C1 Sum Entropy})+0.2(\text{C2 Difference Variance})+0.195(\text{C2 Sum Variance})+0.195(\text{C1 Sum Variance})+0.194(\text{C2 Inertia})+0.194(\text{C1 Difference Variance})+0.193(\text{C1 Inertia})+0.19(\text{C2 Correlation})+0.188(\text{C1 Entropy})+0.179(\text{C1 Correlation})-0.164(\text{C1 Inverse Difference Moment})-0.16(\text{C1 Energy})-0.118(\text{C2 Inverse Difference Moment})-0.114(\text{C2 Energy}) \\
 V2 &= 0.361(\text{C2 Energy})-0.358(\text{C1 Energy})+0.355(\text{C2 Inverse Difference Moment})-0.353(\text{C1 Inverse Difference Moment})+0.28(\text{C1 Entropy})+0.218(\text{C1 Sum Entropy})+0.207(\text{C1 Information Measure2})-0.204(\text{C2 Inertia})-0.204(\text{C1 Inertia})-0.198(\text{C1 Sum Variance})-0.186(\text{C2 Sum Variance})-0.18(\text{C1 Difference Variance})+0.171(\text{C1 Difference Entropy})-0.145(\text{C2 Difference Variance})-0.124(\text{C1 Information Measure1})+0.111(\text{C2 Entropy})-0.104(\text{C2 Correlation})+0.094(\text{C2 Sum Entropy})-0.094(\text{C1 Sum Average})-0.086(\text{C2 Sum Average})+0.086(\text{C2 Difference Entropy})-0.081(\text{C1 Difference Average})-0.053(\text{C2 Difference Average})+0.045(\text{C2 Information Measure2})-0.006(\text{C1 Correlation})+0.001(\text{C2 Information Measure1}) \\
 V3 &= -0.488(\text{C2 Energy})-0.484(\text{C2 Inverse Difference Moment})-0.356(\text{C1 Correlation})-0.28(\text{C2 Correlation})-0.256(\text{C1 Difference Variance})-0.2539(\text{C1 Sum Variance})-0.244(\text{C2 Sum Variance})-0.158(\text{C2 Difference Variance})+0.146(\text{C2 Entropy})+0.112(\text{C2 Information Measure2})+0.103(\text{C2 Sum Entropy})+0.096(\text{C2 Difference Entropy})+0.091(\text{C1 Entropy})+0.088(\text{C1 Information Measure2})-0.087(\text{C1 Difference Average})-0.082(\text{C1 Information Measure1})+0.071(\text{C2 Sum Average})+0.071(\text{C1 Sum Average})+0.059(\text{C1 Sum Entropy})-0.053(\text{C2 Inertia})-0.049(\text{C1 Inertia})+0.045(\text{C1 Difference Entropy})-0.042(\text{C2 Information Measure1})-0.035(\text{C1 Inverse Difference Moment})-0.031(\text{C1 Energy})-0.006(\text{C2 Difference Average})
 \end{aligned}$$

Figure 5.16: List of PCs and Descriptors of hMSCs Cultured on Small versus Large Random Fibers

List of principal components (V1, V2, V3) with corresponding descriptors and linear weights that account for > 95% of the variance between hMSCs cultured on small and large randomly-oriented fibers for 3 days by evaluating 26 Haralick texture features.

$$\begin{aligned}
V1 &= -0.213(C2 \text{ Information Measure1}) + 0.212(C2 \text{ Information Measure2}) + 0.211(C2 \text{ Difference Entropy}) + 0.211(C2 \text{ Sum Entropy}) + 0.21(C2 \text{ Entropy}) + 0.209(C1 \text{ Difference Entropy}) + 0.209(C2 \text{ Difference Average}) + 0.208(C1 \text{ Difference Average}) - 0.206(C1 \text{ Information Measure1}) + 0.205(C2 \text{ Sum Average}) + 0.205(C1 \text{ Sum Entropy}) + 0.205(C1 \text{ Sum Average}) + 0.201(C1 \text{ Information Measure2}) + 0.194(C1 \text{ Entropy}) + 0.193(C2 \text{ Difference Variance}) + 0.193(C2 \text{ Sum Variance}) + 0.193(C1 \text{ Sum Variance}) - 0.192(C2 \text{ Energy}) + 0.191(C2 \text{ Inertia}) + 0.19(C1 \text{ Inertia}) + 0.19(C1 \text{ Difference Variance}) - 0.188(C2 \text{ Inverse Difference Moment}) - 0.18(C1 \text{ Energy}) - 0.169(C1 \text{ Inverse Difference Moment}) + 0.165(C2 \text{ Correlation}) + 0.135(C1 \text{ Correlation}) \\
V2 &= -0.347(C1 \text{ Inverse Difference Moment}) - 0.317(C1 \text{ Energy}) + 0.291(C1 \text{ Correlation}) - 0.268(C1 \text{ Difference Variance}) - 0.263(C1 \text{ Sum Variance}) + 0.261(C1 \text{ Entropy}) - 0.26(C2 \text{ Sum Variance}) - 0.249(C2 \text{ Difference Variance}) - 0.237(C2 \text{ Inertia}) - 0.236(C1 \text{ Inertia}) + 0.223(C1 \text{ Information Measure2}) + 0.179(C1 \text{ Sum Entropy}) + 0.159(C2 \text{ Correlation}) - 0.154(C1 \text{ Information Measure1}) - 0.136(C1 \text{ Difference Average}) + 0.121(C2 \text{ Energy}) - 0.12(C2 \text{ Difference Average}) + 0.113(C2 \text{ Inverse Difference Moment}) + 0.111(C1 \text{ Difference Entropy}) - 0.1(C1 \text{ Sum Average}) - 0.098(C2 \text{ Sum Average}) + 0.094(C2 \text{ Entropy}) + 0.089(C2 \text{ Sum Entropy}) + 0.053(C2 \text{ Information Measure2}) + 0.039(C2 \text{ Difference Entropy}) - 0.008(C2 \text{ Information Measure1}) \\
V3 &= -0.647(C1 \text{ Correlation}) - 0.576(C2 \text{ Correlation}) - 0.227(C1 \text{ Inverse Difference Moment}) - 0.22(C1 \text{ Energy}) + 0.144(C2 \text{ Difference Entropy}) + 0.134(C1 \text{ Entropy}) + 0.129(C2 \text{ Entropy}) - 0.113(C2 \text{ Inertia}) - 0.11(C1 \text{ Inertia}) + 0.1(C2 \text{ Difference Variance}) - 0.098(C2 \text{ Energy}) + 0.094(C2 \text{ Difference Average}) + 0.087(C1 \text{ Sum Entropy}) + 0.086(C1 \text{ Difference Entropy}) + 0.085(C2 \text{ Sum Entropy}) - 0.059(C2 \text{ Sum Average}) - 0.056(C1 \text{ Sum Average}) - 0.056(C1 \text{ Sum Variance}) + 0.055(C2 \text{ Inverse Difference Moment}) + 0.046(C1 \text{ Information Measure1}) + 0.041(C2 \text{ Information Measure2}) + 0.028(C1 \text{ Information Measure2}) - 0.026(C2 \text{ Sum Variance}) + 0.009(C2 \text{ Information Measure1}) - 0.004(C1 \text{ Difference Average}) - 0.002(C1 \text{ Difference Variance})
\end{aligned}$$

Figure 5.16: List of PCs and Descriptors of hMSCs Cultured on Small versus

Large Aligned Fibers

List of principal components (V1, V2, V3) with corresponding descriptors and linear weights that account for > 95% of the variance between hMSCs cultured on small and large aligned fibers for 3 days by evaluating 26 Haralick texture features.

5.4.5 Analysis of SC-35 Descriptors can Track hMSC Differentiation on Micropillars within 3 Days

hMSCs were cultured on micropillars featuring distinct topographies prepared using fabrication methods reported by Unadkat et al. in 2010 [91]. From a large array of topographical feature combinations, four micropillar patterns with varied features (termed TopoA-D) were selected to further analyze the SC-35 organizational differences in cultured hMSCs. These distinct topographies were observed to be osteoinductive and induced osteogenic differentiation to varied extents. Culturing hMSCs for 14 days in basal medium on these topographies resulted in significant differences in percentage of ALP positive cells (**Figure 5.18B**). hMSCs cultured on TopoA had the highest percentage of ALP positive cells ($56\% \pm 5\%$), and a statistically significant ($p < 0.01$) decreasing trend was observed with TopoB ($44\% \pm 3\%$), TopoC ($34\% \pm 1\%$), and TopoD ($20\% \pm 3\%$). hMSCs cultured on flat surfaces in basal medium were used as a negative control and had 0% ALP positive cells, while cells cultured in presence of $1 \mu\text{M}$ *dex* had $78\% \pm 2\%$ ALP positive cells (data not shown).

To track hMSC phenotypic changes at early time points, we sought to investigate the influence of micropillar topography on SC-35 organization 3 days post cell culture using high content textural analysis. Representative confocal images for each condition show that there are no observable differences in SC-35 domains at 3 days for hMSCs cultured on the different micropillars (**Figure 5.18A**). On the other hand, as illustrated in the PCA plot, cell populations cultured on the most osteogenic (TopoA) versus the least osteogenic (TopoD) micropillars could be parsed from each other, as well as the two

intermediary conditions (TopoB versus TopoC) (**Figure 5.18C**) using high content analysis of SC-35 organization. Decision tree analysis generated a predictive classification model that was able to differentiate between cells cultured on four different micropillar topographies with 83% sensitivity and 84% precision (**Figure 5.18D**). Interestingly, cells cultured in the two conditions that induced the least ALP (TopoC and TopoD) showed the most distinct changes in SC-35 organization. 14% of cells cultured in TopoC were incorrectly classified as belonging to TopoA, which elicited a significantly higher percentage of ALP positive hMSCs. Similarly, classification of cells cultured in TopoD, the least ALP-inducing condition, binned 80% correctly and classified 20% of the cells as belonging to TopoB, which induced a significantly higher percentage of ALP positive hMSCs (**Figure 5.18D**). Complete principal component vectors are described in **Figure 5.19**.

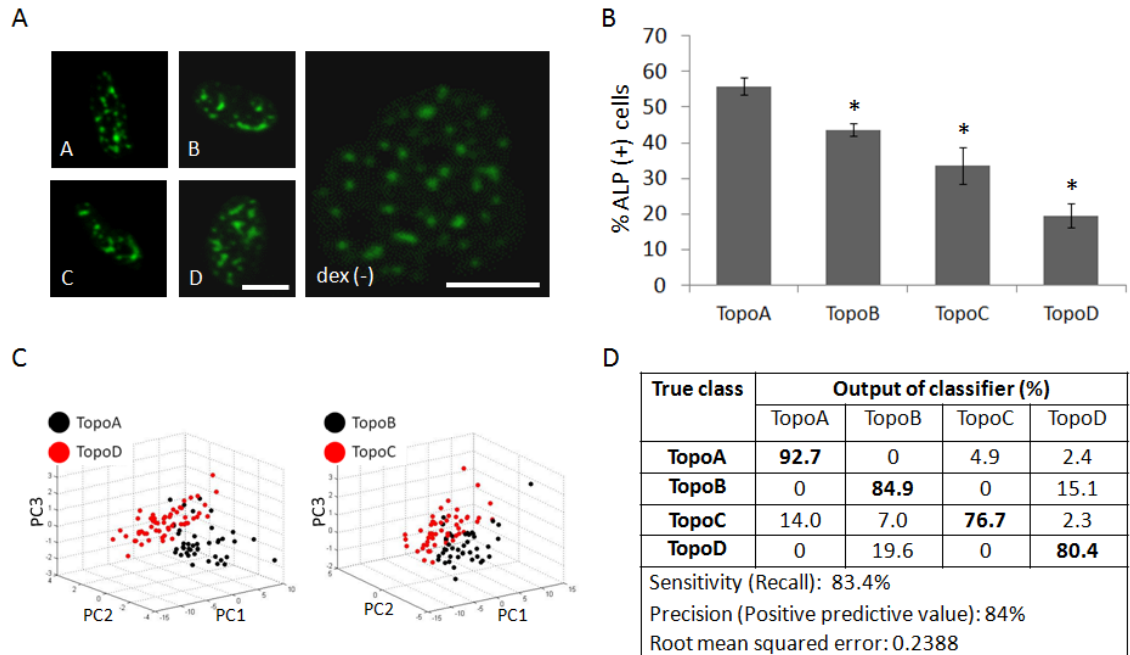


Figure 5.18: SC-35 Descriptors can Identify ALP Expression on Micropillars within 3 Days

hMSCs were cultured on a subset of micropillars (termed TopoA - TopoD) derived from a much larger library of topographies. **(A)** Cells show no substantial qualitative differences in SC-35 organization after 3 days in culture, although at 14 days **(B)** hMSCs cultured in the same conditions displayed significant differences in percentage of ALP positive cells. 3 day SC-35 domain descriptors are capable of identifying differences between the micropillar culture conditions, as seen by **(C)** PCA plots demarcating distinct groupings between the conditions with largest difference in ALP positive cells (TopoA versus TopoD), as well as intermediate ALP positive conditions (TopoB versus TopoC). **(D)** decision tree classification analysis results of PCA-derived principal components. Scale bar: 10 μ m. * indicates statistical significance ($p < 0.01$) with respect to TopoA (most osteogenic) condition.

$$\begin{aligned}
V1 &= -0.221(C2 \text{ Information Measure1}) + 0.218(C2 \text{ Difference Entropy}) + 0.218(C2 \text{ Information Measure2}) + 0.217(C2 \text{ Difference Average}) - 0.216(C1 \text{ Information Measure1}) + 0.215(C2 \text{ Sum Entropy}) + 0.215(C2 \text{ Sum Average}) + 0.215(C1 \text{ Sum Average}) + 0.212(C1 \text{ Difference Average}) + 0.209(C2 \text{ Entropy}) + 0.208(C1 \text{ Difference Entropy}) + 0.204(C2 \text{ Inertia}) + 0.204(C1 \text{ Inertia}) + 0.202(C2 \text{ Difference Variance}) + 0.2(C2 \text{ Sum Variance}) + 0.198(C1 \text{ Sum Variance}) + 0.197(C2 \text{ Correlation}) + 0.197(C1 \text{ Difference Variance}) + 0.195(C1 \text{ Information Measure2}) + 0.194(C1 \text{ Sum Entropy}) - 0.193(C2 \text{ Inverse Difference Moment}) + 0.177(C1 \text{ Correlation}) + 0.166(C1 \text{ Entropy}) - 0.166(C1 \text{ Inverse Difference Moment}) - 0.101(C2 \text{ Energy}) - 0.045(C1 \text{ Energy}) \\
V2 &= 0.428(C2 \text{ Energy}) + 0.39(C1 \text{ Entropy}) + 0.287(C1 \text{ Sum Entropy}) + 0.282(C1 \text{ Information Measure2}) - 0.23(C1 \text{ Sum Variance}) - 0.229(C1 \text{ Inverse Difference Moment}) - 0.211(C2 \text{ Correlation}) - 0.206(C2 \text{ Sum Variance}) - 0.204(C1 \text{ Difference Variance}) + 0.201(C1 \text{ Difference Entropy}) + 0.2(C2 \text{ Entropy}) - 0.162(C1 \text{ Correlation}) - 0.159(C1 \text{ Difference Average}) - 0.155(C2 \text{ Difference Variance}) + 0.152(C2 \text{ Sum Entropy}) - 0.128(C1 \text{ Information Measure1}) - 0.123(C2 \text{ Inertia}) - 0.121(C1 \text{ Inertia}) + 0.105(C2 \text{ Difference Entropy}) + 0.102(C2 \text{ Information Measure2}) - 0.097(C2 \text{ Difference Average}) + 0.084(C1 \text{ Mean Energy}) + 0.073(C2 \text{ Inverse Difference Moment}) - 0.018(C1 \text{ Sum Average}) - 0.015(C2 \text{ Sum Average}) + 0.004(C2 \text{ Information Measure1}) \\
V3 &= 0.753(C1 \text{ Energy}) + 0.354(C2 \text{ Energy}) + 0.198(C2 \text{ Inverse Difference Moment}) + 0.185(C1 \text{ Inertia}) + 0.184(C2 \text{ Inertia}) + 0.181(C1 \text{ Inverse Difference Moment}) + 0.181(C2 \text{ Difference Variance}) + 0.173(C1 \text{ Difference Variance}) + 0.132(C2 \text{ Sum Variance}) + 0.127(C1 \text{ Sum Variance}) - 0.114(C2 \text{ Correlation}) + 0.104(C2 \text{ Sum Average}) + 0.104(C1 \text{ Sum Average}) - 0.101(C1 \text{ Correlation}) + 0.076(C1 \text{ Information Measure1}) - 0.075(C2 \text{ Information Measure2}) + 0.063(C2 \text{ Information Measure1}) - 0.054(C2 \text{ Entropy}) - 0.047(C1 \text{ Information Measure2}) - 0.046(C2 \text{ Sum Entropy}) + 0.04(C1 \text{ Difference Average}) + 0.038(C2 \text{ Difference Average}) - 0.009(C1 \text{ Difference Entropy}) - 0.008(C1 \text{ Sum Entropy}) + 0.007(C1 \text{ Entropy}) - 0.005(C2 \text{ Difference Entropy}) \\
V4 &= -0.405(C1 \text{ Correlation}) + 0.342(C1 \text{ Inverse Difference Moment}) + 0.325(C2 \text{ Inverse Difference Moment}) - 0.268(C1 \text{ Inertia}) - 0.26(C2 \text{ Inertia}) - 0.24(C1 \text{ Sum Average}) - 0.239(C2 \text{ Sum Average}) + 0.228(C2 \text{ Difference Variance}) + 0.221(C1 \text{ Difference Variance}) + 0.22(C2 \text{ Sum Variance}) + 0.192(C2 \text{ Difference Average}) + 0.175(C1 \text{ Difference Average}) - 0.171(C1 \text{ Energy}) + 0.167(C1 \text{ Sum Variance}) + 0.135(C1 \text{ Difference Entropy}) + 0.132(C2 \text{ Difference Entropy}) - 0.098(C2 \text{ Correlation}) + 0.093(C1 \text{ Sum Entropy}) + 0.081(C1 \text{ Entropy}) + 0.072(C1 \text{ Information Measure2}) - 0.068(C2 \text{ Energy}) - 0.061(C2 \text{ Information Measure1}) + 0.058(C2 \text{ Sum Entropy}) - 0.053(C1 \text{ Information Measure1}) + 0.053(C2 \text{ Entropy}) + 0.045(C2 \text{ Information Measure2})
\end{aligned}$$

Figure 5.19: List of PCs and Descriptors of hMSCs Cultured on Micropillars

List of principal components (V1, V2, V3, V4) with corresponding descriptors and linear weights that account for > 95% of the variance between hMSCs cultured on four different micropillar topographies for 3 days by evaluating 26 Haralick texture features.

5.4.6 Pharmacological Inhibition of Signaling Molecules Governing Osteogenesis Results in Quantifiable Alterations in SC-35 Organization

To elucidate the crosstalk between adhesion signaling and SC-35 organization, the roles of several molecules, namely RhoGTPase, FAK1, and β -catenin were specifically inhibited using 0.5 μ g/ml C3 transferase (C3), 1 μ M FAK inhibitor, and 15 μ M FH353, respectively. At the mentioned inhibitor concentrations, the cell viability was not significantly affected at time of SC-35 organization analysis which was performed 3 days post culturing cells in osteogenic induction medium (**Figure 5.20A**). hMSCs were cultured in OS induction medium in the presence of inhibitors for 14 days and osteogenic differentiation was assessed by staining for ALP. As expected, treatment with pharmacological inhibitors resulted in almost no ALP positive cells at 14 days (**Figure 5.20B**).

At 3 days, RhoGTPase inhibition drastically reduced polymerized actin fibers in the cells, whereas treatment with FAK and β -catenin did not significantly influence actin polymerization or cell morphology (**Figure 5.21A**). Interestingly, PCA plot of 3 day assessment of the SC-35 organization showed good separation between the different inhibition treatment groups (**Figure 5.21B**). This is supported by decision tree analysis, which shows almost 95% of cells are correctly classified (**Figure 5.21C**). Complete principal component vectors and the decision tree classifier generated are shown in **Figure 5.22**.

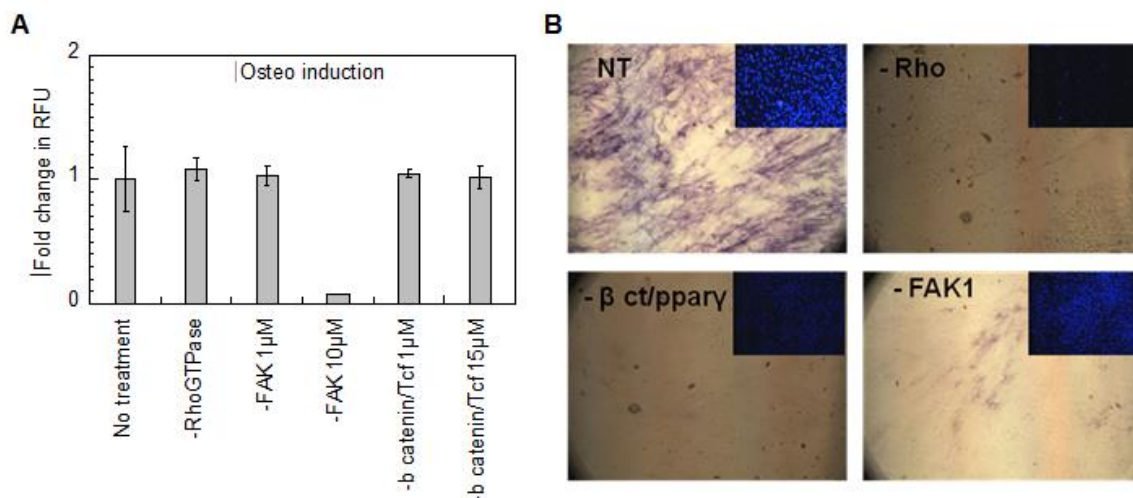


Figure 5.20: Pharmacological Inhibitors Do Not Affect Cell Viability

(A) Fold change in relative fluorescence units shows that the use of pharmacological inhibitors at working concentrations did not significantly affect cell viability. **(B)** hMSCs cultured for 14 days in OS medium supplemented with the inhibitors results in minimal ALP production with respect to the no treatment (NT) control.

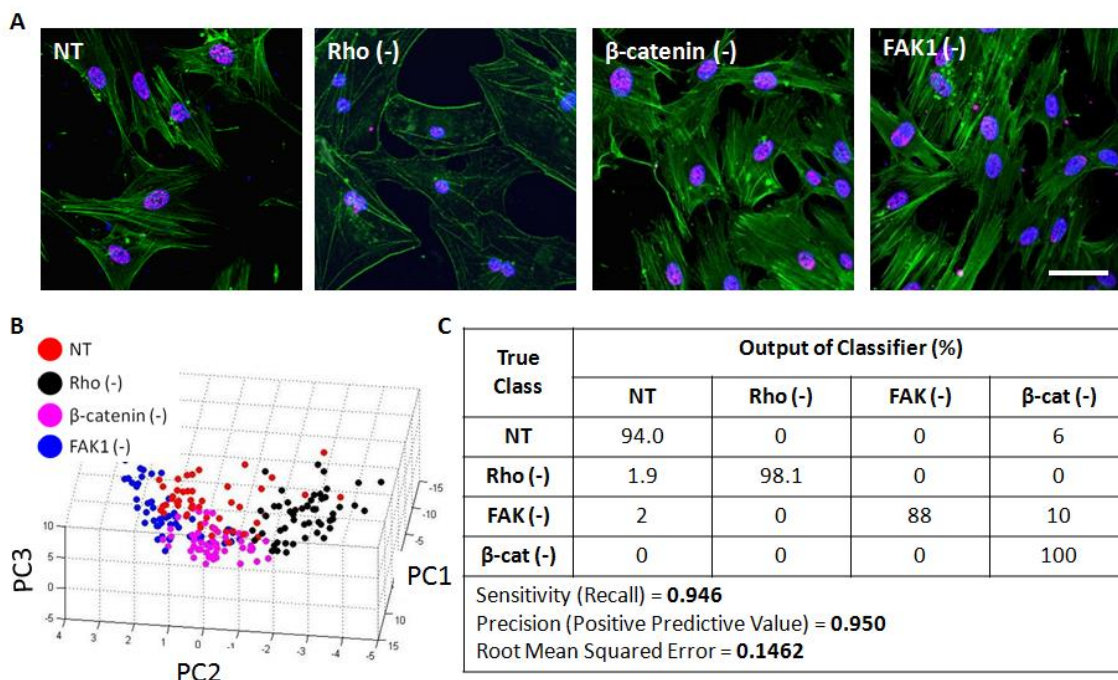


Figure 5.21: Classification of hMSCs Treated with Different Inhibitors Using SC-35 Descriptors

Rho was specifically inhibited using 0.5 $\mu\text{g}/\text{mL}$ C3 transferase (-Rho), FAK was inhibited using 1 μM FAK inhibitor 14 (-FAK), and β -catenin was inhibited using 15 μM FH535. **(A)** 3 days post culturing cells in presence of inhibitors and OS medium, changes in cell morphology were visualized through staining for actin (phalloidin), DNA (Hoeschst), and SC-35 (anti-SC-35 antibodies). **(B)** Subsequently, high content analysis was performed for SC-35 organization and 26 Haralick texture descriptors were evaluated. The descriptors were dimensionally reduced via PCA to principal components that account for 95% of the variance and the principal components were plotted to visualize the cell distribution. **(C)** Cells treated with different inhibitors were classified using J48 decision tree analysis and the output of the classifier has been presented. Scale bar: 10 μm .

$$\begin{aligned}
V1 &= -0.221(C2 \text{ Information Measure1}) + 0.218(C2 \text{ Difference Entropy}) + 0.218(C2 \text{ Information Measure2}) + 0.217(C2 \text{ Difference Average}) - 0.216(C1 \text{ Information Measure1}) + 0.215(C2 \text{ Sum Entropy}) + 0.215(C2 \text{ Sum Average}) + 0.215(C1 \text{ Sum Average}) + 0.212(C1 \text{ Difference Average}) + 0.209(C2 \text{ Entropy}) + 0.208(C1 \text{ Difference Entropy}) + 0.204(C2 \text{ Inertia}) + 0.204(C1 \text{ Inertia}) + 0.202(C2 \text{ Difference Variance}) + 0.2(C2 \text{ Sum Variance}) + 0.198(C1 \text{ Sum Variance}) + 0.197(C2 \text{ Correlation}) + 0.197(C1 \text{ Difference Variance}) + 0.195(C1 \text{ Information Measure2}) + 0.194(C1 \text{ Sum Entropy}) - 0.193(C2 \text{ Inverse Difference Moment}) + 0.177(C1 \text{ Correlation}) + 0.166(C1 \text{ Entropy}) - 0.166(C1 \text{ Inverse Difference Moment}) - 0.101(C2 \text{ Energy}) - 0.045(C1 \text{ Energy}) \\
V2 &= 0.428(C2 \text{ Energy}) + 0.39(C1 \text{ Entropy}) + 0.287(C1 \text{ Sum Entropy}) + 0.282(C1 \text{ Information Measure2}) - 0.23(C1 \text{ Sum Variance}) - 0.229(C1 \text{ Inverse Difference Moment}) - 0.211(C2 \text{ Correlation}) - 0.206(C2 \text{ Sum Variance}) - 0.204(C1 \text{ Difference Variance}) + 0.201(C1 \text{ Difference Entropy}) + 0.2(C2 \text{ Entropy}) - 0.162(C1 \text{ Correlation}) - 0.159(C1 \text{ Difference Average}) - 0.155(C2 \text{ Difference Variance}) + 0.152(C2 \text{ Sum Entropy}) - 0.128(C1 \text{ Information Measure1}) - 0.123(C2 \text{ Inertia}) - 0.121(C1 \text{ Inertia}) + 0.105(C2 \text{ Difference Entropy}) + 0.102(C2 \text{ Information Measure2}) - 0.097(C2 \text{ Difference Average}) + 0.084(C1 \text{ Mean Energy}) + 0.073(C2 \text{ Inverse Difference Moment}) - 0.018(C1 \text{ Sum Average}) - 0.015(C2 \text{ Sum Average}) + 0.004(C2 \text{ Information Measure1}) \\
V3 &= 0.753(C1 \text{ Energy}) + 0.354(C2 \text{ Energy}) + 0.198(C2 \text{ Inverse Difference Moment}) + 0.185(C1 \text{ Inertia}) + 0.184(C2 \text{ Inertia}) + 0.181(C1 \text{ Inverse Difference Moment}) + 0.181(C2 \text{ Difference Variance}) + 0.173(C1 \text{ Difference Variance}) + 0.132(C2 \text{ Sum Variance}) + 0.127(C1 \text{ Sum Variance}) - 0.114(C2 \text{ Correlation}) + 0.104(C2 \text{ Sum Average}) + 0.104(C1 \text{ Sum Average}) - 0.101(C1 \text{ Correlation}) + 0.076(C1 \text{ Information Measure1}) - 0.075(C2 \text{ Information Measure2}) + 0.063(C2 \text{ Information Measure1}) - 0.054(C2 \text{ Entropy}) - 0.047(C1 \text{ Information Measure2}) - 0.046(C2 \text{ Sum Entropy}) + 0.04(C1 \text{ Difference Average}) + 0.038(C2 \text{ Difference Average}) - 0.009(C1 \text{ Difference Entropy}) - 0.008(C1 \text{ Sum Entropy}) + 0.007(C1 \text{ Entropy}) - 0.005(C2 \text{ Difference Entropy}) \\
V4 &= -0.405(C1 \text{ Correlation}) + 0.342(C1 \text{ Inverse Difference Moment}) + 0.325(C2 \text{ Inverse Difference Moment}) - 0.268(C1 \text{ Inertia}) - 0.26(C2 \text{ Inertia}) - 0.24(C1 \text{ Sum Average}) - 0.239(C2 \text{ Sum Average}) + 0.228(C2 \text{ Difference Variance}) + 0.221(C1 \text{ Difference Variance}) + 0.22(C2 \text{ Sum Variance}) + 0.192(C2 \text{ Difference Average}) + 0.175(C1 \text{ Difference Average}) - 0.171(C1 \text{ Energy}) + 0.167(C1 \text{ Sum Variance}) + 0.135(C1 \text{ Difference Entropy}) + 0.132(C2 \text{ Difference Entropy}) - 0.098(C2 \text{ Correlation}) + 0.093(C1 \text{ Sum Entropy}) + 0.081(C1 \text{ Entropy}) + 0.072(C1 \text{ Information Measure2}) - 0.068(C2 \text{ Energy}) - 0.061(C2 \text{ Information Measure1}) + 0.058(C2 \text{ Sum Entropy}) - 0.053(C1 \text{ Information Measure1}) + 0.053(C2 \text{ Entropy}) + 0.045(C2 \text{ Information Measure2})
\end{aligned}$$

Figure 5.22: List of PCs and Descriptors of hMSCs Cultured with Pharmacological Inhibitors

List of principal components (V1, V2, V3, V4) with corresponding descriptors and linear weights that account for > 95% of the variance between hMSCs cultured in OS medium supplemented with pharmacological inhibitors for RhoA, β -catenin, and FAK for 3 days by evaluating 26 Haralick texture features.

5.4.7 Tracking Microenvironment-Mediated Osteogenic Differentiation Using Haralick Texture Features of SC-35 Domains

On the basis of our findings, we propose a model for tracking microenvironment-modulated osteogenic differentiation using SC-35 as a surrogate marker (**Figure 5.23**). According to this model, microenvironmental cues investigated in this manuscript including soluble growth factors, fibrous scaffolds, patterned substrates, and micropillars steer hMSCs towards osteogenic differentiation by 14 days by influencing early cytoskeletal dynamics and intracellular signaling pathways mediated by Rho, FAK, and β -catenin. These signaling cascades induce changes in the transcriptional machinery, thereby modulating the gene expression and SC-35 organizational dynamics. Our model proposes that the effect of microenvironmental cues on stem cell phenotype be tracked using SC-35 organizational metrics at 3 days (**Figure 5.23**).

In this study, the organization of SC-35 domains in hMSCs exposed to the various conditions presented was quantified by using Haralick texture features, which resolve higher-order organizational features [266]. Based on neighboring pixel intensity within confocal images, 13 different Haralick texture features were computed (**Table 5.2**) using two different pixel grouping (termed C1 and C2), resulting in 26 Haralick texture features in total, which were dimensionally reduced using PCA. The principal components were then taken as inputs for a J48 decision tree classifier to create a predictive classification model (**Figure 5.6 - 5.10**).

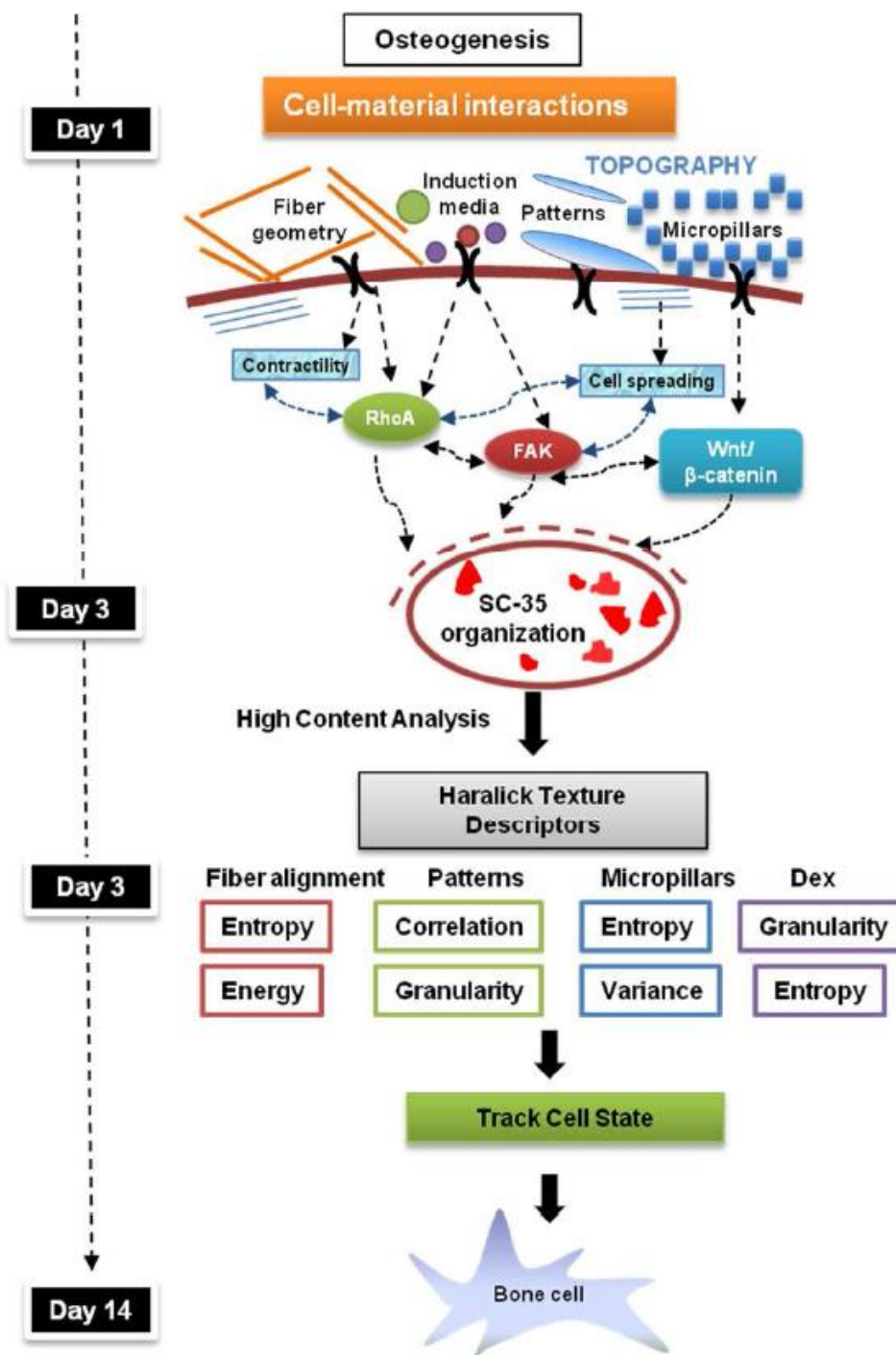


Figure 5.23: Tracking Microenvironment-Modulated Osteogenic Differentiation Using SC-35

Cell-material interactions induce osteogenic differentiation by modulating actin dynamics and signaling cascades mediated by RhoA, FAK, and β -catenin signaling. These

signaling cascades direct changes in the transcriptional machinery that regulate the gene expression and cell phenotype. Our study indicates that SC-35 organizational dynamics are sensitive to these changes and can be used to track osteogenic lineage commitment at early time-points in response to cell-material interactions.

These descriptors can be sub-classified into four groupings: entropy, correlation, granularity, and inertia, which represent a measure of speckle homogeneity, elongation, size, and distribution with respect to nuclear centroid, respectively. The potential biological relevance for each feature has been listed in **Table 5.2**. The contribution of individual descriptors was evaluated by measuring information gain with respect to each condition, using the Weka machine learning software. The top 10 descriptors were ranked on the basis of information gain and listed for each condition in **Table 5.3** and **Table 5.4**. Our attribute evaluation indicated that granularity and entropy descriptors were the most informational texture descriptors accounting for changes in the SC-35 organization in response to soluble cues. Interestingly, the most informational SC-35 organizational Haralick descriptors were different for hMSCs cultured on the distinct topographical platforms. Correlation and granularity descriptors had the maximum information gain about SC-35 organizational dynamics in hMSCs cultured on surface topographies featuring different degrees of continuity (patterns), while entropy and variance descriptors were most informational about SC-35 dynamics in hMSCs cultured on the micropillars. In contrast, on fibrous scaffolds, entropy descriptors provided maximum information gain about SC-35 organizational changes (**Table 5.4**).

These findings show that interactions of hMSCs with different microenvironmental cues lead to specific and distinct emergent patterns of SC-35 descriptors that govern the divergent osteogenic differentiation traits as early as 3 days.

Granularity + Entropy

Media: BA vs. AD vs. OS

Information Gain	Normalize	Haralick Descriptor
1.3308	0.136853	C1 Inverse Difference Moment
1.0881	0.111895	C2 Sum Average
1.0881	0.111895	C1 Sum Average
0.834	0.085765	C1 Entropy
0.834	0.085765	C2 Entropy
0.834	0.085765	C2 Sum Entropy
0.7809	0.080304	C2 Difference Entropy
0.7809	0.080304	C2 Information Measure 2
0.7266	0.07472	C1 Sum Entropy
0.721	0.074144	C2 Information Measure 1
0.7059	0.072591	C2 Difference Average

Granularity + Entropy

Media: BA vs. dex low vs. dex med vs. dex high

Information Gain	Normalize	Haralick Descriptor
1.0761	0.100903	C1 Difference Average
1.0608	0.099468	C2 Energy
1.0274	0.096337	C2 Difference Average
1.026	0.096205	C2 Difference Variance
0.9619	0.090195	C2 Inverse Difference Moment
0.9515	0.08922	C1 Difference Entropy
0.9474	0.088835	C1 Difference Variance
0.9351	0.087682	C2 Information Measure 1
0.9314	0.087335	C1 Sum Variance
0.9105	0.085375	C2 Sum Variance
0.8366	0.078446	C1 Information Measure 1

Table 5.3: Summary of Most Significant Haralick Features Across Growth Factor Conditions

Summary of most significant Haralick features across different growth factor conditions (i.e., adipogenic, osteogenic induction medium, and varying levels of dexamethasone). The features are divided into four groupings: entropy (red), correlation (blue), granularity (purple), and inertia (green), which represent a measure of speckle homogeneity, elongation, size, and distribution with respect to nuclear centroid, respectively.

Correlation + Granularity

Topography: flat vs. cont. vs. discount.

Information Gain	Normalize	Haralick Descriptor
0.458	0.137331	C2 Correlation
0.422	0.126537	C1 Correlation
0.332	0.09955	C1 Inverse Difference Moment
0.312	0.093553	C2 Sum Average
0.312	0.093553	C1 Sum Average
0.302	0.090555	C1 Inertia
0.285	0.085457	C2 Inertia
0.271	0.081259	C2 Energy
0.22	0.065967	C1 Difference Variance
0.212	0.063568	C1 Sum Variance
0.209	0.062669	C1 Difference Average

Entropy + Correlation

Topography: small ali/rdm vs. large ali/rdm

Information Gain	Normalize	Haralick Descriptor
0.794	0.125653	C2 Energy
0.793	0.125495	C1 Entropy
0.71	0.11236	C1 Sum Entropy
0.649	0.102706	C1 Information Measure 2
0.588	0.093053	C1 Difference Entropy
0.574	0.090837	C2 Entropy
0.486	0.076911	C2 Difference Entropy
0.469	0.074221	C2 Sum Entropy
0.459	0.072638	C2 Information Measure 2
0.42	0.066466	C2 Information Measure 1
0.377	0.059661	C1 Information Measure 1

Entropy + Granularity

Topography: topographical micropillars

Information Gain	Normalized	Haralick Descriptor
0.309	0.0489	C1 Mean Energy
0.265	0.041937	C1 Mean Sum Variance
0.245	0.038772	C2 Mean Sum Variance
0.236	0.037348	C1 Mean Difference Variance
0.225	0.035607	C1 Mean Entropy
0.219	0.034657	C2 Mean Difference Variance
0.205	0.032442	C1 Mean Difference Average
0.189	0.02991	C1 Mean Information Measure 1
0.185	0.029277	C2 Mean Energy
0.175	0.027694	C1 Mean Information Measure 2
0.147	0.023263	C2 Mean Difference Average

Table 5.4: Summary of Most Significant Haralick Features Across Different Topographies

Summary of most significant Haralick features across different topographies (i.e., surface texture, fibrous scaffolds, micropillar topographies). The features are divided into four groupings: entropy (red), correlation (blue), granularity (purple), and inertia (green), which represent a measure of speckle homogeneity, elongation, size, and distribution with respect to nuclear centroid, respectively.

5.5 DISCUSSION

In this study, we have developed and demonstrated the applicability of an integrated framework based on high content image informatics to develop predictive classification models that can discern and classify changes in cell state in response to cell-microenvironment interactions.

First, different nuclear proteins (i.e., SC-35, EZH2, RUNX2, lamin, and H3K4me3) were screened to determine how their nuclear organization was influenced at early time-points upon initiation of growth factor-induced differentiation. Our results showed that SC-35 organization was maximally influenced early on (3 days) during the differentiation process. By employing the algorithm presented in this paper, SC-35 organization could be used to generate a predictive model to classify cells exposed to basal, osteogenic, and adipogenic induction media with a positive predictive value of 96%. Further, using SC-35 organization metrics hMSCs exposed to different concentrations of soluble cues, specifically dexamethasone (*dex*), an osteogenic differentiation factor, could be parsed with > 90% precision and sensitivity. This correlated with an upregulation of SC-35 genes during osteogenic induction (**Figure 5.5**).

These findings show that SC-35 domains are highly sensitive to activation via growth factors that steer hMSCs towards distinct lineages. Several accounts of literature suggest that spliceosomes within the SC-35 domains aggregate at the active transcription sites of genes regulating the differentiation of several lineages, including adipogenesis [145], osteogenesis [146], and myogenesis [147]. When transcription is halted via the use of pharmacological inhibitors, splicing factors aggregate into large,

round speckles [195]. In contrast, when transcription is high, the accumulation of splicing factors is reduced, and they redistribute to nucleoplasmic transcription sites [198]. Another notable property of SC-35 domains is that the domains reside in interchromatin regions, which contain little or no DNA [193]. Consequentially, the organization of SC-35 domains may serve as an indirect measure of global chromatin changes regulated by outside-in signaling which links focal adhesions, actin, and the nuclear space.

Biomaterial topography effectively regulates stem cell differentiation by modulating cell-shape [251]. Thus, we sought to elucidate the degree to which SC-35 organization was sensitive to three variable osteogenic microtopographies: surface patterns, fibrous scaffolds, and micropillars. Surface-induced phase separation can be utilized to produce well-defined, easily replicated, and well-characterized surfaces presenting a wide range of topographical features [262]. Here, this fabrication method was adapted to construct surfaces with three distinct patterns: flat, continuous ridges, and discontinuous islands and pits. Our results indicate that osteogenic differentiation is enhanced by hMSCs sensing continuous surfaces. This correlates with previous studies where osteogenic differentiation mediated by β -catenin signaling has been shown to be regulated on grooved surfaces [267]. Furthermore, using SC-35 organization nuclear metrics, the influence of surface topography on osteogenic differentiation could be predicted with > 90% precision and sensitivity.

Next, we applied our high content imaging methodology to predict the differentiation potential of hMSCs cultured on microfibrillar scaffolds prepared by

electrospinning [83, 268, 269]. Electrospun fibrous scaffolds were chosen since they have wide applicability for bone tissue engineering applications [270-272]. Fibers with a larger diameter of 5 μm induced significant osteogenic differentiation in hMSCs ($p < 0.01$) as compared to fibers with a smaller diameter of 2 μm , indicating that the variations in the chosen fiber scaffold geometries modulate osteogenic differentiation. These results are consistent with electrospun fiber geometries reported to regulate osteogenic differentiation [273]. By exposing hMSCs to various growth factors and topographies, we have demonstrated that the onset of osteogenic differentiation on a diverse set of culture conditions can be predicted by mapping early SC-35 organizational features.

There has also been an increased interest in characterizing the role of bulk substrate properties on the differentiation of stem cell populations. In the context of bone, biomaterials with high elastic modulus featuring different topographical patterns have been investigated [274]. Previously, an algorithm-based approach was developed to produce chips featuring over 2,000 micropillars in efforts to identify topographies that maximize mitogenic and osteogenic responses [91]. This study identified "hit" surfaces that corresponded to high alkaline phosphatase expression without the presence of osteogenic growth factors, but the methods presented relied on a population-based readout at a late time-point (10 days) that may not account for potential heterogeneous responses within a particular topographical condition.

As such, we applied our methodology to classify hMSCs cultured on a subset of micropillars chosen from a library of 2,176 distinct, randomly designed surface

topographies using methods previously published [91]. We chose topographies based on their ability to induce varying percentages of ALP positive cells without the presence of *dex* after 14 days in culture. Using our high content analysis, we correctly identified individual cells as belonging to either of four micropillars. Using the classification algorithm based on SC-35 organization, we could predict topography-induced ALP expression as well as quantitatively identify differences in cell state within a culture condition, for example, cells cultured in TopoD, the least ALP-inducing condition, were parsed 80% correctly as cells on TopoD and 20% as cells on TopoB, which induced a significantly higher percentage of ALP positive hMSCs. This is of particular interest when performing studies with cell lines that are innately heterogeneous.

Microenvironmental cues, specifically soluble factors, topography, and substrate surface functionality, have been shown to modulate hMSC differentiation through β -catenin [267, 275], FAK [276, 277], and RhoGTPase [278], which are key signaling molecules that direct osteogenic differentiation [133, 279, 280]. Surface topography modulates Wnt and β -catenin signaling through primary cilia structure [267], and increased Wnt/ β -catenin is observed in hMSCs cultured on rough topographies [281]. Recently, FAK has been implicated in the modulation of hMSC differentiation by microenvironmental cues such as substrate surface functionalities [276] and microtopographies [277], where RhoGTPase has been shown to regulate osteogenesis through fiber geometries [278]. FAK and RhoA have also been shown to positively regulate osteogenesis [282] and negatively regulate adipogenesis of hMSCs using induction medium [283].

An initial microarray analysis of hMSCs cultured in osteoinductive medium for 24 hours showed a significant increase ($p < 0.05$) in RhoA and FAK gene expression as compared to cells cultured in basal medium, which correlated with a significant upregulation ($p < 0.05$) of SC-35 gene expression (**Figure 5.24**). To obtain a more comprehensive understanding of how SC-35 organization is regulated during differentiation, we investigated the influence of β -catenin, FAK, and RhoGTPase-mediated signaling on SC-35 domains. Using our algorithm, SC-35 organization was highly sensitive to specific inhibition of these molecules. Changes in cell state upon inhibition of β -catenin, FAK, and RhoGTPase could be detected and classified with $> 95\%$ precision using our SC-35 imaging-based methodology. This suggests a possible mechanism for how SC-35 organization is responsive to osteogenic differentiation via osteogenic signaling molecules.

In summary, our results indicate that microenvironmental cues affect key signaling molecules, which modulate both the early organization of SC-35, as well as long-term stem cell lineage commitment.

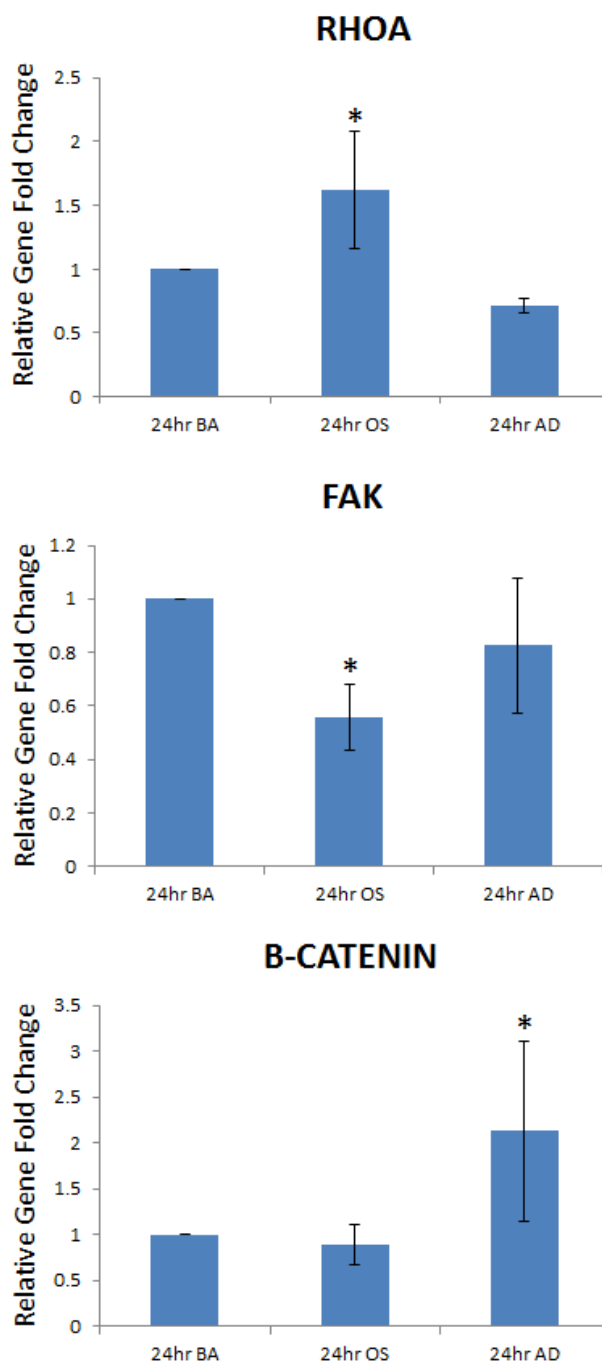


Figure 5.24: Microarray Analysis of RhoA, FAK, and β -Catenin Expression in hMSCs Cultured in BA, AD, and OS Media

hMSCs were cultured in differentiation medium for 24 hours, and the relative gene expression of RhoA, FAK, and β -catenin for hMSCs cultured in AD or OS medium was

analyzed with respect to BA using microarray analysis at 24 hours. Statistical analysis was done using ANOVA where the gene expression in cells cultured in AD or OS medium was statistically compared to gene expression in the BA condition. * indicates statistical significance ($p < 0.01$).

5.6 CONCLUSIONS

In conclusion, we have advanced a methodology based on high content imaging of SC-35 organization in the nucleoplasm, in concert with machine learning approaches, for predictive modeling of hMSC differentiation mediated by various microenvironmental cues (differentiation medium, soluble factors, and substrate topography). The SC-35 parsing approach could successfully detect and classify hMSC differentiated phenotypes on different surface topographies and microfiber geometries (fibrous scaffolds and micropillars). Further, SC-35 organization can capture changes in cell state modulated by signaling molecules involved in osteogenic differentiation, specifically RhoGTPase, FAK, and β -catenin. Such a predictive model may elucidate emergent lineage restrictions in more complex microenvironments and also provide *in silico* informatics of stem cell lineages on biomaterials that steer stem cells toward strategic, regenerative phenotypes.

CHAPTER 6. SUMMARY AND FUTURE DIRECTIONS

6.1 RESEARCH SUMMARY

The overarching goal of this thesis dissertation is to develop single cell biological imaging and machine learning techniques to identify the heterogeneity of stem cell cultures and characterize responses to controllable changes in diverse microenvironments. These objectives help address two significant needs that limit the use of stem cells in regenerative therapies today: (1) improved methods of identifying the phenotypic and functional heterogeneity inherent in stem cell cultures, and (2) classification of long-term stem cell responses to microenvironmental cues at earlier times than current screening methods.

The development and application of the imaging-based methodology presented in this thesis dissertation is predicated on the notion that the cell's pericellular matrix propagates signals from the outside-in that result in structural changes to cell shape and various mechanoresponsive cytoskeletal and nuclear elements. These biological observations reported by many laboratories, in conjunction with *in silico* data processing techniques, gave us the tools and motivation to test our central hypothesis: quantitative metrics descriptive of cytoskeletal and nuclear proteins involved in outside-in signaling can define cell states mediated by microenvironmental cues.

In this thesis dissertation we report that single cell imaging-based profiling of cytoskeletal actin and nuclear mitotic apparatus (NuMA) protein can identify single cell phenotypes in different stem cell populations. We found that actin organization could identify minute distinctions in the phenotypes of human mesenchymal stem cells (hMSCs) cultured on polymeric films and substrate gradients that induce varying

degrees of osteogenic and adipogenic differentiation. We also demonstrate that NuMA organizational features were able to distinguish self-renewing subpopulations of human embryonic and induced pluripotent stem cells from heterogeneous populations, showcasing our ability to identify heterogeneity, a current challenge that limits the use of stem cells in the clinic.

Next, we apply our imaging-based methodology to identify phenotypic and functional heterogeneity in three diverse applications that have potential impact in tissue engineering. As a screening tool, we predict the oncogenicity of a biomaterial library by showing a high-degree of correlation between early NuMA metrics and long-term hMSC telomerase activity. As a classification tool, we identify three neural precursor cell populations extracted from different murine brain regions *ex vivo* that have identical antigen expression but divergent proliferation and differentiation profiles. Lastly, as a cell sourcing tool, we use mCherry-NuMA metrics of live cells to identify and remove unwanted DNA-damaged cells in co-cultures, resulting in an increase of population viability after pharmacological treatment with an agent that targets DNA-damaged cells.

This thesis dissertation also shows that single cell imaging-based profiling is capable of identifying long-term stem cell responses to microenvironmental cues at earlier times than conventional methods. We report that the early (3 day) organization of SC-35 domains, which host post-transcriptional machinery within the interchromatin regions of the nuclear space, vary in hMSCs exposed to a variety of growth factor combinations that induced divergent phenotypic outcomes. As a biomaterial screening

tool, we could also classify via SC-35 imaging the extent of 14 day osteogenic differentiation commitment across a series of surface patterns and fibrous scaffolds. A subset of osteogenic-inducing biomaterials derived from a much larger combinatorial library of micropillar topographies were also explored setting the stage for the exploration of thousands of conditions within one experiment, expediting the discovery of desired structure-function relationships.

In summary, the work presented here shows that single cell imaging-based profiling can be utilized as a robust screening platform to identify cell subtypes in heterogeneous stem cell cultures and predict microenvironment-induced differentiation fates at earlier times and with more resolution than current screening assays.

In order to advance this work, several limitations must be addressed. The intracellular mechanisms that direct observed condition-dependent changes in morphology are not well understood. We hypothesize that actin mediates outside-in signaling from the microenvironment onto the nucleus. As such, studying dynamic changes to actin in response to microenvironmental cues will enhance our understanding of these mechanisms (**Section 6.2.1**). Additionally, although our imaging-based profiling tool provides us with information-rich single cell readouts, it is time-consuming. Thus, by implementing microscopy-based profiling approaches of adherent cells to flow-based systems, a screening tool can be developed that is both high content and high-throughput (**Section 6.2.2**).

6.2 FUTURE DIRECTIONS

6.2.1 Actin Morphology and Signaling Kinetics: A Systems Biology Approach

The cellular microenvironment (soluble growth factors, biomaterial properties) directly affects stem cell morphology and differentiation. Biomaterials exhibiting a wide range of physicochemical properties have been investigated for potential use in guiding stem cell adhesion, proliferation, and differentiation [284, 285]. Although these studies have identified preferred biomaterial-induced stem cell behaviors, cellular signaling pathways initiated by these culture conditions are not well understood. To clarify these mechanisms, computational models have been used to aid in identifying intracellular interactions at the genomic level, with nominal success [286-289]. One of the most recent and comprehensive "first draft" whole-cell computational models conceived includes all molecular interactions of the 525 gene *Mycoplasma genitalium*. Despite the small size of the *M. genitalium* genome, the model is highly complex, consisting of 28 submodels constructed using various computational methods [290].

Due to the genomic, proteomic, and metabolic complexity of stem cells and progenitor cells, a whole-cell computational model using computational tools currently available is not feasible. This thesis dissertation postulates that actin acts as the mediator of signal propagation from the pericellular matrix to the nucleus. To support this hypothesis, quantifying temporal changes of actin and signaling molecules known to directly influence cytoskeletal organization is more sensible than a whole-cell computational modeling approach. RhoA and Rac1, two central members of the Ras GTPase superfamily, regulate the assembly of stress fibers and lamellipodia, respectively

[154, 291]. By determining the interplay between GTPase proteins and actin morphology, we will have a stronger grasp on why particular cytoskeletal and nuclear morphological features identify cell phenotypes and precede microenvironment-induced differentiation.

To probe the dynamic interactions between actin and GTPase proteins, three studies are proposed: (1) time-course study to determine when (< 3 day) actin descriptors capture morphological differences between two divergent culture conditions, (2) quantification of temporal changes in GTPase expression using time-points determined in (1), and (3) study effects of pharmacological perturbations (e.g., the inhibition or activation of actin polymerization) on actin dynamics. Preliminary data from these studies shows that single cell profiling of actin descriptors can identify stem cells cultured in conditions resulting in divergent phenotypic outcomes at much earlier times than the 3 days we report in this dissertation. Additionally, we found a lag between condition-dependent changes in RhoA expression and actin organization.

To fortify the role of cytoskeletal and nuclear descriptors as early identifiers of cell state, future work needs to focus on how these proteins change temporally in response to controlled perturbations in the culture environment. Results from these future studies will help develop improved single cell imaging-based profiling tools to identify cell subtypes and characterize cellular responses to biomaterials with potential utility in regenerative medicine.

(1) Actin morphology time-course study.

hMSCs were cultured on 12 mm glass coverslips in BA growth medium, and fixed/stained for actin at various time-points post-plating. Qualitative observations of the actin morphology show a high level of lamellipodia formation around the periphery of the cells at 30 minutes post-plating (**Figure 6.1A**). As culture time progresses, cells spread, and actin stress fibers begin to form (**Figure 6.1B - 6.1C**). From these preliminary observations we expect high Rac1 expression at early time-points (i.e., within the first 3 hours post-plating). Then, after 3 hours we expect RhoA expression to increase, while Rac1 expression decreases, until they each reach steady-state by 3 days post-plating.

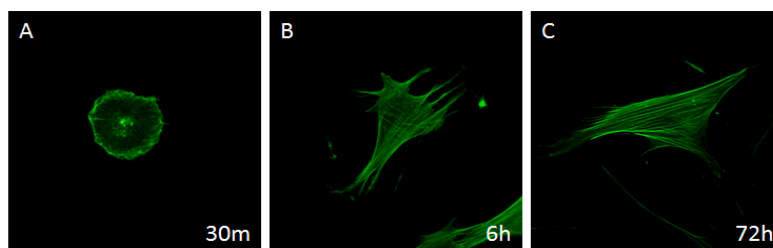
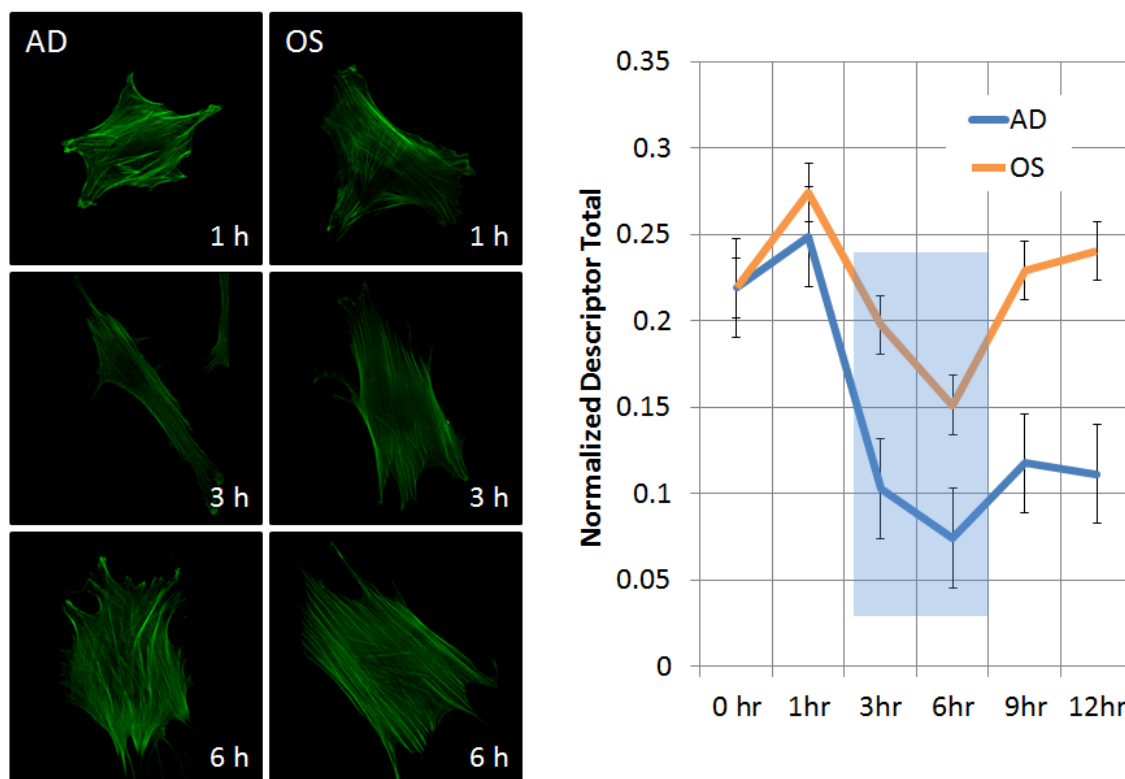


Figure 6.1: Evolution of Actin Polymerization of an hMSC for 3 Days

Following the same culture protocol, we cultured hMSCs for 24 hours in basal medium, switched to either adipogenic (AD) or osteogenic (OS) induction medium, and fixed/stained for actin at various time-points. **Figure 6.2** shows representative actin images of hMSCs in AD (left images in panel) and OS (right images in panel) induction medium for 1, 3, and 6 hours. To determine when actin descriptors begin to parse these two divergent culture conditions, single cell imaging-based profiling was utilized to plot a normalized descriptor distribution for each time-point (plot in **Figure 6.2**). We found

that the descriptors between AD and OS culture conditions began to diverge in as little as 3 hours after treatment.

In this dissertation we show that 3 day morphological descriptors can accurately identify phenotypic outcomes from culture conditions across a wide range of growth factor and biomaterial conditions. Although our approach can classify differentiation outcomes much sooner than conventional assays, the results from this preliminary study suggest that morphological differences arise even faster than the 3 days that we report.



(Graph) Descriptor analysis shows that actin morphology can parse between the AD and OS culture conditions in as little as 3 hours. Light blue box denotes time frame of interest based on these preliminary results. The differences in descriptors between the two culture conditions persist for the remaining time-points.

(2) Quantification of temporal changes in GTPase expression.

To determine whether differences in actin morphology in as little as 3 hours post-AD and OS media treatments (**Figure 6.2**) also corresponds to changes in GTPase expression, we repeated the study and in lieu of fixing/staining for actin, lysed the cell cultures and used Western Blotting to determine RhoA expression (**Figure 6.3**). Western Blot bands at 3 hour and 6 hour time-points of hMSCs cultured in AD or OS medium show that RhoA expression is comparable between both AD and OS conditions at 3 hours. However, at 6 hours there is a drop in RhoA expression in the AD condition, and an increase in the OS condition. Even though we found descriptor differences at 3 hours after AD and OS treatment, RhoA expression only changed at the 6 hour time-point.

One possibility for this observation could be that condition-dependent changes in actin morphology precede RhoA expression. This speculation contradicts previous findings that suggest RhoA expression is a precursor of actin polymerization [133]. Due to the dynamic nature of actin and GTPases it is possible that they both affect each other simultaneously. To decouple actin morphology and GTPase expression, pharmacological agents could be introduced to affect actin (i.e., polymerize or depolymerize) and/or RhoA (i.e., inhibit or enhance expression) independently.

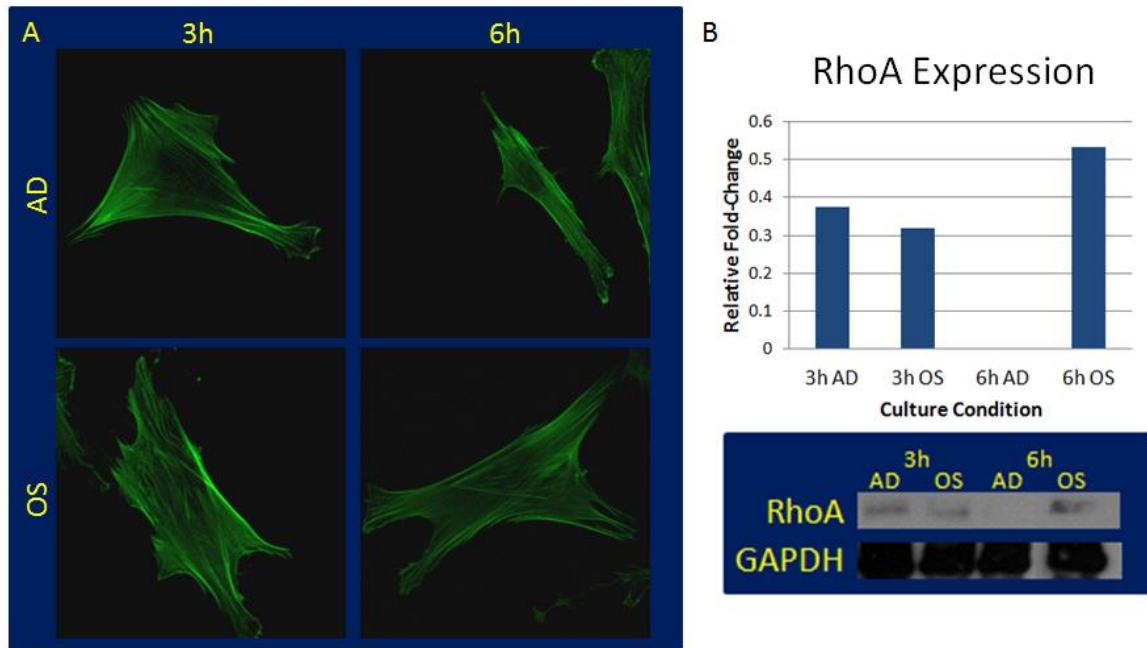


Figure 6.3: RhoA Expression Undergoes Temporal Media-Dependent Changes

(A) hMSCs cultured in AD or OS induction medium for either 3 or 6 hours. **(B)** Relative fold-change (using an osteogenic control) shows no significant changes between AD and OS culture conditions at 3 hours, but at 6 hours a significant decrease and increase in RhoA expression for AD and OS conditions, respectively.

(3) Effects of pharmacological perturbations on actin dynamics.

In order to develop perturbation protocols to decouple RhoA expression from actin morphology, hMSCs were cultured on 12 mm glass coverslips, and C3 transferase, a RhoA inhibitor, was introduced to the cell cultures. Next, the actin cytoskeleton was qualitatively observed at different time-points (**Figure 6.4**). 30 minutes after introducing the inhibitor, actin was not significantly disrupted. However, polymerized actin was significantly affected after 3 and 6 hours post-RhoA inhibition. This lag in response

coincides with the time it took to observe changes in actin morphology in response to AD and OS treatments in as little as 3 hours (**Figure 6.2**) and differences in RhoA expression observed at 6 hours (**Figure 6.3**). Taken together, these preliminary findings show that: (1) actin morphology can be affected by differentiation-inducing soluble cues in as little as 3 hours post-induction, (2) RhoA expression by these same cues is different in as little as 6 hours post-induction, and (3) pharmacological inhibitors have the potential to decouple actin and GTPase proteins to better understand the role of actin dynamics in identifying the predilection for cellular phenotypes.

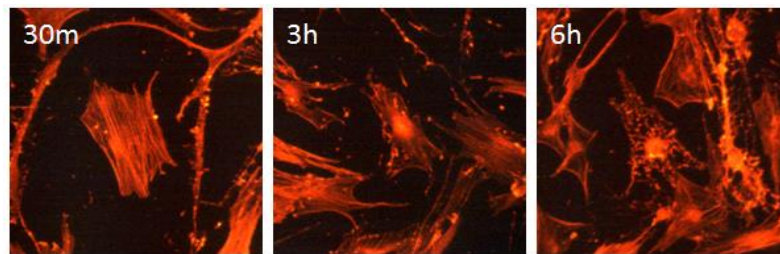


Figure 6.4: Preliminary Pharmacological Inhibitor Study

hMSCs were exposed to 2 $\mu\text{g}/\text{mL}$ of C3 transferase, fixed/stained with Texas Red phalloidin, and imaged at several time-points (30 minutes, 3, and 6 hours post-plating).

6.2.2 High Content and High-Throughput Profiling of Live Cell Cultures

One fundamental limitation preventing the extensive use of stem cells in the clinic is the inability to differentiate cells into homogeneous populations of desired phenotypes [246, 247]. With the use of differentiation-inducing growth factors, populations of naïve human mesenchymal stem cells (hMSCs) only achieve upwards of 75% osteoblast and 40% adipogenic differentiation [47]. Additionally, the clinical use of neural stem cells (NSCs) has been limited due to the inability of separating NSCs from other cell types when derived from native tissues [248]. By reducing heterogeneities nascent to hMSC and NSC populations, mature cell phenotypes could be isolated and expanded to allow for their use in regenerative therapies.

Currently, two types of imaging-based cell sorting platforms are prominently used in cell sorting applications: laser capture and microdissection (LCM) and fluorescence-activated cell sorting (FACS). LCM is a microscopy technique used for purifying cell subtypes from heterogeneous tissue sections or live cell cultures [292]. This is accomplished by either cutting out a "raft" of polyethylene terephthalate (PET) membrane directly under cells of interest, or by utilizing laser ablation to remove unwanted cells. In contrast, fluorescence-activated cell sorting (FACS) is a technique that utilizes the principle of flow-based cytometry to isolate a homogeneous cell population of interest from an otherwise heterogeneous sample [293]. Live cells in suspension are passed through a detector at a rate exceeding thousands of cells per second, which allows the user to set gating criteria for several detector channels (i.e., forward scatter, side scatter, and fluorescence) [294]. Individual cells that pass through the detectors are

charged if they meet user-specified criteria. Based on the charge of the cell, the cells can then be sorted into separate groupings [293].

Unfortunately, several shortcomings are associated with sorting cells from heterogeneous populations via LCM and FACS. Since LCM is microscopy-based, it can be adapted to provide sorting criteria based on high content information. Although rich in information about cell state, this method has low throughput in comparison to flow-based systems. In contrast, FACS is extremely high-throughput (capable of sorting up to thousands of cells per second), but the sorting criteria is low in information (i.e., forward scatter, side-scatter, and a handful of spectral bands) in comparison to the capabilities of LCM, which can be tailored to acquire hundreds of morphological descriptors per cell.

In order to address the limitations of current cell sorting systems, future work needs to focus on combining the rapid screening of FACS with the information-rich capabilities of LCM. To test the effectiveness of a single cell imaging-based system that is both high-throughput and high content, it is necessary to discover new cell subtype-specific descriptors using high content (i.e., LCM) and high-throughput (i.e., FACS) sorting systems, and culture and differentiate isolated cell subtypes to assess sorting efficiency. Two candidate high content and high-throughput screening tools, respectively are proposed: laser capture and microdissection (LCM) and fluorescence-activated cell sorting (FACS), which will be discussed in more detail below.

(1) High content cellular profiling: laser capture and microdissection (LCM)

For the LCM portion of this study, hMSCs fluorescently labeled with actin, NuMA, and SC-35 will be cultured on PET membrane slides (Zeiss). These cultures will be treated with a 50:50 solution of adipogenic/osteogenic induction medium. Next, using the LCM microscope's (Zeiss PALM) CCD camera, images of the live cell cultures will be acquired, and a Matlab-based script will be used to identify regions of interest (ROIs) to extract single cell morphologic descriptors in real-time. These descriptors will serve as test sets for a classifier that will determine whether or not cells are designated to be ablated (**Figure 6.5B**). To assess the efficacy of this sorting strategy, hMSCs will be cultured for 14 days and differentiation assays will be used to compare differentiation relative to a no-treatment group. Using LCM, we were able to selectively remove one cell from a population, without affecting surrounding cells, as seen in a proof-of-concept demonstration summarized in **Figure 6.6**.

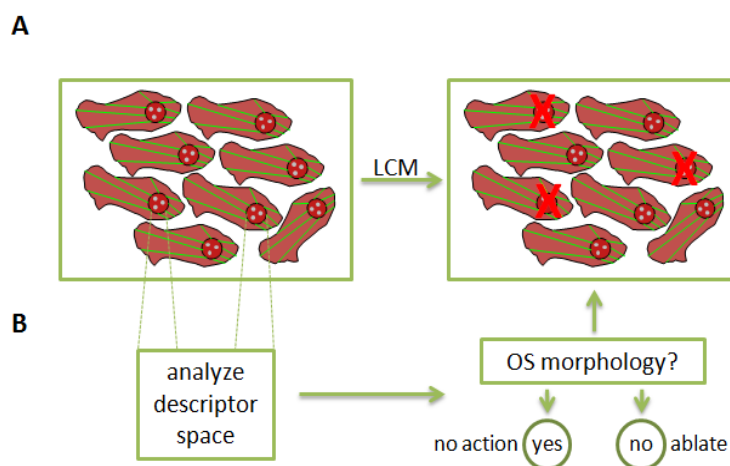


Figure 6.5: Schematic of LCM Workflow

(A) hMSCs labeled with fluorescent reporters (e.g., actin, green; NuMA, red) cultured on PET membranes are subject to laser ablation based on descriptors of reporter proteins.

(B) Descriptors from reporter proteins are acquired, and compared to an existing database of lineage-specific descriptors. If cells are categorized as phenotype of interest (e.g., osteoblast, OS), then no action is taken; otherwise, cell nucleus is ablated (denoted by red X's in **(A)**).

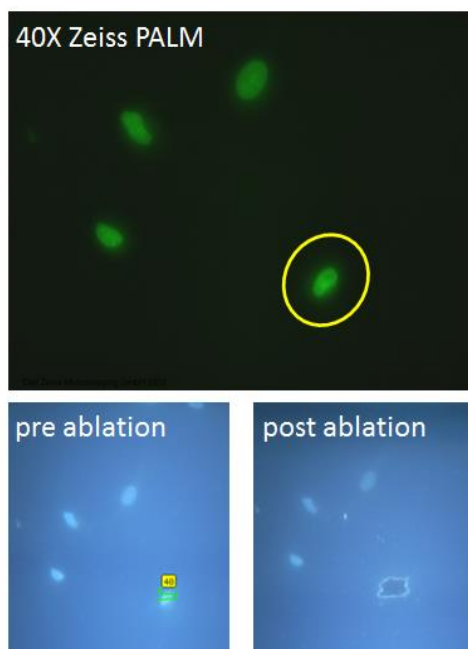


Figure 6.6: Zeiss PALM used to selectively ablate MSCs

hMSCs were cultured on a PET polymer and then imaged with a Zeiss PALM LCM microscope (top image). A cell was selected (yellow circle) and then the laser was used to remove the cell, while keeping the other cells intact (bottom images).

(2) High-throughput cellular profiling: fluorescence-activated cell sorting (FACS)

For the FACS portion of the study, cell cultures of two distinct subtypes (e.g., neurons and astrocytes) will be fixed and immunolabeled with reporter proteins (e.g., actin and NuMA). Cells will be placed in suspension, and FACS will be used to identify cell subtype-specific differences in detector channel readouts (e.g., granularity, fluorescence) (**Figure 6.7A**). This gating criteria will be used to categorize and separate cell subtypes in heterogeneous cultures (e.g., tissue sample consisting of neurons and astrocytes) engineered with our reporter proteins (**Figure 6.7B**). Post-FACS treatment, cells will be cultured and assayed for phenotype-specific markers to determine the effectiveness of this sorting approach.

One of the key findings of this thesis dissertation is the ability to attain information-rich datasets to identify cell subtypes and predict biomaterial responses of individual cells. However, one of the caveats is that using conventional microscopes the screening process is time-consuming. Flow-based systems are amongst the fastest systems available for single cell analysis. Therefore, by combining the principles of microscopy and flow, microenvironment-sensitive morphologic descriptors can be derived from single cell imaging of cells in suspension resulting in a profiling system that is both accurate (high content) and rapid (high-throughput).

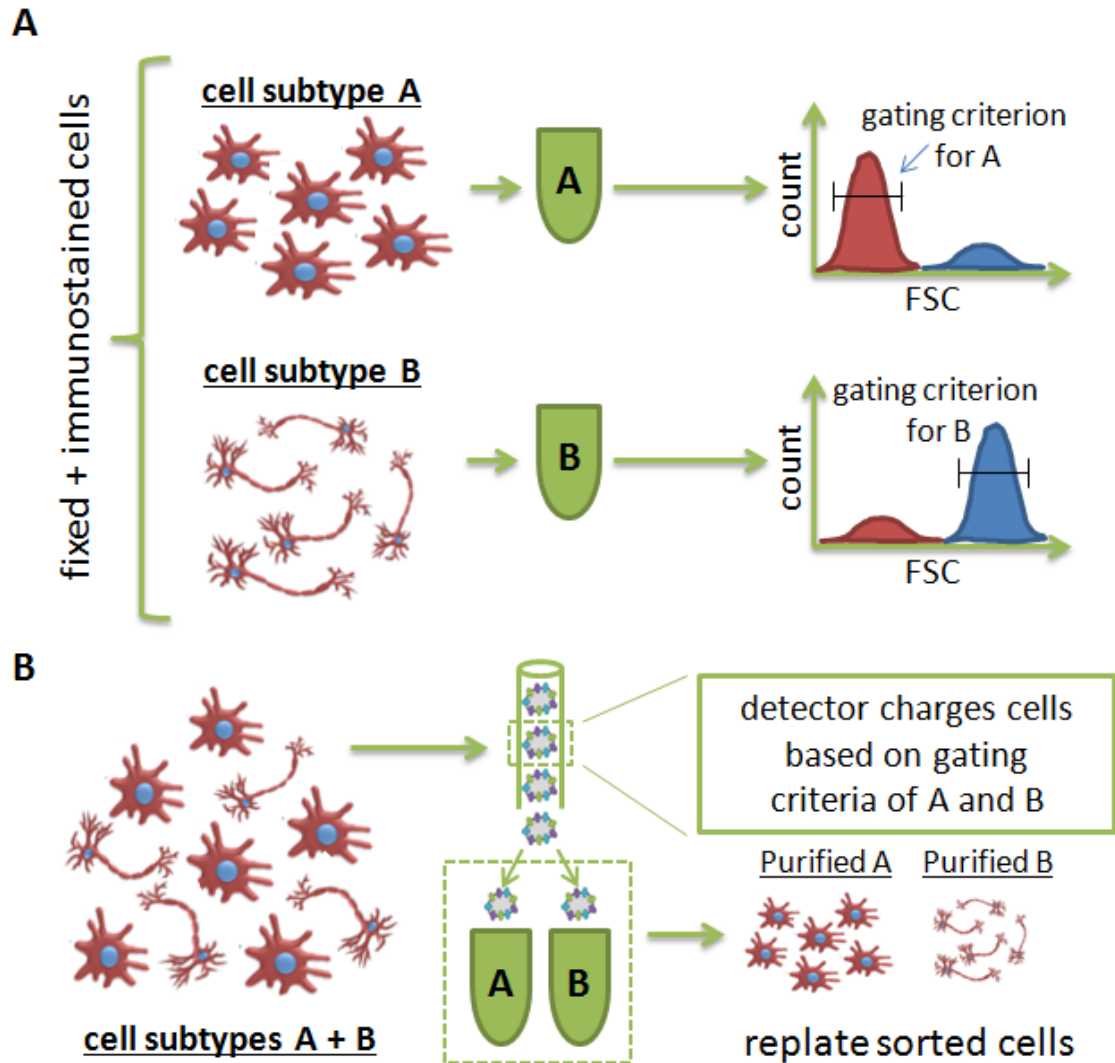


Figure 6.7: Schematic of FACS Workflow

(A) Cells cultured in conditions known to elicit differences in morphology and function (e.g., cell subtypes A and B) will be fixed and immunolabeled for proteins of interest (e.g., actin, NuMA). Cells will then be suspended and flowed through FACS to identify differences in detector channel readouts (e.g., forward- and side-scatter). **(B)** Next, live heterogeneous cell cultures will be suspended and flowed through FACS. Based on gating criteria identified in **(A)**, cells will be sorted into subtypes A and B, and then replated.

6.3 CLOSING THOUGHTS

A major caveat to imaging-based cellular profiling in general is that cell reporters are labeled (i.e., exogenous fluorophores and endogenous genomic modifications), which may have adverse effects on cell behavior. Further, these labeled cells cannot be deployed in a therapeutic workflow. Thus, it is worthwhile to explore options that are minimally invasive to cells in culture. For example, Coherent Anti-Stokes Raman Scattering (CARS) spectroscopy is a non-invasive technique capable of imaging intracellular macromolecules including proteins, lipids, and nucleic acids [295, 296]. The CARS methodology works by applying vibrational bands at specific molecular frequencies capable of identifying spectral bands specific to various macromolecules.

Using non-invasive methods like CARS, live cells can be "digitally stained" in real-time with image sensitivity comparable to imaging resolutions achieved by fluorescence microscopy. By combining the imaging-based methodology presented in this dissertation with CARS-based imaging, it is possible to identify cellular responses to an array of microenvironmental cues on live cells without the introduction of fluorescent probes. Due to a mutual interest in this objective, our laboratory is actively collaborating with Dr. Cicerone's laboratory, which is one of the pioneer labs in CARS technology at NIST. To-date, our collaboration has resulted in a joint publication that highlights the ability of CARS-based imaging in identifying hMSCs cultured in either AD, BA, and OS induction media [296]. Future work in imaging-based label-less cellular profiling has the potential to track single cells, identify phenotypes in heterogeneous cultures, and predict cellular responses to biomaterials, all without perturbing the cells.

CHAPTER 7. APPENDIX

Note: Sections of this chapter have been reproduced from the following publication:

Liu E, Vega S, Treiser MD, Sung H-J, and Moghe PV. (2011) Fluorescence Imaging of Cell-Biomaterial Interactions. In: P Ducheyne, KE Healy, DW Hutmacher, DW Grainger, CJ Kirkpatrick (eds.) Comprehensive Biomaterials, vol. 3, pp. 291-303 Elsevier.

7.1 TOOLS AND TECHNIQUES FOR CELLULAR IMAGING

7.1.1 Epifluorescence and Deconvolution Microscopy

Epifluorescence microscopy, also referred to as wide-field fluorescence microscopy (WFM), is the most commonly used fluorescence microscopy method in life sciences. Fluorescence microscopy allows visualization of cell morphology, cellular/subcellular compartments as well as cellular markers of disease (e.g., cancer versus normal cells) or phenotype (e.g., stem cell lineage). The optics of an epifluorescence microscope are illustrated in **Figure 7.1**. Briefly, light of a specific wavelength (usually in the ultraviolet or blue, green regions of the visible spectrum) is generated by passing multispectral light from an arc-discharge lamp or other source through a wavelength-selective bandpass filter (excitation filter). Selected wavelengths passed by the excitation filter are then reflected from a dichromatic mirror or beamsplitter through the microscope objective to expose the specimen with intense light. If the specimen fluoresces, the emission light gathered by the object passes back through the dichromatic mirror and is subsequently filtered by another bandpass filter (emission filter), which blocks the unwanted excitation wavelengths. Emitted light is then collected by a detector such as a CCD camera.

The application of an array of fluorophores has made it possible to identify cells and subcellular components with a high degree of specificity amidst nonfluorescing material. Through the use of multiple-fluorophore labeling, different probes can simultaneously identify several target molecules. Conventional epifluorescence microscopy can also be used to visualize three-dimensional samples from a series of

two-dimensional images taken at different focal planes. The drawback of this method is that light emitted from planes above and below the in-focus regions are also captured in each optical section. This is because the entire specimen is illuminated by the excitation light source, which causes the whole sample to emit fluorescence in the form of radiated light that is collected by the CCD camera (detector). This results in a reduction of both lateral resolution and depth discrimination.

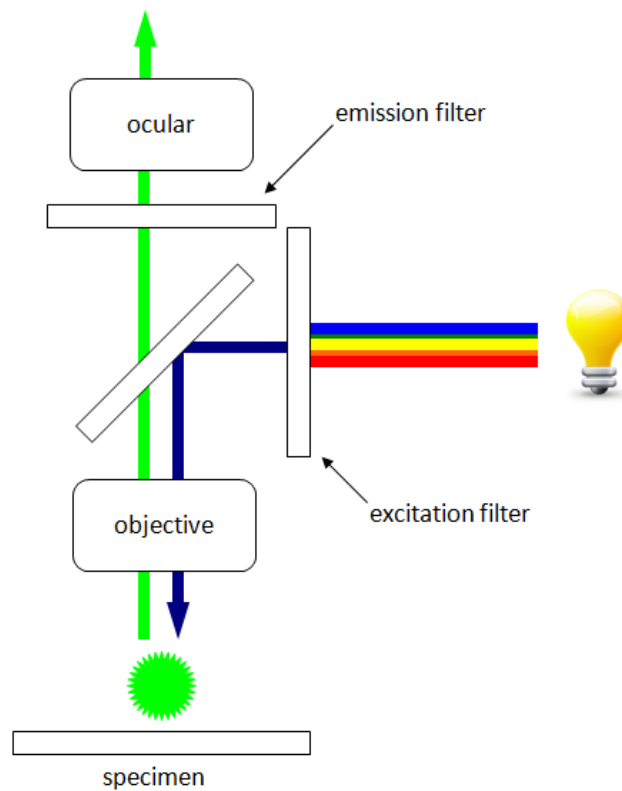


Figure 7.1: Schematic of an Epifluorescence Microscope System

In order to remove unwanted out-of-focus information from each two-dimensional image in the series, deconvolution, based on the underlying physics of image information, can be used to improve the quality of images. Deconvolution

methods determine how much out-of-focus light is expected for the optics in use and then seeks to redistribute this light to its points of origin in the specimen. In order to restore the original 'clean' image from the convolved 'blurred' three-dimensional image, mathematical algorithms are utilized to segregate the original distribution of point sources that gave rise to the specimen image. Widely used methods include: nearest neighbors, wiener filters, linear least squares, nonlinear least squares, maximum likelihood, blind deconvolution, and Lucy-Richardson deconvolution [297-301]. In general, there is no 'universally optimal' deconvolution algorithm. Methods that require more computing power yield better image restoration results. However, the advent of confocal and more recently two-photon imaging has limited the use of deconvolution-based methods.

7.1.2 Confocal Microscopy

The name 'confocal' originates from the configuration based on the use of point illumination and a pinhole in an optically conjugate plane in front of a detector to eliminate out-of-focus information. Excitation light that is focused on the specimen by the object is initially passed through a small aperture, often a slit or a pinhole. Fluorescence emissions that originate from above or below the plane of focus are then blocked by a second aperture or slit in front of the detector. The smaller the second aperture, the higher the rejection rate of out-of-focus light and the thinner the resulting optical sections. Thin optical sections have greatly improved contrast and axial

resolution, but they are obtained at the expense of overall specimen brightness or signal strength.

There are two major approaches to achieve confocal microscopy using commercial instruments: point scanning confocal laser scanning microscopy (CLSM) and spinning disk confocal microscopy. CLSM is the most widely used confocal microscopy in life sciences; the basic principle is illustrated in **Figure 7.2**. An excitation laser source is scanned across the specimen in a point-by-point raster pattern. The emitted light is then collected by the objective, passed through a small pinhole, and detected by a photomultiplier tube (PMT). The output from the PMT is assembled into an image and displayed by the computer.

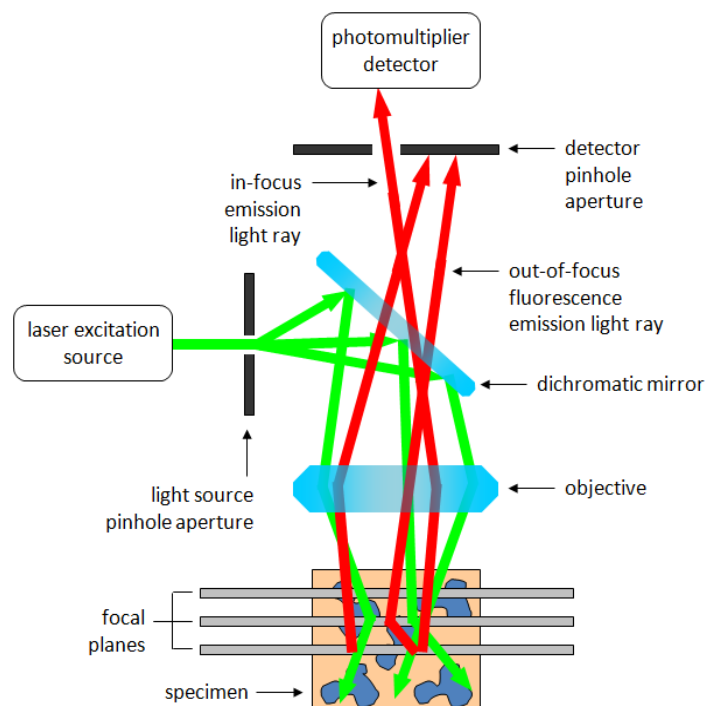


Figure 7.2: Schematic of a Laser Scanning Confocal Microscope System

CLSM has many advantages. It allows for extremely thin optical sectioning of specimens, permitting the imaging of structures and intracellular features in greater detail than conventional epifluorescence microscopy. The drawbacks of CLSM are that these systems compromise detectable fluorescence in order to deliver their high degree of confocality. Because of the pinhole's small apertures, a large amount of light gets rejected, thus detectable emissions from the specimen must be bright enough to be captured through the use of high numerical aperture (NA) objectives. The use of intense lasers addresses the low-light emission problem. However, the intensity of the laser light causes photobleaching in fluorescent probes and phototoxicity in the specimen itself. Additionally, CLSM's point-by-point acquisition technique is time consuming, making this system less capable of recording short-time biological events. For example, acquiring a 1024 by 1024 high-resolution single optical section image from most laser scanning confocal microscopes requires approximately 0.5 to 1 second. This is not rapid enough to capture certain dynamic cellular phenomena, in particular, intracellular dynamics such as the visualization of calcium ion transients that occur in 1/10th to 1/5th of a second [302-304].

The speed limitations imposed by CLSM can be overcome by using the second approach used to achieve confocal microscopy: a spinning disk confocal system. An array of beams can be used in parallel, which make it potentially useful for higher speed image acquisition in comparison to CLSM. The inherent parallelism of a spinning disk confocal system avoids fluorophore saturation, enabling higher levels of excitation to be used [305-308]. The spinning disk is also called the Nipkow spinning disk confocal

system, named after Paul Nipkow, who first proposed the principle of generating images using an array of pinholes in 1883 [305].

Figure 7.3 shows a diagram of the Nipkow spinning disc system. A conventional light source (mercury or xenon arc lamp) or laser passes through an excitation filter before being directed onto a spinning Nipkow disk in which 20,000 - 200,000 pinholes are arranged in spirals of constant pitch [308]. As light falls on one side of the disk, a subregion corresponding to about a thousand pinholes is illuminated and imaged. A partial rotation of a Nipkow disk (ranging from 1,800 to 5,000 RPM) scans the sample; the induced fluorescence (reflected light) produced by the specimen is collected by the objective lens and reflected off a beam splitter to highly reflective mirrors which amplify the collected light to the conjugate apertures on the other side of the spinning disk. Thin in-focus fluorescence from the specimen passes through the conjugate apertures and a barrier filter before being detected. In contrast, out-of-focus light from the specimen does not have a conjugate aperture to pass through, and is blocked by the disk. The time taken to traverse the field of view is so short that images can be seen in real-time by an eyepiece or acquired using a camera that is synchronized with the rotation of the disk [305-308].

Many of the biological applications using microscopy entail imaging living specimens or deep tissues. The complex nature of cellular materials means that the passage of light is affected in ways that cannot be accurately modeled, resulting in image quality falling well below theoretical resolution limits. Different imaging systems are not equally affected by this decrease in spatial accuracy as the focal plane moves

further from the sample. CLSM is generally more tolerant to increasing working distance than wide-field microscopy systems, where out-of-focus light poses a major challenge. Absorption and scattering of light also contribute to the reduction in image quality, particularly, in thicker three-dimensional specimens, although these factors become less pronounced with increasing excitation wavelengths. The typical spatial limit of penetration of confocal microscopy for highly scattered cells and tissue samples is about 200 nanometers [113, 309, 310], which may limit imaging of living specimens or deep tissues. This is one of the main reasons multiphoton imaging (MPM) is the imaging technique of choice for three-dimensional tissue imaging.

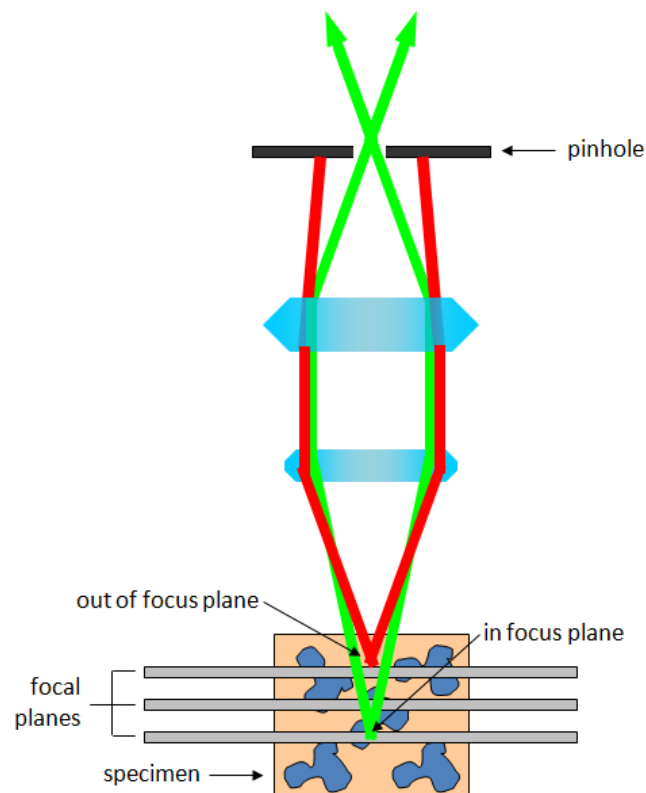


Figure 7.3: Schematic of a Spinning Disk Confocal Microscope System

7.1.3 Multiphoton Microscopy

Multiphoton microscopy (MPM) presents a major advantage over confocal microscopy because of deeper tissue penetration (in the order of millimeters), more efficient light detection, reduced photobleaching/phototoxicity, and enhanced spectral accessibility and flexibility [111-114, 311, 312]. The term MPM is a generic term for the following techniques: two-photon excitation (TPE) microscopy, three-photon excitation microscopy, second-harmonic generation MPM, and third-harmonic generation MPM [114]. All of these techniques use nonlinear excitation to generate fluorescence limited to a thin raster-scanned plane. With the advent of ultrafast (in the order of femtoseconds) pulsating lasers, such as Ti:Sapphire and Nd:YLF lasers, MPM, TPE microscopy in particular, has become a viable tool to monitor complex biological samples.

The phenomenon of TPE arises from simultaneous absorption of two photons in a single quantized event [114]. Since the energy of a photon is inversely proportional to its wavelength, the two absorbed photons must have a wavelength of about twice that required for one-photon excitation. For example, a fluorophore that normally absorbs blue light (~488 nanometer wavelength) can also be excited by two photons of infrared light (~960 nanometer wavelength). Since TPE depends on simultaneous absorption, the resulting fluorescence emission varies with the square of the excitation intensity. In order to produce a significant number of two-photon absorption events, photon density must be ~1 million times that required to generate the same number of one-photon excitations.

In a MPM microscope, TPE is generated by focusing a single pulsed laser through the microscope optics. As the laser beam is focused, the photon density increases as it approaches the focal plane and the probability of two photons interacting simultaneously with a single fluorophore increases. The laser focal point is the location with highest probability along the optical path where the photons are crowded enough to generate significant occurrence of TPE. **Figure 7.4** illustrates the generation of TPE in a fluorophore-containing specimen at the microscope focal point and peripheral areas. Above the focal point, the photon density is not sufficient for two photons to pass within the absorption cross-section of a single fluorophore at the same instant. However, at the focal point, the photons are so closely spaced that it is possible to find two of them within the absorption cross-section of a single fluorophore simultaneously.

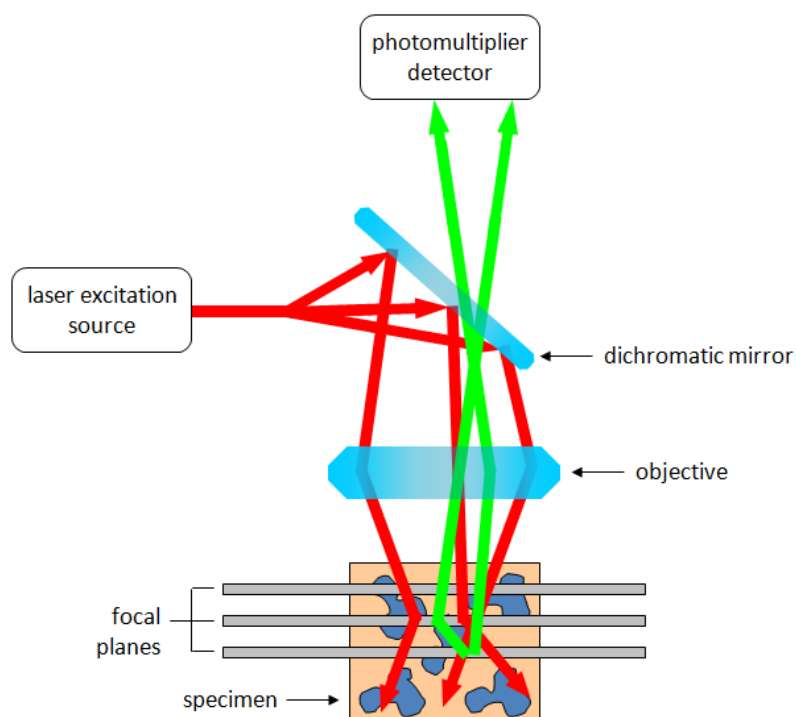


Figure 7.4: Schematic of a Multiphoton Microscope System

The narrow localization of TPE to the illumination focal point is the basis for the technique's most significant advantages over confocal microscopy. In a conventional confocal microscope, although fluorescence is excited throughout the specimen's entire illuminated volume, only signals originating from the focal plane pass through the confocal pinhole, allowing background-free images to be collected. By contrast, TPE only generates fluorescence at the focal plane, and since no background fluorescence is produced, a pinhole is not necessary.

Dramatic differences between the excitation regions of confocal and TPE microscopy results in divergent photo bleaching patterns in each method. The laser of a confocal system excites fluorophores above and below the focal plane, contributing to the bleaching observed in these extensive areas. In contrast, TPE only occurs at the focal plane; therefore, bleaching is confined to this area.

The most powerful advantage of TPE is the ability to provide superior optical sectioning at greater depths in thick specimens than conventional CLSM or WFM due to the effect of three factors: (1) absence of out-of-focus absorption allows for more of the excitation light photons to reach the desired specimen region, (2) red and infrared light scatters less light at shorter wavelengths, and (3) the effects of light scattering are less detrimental in TPE than in conventional CLSM systems. Further comparisons between multiphoton and confocal microscopy can be found in **Table 7.1**.

<i>Imaging techniques</i>	<i>Wide field</i>	<i>Confocal</i>		<i>Multiphoton excitation</i>
		<i>Laser scanning</i>	<i>Spinning disk</i>	
Light source	Wide band lamp	Narrow band laser (UV-far red)	Wide band lamp or narrow band laser	Tunable infrared laser
Lateral resolution	Poor	~250 nm	~250 nm	Slightly worse than 250 nm
Axial resolution	Poor	500-800 nm	500-800 nm	~500 nm
Detection approach	Volume detection	Limit detection to single plane		Limit excitation to single focal plane
Aperture requirement	No	Yes	Yes	No
Image penetration depth	-	< 200 μ m	< 200 μ m	Up to 1 mm
3D sectioning capability	No	Yes	Yes	Yes
Multiobjectives	No	No	Yes	No
Comments	Good for regular use.	High-resolution but relatively low sensitivity and low speed. High intensity excitation can cause photodamage and limits use for some live cell imaging.	Equipped with thousands of microlenses. Imaging of entire field. Fast imaging speed, less photodamage. Good for time-lapse imaging.	Longer wavelength excitation renders deeper penetration. Less photodamage.

Table 7.1: Comparison of Wide-Field, Confocal, and Multiphoton Microscopy

It should be noted that the image resolution obtained with TPE is not better than that achieved in a well-aligned confocal microscope in spite of the advantages of TPE mentioned earlier. The utilization of longer excitation wavelengths actually results in a larger resolution spot. If a biological structure cannot be resolved in an ideal confocal microscope, it will similarly not be resolved in a TPE laser scanning microscope. It is also important to note that imaging thin specimens using TPE microscopy does not necessarily benefit significantly over conventional CLSM. The reason is that slightly increased photobleaching may occur in the focal plane when using TPE over CLSM in thin specimens, although total photobleaching in a thick specimen is greatly reduced in TPE when compared to CLSM.

Despite the advantages of MPM in three-dimensional tissue imaging, the depth of penetration and image quality are limited by the ability to effectively label thick

samples such as tissues. Introducing fluorescence labels into tissues becomes increasingly difficult at greater depths. One way to overcome this difficulty is by expressing GFP within transgenic animals and imaging with TPE mode *in vivo*, where conventional immunolabeling deep into tissue organs is barely accessible [312].

7.1.4 FRET and TIRFM

Fluorescence Resonance Energy Transfer (FRET), a widespread technique in molecular biology and biophysics, has been typically used to screen molecular conformation, molecular proximity, protein-protein interactions, and biosensing in cell biology [313-315]. More recently, FRET has been adapted to quantitatively analyze parameters of cell adhesion-related phenomena, such as molecular changes in matrix proteins, bonds between integrins and ligands, and changes in the crosslinking density of hydrogel-based extracellular matrix analogs [316].

FRET is an interaction between the electronic excited states of two dye molecules. Excitation is transferred from a donor molecule to an acceptor molecule without the emission of a photon. The emission spectrum of the donor must overlap the excitation spectrum of the acceptor; the extent of this overlap determines the FRET efficiency. Furthermore, donor-acceptor transition dipole orientations must be approximately parallel [312, 314, 315, 317]. FRET's intermolecular separation depends on the inverse sixth power of the distance, so it falls off rapidly with distance, usually in the order of 10 nanometers which is comparable to dimensions of biological macromolecules. When FRET occurs, the fluorescence of the donor molecule is

quenched, the emission of the acceptor fluorophore is sensitized, and the donor lifetime is reduced. Therefore, FRET has a direct effect on rates of donor photobleaching and acceptor fluorescence depolarization. There are several ways that FRET can be measured depending on which of the consequences is being monitored. These methods are based on: quenching of donor fluorescence, sensitized emission of acceptor fluorescence, reduction in donor lifetime, and depolarization of acceptor fluorescence.

Because energy transfer is limited to distances of < 10 nanometers, the detection of FRET provides valuable information about the spatial relationships of fusion proteins on a subresolution scale. Moreover, it gives us a powerful tool for measuring the proximity of molecular species at a level beyond the resolution of any optical microscope.

Another high-resolution imaging approach that has been recently adapted to study cell-biomaterial interactions is Total Internal Reflectance Fluorescence Microscopy (TIRFM). TIRFM has gained popularity in the study of cellular processes and single biological molecules. Briefly, it utilizes an evanescent field generated in the lower refractive index medium during total internal reflection. Light from the fluorescent molecules can then be collected by an objective lens and recorded using a detector such as a CCD camera [318]. The chief advantage of this method is the thinness and exponential decay of the illumination.

Currently, TIRFM can be broken down into two categories: prism-type TIRFM and objective-type TIRFM. Prism-type TIRFM makes use of a prism made of higher refractive material than the biological sample. Light at an acute angle travels through the prism, a

refractive index-matched immersion fluid, and the sample's coverslip until finally reaching the interface between the sample and the coverslip, where it undergoes total internal reflection. Since the prism is on the coverslip, prism-type TIRFM usually requires illumination and the light collection to come from opposite sides of the microscope. In contrast, objective-type TIRFM uses a high-NA objective lens instead of a prism to introduce light at a supercritical angle, which is implemented either through the use of an opaque disk in the conjugate back focal plane of the microscope (to block all subcritical angles of light), or by focusing a laser beam off-axis towards the back focal plane of the objective lens. Light focused at the back focal plane by either method is then redirected towards the sample with angles dependent upon the position of the focused beam with angles of excitation increasing with distance from the center of the back focal plane.

TIRFM has a wide range of applications in cell and molecular biology, particularly, for viewing single molecules anchored to planar surfaces and to study the position and dynamics of molecules and organelles in living culture cells near the contact regions with glass substrates [319]. In the biomaterials community, TIRFM has been applied to study cell adhesion-related responses on biomaterials, such as changes in the contact area and adhesion strength on biomaterial surfaces, analysis of bond strength, and real-time measurement of cell/substrate separation distances following exposure to flow [320, 321].

Despite the simplicity of TIRFM, it provides remarkably good optical sectioning equal to or better than any other technique. However, its utility is limited to the study of

fluorescent molecules within 100 nanometers of the sample's coverslip. Thus, it cannot be applied to study cell-biomaterial interactions in three-dimensional scaffolds or thick tissue sections.

7.1.5 Flow Cytometry

In conventional flow cytometers, cells suspended in solution are passed through a detector at a rate exceeding thousands of cells per second [294, 322]. For each cell that passes, a detector is capable of acquiring several channels of information, which include: forward scatter, side-scatter, and several spectral bands [294, 323]. With the advent of fluorescence-activated cell sorting (FACS), the information attained by standard flow cytometers can be utilized to purify cell populations based on user-specified criteria from an otherwise heterogeneous cell sample [293]. More recently, with the integration of CCD camera technology, optical filtration, and digital computing, the combination of these traits for more advanced imaging-based cellular profiling are beginning to be realized [324].

7.2 FLUORESCENCE-BASED PROBES FOR CELLULAR PROFILING

The high-resolution imaging methods presented **Section 7.1** would not be possible without the use of fluorophores. Fluorophore-tagged markers are capable of identifying specific molecular targets and have been used for numerous applications, including the observation and analysis of various cell-biomaterial interactions. In this section, an overview of three different fluorophore markers is discussed: fluorophore-tagged antibodies, quantum dot-based probes, and fluorescent proteins.

7.2.1 Fluorophore-Tagged Antibodies

Immunostaining is a general term in biochemistry that applies to any use of an antibody-based method to detect a specific protein in a sample. Tagging of a fluorophore to an antibody improves the visualization of the antigens or antigen epitopes where the antibody binds. Antibodies can come in different varieties known as isotypes or classes. There are five antibody isotypes: IgA, IgD, IgE, IgG, and IgM [325]. They are each named with an 'Ig' prefix that stands for immunoglobulin, another name for antibody, and differ in their biological properties, functional locations, and ability to deal with different antigens. Due to their high specificity, IgGs are the most common antibody isotype for their immunostaining applications. The Ig monomer is a 'Y'-shaped molecule that consists of two identical heavy chains and two identical light chains. Each chain is composed of structural domains termed Ig domains. While the arms of Y-shaped antibodies have antigen-recognition sites, the root of these antibodies, where the heavy chains reside, provide a site to tag a fluorophore.

There are two ways to detect target protein molecules. A directly labeled fluorophore-conjugated primary antibody can be used to detect a target protein; this immunostaining technique is known as the direct method. Alternatively, a broader species-specific fluorophore-labeled secondary antibody is used to detect and attach to a primary antibody bound to a target protein; this is known as the indirect method [115, 326-329]. Both methods have their respective advantages and disadvantages. The direct method is simpler, more convenient, and less prone to artifacts than the indirect method. Although the indirect method is more cumbersome, it offers better signal amplification. This is achieved by several fluorophore-conjugated secondary antibodies binding to a single primary antibody. Moreover, secondary antibodies with fluorophores at various excitation/emission spectra are readily available from commercial sources, which make it easier to select probes for multicolor imaging applications.

7.2.2 Quantum Dot-Based Probes

Quantum dots (qdots) are nanoscale semiconductors and defined as particles with physical dimensions smaller than the exciton Bohr radius [330]. Metal and semiconductor nanoparticles, usually composed of groups II-VI or II-V elements, with 2 to 6 nanometers in diameter, have been used extensively due to their similarity in physical size to biological components such as nucleic acids and proteins [331]. Quantum dots have been used in the following applications: FRET analysis, gene technology via qdot-conjugated oligonucleotide probes, fluorescent labeling of cellular proteins, tracking of cellular movement, pathogen and toxin detection, *in vivo* imaging,

and tumor biology research [314, 330, 332-340]. Despite the growing impact of qdots, there are several barriers that need to be overcome, such as cytotoxicity and alteration of cell functions that accompanies the cellular uptake of qdots.

7.2.3 GFP and Variants

GFP was originally derived from the jellyfish *Aequorea Victoria* [341]. It has 238 amino acid residues and a green fluorophore which is comprised of only three amino acids: Ser65-Tyr66-Gly67. The stable protein structure is formed by beta sheets, which feature conformations that make up an 11-stranded drum-like structure [121]. The stability of GFP allows it to withstand pH levels ranging from mildly acidic (pH = 5.5) to extremely basic (pH = 12) and can also resist temperatures of up to 65°C. GFP has major and minor excitation peaks at wavelengths of 395 and 475 nanometers, respectively. Several modifications have been made from the original GFP, most notably the reduction of the dual excitation peaks of 395 and 475 nanometers down to one excitation peak of 488 nanometers, which is in the visible blue-light range. The emission peak of original and modified GFP is detected at 509 nanometers, which is in the visible green region of the electromagnetic spectrum [121, 341]. XFP variants with spectra that range from blue to red (shown in **Table 7.2**) can be used for live cell imaging.

In order for biomaterial scientists to utilize GFP fusion proteins to capture cellular and subcellular responses to biomaterials, the construction and expression of GFP can be easily accomplished via standard molecular biology techniques. By introducing GFP into host cells, one can visualize GFP-tagged whole cells, subcellular

organisms, and cytoskeletal structure/organization. This form of targeting allows the microscopist and the biomaterial scientist alike to study cellular behavior by observing GFP-tagged proteins and capture information at a level that was previously inaccessible, both spatially and temporally [342]. Apart from aforementioned GFP-based markers, phytochromes, light-sensitive photoreceptors, along with other proteins in the phytochrome signaling network, have been utilized to reversibly control the translocation of proteins to the cell membrane [343].

<i>Species / Source</i>	<i>Fluorescence Proteins</i>	<i>Excitation (nm)</i>	<i>Emission (nm)</i>
Green	EGFP	489	508
Cyan	ECFP	434/453	477/501
Yellow	EYFP	514	527
Red	DsRed	558	583

Table 7.2: List of Common Fluorescence Proteins

CHAPTER 8. REFERENCES

1. Furth, M.E., A. Atala, and M.E. Van Dyke, *Smart biomaterials design for tissue engineering and regenerative medicine*. Biomaterials, 2007. **28**(34): p. 5068-73.
2. Langer, R. and D.A. Tirrell, *Designing materials for biology and medicine*. Nature, 2004. **428**(6982): p. 487-92.
3. Tsang, V.L. and S.N. Bhatia, *Fabrication of three-dimensional tissues*. Tissue Engineering li: Basics of Tissue Engineering and Tissue Applications, 2007. **103**: p. 189-205.
4. Weigel, T., G. Schinkel, and A. Lendlein, *Design and preparation of polymeric scaffolds for tissue engineering*. Expert review of medical devices, 2006. **3**(6): p. 835-51.
5. Bisceglie, V., *Über die antineoplastische immunität; heterologe Einpflanzung von Tumoren in Hühner-embryonen*. Ztschr f Krebsforsch, 1933(40): p. 122-140.
6. Chick, W.L., A.A. Like, and V. Lauris, *Beta cell culture on synthetic capillaries: an artificial endocrine pancreas*. Science, 1975. **187**(4179): p. 847-9.
7. Macchiarini, P., et al., *Clinical transplantation of a tissue-engineered airway*. Lancet, 2008. **372**(9655): p. 2023-30.
8. Kropp, B.P. and J.B. Zwischenberger, *Tissue-engineered autologous bladders: new possibilities for cystoplasty*. Nature clinical practice. Urology, 2006. **3**(11): p. 588-9.
9. Mangera, A. and C.R. Chapple, *Tissue engineering in urethral reconstruction*. F1000 medicine reports, 2010. **2**: p. 65.
10. Ma, P.X., *Biomimetic materials for tissue engineering*. Advanced drug delivery reviews, 2008. **60**(2): p. 184-98.
11. Hubbell, J.A., *Biomaterials in tissue engineering*. Bio/technology, 1995. **13**(6): p. 565-76.
12. Zhao, J., et al., *Recruitment of endogenous stem cells for tissue repair*. Macromolecular bioscience, 2008. **8**(9): p. 836-42.
13. Buinewicz, B. and B. Rosen, *Acellular cadaveric dermis (AlloDerm): a new alternative for abdominal hernia repair*. Annals of plastic surgery, 2004. **52**(2): p. 188-94.
14. Frazza, E.J. and E.E. Schmitt, *A new absorbable suture*. Journal of biomedical materials research, 1971. **5**(2): p. 43-58.
15. Athanasiou, K.A., et al., *Orthopaedic applications for PLA-PGA biodegradable polymers*. Arthroscopy : the journal of arthroscopic & related surgery : official publication of the Arthroscopy Association of North America and the International Arthroscopy Association, 1998. **14**(7): p. 726-37.
16. Knowles, J.C., *Development of a natural degradable polymer for orthopaedic use*. Journal of medical engineering & technology, 1993. **17**(4): p. 129-37.
17. Morrison, W.A., *Progress in tissue engineering of soft tissue and organs*. Surgery, 2009. **145**(2): p. 127-30.
18. Nose, Y. and H. Okubo, *Artificial organs versus regenerative medicine: is it true?* Artificial organs, 2003. **27**(9): p. 765-71.
19. Kohn, J., W.J. Welsh, and D. Knight, *A new approach to the rationale discovery of polymeric biomaterials*. Biomaterials, 2007. **28**(29): p. 4171-7.
20. Godbey, W.T. and A. Atala, *In vitro systems for tissue engineering*. Annals of the New York Academy of Sciences, 2002. **961**: p. 10-26.
21. Chwalek, K., et al., *Glycosaminoglycan-based hydrogels to modulate heterocellular communication in in vitro angiogenesis models*. Scientific reports, 2014. **4**: p. 4414.
22. Kaihara, S., et al., *Silicon micromachining to tissue engineer branched vascular channels for liver fabrication*. Tissue engineering, 2000. **6**(2): p. 105-17.
23. Miller, J.S., et al., *Rapid casting of patterned vascular networks for perfusable engineered three-dimensional tissues*. Nature materials, 2012. **11**(9): p. 768-74.

24. Griffith, L.G. and G. Naughton, *Tissue engineering--current challenges and expanding opportunities*. Science, 2002. **295**(5557): p. 1009-14.
25. Johnson, P.C., et al., *Strategic directions in tissue engineering*. Tissue engineering, 2007. **13**(12): p. 2827-37.
26. Hootman, J.M. and C.G. Helmick, *Projections of US prevalence of arthritis and associated activity limitations*. Arthritis and rheumatism, 2006. **54**(1): p. 226-9.
27. Cheng, Y.J., et al., *Prevalence of diagnosed arthritis and arthritis-attributable activity limitation among adults with and without diagnosed diabetes: United States, 2008-2010*. Diabetes care, 2012. **35**(8): p. 1686-91.
28. *Summary health statistics for U.S. adults: national health interview survey; Tables 7, 8*. Center for Disease Control, 2008.
29. *National Osteoporosis Foundation*. Osteoporosis Statistics 2008; Available from: <http://www.nof.org/>.
30. Bielack, S.S., et al., *Delaying surgery with chemotherapy for osteosarcoma of the extremities*. Expert opinion on pharmacotherapy, 2004. **5**(6): p. 1243-56.
31. Rosenberg, E. and L.F. Rose, *Biologic and clinical considerations for autografts and allografts in periodontal regeneration therapy*. Dental clinics of North America, 1998. **42**(3): p. 467-90.
32. Erbe, E.M., et al., *Potential of an ultraporous beta-tricalcium phosphate synthetic cancellous bone void filler and bone marrow aspirate composite graft*. European spine journal : official publication of the European Spine Society, the European Spinal Deformity Society, and the European Section of the Cervical Spine Research Society, 2001. **10 Suppl 2**: p. S141-6.
33. Priya, S.G., H. Jungvid, and A. Kumar, *Skin tissue engineering for tissue repair and regeneration*. Tissue engineering. Part B, Reviews, 2008. **14**(1): p. 105-18.
34. Iwasa, J., et al., *Clinical application of scaffolds for cartilage tissue engineering*. Knee surgery, sports traumatology, arthroscopy : official journal of the ESSKA, 2009. **17**(6): p. 561-77.
35. Hutmacher, D.W., *Scaffolds in tissue engineering bone and cartilage*. Biomaterials, 2000. **21**(24): p. 2529-43.
36. Kielpinski, G., et al., *Roadmap to approval: use of an automated sterility test method as a lot release test for Carticel, autologous cultured chondrocytes*. Cytotherapy, 2005. **7**(6): p. 531-41.
37. Eaglstein, W.H. and V. Falanga, *Tissue engineering and the development of Apligraf, a human skin equivalent*. Clinical Therapeutics, 1997. **19**(5): p. 894-905.
38. Strehl, R., et al., *Proliferating cells versus differentiated cells in tissue engineering*. Tissue engineering, 2002. **8**(1): p. 37-42.
39. McKay, R., *Stem cells--hype and hope*. Nature, 2000. **406**(6794): p. 361-4.
40. Watt, F.M. and B.L. Hogan, *Out of Eden: stem cells and their niches*. Science, 2000. **287**(5457): p. 1427-30.
41. Murphy, S.V. and A. Atala, *Organ engineering--combining stem cells, biomaterials, and bioreactors to produce bioengineered organs for transplantation*. BioEssays : news and reviews in molecular, cellular and developmental biology, 2013. **35**(3): p. 163-72.
42. Thomson, J.A., et al., *Embryonic stem cell lines derived from human blastocysts*. Science, 1998. **282**(5391): p. 1145-7.
43. Takahashi, K., et al., *Induction of pluripotent stem cells from adult human fibroblasts by defined factors*. Cell, 2007. **131**(5): p. 861-72.

44. Takahashi, K. and S. Yamanaka, *Induction of pluripotent stem cells from mouse embryonic and adult fibroblast cultures by defined factors*. Cell, 2006. **126**(4): p. 663-76.
45. Morrison, S.J., N. Uchida, and I.L. Weissman, *The biology of hematopoietic stem cells*. Annual Review of Cell and Developmental Biology, 1995. **11**: p. 35-71.
46. Verfaillie, C.M., *Hematopoietic stem cells for transplantation*. Nature immunology, 2002. **3**(4): p. 314-7.
47. Pittenger, M.F., et al., *Multilineage potential of adult human mesenchymal stem cells*. Science, 1999. **284**(5411): p. 143-7.
48. Jaiswal, N., et al., *Osteogenic differentiation of purified, culture-expanded human mesenchymal stem cells in vitro*. Journal of cellular biochemistry, 1997. **64**(2): p. 295-312.
49. Halvorsen, Y.D., et al., *Extracellular matrix mineralization and osteoblast gene expression by human adipose tissue-derived stromal cells*. Tissue engineering, 2001. **7**(6): p. 729-41.
50. Cho, H.H., et al., *Induction of osteogenic differentiation of human mesenchymal stem cells by histone deacetylase inhibitors*. Journal of cellular biochemistry, 2005. **96**(3): p. 533-42.
51. Dragoo, J.L., et al., *Bone induction by BMP-2 transduced stem cells derived from human fat*. Journal of orthopaedic research : official publication of the Orthopaedic Research Society, 2003. **21**(4): p. 622-9.
52. Zhang, X., et al., *Runx2 overexpression enhances osteoblastic differentiation and mineralization in adipose--derived stem cells in vitro and in vivo*. Calcified Tissue International, 2006. **79**(3): p. 169-78.
53. Ducy, P., T. Schinke, and G. Karsenty, *The osteoblast: a sophisticated fibroblast under central surveillance*. Science, 2000. **289**(5484): p. 1501-4.
54. Nakashima, K. and B. de Crombrughe, *Transcriptional mechanisms in osteoblast differentiation and bone formation*. Trends in genetics : TIG, 2003. **19**(8): p. 458-66.
55. Cohen, M.M., Jr., *The new bone biology: pathologic, molecular, and clinical correlates*. American journal of medical genetics. Part A, 2006. **140**(23): p. 2646-706.
56. Liu, E., et al., *Parsing the early cytoskeletal and nuclear organizational cues that demarcate stem cell lineages*. Cell cycle, 2010. **9**(11): p. 2108-17.
57. Treiser, M.D., et al., *Cytoskeleton-based forecasting of stem cell lineage fates*. Proceedings of the National Academy of Sciences of the United States of America, 2010. **107**(2): p. 610-5.
58. Miyama, K., et al., *A BMP-inducible gene, dlx5, regulates osteoblast differentiation and mesoderm induction*. Dev Biol, 1999. **208**(1): p. 123-33.
59. Ryoo, H.M., et al., *Stage-specific expression of Dlx-5 during osteoblast differentiation: involvement in regulation of osteocalcin gene expression*. Mol Endocrinol, 1997. **11**(11): p. 1681-94.
60. Burdick, J.A. and G.D. Prestwich, *Hyaluronic acid hydrogels for biomedical applications*. Advanced materials, 2011. **23**(12): p. H41-56.
61. Karp, J.M., et al., *Fibrin-filled scaffolds for bone-tissue engineering: An in vivo study*. Journal of biomedical materials research. Part A, 2004. **71**(1): p. 162-71.
62. Salgado, A.J., O.P. Coutinho, and R.L. Reis, *Novel starch-based scaffolds for bone tissue engineering: cytotoxicity, cell culture, and protein expression*. Tissue engineering, 2004. **10**(3-4): p. 465-74.
63. Wahl, D.A. and J.T. Czernuszka, *Collagen-hydroxyapatite composites for hard tissue repair*. European cells & materials, 2006. **11**: p. 43-56.

64. Christenson, L., et al., *Biomaterials for tissue engineering: summary*. Tissue engineering, 1997. **3**(1): p. 71-3; discussion 73-6.
65. Salgado, A.J., O.P. Coutinho, and R.L. Reis, *Bone tissue engineering: state of the art and future trends*. Macromolecular bioscience, 2004. **4**(8): p. 743-65.
66. Kneser, U., et al., *Tissue engineering of bone: the reconstructive surgeon's point of view*. Journal of cellular and molecular medicine, 2006. **10**(1): p. 7-19.
67. Langer, R. and J.P. Vacanti, *Tissue engineering*. Science, 1993. **260**(5110): p. 920-6.
68. Athanasiou, K.A., G.G. Niederauer, and C.M. Agrawal, *Sterilization, toxicity, biocompatibility and clinical applications of polylactic acid/polyglycolic acid copolymers*. Biomaterials, 1996. **17**(2): p. 93-102.
69. Wan, Y., et al., *Adhesion and proliferation of OCT-1 osteoblast-like cells on micro- and nano-scale topography structured poly(L-lactide)*. Biomaterials, 2005. **26**(21): p. 4453-9.
70. Stevens, M.M. and J.H. George, *Exploring and engineering the cell surface interface*. Science, 2005. **310**(5751): p. 1135-8.
71. Ertel, S.I. and J. Kohn, *Evaluation of a series of tyrosine-derived polycarbonates as degradable biomaterials*. Journal of biomedical materials research, 1994. **28**(8): p. 919-30.
72. Hoven, V.P., Poopattanapong, A., and Kohn, J., *Acid-Containing Tyrosine-Derived Polycarbonates: Wettability and Surface Reactivity*. Macromolecular Symposia, 2004. **216**: p. 87-98.
73. Tziampazis, E., J. Kohn, and P.V. Moghe, *PEG-variant biomaterials as selectively adhesive protein templates: model surfaces for controlled cell adhesion and migration*. Biomaterials, 2000. **21**(5): p. 511-20.
74. Yu, C. and J. Kohn, *Tyrosine-PEG-derived poly(ether carbonate)s as new biomaterials. Part I: synthesis and evaluation*. Biomaterials, 1999. **20**(3): p. 253-64.
75. Pulapura, S. and J. Kohn, *Tyrosine-derived polycarbonates: backbone-modified "pseudo"-poly (amino acids) designed for biomedical applications*. Biopolymers, 1992. **32**(4): p. 411-7.
76. Tangpasuthadol, V., et al., *Hydrolytic degradation of tyrosine-derived polycarbonates, a class of new biomaterials. Part II: 3-yr study of polymeric devices*. Biomaterials, 2000. **21**(23): p. 2379-87.
77. Magno, M.H.R., et al., *Synthesis, degradation and biocompatibility of tyrosine-derived polycarbonate scaffolds*. Journal of Materials Chemistry, 2010. **20**(40): p. 8885-8893.
78. Discher, D.E., P. Janmey, and Y.L. Wang, *Tissue cells feel and respond to the stiffness of their substrate*. Science, 2005. **310**(5751): p. 1139-43.
79. Engler, A.J., et al., *Matrix elasticity directs stem cell lineage specification*. Cell, 2006. **126**(4): p. 677-89.
80. Takahashi, Y. and Y. Tabata, *Effect of the fiber diameter and porosity of non-woven PET fabrics on the osteogenic differentiation of mesenchymal stem cells*. J Biomater Sci Polym Ed, 2004. **15**(1): p. 41-57.
81. Tuan, R.S., et al., *Multilineage differentiation of human mesenchymal stem cells in a three-dimensional nanofibrous scaffold*. Biomaterials, 2005. **26**(25): p. 5158-5166.
82. Zinger, O., et al., *Differential regulation of osteoblasts by substrate microstructural features*. Biomaterials, 2005. **26**(14): p. 1837-47.
83. Yim, E.K., et al., *Nanotopography-induced changes in focal adhesions, cytoskeletal organization, and mechanical properties of human mesenchymal stem cells*. Biomaterials, 2010. **31**(6): p. 1299-306.

84. Chalut, K.J., et al., *Deformation of stem cell nuclei by nanotopographical cues*. Soft matter, 2010. **6**(8): p. 1675-1681.
85. Hale, C.M., et al., *Dysfunctional connections between the nucleus and the actin and microtubule networks in laminopathic models*. Biophysical journal, 2008. **95**(11): p. 5462-75.
86. Ratner, B.D. and S.J. Bryant, *Biomaterials: where we have been and where we are going*. Annual review of biomedical engineering, 2004. **6**: p. 41-75.
87. Dadsetan, M., et al., *Surface chemistry mediates adhesive structure, cytoskeletal organization, and fusion of macrophages*. Journal of biomedical materials research. Part A, 2004. **71**(3): p. 439-48.
88. Charest, J.L., et al., *Combined microscale mechanical topography and chemical patterns on polymer cell culture substrates*. Biomaterials, 2006. **27**(11): p. 2487-94.
89. Anderson, D.G., S. Levenberg, and R. Langer, *Nanoliter-scale synthesis of arrayed biomaterials and application to human embryonic stem cells*. Nature Biotechnology, 2004. **22**(7): p. 863-6.
90. Hubbell, J.A., *Biomaterials science and high-throughput screening*. Nature Biotechnology, 2004. **22**(7): p. 828-9.
91. Unadkat, H.V., et al., *An algorithm-based topographical biomaterials library to instruct cell fate*. Proceedings of the National Academy of Sciences of the United States of America, 2011. **108**(40): p. 16565-70.
92. Flaim, C.J., S. Chien, and S.N. Bhatia, *An extracellular matrix microarray for probing cellular differentiation*. Nature methods, 2005. **2**(2): p. 119-25.
93. Weber, N., et al., *Small changes in the polymer structure influence the adsorption behavior of fibrinogen on polymer surfaces: validation of a new rapid screening technique*. Journal of biomedical materials research. Part A, 2004. **68**(3): p. 496-503.
94. Dittrich, P.S. and A. Manz, *Lab-on-a-chip: microfluidics in drug discovery*. Nature reviews. Drug discovery, 2006. **5**(3): p. 210-8.
95. Levisky, J.M. and R.H. Singer, *Gene expression and the myth of the average cell*. Trends in cell biology, 2003. **13**(1): p. 4-6.
96. Nolan, K., et al., *Tissue engineering and biomaterials in regenerative medicine*. Cell Transplant, 2008. **17**(3): p. 241-3.
97. Abraham, S., N. Eroshenko, and R.R. Rao, *Role of bioinspired polymers in determination of pluripotent stem cell fate*. Regen Med, 2009. **4**(4): p. 561-78.
98. Stosich, M.S., et al., *Bioengineering strategies to generate vascularized soft tissue grafts with sustained shape*. Methods, 2009. **47**(2): p. 116-21.
99. Sundelacruz, S. and D.L. Kaplan, *Stem cell- and scaffold-based tissue engineering approaches to osteochondral regenerative medicine*. Semin Cell Dev Biol, 2009. **20**(6): p. 646-55.
100. Shea, L.D., et al., *Engineered bone development from a pre-osteoblast cell line on three-dimensional scaffolds*. Tissue engineering, 2000. **6**(6): p. 605-17.
101. Choy, G., P. Choyke, and S.K. Libutti, *Current advances in molecular imaging: noninvasive in vivo bioluminescent and fluorescent optical imaging in cancer research*. Mol Imaging, 2003. **2**(4): p. 303-12.
102. Causa, F., P.A. Netti, and L. Ambrosio, *A multi-functional scaffold for tissue regeneration: the need to engineer a tissue analogue*. Biomaterials, 2007. **28**(34): p. 5093-9.
103. Sun, T., et al., *Development of a 3D cell culture system for investigating cell interactions with electrospun fibers*. Biotechnol Bioeng, 2007. **97**(5): p. 1318-28.

104. Pasquinelli, G., et al., *Mesenchymal stem cell interaction with a non-woven hyaluronan-based scaffold suitable for tissue repair*. J Anat, 2008. **213**(5): p. 520-30.
105. Reed, C.R., et al., *Composite tissue engineering on polycaprolactone nanofiber scaffolds*. Annals of plastic surgery, 2009. **62**(5): p. 505-12.
106. Sundqvist, T., M. Jakobson, and K.E. Magnusson, *Spatial distribution of cell fluorescence determined with a diode-matrix (32 x 32 elements) and computer controlled epifluorescence microscopy*. Int J Biomed Comput, 1985. **17**(2): p. 107-14.
107. Griffin, D.K., et al., *Fluorescent in-situ hybridization to interphase nuclei of human preimplantation embryos with X and Y chromosome specific probes*. Hum Reprod, 1991. **6**(1): p. 101-5.
108. Kraker, W.J., et al., *Fluorescent in situ hybridization: use of whole chromosome paint probes to identify unbalanced chromosome translocations*. Mayo Clin Proc, 1992. **67**(7): p. 658-62.
109. Han, K., et al., *Quantifying chromosome changes and lineage involvement in myelodysplastic syndrome (MDS) using fluorescent in situ hybridization (FISH)*. Leukemia, 1994. **8**(1): p. 81-6.
110. Chaumeil, J., et al., *Combined immunofluorescence, RNA fluorescent in situ hybridization, and DNA fluorescent in situ hybridization to study chromatin changes, transcriptional activity, nuclear organization, and x-chromosome inactivation*. Methods Mol Biol, 2008. **463**: p. 297-308.
111. Xu, C., et al., *Multiphoton fluorescence excitation: new spectral windows for biological nonlinear microscopy*. Proceedings of the National Academy of Sciences of the United States of America, 1996. **93**(20): p. 10763-8.
112. Masters, B.R., et al., *Multiphoton excitation microscopy, confocal microscopy, and spectroscopy of living cells and tissues; functional metabolic imaging of human skin in vivo*. Methods Enzymol, 1999. **307**: p. 513-36.
113. Konig, K., *Multiphoton microscopy in life sciences*. J Microsc, 2000. **200**(Pt 2): p. 83-104.
114. Zipfel, W.R., R.M. Williams, and W.W. Webb, *Nonlinear magic: multiphoton microscopy in the biosciences*. Nature Biotechnology, 2003. **21**(11): p. 1369-77.
115. Nadakavukaren, K.K. and O.H. Griffith, *Photoelectron imaging of cytoskeletal elements*. Ultramicroscopy, 1985. **17**(1): p. 31-42.
116. Pereira, M.C., et al., *Myofibrillar breakdown and cytoskeletal alterations in heart muscle cells during invasion by Trypanosoma cruzi: immunological and ultrastructural study*. J Submicrosc Cytol Pathol, 1993. **25**(4): p. 559-69.
117. Pietrasanta, L.I., A. Schaper, and T.M. Jovin, *Imaging subcellular structures of rat mammary carcinoma cells by scanning force microscopy*. J Cell Sci, 1994. **107** (Pt 9): p. 2427-37.
118. Elson, E.L. and H. Qian, *Interpretation of fluorescence correlation spectroscopy and photobleaching recovery in terms of molecular interactions*. Methods Cell Biol, 1989. **30**: p. 307-32.
119. Dammermann, A. and A. Merdes, *Assembly of centrosomal proteins and microtubule organization depends on PCM-1*. J Cell Biol, 2002. **159**(2): p. 255-66.
120. Becker, B.E., S.J. Romney, and D.L. Gard, *XMAP215, XKCM1, NuMA, and cytoplasmic dynein are required for the assembly and organization of the transient microtubule array during the maturation of Xenopus oocytes*. Dev Biol, 2003. **261**(2): p. 488-505.
121. Chalfie, M., *Green fluorescent protein*. Photochem Photobiol, 1995. **62**(4): p. 651-6.
122. Perlman, Z.E., et al., *Multidimensional drug profiling by automated microscopy*. Science, 2004. **306**(5699): p. 1194-8.

123. Tanaka, M., et al., *An unbiased cell morphology-based screen for new, biologically active small molecules*. PLoS biology, 2005. **3**(5): p. e128.
124. Kim, J.J., S.L. Vega, and P.V. Moghe, *A high content imaging-based approach for classifying cellular phenotypes*. Methods in molecular biology, 2013. **1052**: p. 41-8.
125. Liu, E., et al., *Quantitative biorelevant profiling of material microstructure within 3D porous scaffolds via multiphoton fluorescence microscopy*. Journal of biomedical materials research. Part B, Applied biomaterials, 2007. **82**(2): p. 284-97.
126. Liu, E., et al., *High-content profiling of cell responsiveness to graded substrates based on combinatorially variant polymers*. Combinatorial chemistry & high throughput screening, 2009. **12**(7): p. 646-55.
127. Treiser, M.D., et al., *Profiling cell-biomaterial interactions via cell-based fluororeporter imaging*. Biotechniques, 2007. **43**(3): p. 361-6, 368.
128. Vega, S.L., et al., *High-content imaging-based screening of microenvironment-induced changes to stem cells*. Journal of biomolecular screening, 2012. **17**(9): p. 1151-62.
129. Sung, H.-J., et al., *Synthetic polymeric substrates as potent pro-oxidant versus anti-oxidant regulators of cytoskeletal remodeling and cell apoptosis*. Journal of Cell physiology, 2009. **218**(3): p. 549-557.
130. Meredith, J.C., A. Karim, and E.J. Amis, *High-throughput measurement of polymer blend phase behavior*. Macromolecules, 2000. **33**(16): p. 5760-5762.
131. Amis, E.J., *Reaching beyond discovery*. Nature materials, 2004. **3**(2): p. 83-5.
132. Rodriguez, J.P., et al., *Cytoskeletal organization of human mesenchymal stem cells (MSC) changes during their osteogenic differentiation*. Journal of cellular biochemistry, 2004. **93**(4): p. 721-31.
133. McBeath, R., et al., *Cell shape, cytoskeletal tension, and RhoA regulate stem cell lineage commitment*. Developmental cell, 2004. **6**(4): p. 483-95.
134. Juliano, R.L., *Signal transduction by cell adhesion receptors and the cytoskeleton: functions of integrins, cadherins, selectins, and immunoglobulin-superfamily members*. Annual review of pharmacology and toxicology, 2002. **42**: p. 283-323.
135. Kapur, R. and A.S. Rudolph, *Cellular and cytoskeleton morphology and strength of adhesion of cells on self-assembled monolayers of organosilanes*. Experimental cell research, 1998. **244**(1): p. 275-85.
136. Lelievre, S., V.M. Weaver, and M.J. Bissell, *Extracellular matrix signaling from the cellular membrane skeleton to the nuclear skeleton: a model of gene regulation*. Recent progress in hormone research, 1996. **51**: p. 417-32.
137. Gieni, R.S. and M.J. Hendzel, *Mechanotransduction from the ECM to the genome: are the pieces now in place?* Journal of cellular biochemistry, 2008. **104**(6): p. 1964-87.
138. Sikavitsas, V.I., J.S. Temenoff, and A.G. Mikos, *Biomaterials and bone mechanotransduction*. Biomaterials, 2001. **22**(19): p. 2581-93.
139. Pajerowski, J.D., et al., *Physical plasticity of the nucleus in stem cell differentiation*. Proceedings of the National Academy of Sciences of the United States of America, 2007. **104**(40): p. 15619-15624.
140. Olson, M.O., K. Hingorani, and A. Szebeni, *Conventional and nonconventional roles of the nucleolus*. International review of cytology, 2002. **219**: p. 199-266.
141. Gribbon, C., et al., *Association of the nuclear matrix component NuMA with the Cajal body and nuclear speckle compartments during transitions in transcriptional activity in lens cell differentiation*. European journal of cell biology, 2002. **81**(10): p. 557-66.

142. Dillon, N. and R. Festenstein, *Unravelling heterochromatin: competition between positive and negative factors regulates accessibility*. Trends in genetics : TIG, 2002. **18**(5): p. 252-8.
143. Bissell, M.J., et al., *Tissue structure, nuclear organization, and gene expression in normal and malignant breast*. Cancer research, 1999. **59**(7 Suppl): p. 1757-1763s; discussion 1763s-1764s.
144. Antoniou, M., et al., *Nuclear organization of splicing snRNPs during differentiation of murine erythroleukemia cells in vitro*. The Journal of cell biology, 1993. **123**(5): p. 1055-68.
145. Szczerbal, I. and J.M. Bridger, *Association of adipogenic genes with SC-35 domains during porcine adipogenesis*. Chromosome research : an international journal on the molecular, supramolecular and evolutionary aspects of chromosome biology, 2010. **18**(8): p. 887-95.
146. Romero-Prado, M., et al., *Functional characterization of human mesenchymal stem cells that maintain osteochondral fates*. Journal of cellular biochemistry, 2006. **98**(6): p. 1457-70.
147. Moen, P.T., Jr., et al., *Repositioning of muscle-specific genes relative to the periphery of SC-35 domains during skeletal myogenesis*. Molecular biology of the cell, 2004. **15**(1): p. 197-206.
148. Ingber, D.E., *Cellular basis of mechanotransduction*. The Biological bulletin, 1998. **194**(3): p. 323-5; discussion 325-7.
149. Wang, N., J.P. Butler, and D.E. Ingber, *Mechanotransduction across the cell surface and through the cytoskeleton*. Science, 1993. **260**(5111): p. 1124-7.
150. Janmey, P.A., *The cytoskeleton and cell signaling: component localization and mechanical coupling*. Physiological reviews, 1998. **78**(3): p. 763-81.
151. Ingber, D.E., *Mechanosensation through integrins: cells act locally but think globally*. Proceedings of the National Academy of Sciences of the United States of America, 2003. **100**(4): p. 1472-4.
152. Ren, X.D., W.B. Kiosses, and M.A. Schwartz, *Regulation of the small GTP-binding protein Rho by cell adhesion and the cytoskeleton*. The EMBO journal, 1999. **18**(3): p. 578-85.
153. Ridley, A.J., *Rho GTPases and actin dynamics in membrane protrusions and vesicle trafficking*. Trends in cell biology, 2006. **16**(10): p. 522-9.
154. Ridley, A.J. and A. Hall, *The small GTP-binding protein rho regulates the assembly of focal adhesions and actin stress fibers in response to growth factors*. Cell, 1992. **70**(3): p. 389-99.
155. Chen, C.S., et al., *Cell shape provides global control of focal adhesion assembly*. Biochemical and biophysical research communications, 2003. **307**(2): p. 355-61.
156. Schoenwaelder, S.M. and K. Burridge, *Bidirectional signaling between the cytoskeleton and integrins*. Current opinion in cell biology, 1999. **11**(2): p. 274-86.
157. Chen, C.S., et al., *Geometric control of cell life and death*. Science, 1997. **276**(5317): p. 1425-8.
158. Huang, S. and D.E. Ingber, *A discrete cell cycle checkpoint in late G(1) that is cytoskeleton-dependent and MAP kinase (Erk)-independent*. Experimental cell research, 2002. **275**(2): p. 255-64.
159. Huang, S., C.S. Chen, and D.E. Ingber, *Control of cyclin D1, p27(Kip1), and cell cycle progression in human capillary endothelial cells by cell shape and cytoskeletal tension*. Molecular biology of the cell, 1998. **9**(11): p. 3179-93.

160. Chen, C.S., C. Brangwynne, and D.E. Ingber, *Pictures in cell biology: squaring up to the cell-shape debate*. Trends in cell biology, 1999. **9**(7): p. 283.
161. Lelievre, S.A., M.J. Bissell, and P. Pujuguet, *Cell nucleus in context*. Critical reviews in eukaryotic gene expression, 2000. **10**(1): p. 13-20.
162. Lelievre, S.A., et al., *Tissue phenotype depends on reciprocal interactions between the extracellular matrix and the structural organization of the nucleus*. Proceedings of the National Academy of Sciences of the United States of America, 1998. **95**(25): p. 14711-6.
163. Akhtar, A. and S.M. Gasser, *The nuclear envelope and transcriptional control*. Nature reviews. Genetics, 2007. **8**(7): p. 507-17.
164. Spector, D.L., *The dynamics of chromosome organization and gene regulation*. Annual review of biochemistry, 2003. **72**: p. 573-608.
165. Gaspar-Maia, A., et al., *Open chromatin in pluripotency and reprogramming*. Nature reviews. Molecular cell biology, 2011. **12**(1): p. 36-47.
166. Jaenisch, R. and A. Bird, *Epigenetic regulation of gene expression: how the genome integrates intrinsic and environmental signals*. Nature genetics, 2003. **33** Suppl: p. 245-54.
167. Bird, A.P., *CpG-rich islands and the function of DNA methylation*. Nature, 1986. **321**(6067): p. 209-13.
168. Prendergast, J.G., et al., *Chromatin structure and evolution in the human genome*. BMC evolutionary biology, 2007. **7**: p. 72.
169. Jensen, O.N., *Interpreting the protein language using proteomics*. Nature reviews. Molecular cell biology, 2006. **7**(6): p. 391-403.
170. Kaji, K., et al., *The NuRD component Mbd3 is required for pluripotency of embryonic stem cells*. Nature cell biology, 2006. **8**(3): p. 285-92.
171. Shen, S., J. Li, and P. Casaccia-Bonnel, *Histone modifications affect timing of oligodendrocyte progenitor differentiation in the developing rat brain*. The Journal of cell biology, 2005. **169**(4): p. 577-89.
172. Lee, J.H., S.R. Hart, and D.G. Skalnik, *Histone deacetylase activity is required for embryonic stem cell differentiation*. Genesis, 2004. **38**(1): p. 32-8.
173. Yang, C.H., E.J. Lambie, and M. Snyder, *NuMA: an unusually long coiled-coil related protein in the mammalian nucleus*. The Journal of cell biology, 1992. **116**(6): p. 1303-17.
174. Du, Q., et al., *LGN blocks the ability of NuMA to bind and stabilize microtubules. A mechanism for mitotic spindle assembly regulation*. Current biology : CB, 2002. **12**(22): p. 1928-33.
175. Haren, L. and A. Merdes, *Direct binding of NuMA to tubulin is mediated by a novel sequence motif in the tail domain that bundles and stabilizes microtubules*. Journal of cell science, 2002. **115**(Pt 9): p. 1815-24.
176. Luderus, M.E., et al., *Binding of matrix attachment regions to lamin polymers involves single-stranded regions and the minor groove*. Molecular and cellular biology, 1994. **14**(9): p. 6297-305.
177. Wong, R.W., G. Blobel, and E. Coutavas, *Rae1 interaction with NuMA is required for bipolar spindle formation*. Proceedings of the National Academy of Sciences of the United States of America, 2006. **103**(52): p. 19783-7.
178. Radulescu, A.E. and D.W. Cleveland, *NuMA after 30 years: the matrix revisited*. Trends in cell biology, 2010. **20**(4): p. 214-22.
179. Kim, S.K., *Cell polarity: new PARTners for Cdc42 and Rac*. Nature cell biology, 2000. **2**(8): p. E143-5.

180. Lin, D., et al., *A mammalian PAR-3-PAR-6 complex implicated in Cdc42/Rac1 and aPKC signalling and cell polarity*. Nature cell biology, 2000. **2**(8): p. 540-7.
181. Lechler, T. and E. Fuchs, *Asymmetric cell divisions promote stratification and differentiation of mammalian skin*. Nature, 2005. **437**(7056): p. 275-80.
182. Dellaire, G. and D.P. Bazett-Jones, *PML nuclear bodies: dynamic sensors of DNA damage and cellular stress*. BioEssays : news and reviews in molecular, cellular and developmental biology, 2004. **26**(9): p. 963-77.
183. Lamond, A.I. and D.L. Spector, *Nuclear speckles: a model for nuclear organelles*. Nature reviews. Molecular cell biology, 2003. **4**(8): p. 605-12.
184. Berezney, R. and D.S. Coffey, *Identification of a nuclear protein matrix*. Biochemical and biophysical research communications, 1974. **60**(4): p. 1410-7.
185. Capco, D.G., K.M. Wan, and S. Penman, *The nuclear matrix: three-dimensional architecture and protein composition*. Cell, 1982. **29**(3): p. 847-58.
186. Nickerson, J.A., et al., *The nuclear matrix revealed by eluting chromatin from a cross-linked nucleus*. Proceedings of the National Academy of Sciences of the United States of America, 1997. **94**(9): p. 4446-50.
187. Kempf, T., et al., *Isolation of human NuMA protein*. FEBS letters, 1994. **354**(3): p. 307-10.
188. Harborth, J., et al., *Self assembly of NuMA: multiarm oligomers as structural units of a nuclear lattice*. The EMBO journal, 1999. **18**(6): p. 1689-700.
189. Merdes, A. and D.W. Cleveland, *The role of NuMA in the interphase nucleus*. Journal of cell science, 1998. **111 (Pt 1)**: p. 71-9.
190. Vidi, P.A., et al., *Interconnected contribution of tissue morphogenesis and the nuclear protein NuMA to the DNA damage response*. Journal of cell science, 2012. **125**(Pt 2): p. 350-61.
191. Spector, D.L. and A.I. Lamond, *Nuclear Speckles*. Cold Spring Harbor perspectives in biology, 2011. **3**(2).
192. Misteli, T. and D.L. Spector, *Protein phosphorylation and the nuclear organization of pre-mRNA splicing*. Trends in cell biology, 1997. **7**(4): p. 135-8.
193. Thiry, M., *The interchromatin granules*. Histology and histopathology, 1995. **10**(4): p. 1035-45.
194. Shopland, L.S., et al., *Clustering of multiple specific genes and gene-rich R-bands around SC-35 domains: evidence for local euchromatic neighborhoods*. The Journal of cell biology, 2003. **162**(6): p. 981-90.
195. Melcak, I., et al., *Nuclear pre-mRNA compartmentalization: trafficking of released transcripts to splicing factor reservoirs*. Molecular biology of the cell, 2000. **11**(2): p. 497-510.
196. Spector, D.L., X.D. Fu, and T. Maniatis, *Associations between distinct pre-mRNA splicing components and the cell nucleus*. The EMBO journal, 1991. **10**(11): p. 3467-81.
197. Bridge, E., et al., *Dynamic organization of splicing factors in adenovirus-infected cells*. Journal of virology, 1995. **69**(1): p. 281-90.
198. Jimenez-Garcia, L.F. and D.L. Spector, *In vivo evidence that transcription and splicing are coordinated by a recruiting mechanism*. Cell, 1993. **73**(1): p. 47-59.
199. Tenney, R.M. and D.E. Discher, *Stem cells, microenvironment mechanics, and growth factor activation*. Current opinion in cell biology, 2009. **21**(5): p. 630-5.
200. Peters, A., D.M. Brey, and J.A. Burdick, *High-throughput and combinatorial technologies for tissue engineering applications*. Tissue engineering. Part B, Reviews, 2009. **15**(3): p. 225-39.

201. Kunisada, Y., M. Shoji, and M. Hosoya, *A gene expression-based screening system for compounds influencing differentiation of mouse embryonic stem cells*. Journal of biomolecular screening, 2012. **17**(2): p. 140-51.
202. Bowtell, D.D., *Options available--from start to finish--for obtaining expression data by microarray*. Nature genetics, 1999. **21**(1 Suppl): p. 25-32.
203. Velculescu, V.E., et al., *Serial analysis of gene expression*. Science, 1995. **270**(5235): p. 484-7.
204. Schena, M., et al., *Quantitative monitoring of gene expression patterns with a complementary DNA microarray*. Science, 1995. **270**(5235): p. 467-70.
205. Maffia, A.M., 3rd, I.I. Kariv, and K.R. Oldenburg, *Miniaturization of a Mammalian Cell-Based Assay: Luciferase Reporter Gene Readout in a 3 Microliter 1536-Well Plate*. Journal of biomolecular screening, 1999. **4**(3): p. 137-142.
206. Lockhart, D.J., et al., *Expression monitoring by hybridization to high-density oligonucleotide arrays*. Nature Biotechnology, 1996. **14**(13): p. 1675-80.
207. Liu, E., et al., *High-content profiling of cell responsiveness to graded substrates based on combinatorially variant polymers*. Comb Chem High Throughput Screen, 2009. **12**(7): p. 646-55.
208. Ludwig, T.E., et al., *Derivation of human embryonic stem cells in defined conditions*. Nature Biotechnology, 2006. **24**(2): p. 185-7.
209. Briggs, T., et al., *Osteogenic differentiation of human mesenchymal stem cells on poly(ethylene glycol)-variant biomaterials*. Journal of biomedical materials research. Part A, 2009. **91**(4): p. 975-84.
210. Moore, N.M., et al., *Synergistic enhancement of human bone marrow stromal cell proliferation and osteogenic differentiation on BMP-2-derived and RGD peptide concentration gradients*. Acta Biomaterialia, 2011. **7**(5): p. 2091-2100.
211. Gallant, N.D., et al., *Universal gradient substrates for "click" biofunctionalization*. Advanced materials, 2007. **19**(7): p. 965-+.
212. Moore, N.M., et al., *The use of immobilized osteogenic growth peptide on gradient substrates synthesized via click chemistry to enhance MC3T3-E1 osteoblast proliferation*. Biomaterials, 2010. **31**(7): p. 1604-1611.
213. Jin, H.J., et al., *Down-regulation of CD105 is associated with multi-lineage differentiation in human umbilical cord blood-derived mesenchymal stem cells*. Biochemical and biophysical research communications, 2009. **381**(4): p. 676-81.
214. Delorme, B., et al., *Specific plasma membrane protein phenotype of culture-amplified and native human bone marrow mesenchymal stem cells*. Blood, 2008. **111**(5): p. 2631-5.
215. Dahl, K.N. and A. Kalinowski, *Nucleoskeleton mechanics at a glance*. Journal of cell science, 2011. **124**(Pt 5): p. 675-8.
216. Kumar, A. and G.M. Whitesides, *Patterned condensation figures as optical diffraction gratings*. Science, 1994. **263**(5143): p. 60-2.
217. Phillips, J.E., et al., *Human mesenchymal stem cell differentiation on self-assembled monolayers presenting different surface chemistries*. Acta Biomaterialia, 2010. **6**(1): p. 12-20.
218. Goldschneider, I., et al., *Analysis of rat hemopoietic cells on the fluorescence-activated cell sorter. I. Isolation of pluripotent hemopoietic stem cells and granulocyte-macrophage progenitor cells*. The Journal of experimental medicine, 1980. **152**(2): p. 419-37.

219. Klimanskaya, I., N. Rosenthal, and R. Lanza, *Derive and conquer: sourcing and differentiating stem cells for therapeutic applications*. Nature reviews. Drug discovery, 2008. **7**(2): p. 131-42.
220. Chamberlain, G., et al., *Concise review: mesenchymal stem cells: their phenotype, differentiation capacity, immunological features, and potential for homing*. Stem Cells, 2007. **25**(11): p. 2739-49.
221. Tolar, J., et al., *Sarcoma derived from cultured mesenchymal stem cells*. Stem Cells, 2007. **25**(2): p. 371-9.
222. Tysnes, B.B., *Tumor-initiating and -propagating cells: cells that we would like to identify and control*. Neoplasia, 2010. **12**(7): p. 506-15.
223. Chandramouly, G., et al., *The control of tissue architecture over nuclear organization is crucial for epithelial cell fate*. J Cell Sci, 2007. **120**(Pt 9): p. 1596-606.
224. DiPaolo, J.A. and B.C. Casto, *Quantitative studies of in vitro morphological transformation of Syrian hamster cells by inorganic metal salts*. Cancer research, 1979. **39**(3): p. 1008-13.
225. Li, N., et al., *Genetically transforming human mesenchymal stem cells to sarcomas: changes in cellular phenotype and multilineage differentiation potential*. Cancer, 2009. **115**(20): p. 4795-806.
226. Power, J., et al., *Oligodendrocyte precursor cells from different brain regions express divergent properties consistent with the differing time courses of myelination in these regions*. Dev Biol, 2002. **245**(2): p. 362-75.
227. Graham, F.L., et al., *Characteristics of a human cell line transformed by DNA from human adenovirus type 5*. The Journal of general virology, 1977. **36**(1): p. 59-74.
228. Boussif, O., et al., *A versatile vector for gene and oligonucleotide transfer into cells in culture and in vivo: polyethylenimine*. Proceedings of the National Academy of Sciences of the United States of America, 1995. **92**(16): p. 7297-301.
229. Hande, K.R., *Etoposide: four decades of development of a topoisomerase II inhibitor*. European journal of cancer, 1998. **34**(10): p. 1514-21.
230. Torres, K. and S.B. Horwitz, *Mechanisms of Taxol-induced cell death are concentration dependent*. Cancer research, 1998. **58**(16): p. 3620-6.
231. Bourke, S.L. and J. Kohn, *Polymers derived from the amino acid L-tyrosine: polycarbonates, polyarylates and copolymers with poly(ethylene glycol)*. Advanced drug delivery reviews, 2003. **55**(4): p. 447-66.
232. Kholodovych, V., et al., *Prediction of biological response for large combinatorial libraries of biodegradable polymers: Polymethacrylates as a test case*. Polymer, 2008. **49**(10): p. 2435-2439.
233. Burness, M.L. and D.A. Sipkins, *The stem cell niche in health and malignancy*. Semin Cancer Biol. **20**(2): p. 107-15.
234. Liu, C., et al., *Multiple tumor types may originate from bone marrow-derived cells*. Neoplasia, 2006. **8**(9): p. 716-24.
235. Rosland, G.V., et al., *Long-term cultures of bone marrow-derived human mesenchymal stem cells frequently undergo spontaneous malignant transformation*. Cancer research, 2009. **69**(13): p. 5331-9.
236. Sher, F., et al., *Oligodendrocyte differentiation and implantation: new insights for remyelinating cell therapy*. Curr Opin Neurol, 2008. **21**(5): p. 607-14.
237. Raff, M., et al., *Timing cell-cycle exit and differentiation in oligodendrocyte development*. Novartis Found Symp, 2001. **237**: p. 100-7; discussion 107-12, 158-63.

238. Wani, M.C., et al., *Plant antitumor agents. VI. The isolation and structure of taxol, a novel antileukemic and antitumor agent from Taxus brevifolia*. Journal of the American Chemical Society, 1971. **93**(9): p. 2325-7.
239. Abad, P.C., et al., *NuMA influences higher order chromatin organization in human mammary epithelium*. Molecular biology of the cell, 2007. **18**(2): p. 348-61.
240. Weaver, V.M., et al., *Degradation of nuclear matrix and DNA cleavage in apoptotic thymocytes*. Journal of cell science, 1996. **109** (Pt 1): p. 45-56.
241. Knowles, D.W., et al., *Automated local bright feature image analysis of nuclear protein distribution identifies changes in tissue phenotype*. Proceedings of the National Academy of Sciences of the United States of America, 2006. **103**(12): p. 4445-50.
242. Behrend, L., G. Henderson, and R.M. Zwacka, *Reactive oxygen species in oncogenic transformation*. Biochemical Society transactions, 2003. **31**(Pt 6): p. 1441-4.
243. Fruehauf, J.P. and F.L. Meyskens, Jr., *Reactive oxygen species: a breath of life or death?* Clinical cancer research : an official journal of the American Association for Cancer Research, 2007. **13**(3): p. 789-94.
244. Valko, M., et al., *Free radicals, metals and antioxidants in oxidative stress-induced cancer*. Chemico-biological interactions, 2006. **160**(1): p. 1-40.
245. Sung, H.J., et al., *Synthetic polymeric substrates as potent pro-oxidant versus anti-oxidant regulators of cytoskeletal remodeling and cell apoptosis*. J Cell Physiol, 2009. **218**(3): p. 549-57.
246. Li, J.Y., et al., *Critical issues of clinical human embryonic stem cell therapy for brain repair*. Trends in neurosciences, 2008. **31**(3): p. 146-53.
247. Rossi, F. and E. Cattaneo, *Opinion: neural stem cell therapy for neurological diseases: dreams and reality*. Nature reviews. Neuroscience, 2002. **3**(5): p. 401-9.
248. Keyoung, H.M., et al., *High-yield selection and extraction of two promoter-defined phenotypes of neural stem cells from the fetal human brain*. Nature Biotechnology, 2001. **19**(9): p. 843-50.
249. Caplan, A.I., *Mesenchymal stem cells*. Journal of orthopaedic research : official publication of the Orthopaedic Research Society, 1991. **9**(5): p. 641-50.
250. Curran, J.M., R. Chen, and J.A. Hunt, *The guidance of human mesenchymal stem cell differentiation in vitro by controlled modifications to the cell substrate*. Biomaterials, 2006. **27**(27): p. 4783-93.
251. Discher, D.E., D.J. Mooney, and P.W. Zandstra, *Growth factors, matrices, and forces combine and control stem cells*. Science, 2009. **324**(5935): p. 1673-7.
252. Guilak, F., et al., *Control of stem cell fate by physical interactions with the extracellular matrix*. Cell stem cell, 2009. **5**(1): p. 17-26.
253. Anderson, D.G., et al., *Biomaterial microarrays: rapid, microscale screening of polymer-cell interaction*. Biomaterials, 2005. **26**(23): p. 4892-7.
254. Moe, A.A., et al., *Microarray with micro- and nano-topographies enables identification of the optimal topography for directing the differentiation of primary murine neural progenitor cells*. Small, 2012. **8**(19): p. 3050-61.
255. Kilian, K.A., et al., *Geometric cues for directing the differentiation of mesenchymal stem cells*. Proceedings of the National Academy of Sciences of the United States of America, 2010. **107**(11): p. 4872-7.
256. Kim, J.J., S.L. Vega, and P.V. Moghe, *A high content imaging-based approach for classifying cellular phenotypes*. Methods in molecular biology, 2013. **1052**: p. 1-8.

257. Wei, Y., et al., *CDK1-dependent phosphorylation of EZH2 suppresses methylation of H3K27 and promotes osteogenic differentiation of human mesenchymal stem cells*. Nature cell biology, 2011. **13**(1): p. 87-94.
258. Akter, R., et al., *Effect of lamin A/C knockdown on osteoblast differentiation and function*. Journal of bone and mineral research : the official journal of the American Society for Bone and Mineral Research, 2009. **24**(2): p. 283-93.
259. Swift, J., et al., *Nuclear lamin-A scales with tissue stiffness and enhances matrix-directed differentiation*. Science, 2013. **341**(6149): p. 1240104.
260. Lee, K.S., et al., *Runx2 is a common target of transforming growth factor beta1 and bone morphogenetic protein 2, and cooperation between Runx2 and Smad5 induces osteoblast-specific gene expression in the pluripotent mesenchymal precursor cell line C2C12*. Molecular and cellular biology, 2000. **20**(23): p. 8783-92.
261. Noer, A., L.C. Lindeman, and P. Collas, *Histone H3 modifications associated with differentiation and long-term culture of mesenchymal adipose stem cells*. Stem cells and development, 2009. **18**(5): p. 725-36.
262. Boltau, M., et al., *Surface-induced structure formation of polymer blends on patterned substrates*. Nature, 1998. **391**(6670): p. 877-879.
263. Carlson, A.L., et al., *Microfibrous substrate geometry as a critical trigger for organization, self-renewal, and differentiation of human embryonic stem cells within synthetic 3-dimensional microenvironments*. Faseb Journal, 2012. **26**(8): p. 3240-3251.
264. Lim, S.K., et al., *Tyrosine phosphorylation of transcriptional coactivator WW-domain binding protein 2 regulates estrogen receptor alpha function in breast cancer via the Wnt pathway*. Faseb Journal, 2011. **25**(9): p. 3004-18.
265. Wang, W.C., et al., *IL-6 augmented motility of airway epithelial cell BEAS-2B via Akt/GSK-3beta signaling pathway*. Journal of cellular biochemistry, 2012. **113**(11): p. 3567-75.
266. Haralick, R.M., Shanmugam, K., Dinstein, I., *Texture Features for Image Classification*. Systems, Man and Cybernetics, 1973. **SMC-3**(6): p. 610-621.
267. McMurray, R.J., et al., *Surface topography regulates wnt signaling through control of primary cilia structure in mesenchymal stem cells*. Scientific reports, 2013. **3**: p. 3545.
268. Kumar, G., et al., *The determination of stem cell fate by 3D scaffold structures through the control of cell shape*. Biomaterials, 2011. **32**(35): p. 9188-96.
269. Nathan, A.S., et al., *Mechano-topographic modulation of stem cell nuclear shape on nanofibrous scaffolds*. Acta biomaterialia, 2011. **7**(1): p. 57-66.
270. Shin, M., H. Yoshimoto, and J.P. Vacanti, *In vivo bone tissue engineering using mesenchymal stem cells on a novel electrospun nanofibrous scaffold*. Tissue engineering, 2004. **10**(1-2): p. 33-41.
271. Li, C., et al., *Electrospun silk-BMP-2 scaffolds for bone tissue engineering*. Biomaterials, 2006. **27**(16): p. 3115-24.
272. Yang, W., et al., *In vivo bone generation via the endochondral pathway on three-dimensional electrospun fibers*. Acta Biomaterialia, 2013. **9**(1): p. 4505-12.
273. Takahashi, Y. and Y. Tabata, *Effect of the fiber diameter and porosity of non-woven PET fabrics on the osteogenic differentiation of mesenchymal stem cells*. Journal of Biomaterials Science-Polymer Edition, 2004. **15**(1): p. 41-57.
274. Dalby, M.J., et al., *The control of human mesenchymal cell differentiation using nanoscale symmetry and disorder*. Nature materials, 2007. **6**(12): p. 997-1003.
275. Hwang, N.S., et al., *Biomaterials directed in vivo osteogenic differentiation of mesenchymal cells derived from human embryonic stem cells*. Tissue engineering. Part A, 2013. **19**(15-16): p. 1723-32.

276. Bai, B., et al., *Activation of the ERK1/2 signaling pathway during the osteogenic differentiation of mesenchymal stem cells cultured on substrates modified with various chemical groups*. Biomed Res Int, 2013. **2013**: p. 361906.
277. Teo, B.K., et al., *Nanotopography modulates mechanotransduction of stem cells and induces differentiation through focal adhesion kinase*. ACS Nano, 2013. **7**(6): p. 4785-98.
278. Ozdemir, T., et al., *Substrate curvature sensing through Myosin IIa upregulates early osteogenesis*. Integr Biol (Camb), 2013. **5**(11): p. 1407-16.
279. de Boer, J., et al., *Wnt signaling inhibits osteogenic differentiation of human mesenchymal stem cells*. Bone, 2004. **34**(5): p. 818-26.
280. Salasnyk, R.M., et al., *Activation of FAK is necessary for the osteogenic differentiation of human mesenchymal stem cells on laminin-5*. Journal of cellular biochemistry, 2007. **100**(2): p. 499-514.
281. Galli, C., et al., *Rough surface topography enhances the activation of Wnt/beta-catenin signaling in mesenchymal cells*. Journal of biomedical materials research. Part A, 2010. **95**(3): p. 682-90.
282. Liao, X., et al., *The effect of differentiation induction on FAK and Src activity in live HMSCs visualized by FRET*. PLoS One, 2013. **8**(8): p. e72233.
283. Xu, B., Y. Ju, and G. Song, *Role of p38, ERK1/2, focal adhesion kinase, RhoA/ROCK and cytoskeleton in the adipogenesis of human mesenchymal stem cells*. J Biosci Bioeng, 2013.
284. Abraham, S., N. Eroshenko, and R.R. Rao, *Role of bioinspired polymers in determination of pluripotent stem cell fate*. Regenerative medicine, 2009. **4**(4): p. 561-78.
285. Nolan, K., et al., *Tissue engineering and biomaterials in regenerative medicine*. Cell transplantation, 2008. **17**(3): p. 241-3.
286. Covert, M.W., et al., *Integrating high-throughput and computational data elucidates bacterial networks*. Nature, 2004. **429**(6987): p. 92-6.
287. Di Ventura, B., et al., *From in vivo to in silico biology and back*. Nature, 2006. **443**(7111): p. 527-33.
288. Orth, J.D., et al., *A comprehensive genome-scale reconstruction of Escherichia coli metabolism--2011*. Molecular systems biology, 2011. **7**: p. 535.
289. Thiele, I., et al., *Genome-scale reconstruction of Escherichia coli's transcriptional and translational machinery: a knowledge base, its mathematical formulation, and its functional characterization*. PLoS computational biology, 2009. **5**(3): p. e1000312.
290. Karr, J.R., et al., *A whole-cell computational model predicts phenotype from genotype*. Cell, 2012. **150**(2): p. 389-401.
291. Ridley, A.J., et al., *The small GTP-binding protein rac regulates growth factor-induced membrane ruffling*. Cell, 1992. **70**(3): p. 401-10.
292. Espina, V., et al., *Laser-capture microdissection*. Nature protocols, 2006. **1**(2): p. 586-603.
293. Herzenberg, L.A., et al., *The history and future of the fluorescence activated cell sorter and flow cytometry: a view from Stanford*. Clinical Chemistry, 2002. **48**(10): p. 1819-27.
294. Davey, H.M. and D.B. Kell, *Flow cytometry and cell sorting of heterogeneous microbial populations: the importance of single-cell analyses*. Microbiological reviews, 1996. **60**(4): p. 641-96.
295. Pliss, A., et al., *Biophotonic probing of macromolecular transformations during apoptosis*. Proceedings of the National Academy of Sciences of the United States of America, 2010. **107**(29): p. 12771-6.

296. Lee, Y.J., et al., *Quantitative, label-free characterization of stem cell differentiation at the single-cell level by broadband coherent anti-Stokes Raman scattering microscopy*. Tissue engineering. Part C, Methods, 2014. **20**(7): p. 562-9.
297. Swedlow, J.R., *Quantitative fluorescence microscopy and image deconvolution*. Methods Cell Biol, 2003. **72**: p. 349-67.
298. Sibarita, J.B., *Deconvolution microscopy*. Adv Biochem Eng Biotechnol, 2005. **95**: p. 201-43.
299. Conchello, J.A. and M.E. Dresser, *Extended depth-of-focus microscopy via constrained deconvolution*. J Biomed Opt, 2007. **12**(6): p. 064026.
300. Pankajakshan, P., et al., *Parametric blind deconvolution for confocal laser scanning microscopy*. Conf Proc IEEE Eng Med Biol Soc, 2007. **2007**: p. 6532-5.
301. Vicidomini, G., et al., *Application of the split-gradient method to 3D image deconvolution in fluorescence microscopy*. J Microsc, 2009. **234**(1): p. 47-61.
302. Coley, H.M., et al., *Examination by laser scanning confocal fluorescence imaging microscopy of the subcellular localisation of anthracyclines in parent and multidrug resistant cell lines*. Br J Cancer, 1993. **67**(6): p. 1316-23.
303. Aigner, J., et al., *[Realistic imaging of cell systems using confocal laser scanning microscopy exemplified by 3-dimensional chondrocyte culture]*. Laryngorhinootologie, 1997. **76**(4): p. 248-51.
304. Lopez, C., M.N. Pons, and E. Morgenroth, *Evaluation of microscopic techniques (epifluorescence microscopy, CLSM, TPE-LSM) as a basis for the quantitative image analysis of activated sludge*. Water Res, 2005. **39**(2-3): p. 456-68.
305. Nakano, A., *Spinning-disk confocal microscopy -- a cutting-edge tool for imaging of membrane traffic*. Cell Struct Funct, 2002. **27**(5): p. 349-55.
306. Adams, M.C., et al., *A high-speed multispectral spinning-disk confocal microscope system for fluorescent speckle microscopy of living cells*. Methods, 2003. **29**(1): p. 29-41.
307. Maddox, P.S., et al., *Spinning disk confocal microscope system for rapid high-resolution, multimode, fluorescence speckle microscopy and green fluorescent protein imaging in living cells*. Methods Enzymol, 2003. **360**: p. 597-617.
308. McAllister, R.G., D.R. Sisan, and J.S. Urbach, *Design and optimization of a high-speed, high-sensitivity, spinning disk confocal microscopy system*. J Biomed Opt, 2008. **13**(5): p. 054058.
309. Periasamy, A., et al., *An evaluation of two-photon excitation versus confocal and digital deconvolution fluorescence microscopy imaging in Xenopus morphogenesis*. Microsc Res Tech, 1999. **47**(3): p. 172-81.
310. Rubart, M., *Two-photon microscopy of cells and tissue*. Circ Res, 2004. **95**(12): p. 1154-66.
311. Goksor, M., J. Enger, and D. Hanstorp, *Optical manipulation in combination with multiphoton microscopy for single-cell studies*. Appl Opt, 2004. **43**(25): p. 4831-7.
312. Sahai, E., et al., *Simultaneous imaging of GFP, CFP and collagen in tumors in vivo using multiphoton microscopy*. BMC Biotechnol, 2005. **5**: p. 14.
313. Gertler, A., et al., *Fluorescence resonance energy transfer (FRET) microscopy in living cells as a novel tool for the study of cytokine action*. J Dairy Res, 2005. **72 Spec No**: p. 14-9.
314. Jares-Erijman, E.A. and T.M. Jovin, *Imaging molecular interactions in living cells by FRET microscopy*. Curr Opin Chem Biol, 2006. **10**(5): p. 409-16.

315. Xu, X., J.A. Brzostowski, and T. Jin, *Using quantitative fluorescence microscopy and FRET imaging to measure spatiotemporal signaling events in single living cells*. Methods Mol Biol, 2006. **346**: p. 281-96.
316. Huebsch, N.D. and D.J. Mooney, *Fluorescent resonance energy transfer: A tool for probing molecular cell-biomaterial interactions in three dimensions*. Biomaterials, 2007. **28**(15): p. 2424-37.
317. Periasamy, A. and R.N. Day, *Visualizing protein interactions in living cells using digitized GFP imaging and FRET microscopy*. Methods Cell Biol, 1999. **58**: p. 293-314.
318. Nishikawa, S., [Basics of TIRFM]. Nippon Rinsho, 2007. **65**(2): p. 263-9.
319. Axelrod, D., *Chapter 7: Total internal reflection fluorescence microscopy*. Methods Cell Biol, 2008. **89**: p. 169-221.
320. Burmeister, J.S., et al., *Application of total internal reflection fluorescence microscopy to study cell adhesion to biomaterials*. Biomaterials, 1998. **19**(4-5): p. 307-25.
321. Curtis, A.S., *Cell reactions with biomaterials: the microscopies*. European cells & materials, 2001. **1**: p. 59-65.
322. Balfoort, H.W., et al., *Flow-Cytometry - Instrumentation and Application in Phytoplankton Research*. Hydrobiologia, 1992. **238**: p. 89-97.
323. Aeschbacher, M., C.A. Reinhardt, and G. Zbinden, *A rapid cell membrane permeability test using fluorescent dyes and flow cytometry*. Cell Biology and Toxicology, 1986. **2**(2): p. 247-55.
324. Zuba-Surma, E.K., et al., *The ImageStream System: a key step to a new era in imaging*. Folia histochemica et cytobiologica / Polish Academy of Sciences, Polish Histochemical and Cytochemical Society, 2007. **45**(4): p. 279-90.
325. Cox, G., *Optical imaging techniques in cell biology* 2007: CRC/Taylor & Francis Group. 268.
326. Faulk, W.P. and W. Hijmans, *Recent developments in immunofluorescence*. Prog Allergy, 1972. **16**: p. 9-39.
327. Harris, P.J., *Cytology and immunocytochemistry*. Methods Cell Biol, 1986. **27**: p. 243-62.
328. Matthews, J.B., *Immunocytochemical methods: a technical overview*. J Oral Pathol, 1987. **16**(4): p. 189-95.
329. Javois, L.C. and J.M. Mullins, *Overview of fluorescence photomicrography*. Methods Mol Biol, 1994. **34**: p. 331-4.
330. Jamieson, T., et al., *Biological applications of quantum dots*. Biomaterials, 2007. **28**(31): p. 4717-32.
331. Chan, W.C., et al., *Luminescent quantum dots for multiplexed biological detection and imaging*. Curr Opin Biotechnol, 2002. **13**(1): p. 40-6.
332. Jaiswal, J.K., et al., *Use of quantum dots for live cell imaging*. Nature methods, 2004. **1**(1): p. 73-8.
333. Pinaud, F., et al., *Advances in fluorescence imaging with quantum dot bio-probes*. Biomaterials, 2006. **27**(9): p. 1679-87.
334. Weng, J., et al., *Highly luminescent CdTe quantum dots prepared in aqueous phase as an alternative fluorescent probe for cell imaging*. Talanta, 2006. **70**(2): p. 397-402.
335. Yang, D.Z., S.K. Xu, and Q.F. Chen, [Applications of quantum dots to biological probes]. Guang Pu Xue Yu Guang Pu Fen Xi, 2007. **27**(9): p. 1807-10.
336. Misra, R.D., *Quantum dots for tumor-targeted drug delivery and cell imaging*. Nanomed, 2008. **3**(3): p. 271-4.
337. Smith, A.M., et al., *Bioconjugated quantum dots for in vivo molecular and cellular imaging*. Advanced drug delivery reviews, 2008. **60**(11): p. 1226-40.

- 338. Sunbul, M., et al., *Enzyme catalyzed site-specific protein labeling and cell imaging with quantum dots*. Chem Commun (Camb), 2008(45): p. 5927-9.
- 339. Tian, J., et al., *Controllable synthesis and cell-imaging studies on CdTe quantum dots together capped by glutathione and thioglycolic acid*. J Colloid Interface Sci, 2009. **336**(2): p. 504-9.
- 340. Walling, M.A., J.A. Novak, and J.R. Shepard, *Quantum dots for live cell and in vivo imaging*. Int J Mol Sci, 2009. **10**(2): p. 441-91.
- 341. Prendergast, F.G. and K.G. Mann, *Chemical and physical properties of aequorin and the green fluorescent protein isolated from Aequorea forskalea*. Biochemistry, 1978. **17**(17): p. 3448-53.
- 342. March, J.C., G. Rao, and W.E. Bentley, *Biotechnological applications of green fluorescent protein*. Appl Microbiol Biotechnol, 2003. **62**(4): p. 303-15.
- 343. Levskaya, A., et al., *Spatiotemporal control of cell signalling using a light-switchable protein interaction*. Nature, 2009.